Observing and Modeling Water Activity and Surface Changes over Dust Cover on Comet 67P/Churyumov-Gerasimenko

Von der Fakultät für Elektrotechnik, Informationstechnik, Physik
der Technischen Universität Carolo-Wilhelmina zu Braunschweig

zur Erlangung des Grades eines
Doktors der Naturwissenschaften (Dr. rer. nat.)

genehmigte Dissertation

von Hu, Xuanyu
aus Hunan, China

eingereicht am: 06/04/2017
Disputation am: 06/07/2017

1. Referentin oder Referent: Prof. Dr. Jürgen Blum
2. Referentin oder Referent: Prof. Dr. Jürgen Oberst

Druckjahr: 2018

Bibliografische Information der Deutschen Nationalbibliothek

Die Deutsche Nationalbibliothek verzeichnet diese Publikation in der Deutschen Nationalbibliografie; detaillierte bibliografische Daten sind im Internet über `http://dnb.d-nb.de` abrufbar.

Dissertation an der Technischen Universität Braunschweig,
Fakultät für Elektrotechnik, Informationstechnik, Physik

ISBN 978-3-944072-60-9

uni-edition GmbH 2018
http://www.uni-edition.de

Printed in Germany

Cover figure: nucleus of comet 67P/Churyumov-Gerasimenko imaged by the wide-angle camera of OSIRIS onboard Rosetta spacecraft at a distance of about 25 km from the nucleus surface on January 10, 2015. Credit: ESA/Rosetta/MPS for OSIRIS Team MPS/UPD/LAM/IAA/SSO/INTA/UPM/DASP/IDA

Contents

Abstract

It was not without a slight regret that, due to a delay in the launch of the spacecraft, the original target of the Rosetta mission, 46P/Wirtanen, a small Jupiter-Family comet with a kilometer-sized and widely active nucleus, had to be replaced with a more massive object, 67P/Churyumov-Gerasimenko (67P), likely with a less rejuvenated nucleus surface resembling most other Jupiter-Family members that had been explored *in situ* (Lamy et al. 2007) (Section 1).

The excitement of the Mission was nonetheless unabated and culminated in 2014 when Rosetta arrived in 67P after a ten-year chase, starting to escort the comet throughout its following perihelion passage (Section 2). What Rosetta discovered through the onboard cameras of OSIRIS was one of the most irregular objects ever encountered. The nucleus of 67P is shaped as a dumbbell, hinting at its formation by the merger of two independent bodies, and encompasses a rich variety of morphologies that reflect a complex history of not only cometary formation but also evolution governed by activity and gravity of the nucleus (Sierks et al. 2015, Thomas et al. 2015b). The northern hemi-nucleus is buried by a smooth cover of dust deposits, typically some meters in thickness, in contrast to the south exposing more rugged, consolidated terrains. As with all other comets, 67P nucleus is dark and very little fresh volatiles, in particular water ice, could be found on its surface (Capaccioni et al. 2015). The inner-coma was a tumultuous environment of outflowing gases disrupting and dragging dust debris from the nucleus on a global scale, in response to solar illumination. Changes of the nucleus surface had been continuously observed during the two-year rendezvous.

Characterizing the distribution of activity and surface changes over the nucleus were among the main scientific objectives of OSIRIS (Keller et al. 2007), that would shed light on the physical and compositional properties of the nucleus and its evolution. The activity of the surface area can be manifested in dust jets sourced therefrom. With accurate description of observation geometry, spatial structures of events near the nucleus can be reconstructed from their projections in images, even with a single observation. Ideally, nucleus changes are indicated by visual contrast of the surface pattern in different observations. In the case of 67P, the practicality of this rationale is often limited by the vastly dissimilar illumination and viewing conditions of different images. With this issue in mind, a classic photometric technique presented by Rindfleisch (1966) is proposed here specifically for deriving surface topography from a single image. The comparison of topographies over time provides a reliable means of verification and, given proper constraints, quantification of surface changes. These geometric and photometric methods for analyzing OSIRIS observations are discussed in Section 3, and should be of general in-

terest to a reader without background of image analysis.

To derive the nucleus properties of 67P from the observed dust activity and surface changes relies on modeling of the realistic thermo-physical conditions of nucleus at the epochs of observations. Little water ice on the surface of 67P suggests that the ice is, in general, buried and sublimates from underneath a prevalent, desiccated dust mantle. The presence of this insulating and suffocating dust mantle significantly modulates the heat transport and outgassing rate of the nucleus compared with a bare icy nucleus surface (Gundlach et al. 2011, Gundlach and Blum 2012). While the formation and nature of the mantle have long been established from a modeling standpoint, the application of such models seems far from popular (Mekler et al. 1990). The reluctance had probably resulted in part from the entrenched perception of limited active areas over comet nuclei in convenient coincidence with the scarcity of water ice exposed on the surface. In the case of 67P, this correlation is doubtful and tenuous at best. Section 4 is dedicated to the general formulation of cometary thermo-physical models with numerical recipes. Strategies for model parameterization are discussed that should facilitate the characterization of nucleus subsurface properties, such as thickness of the dust mantle, ice abundance, etc.

The application of thermal models to 67P, with an irregular-shaped nucleus, necessitates an elaborate treatment of illumination condition to account for prevalent shadowing effect arising from significant topographic concavities. The concavities may also give rise to non-negligible re-absorption of thermal radiation from the nucleus itself. The use of a realistic shape model is mandatory for evaluation of energy input. It is beneficial to furnish the shape model with a more detailed "landscape" database describing the local horizon at any point of the nucleus and mutual viewing conditions at two distinct locations. The concept and construction of this landscape database are detailed in Section 5.

The thermal model is subsequently applied to analyzing OSIRIS observations of dust activity (Section 6). While the sources of dust ejection observed as streams of faint brightness from the nucleus are difficult to determine in general, some dust jets had been observed to continue recurrently after daily sunset, in which case their footprints could be confined against the shadowed nucleus. Once the source area is constrained, the thermal models can be parameterized and applied to simulate the thermo-physical conditions of the local nucleus subsurface under which the observed dust activity could have occurred. It will be shown that these observed "sunset jets" were probably continuation of nominal dust activity from the day-side, sustained by water outgassing from depths that had remained warm enough for about one hour after sunset. In particular, the water ice probably had located at some shallow depths of merely a few millimeters.

The sunset jets originated mostly from the dust-covered terrains. This contests one of the early intuitions that the prevalent dust cover over northern hemi-nucleus of 67P was inactive, supposedly because meter-thick dry dust would insulate the icy interior from insolation and, thus, suffocate water activity. When 67P reached 2 AU inbound from the Sun, the dust cover had been widely altered (Section 7). It will be shown that these changes were erosive in nature and induced by sublimation of water accumulated over months. The quantification of the changes based on OSIRIS observations in comparison

with the estimation of accumulated water ice loss via thermo-physical modeling revealed a low ice abundance on the order of 1% in the dust cover on average. These results call for future effort into a fundamental but unresolved question regarding physics of cometary activity and evolution, namely, the detailed mechanism of ejection of dust induced by sublimation of lesser amounts of water ice underneath.

Kurzfassung

Die Euphorie über die Rosetta Mission erreichte ihren Höhepunkt im Jahr 2014, als die Raumsonde nach 10 Jahren Reise den Kometen 67P/Tschurjumow-Gerassimenko erreichte, um ihn über die nächsten zwei Jahre auf seiner Bahn um die Sonne zu begleiten. Dieser ungewöhnlich geformte Komet zeigt eine Vielfalt an Oberflächenmorphologie, welche die komplexe Geschichte seiner Entstehung und weiteren Evolution, geformt durch kometare Aktivität unter extrem geringer Gravitation, wiederspiegelt.

Das Verständnis von Aktivität und der dadurch hervorgerufenen Oberflächenänderungen war eine zentrale wissenschaftliche Zielsetzung für OSIRIS, dem Kamerasystem auf Rosetta. Dies sollte Aufschluss geben über die veränderlichen physikalischen Eigenschaften und die Materialzusammensetzung des Nukleus. In der vorliegenden Arbeit werden zunächst grundlegende geometrische und photometrische Methoden der Bildanalyse aufgearbeitet, welche die Lokalisierung von Staubaktivität und die Quantifizierung von Oberflächenveränderungen auf Komet 67P anhand von OSIRIS Bilddaten ermöglichen.

Um aus diesen Beobachtungen auf die physikalischen Eigenschaften des Nukleus zu schließen, ist eine Modellierung der thermophysikalischen Bedingungen in ausgewählten Zeiträumen nötig. Die Formulierung und Implementierung zweier thermophysikalischer Kometenmodelle sowie Strategien der Modellparametrisierung werden in dieser Arbeit ausgeführt. Die Modelle ermöglichen die Bestimmung von Eigenschaften wie der Dicke des ausgetrockneten Staubmantels und den Eisanteil des Kometen. Die Voraussetzung dafür ist eine aufwändige Bestimmung des Energieeintrags über die unregelmäßigen Landschaften, was insbesondere für die vorherrschende Schattenbedingungen und reflektierte thermische Strahlung gilt, die sich aus der komplexen Topographie ergeben.

Staubjets auf der Nachtseite wurden immer wieder auf 67P beobachtet, vielfach in der Nähe der Tag-Nacht-Grenze. Die thermophysikalischen Modelle werden parametriert und angewendet, um die thermischen und mechanischen Bedingungen in Schichten unter deren Quellenbereichen zu simulieren und die dort beobachtete Staubaktivität nach Sonnenuntergang zu erklären. Die Modelle zeigen, dass diese Jets wahrscheinlich aus Tiefen von wenigen Millimetern unterhalb der Oberfläche entstanden, wo durch Restwärme auch eine Stunde nach der Dunkelheit vorhandenes Wassereis verdampfen konnte.

In den Quellenbereichen dieser Jets haben erhebliche Oberflächenänderungen stattgefunden, als der Komet einen Abstand von 2 Astronomischen Einheiten zur Sonne erreichte. Ein Ergebnis dieser Arbeit ist, dass diese Veränderungen, sowie zahlreiche andere, die in ähnlichen Breiten gefunden wurden, in der Natur erosiv waren und durch die Sub-

limation von Wassereis verursacht wurden, welches über Monate angesammelt wurde. Vergleicht man quantitativ die Veränderungen basierend auf OSIRIS Beobachtungen mit dem akkumulierten Wassereisverlust aus den thermophysikalischen Modellen, ergibt sich ein niedriger Eisanteil in der Größenordnung von 1% im Staubmantel. Diese Ergebnisse adressieren eine fundamentale, aber ungelöste Frage nach der Physik der Kometenaktivität und -evolution, konkreter dem detaillierten Mechanismus des Ausstoßes von Staub, der durch Sublimation von geringeren Mengen an Wassereis verursacht wird.

1 To Study Comets

1.1 Frozen relics of early solar system

On what might appear to be fortuitous occasions, comets may become visible to the unaided eyes, displaying a pair of luminous tails from the night sky that sometimes even outshine stars (Fig. 1.1). Records of their prominent appearances have been nearly uninterrupted but nonetheless sparse for over two millennia (Yeomans et al. 1986). There is little surprise that our inquisitive but unprepared minds would long be held in awe of these ethereal and imposing events, predisposed to perceive their unusual sightings as ill omens in the continuity of worldly misfortunes (Fig. 1.2).

Our understanding of comet apparitions as astronomical phenomena, rather than astrological presages, improved symbolically with the development in the field of Celestial Mechanics, in particular, the discovery of elliptical motion of planets by Johannes Kepler and later the inauguration of Isaac Newton's *Principia* in 1687. Once equipped with a unified theory to explain the motions of planets and comets alike, Edmond Halley would identify four historical apparitions, in 1456, 1531, 1607, and 1682, respectively, made by the same comet, and anticipate its future return, writing "after the period of 76 years or more, about the end of the year 1758, or the beginning of the next" (Hughes 1987). In an emblematic triumph and celebration of the law of universal gravitation, the comet was spotted by astronomer Johann Georg Palitzsch on Christmas Day in 1758, thus proving its periodic returns along a highly elliptical orbit around the Sun unlike those of any known planets. Some marginal delay in the perihelion passage of the comet in March the following year caused by planetary perturbations had been forecast by Alexis Clairaut, Joseph Lalande, and Nicole-Reine Lepaute (Grier 2007). Halley's comet, which has since then borne the name of its first comprehender, is now known to have been an infrequent but regular visitor for at least thousands of years (Fig. 1.2).

Distant voyager The sporadic apparitions of a comet are among the indications of its distant origin from Earth and the Sun (Yeomans 2007). Halley's comet can only be observed (by unaided eyes) every ~75 years, when it returns from the furthest distance of more than 30 AU[i] from Earth, i.e., beyond Neptune, along a highly elliptical orbit (Yeomans and Kiang 1981) (Fig. 1.3). Another famous visitor, comet Hale-Bopp (formally C/1995 O1), that made a spectacular, year-long appearance around 1997 (Fig. 1.1), will return in some 2000 years. The current outbound journey will take it beyond 350 AU from the Sun in about 1000 years (Marsden 1997) (Fig. 1.3).

[i] 1 AU $\approx 1.5 \times 10^8$ km.

Figure 1.1: Images of comet Hale-Bopp in the night sky (©Philipp Salzgeber). The comet displays a curved, yellowish dust tail and a straight, light blue ion tail away from the Sun, seen here just below the horizon. In both images, the curvatures of the dust tails suggest the apparent movement of the comet from right to left. Permission to use the images granted by Philipp Salzgeber.

Figure 1.2: Record of apparition of comet Halley in 240 BC by ancient Chinese, as documented in Shi-Ji. It was stated that, from the highlighted text on the right, the comet (“ 彗星 ”) first appeared from the East (“ 東 ”), followed by its sightings in the North (“ 北 ”) and West (“ 西 ”). The reappearance of Halley’s comet in the West had coincided with the death of the Queen Mother of the hitherto deceased ruler (i.e., the Grandmother of the reigning King) of the *Qin State* during the *Warring States Period* in ancient China. This figure is adapted from an image file from Wikipedia, being a photograph of work of art in the public domain. Source of photograph is Fig. 5.2 in Xu et al. (2000).

The size, shape, and orientation of such cometary orbits as for Halley and Hale-Bopp returning after extended periods suggest that these comets originated from the outer rims of the solar system. In particular, the existence of the profound yet diffuse Oort cloud of small icy objects, probably leftover materials forming the large planets, or planetesimals, residing as far as tens of thousands of AU from the Sun, has been theorized to be a possible source region (Dones et al. 2004). The objects dwelling in the Oort cloud are hardly bound by the gravitation of the Sun; those that would venture into the inner solar system may have been excited by the stars passing near or threading through the Cloud via gravitational perturbations.

While comets such as Hale-Bopp retreat to the outer stretches of the solar system, there exists a distinct class of comets that are more confined to the inner solar system not far beyond Jupiter and return every few years (see the current orbit of comet 67P/Churyumov-Gerasimenko in comparison with the orbits of Halley and Hale-Bopp in Fig. 1.3). These short-period comets[ii], most of which with small orbit inclination and

[ii]The current cometary taxonomy adopts the distinction between short-period and long-period comets by the orbital period of ~200 years (Levison et al. 2001). Halley’s comet falls into the former category and represents a distinctive sub-class of “Halley-type” comets with an orbital period of between 20 and 200

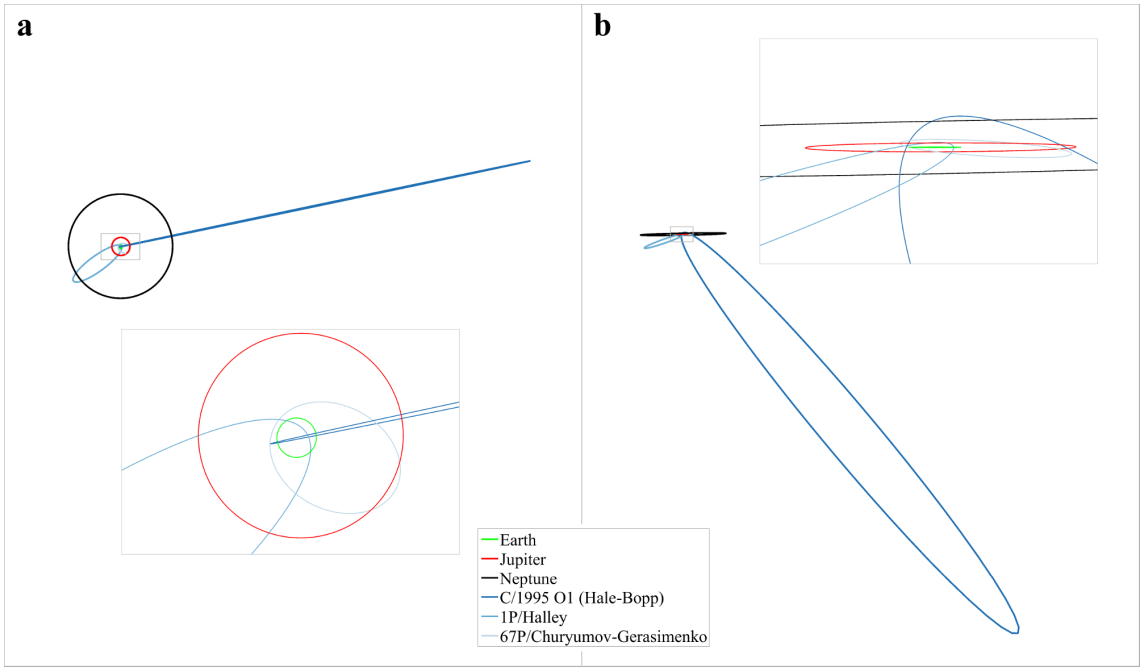

Figure 1.3: Diagrammatic illustration of current orbits of comet 1P/Halley, the long-period comet Hale-Bopp, and a short-period comet 67P/Churyumov-Gerasimenko, in comparison with the planetary orbits of Earth, Jupiter, and Neptune. Panels **a** and **b** are views over the North Pole and along the Equator of the *ecliptic* system, respectively. In the nested panels are the enlarged views encompassing the full Jovian orbit.

aphelia close to the Jovian orbit are also known as the "Jupiter-Family" comets, probably originated from some distant yet far less remote regions than the Oort cloud. For some time, the production of these comets was attributed to a near-circular strip from about 30 to 50 AU bounding the Neptunian orbit, known as the Kuiper Belt (Stern and Colwell 1997), of which Pluto is a prominent inhabitant. More likely, as it turned out, the short-period comets should have mostly come from the more dynamic "scattered disk" (Morbidelli 2005). The scattered objects may occupy distinctly elliptical orbits, with perihelia approaching the inner bound of the Kuiper Belt and aphelia lying far beyond, e.g., to 100 AU from the Sun, and are, therefore, susceptible to the gravitational perturbation of Neptune.

Distinction of tails It has been realized for over a thousand years that the cometary tails are directed away from the Sun, and that the brightness results inferably from sunlight (Yeomans et al. 1986). One tail, exhibiting a bluish hue, follows a nearly straight path but may display complex structures, such as filaments and knots. The true nature of this tail only started to be uncovered from the mid-nineteenth century with the advent of spectroscopic observations (Hogg 1929). The tail is made from gases, ionized by solar radiation, e.g., $CO + h\nu \rightarrow CO^+ + e^-$ (Combi and Delsemme 1980), and tracing the magnetotail of the comet far-stretched against the solar wind. The most manifest particles

years and, thus, possibly overlapping with the long-period comets.

in the ion tail, such as CO^+, are not directly indicative of the true abundances of the cometary constituents. For instance, the most abundant volatile species escaping from comets is water; the molecules, however, are quickly broken down into daughter species in a variety of pathways of photochemical reactions. The photolysis of water largely obscured its plenitude, usually in far excess of that of other volatiles, such as CO and CO_2 (Festou et al. 2004).

The other tail, pale and often curved backward along the cometary orbit around the Sun (Fig. 1.1), is made up of dust fragments ejected from the crumbling object. The nature of these refractory species is far less well known than the volatile components before *in situ* exploration of comets became a reality (A'Hearn 2004). The curvature of the tail suggests that the motion of the dust particles is significantly influenced by the gravitation of the Sun. The gravitational force of the Sun on a spherical particle of radius r_d, mass density ρ_d, and located at the heliocentric distance of $r_\odot$ is

$$F_\mathrm{g} = G\frac{M_\odot m_\mathrm{d}}{r_\odot^2} = G\frac{4\pi M_\odot r_\mathrm{d}^3 \rho_\mathrm{d}}{3r_\odot^2}\,, \tag{1.1}$$

where $M_\odot$ and $m_\mathrm{d} = \frac{4}{3}\pi r_\mathrm{d}^3 \rho_\mathrm{d}$ are the solar and particle masses, respectively. The particle is also subject to a repulsive force arising from the solar radiation pressure. The pressure due to total *absorption* of the radiation flux on the object is (Carroll and Ostlie 2007),

$$P_\mathrm{rad} = \left(\frac{1\ \mathrm{AU}}{r_\odot}\right)^2 \frac{C_\odot}{c}\,, \tag{1.2}$$

where c is the speed of light and where the solar constant is $C_\odot = 1361\mathrm{Wm}^{-2}$. The radiation force acting on the particle of cross section πr_d^2 is then,

$$F_\mathrm{rad} = P_\mathrm{rad}\,\pi r_\mathrm{d}^2\,. \tag{1.3}$$

With F_rad and F_g both inversely proportional to $r_\odot^2$, the motion of the dust particle is essentially governed by its size. Introduce the ratio of the radiation pressure and gravitational force as follows (Finson and Probstein 1968),

$$\beta = \frac{F_\mathrm{rad}}{F_\mathrm{g}} = \frac{1}{r_\mathrm{d}}\frac{3r_\mathrm{AU}^2 C_\odot}{4GM_\odot \rho_\mathrm{d} c}\,. \tag{1.4}$$

Smaller particles with larger β are more likely pushed outwards by prevailing solar radiation, whereas larger particles are more susceptible to the attraction of the solar mass. Because the solar radiation pressure always counteracts collinearly solar gravitation (i.e., $\beta > 0$), the ejected particles experiencing a reduced "effective" gravitation are relaxed to higher heliocentric orbits or even unbounded trajectories. As older ejecta have swung further upwards overtime, the particles form a tail that always drops backwards[iii]. The actual shape of the dust tail depends on other factors, as well, such as the size distribution of dust (Fulle 2004).

[iii] It can also be illustrated via a solution to the equation, $\ddot{\mathbf{r}} = -(1-\beta)\frac{GM_\odot}{|\mathbf{r}|^3}\mathbf{r}$, for trajectories of the particles for different β, where $\mathbf{r}$ is the vectorized barycentric position of the particle (Kramer et al. 2014).

Ice and dust The distinguished cometary tails of ions and dust hint at the existence of a "snowball", being a frozen assemblage of volatiles and dust grains that are energized by solar heat but otherwise remain quiescent or stable far from the Sun (Whipple 1950). Beyond the "snowline" (currently at roughly 5 AU from the Sun and roughly delineated by the Jovian orbit in Fig. 1.3; lower in the early stage of solar system), the volatiles were in the form of ices that could be mixed with the dust grains to form the cometary nucleus in the aerodynamic condition of the solar nebula or protoplanetary disk (Weidenschilling 2004, Blum et al. 2014, Davidsson et al. 2016b). The nucleus would be more difficult to detect, i.e., shrouded by a coma of dust fragments when the comet is active and otherwise too faint or minute to be discernible from afar. Preserved far outside the snowline since their formation, comets are inferred to have not been altered by solar heating before entering the inner solar system.

Thus, the apparitions of comets displaying prominent activity seem all the more remarkable and fortunate, considering that we are witnessing the unraveling of some most ancient entities in the solar system bearing on the recipes for the formation of planets.

1.2 Woken nucleus in sight

Armada to Halley's comet Halley's comet made an anticipated return in the year 1986. At that time, Earth was distant from the comet, making the latter seem less bright than reported during previous passages and than the apparitions of some other great comets (Yeomans 2007). Any disappointment would be dispelled by the attention to the enterprise involving five spaceships to intercept Halley's comet, daring the tumultuous environment near the nucleus during its perihelion passage. The *Armada*, as is often referred to, comprised an European probe Giotto, twin spacecraft Vega 1 and 2 from Soviet Union, and Japanese probes, Suisei and Sakigake. Giotto, in particular, ventured perilously far into (the inner-coma of) Halley's comet and recorded the very first clear sight of the irregular-shaped nucleus (Fig. 1.4) (Keller et al. 1986).

The historical feat brought about a drastic improvement on our understanding of comets. During the encounter, Giotto probe was bombarded by the dust fragments spurting from the nucleus that, even with the protection of a shield, damaged the onboard camera after the closest approach at some 600 km from the nucleus and nearly crippled the blinded spacecraft. The impacts of dust grains revealed a much more "dusty" nucleus than previously thought, i.e., with a higher abundance of refractory materials than that of volatile ices (Keller 1989). Water molecules were *directly* detected by the mass spectrometer onboard Giotto (Krankowsky et al. 1986); their spectral signatures as well as those of other volatiles, such as CO_2 and CO, are picked up by instruments onboard Vega 1 (Combes et al. 1986).

Halley Armada is the pioneer and inspiration to a succession of space missions to greet comets when they pass by (Fig. 1.5). The primary targets of these missions were Jupiter-Family comets.

Deep Space 1 to Borrelly's comet The second fly-by of a space probe around a comet would be performed by Deep Space 1 that encountered 19P/Borrelly on its extended mis-

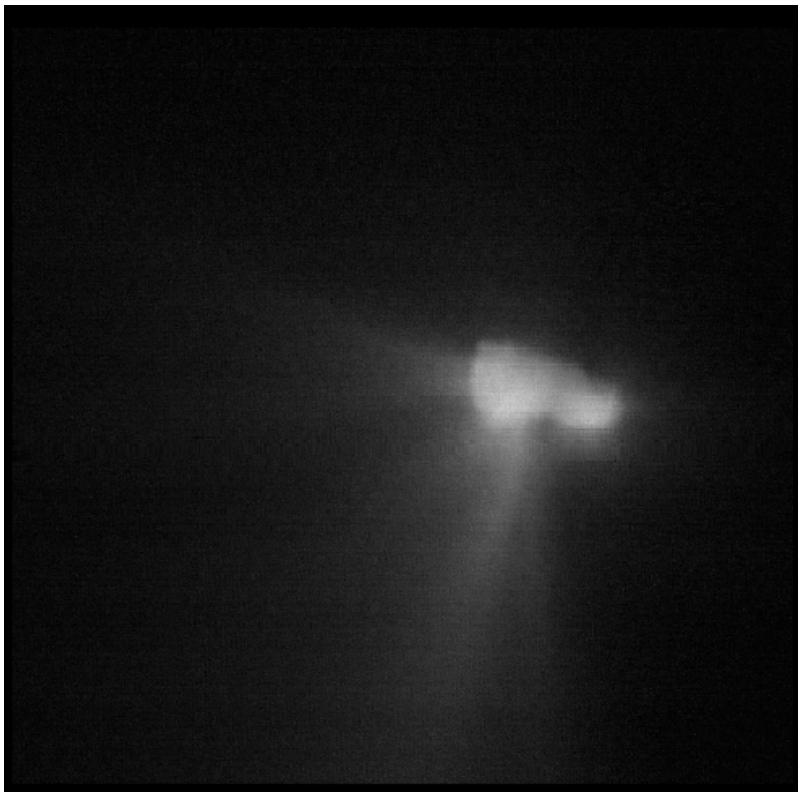

Figure 1.4: Image of the nucleus of Halley's comet taken by the television system onboard Vega 2 spacecraft on March 9, 1986, at a distance of ~8000 km from the nucleus (Sagdeev et al. 1986). The nucleus has dimensions of approximately 15 km by 10 km seen from the image (Keller et al. 1986, Sagdeev et al. 1986). Credit and source data set: Abergel J., Bertaux G., Avanessov G.A., Tarnopolsky V.I., Zhulov B.S., Kondor A., Merenyi E., Foldy C., Szego K., Toth I., and A. V. Dyachkov, VEGA2 TV SYSTEM IMAGES PROCESSED BY KFKI V1.0, VEGA2-C-TVS-3-RDR-HALLEY-PROCESSED-V1.0, NASA Planetary Data System, 1997.

sion in 2001, returning images of the highest resolution of any comet by then (Soderblom et al. 2002, Oberst et al. 2004). The elongated, 8-km-sized dark nucleus exhibits variations in morphology and surface brightness, or albedo, on spatial scales of 100 m.

Stardust to Wild 2 A recent Jupiter Family member, Comet 81P/Wild 2, was the target of the Stardust mission. The spacecraft set out in 1999 and flew by the asteroid 5535 Annefrank before it encountered the comet in Jan. 2004, reaching the closest distance of 236 km (Brownlee et al. 2004). The chief goal of the mission was achieved when the Capsule containing the dust samples collected in the coma of Wild 2 and the traversed space returned to Earth in early 2006. Silicates and organic compounds were found in abundance in the samples. The presence of minerals particles forming in high temperature suggests their origin from the inner solar system before transport to the outer stretches, such as Kuiper Belt and the scattered disk, where they were incorporated into the nucleus upon formation (Brownlee et al. 2006).

Deep Impact to Tempel 1 The spacecraft Deep Impact visited comet 9P/Tempel 1 around mid 2005. Rather than a brief encounter, the mission involved continuous operation with the spacecraft and conducting *in situ* investigations around the target. On the 4th of July, the spacecraft discharged an impactor to crash on the nucleus and captured the instant as well as the aftermath of the ten-kilometer-per-second collision that blasted out fresh icy materials from the interior (A'Hearn et al. 2005, Sunshine et al. 2007). The event was also monitored by ground-based observations and by Rosetta, the European Flagship having just embarked on its ten-year journey to reach comet 67P/Churyumov-Gerasimenko. The impact has likely excavated more dust than volatile ices in mass from the nucleus that is an icy "dirtball" instead of a dirty "snowball" (Küppers et al. 2005).

Deep Impact (EPOXI) to Hartley 2 After the completion of the nominal mission, the Deep Impact spacecraft was steered to fly by comet 103P/Hartley 2 in Nov. 2011, as part of the extended mission designated as EPOXI (A'Hearn et al. 2011). Hartley 2 is the third distinctly elongated object (after Halley's and Borrelly's comets) visited by a spacecraft. Though Hartley 2 is highly active in terms of water production, the main driver of its activity appears to be sublimation of CO_2 ice that fuels the ejection of water-icy grains from the nucleus.

Stardust-NExT revisiting Tempel 1 The extended phase of the Stardust mission, NExT (New Exploration of Tempel 1), saw the redirection of the spacecraft to approach Tempel 1 for a revisit in nearly six years after the exploration by Deep Impact. The images in comparison with those by Deep Impact provided the first concrete evidence of morpological changes on a comet, as a probable result of cometary activity. The crater resulting from the impact experiment years ago was recognizable.

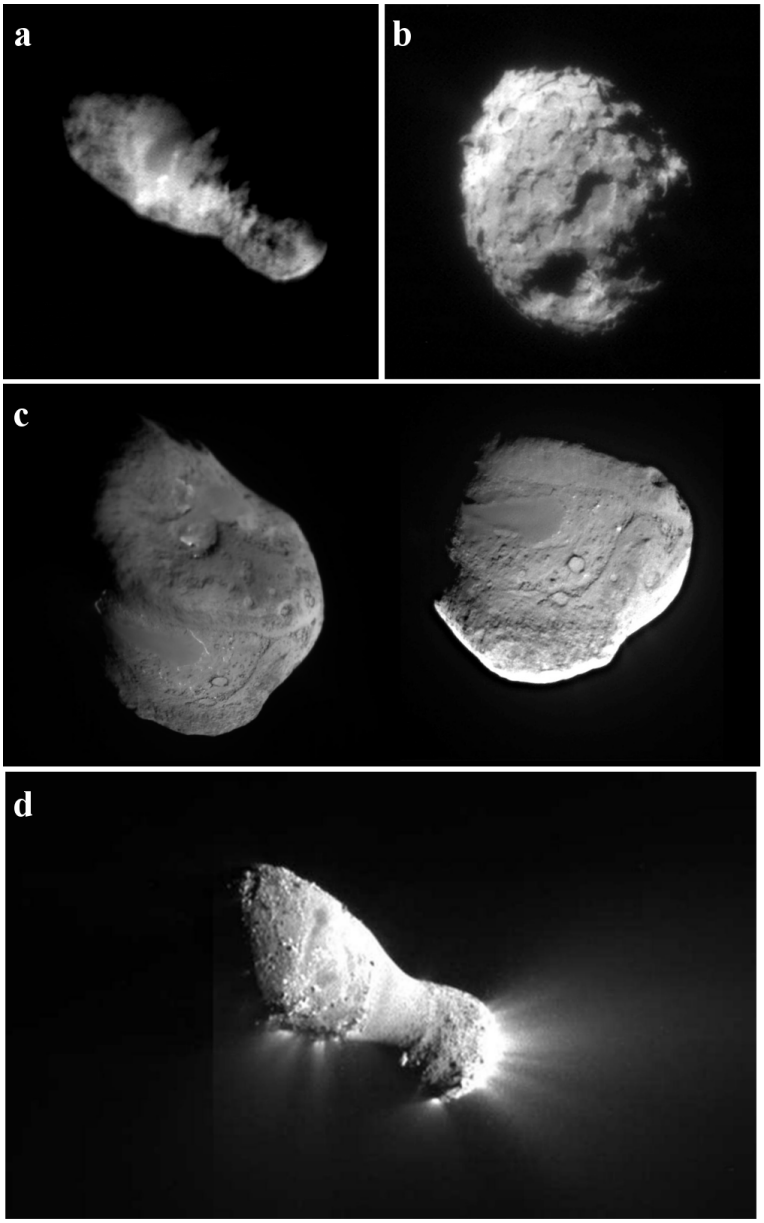

Figure 1.5: Nuclei of comet Borrelly (**a**) imaged by Deep Space 1, comet Wild 2 (**b**) imaged by Stardust, comet Tempel 1 (**c**) imaged by Deep Impact (left) and Stardust(-NExT) (right), and comet Hartley 2 (**d**) imaged by Deep Impact (EPOXI). The nucleus of Borrelly has dimensions of 8 km by 2 km as seen from the image (Oberst et al. 2004). The shape of Wild 2 nucleus can be approximated by a tri-axial ellipsoid with semi-axes 1.65 km, 2 km, and 2.75 km. (Brownlee et al. 2004). The longest and shortest dimensions of the Tempel 1 nucleus are 7.6 km and 4.9 km, respectively (A'Hearn et al. 2005). The maximum length of the Hartley 2 nucleus is ~2.3 km (A'Hearn et al. 2011). Image credit: **a**: NASA/JPL; **b**: NASA/JPL-Caltech; **c**: NASA/JPL/UMD (left) and NASA/JPL-Caltech/Cornell (right); **d**: NASA/JPL-Caltech/UMD.

2 Rosetta at 67P/Churyumov-Gerasimenko

The mission of Rosetta represents a milestone in the age of planetary exploration and of space science in general. The mission, which entailed the voyage of an orbiter, Rosetta, and a lander, Philae [i], to escort and perform a detailed exploration of a comet, was built on the legacy of the pioneering European space probe, Giotto, that flew by 1P/Halley in 1986 and acquired the first ever close observation of a comet nucleus (Reinhard 1986, Keller et al. 1986). The initially planned journey to comet 46P/Wirtanen was aborted due to the failure of the rocket system before takeoff. With the launch being eventually postponed by more than a year and, thereby, missing the optimal time-window to reach the original target, it was decided that Rosetta would aim for an alternative destination, the larger, more massive Jupiter-Family member of 67P/Churyumov-Gerasimenko (hereafter 67P).

If comets are pristine remnants from outer reaches of the early solar system and had only recently wandered inwards and warmed up, Rosetta presents the best opportunity so far, and likely in many years to come, to glean and piece together clues about the formation of the solar system. The physical and chemical properties of the nucleus are determined by and, thus, may mirror the conditions under which it was formed. On the other hand, space weathering, activity of volatile sublimation and mass ejection driven by solar heating, etc., obscure the original structure, composition of the nucleus, at least insofar as the surface layers are concerned. A blessing in disguise is that cometary activity must, at least to a certain extent, periodically rejuvenate the nucleus surface via exposing fresh materials from the cold interiors. At any rate, it becomes an inevitable task to gather observations that may shed light on not only the processes that molded but also those transforming the comet.

The measurement goals of Rosetta are summarized as, in the words of Schwehm and Schulz (1999), “

- Global characterization of the nucleus, determination of dynamic properties, surface morphology and composition.
- Determination of chemical, mineralogical and isotopic compositions of volatiles and refractories in a cometary nucleus.
- Determination of the physical properties and interrelation of volatiles and refractories in a cometary nucleus.

[i] The ensemble of the spacecraft Rosetta and Philae is hereafter referred to collectively as Rosetta.

- Study of the development of cometary activity and the processes in the surface layer of the nucleus and inner coma (dust/gas interaction). ”

These guidelines proposed for the investigation on Wirtanen remain valid for the new target of exploration, 67P.

2.1 Comet 67P

Rosetta’s target, 67P, was named after Klim Ivanovich Churyumov and Svetlana Ivanovna Gerasimenko, who made the first discovery of the comet in 1969. Various observational campaigns and modeling analyses prior to the selection of the comet as the mission target, conducted mostly around comet apparitions not far from perihelion, suggest that 67P is an exemplary Jupiter-Family comet (Schleicher 2006). Among common characteristics is the notable ellipticity of the present-day orbit, under intermittent gravitational perturbations of Jupiter. The production of volatiles and dust is strongly dependent on the heliocentric distance of the comet; the production peaks slightly after perihelion and exhibits asymmetry before and after, alluding to a significant obliquity of the rotation axis. Water is the main driver of the dust activity. The surface is probably overall inert with localized source regions that account for up to a few percent of the total surface area.

2.1.1 Orbit

Given the current little-inclined, short-periodic, and distinctly elliptical orbit (Tab. 2.1), the trails of 67P through the inner solar system have been variable and strongly perturbed by the gravitation of Jupiter (Królikowska 2003). It seems that, at least until 1840, the comet had remained distant enough from the Sun, i.e., probably never closer than 4 AU, so that strong modifications of the object due to activity were out of the question (ESA 2017b). The approach to Jupiter then lowered the perihelion to about 3 AU from the Sun, followed by a continuous decay of the orbit. The most recent encounter of 67P with Jupiter from little more than 0.05 AU further decreased its perihelion distance to the present-day 1.3 AU and its orbital period to about 6.5 years. 67P has stayed on its current orbit and experienced nearly ten perihelion passages since then.

2.1.2 Shape and orientation of nucleus

There was a paucity of effort in investigating the properties of the 67P nucleus until its selection as the eventual target of Rosetta. A systematic observing campaign had been established aimed for a detailed “portrait” of the nucleus in preparation for the mission since 2003 (Lamy et al. 2007).

The optical light curves of 67P collected by ground-based and space-borne telescopes, e.g., New Technology Telescope by the European Southern Observatory and the Hubble Space Telescope (HST), were used to determine the dimensions, rotation period, and orientation of the rotation axis for 67P (Lamy et al. 2006, Lowry et al. 2006). Meanwhile, the dedicated observation of thermal emission from the nucleus (performed with the Spitzer Space Telescope) yielded constraint on the albedo, a parameter that strongly influences the size determination of the object (Lamy et al. 2008, Kelley et al. 2009).

Table 2.1: Heliocentric orbit characteristics of 67P[*] as of Jul. 2016 (JPL 2016)

Elements/Parameters [**]	Symbol/Expression	Value	
Semi-major axis	a	3.47	AU
Eccentricity	e	0.641	
Inclination	i	7.05	degree
Longitude of ascending node	Ω	50.1	degree
Argument of perihelion	ω	12.8	degree
Mean anomaly at epoch t_0 [***]	M_0	52.7	degree
Distance of perihelion	$a(1-e)$	1.24	AU
Orbital period	t_P	6.45	year
Mean motion	n	0.153	degree/day

[*] The parameters are defined with respect to the ecliptic coordinate system in reference to epoch J2000.0.

[**] The reader is referred to Brouwer and Clemence (1961) for general definition of and connection between the orbital parameters.

[***] t_0 = 2457247.7 JD, corresponding roughly to early Aug. 13, 2015.

Depending on various assumptions on the convexity, surface reflectance, etc., of the object, the light curves can be exploited to resolve the shape, and in the same process, the rotation state of the nucleus via an inversion problem (Kaasalainen and Torppa 2001, Kaasalainen et al. 2002). The HST observations exhibit complex signals that cannot be accounted for by light reflected from a prolate-spheroidal body (Lamy et al. 2006). These deviations can be reasonably attributed to the topographic variations omitted from a simple spheroid. A better fitting of the light curve can be achieved via elaborate, though rarely unique, reconstruction of the nucleus shape for given or tentative orientation of the rotation axis and rotation period (Fig. 2.1).

Table 2.2: Approximate dimensions and rotation state of 67P nucleus

Parameter		Value	
Radius[*1]		1.98 ± 0.02	km
Semi-major axis[*†1]		2.41	km
Semi-minor axis[*†1]		1.55	km
Rotation period[2]		12.76	hour
	Rotation	Prograde	Retrograde
Celestial pole[1]	Longitude[◇]	$40^\circ{}^{+70^\circ}_{-20^\circ}$	$250^\circ \pm 30^\circ$
	Latitude[◇]	$70^\circ \pm 10^\circ$	$-70^\circ \pm 10^\circ$

[*] Geometric albedo of 0.04 is assumed.

[†] For an approximating *prolate* spheroid.

[◇] Referred to the ecliptic coordinate system.

[1] Lamy et al. (2006).

[2] Lowry et al. (2012).

The determination of the rotation-axis orientation is itself quite an intricate task, for

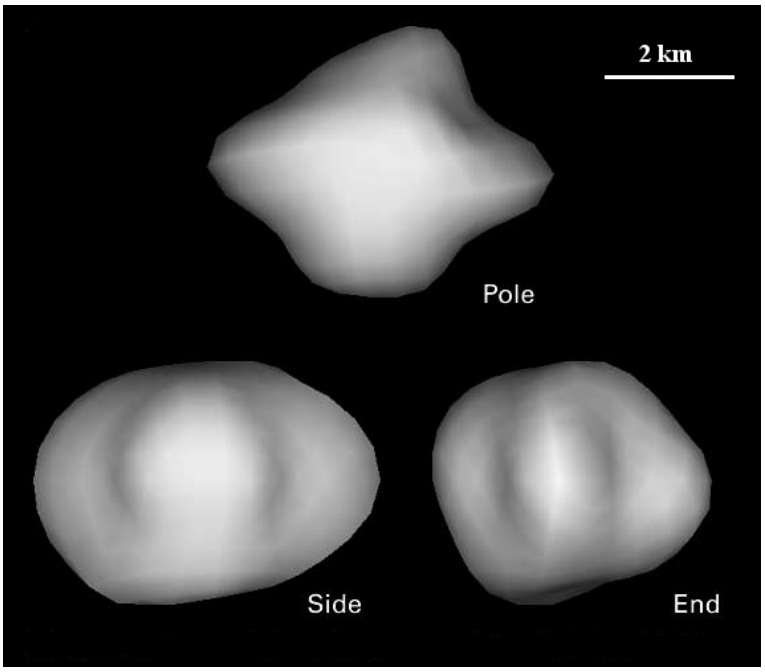

Figure 2.1: Shape model of 67P nucleus reconstructed from light curves of the comet collected by the HST (Lamy et al. 2006). Credit: NASA, ESA, Philippe Lamy (Laboratoire d'Astronomie Spatiale, France).

which results are not always unequivocal. The solution obtained by Davidsson and Gutiérrez (2005) involved a comprehensive characterization of the nucleus properties and activity of 67P, that ensures not only fitting of the light curves but also accounting for the water production rate and other measurable non-gravitational changes. The approximating dimensions and the possible orientations of 67P nucleus, based on the work of Lamy et al. (2006), are summarized in Tab. 2.2. Further studies (preceding the Rosetta mission) would suggest that the *prograde* rotation was more likely, and consequently the uncertainties in the orientation of the rotation axis (i.e., the celestial pole on 67P) could be reduced (Lowry et al. 2012).

The equinoxes reside along the intersection between the orbital plane and the equatorial plane of a rotating body. The obliquity, or the tilt of the rotation axis with respect to the normal of the orbital plane, and the orbital eccentricity of the body give rise to the alternation of seasons on 67P. Given the present-day orbital and rotational parameters and neglecting any change in the rotation axis, it can be inferred that the northern hemisphere is subject to lengthy but cool summer when the comet draws away from the Sun, whereas the south experiences short and intense summer around the perihelion [ii].

[ii] One cursory way to see this is to note that: 1) the perihelion is at roughly $\Omega + \omega \approx 60°$ in the ecliptic system (assuming $i \approx 0°$, see Tab. 2.1), and 2) the solstice or the right ascension of the rotation axis in the case of prograde rotation is *possibly* close (Tab. 2.2)

2.1.3 Physical properties of nucleus

As should already be evident, it is difficult to characterize the properties of the cometary nuclei without considering their activity of volatile outgassing and the flow-induced dust ejection. Cometary nuclei are soft, porous mixtures of refractory components, such as silicates and minerals, organic compounds, and volatile ices that sublimate when exposed to heat. The bulk mass density of the nucleus can be estimated via modeling of the non-gravitational forces that induce changes of orientation of the rotation axis, rotation rate, orbital motion, etc. (Froeschlé and Rickman 1986, Rickman and Froeschlé 1986). In the case of 67P, Davidsson and Gutiérrez (2005) derived a low bulk density in the range between 100 and 370 $\mathrm{kg\,m^{-3}}$.

Albedo Albedo of the nucleus can be generally understood as characterizing the light-reflective efficiency and thus a brightness measure of the surface. Cometary nuclei are dark objects with globally averaged albedo on the order of 0.01. Among various definitions that must be carefully distinguished, the geometric albedo quantifies the disk-integrated reflectance of the object in reference to a perfectly diffusing disk at zero phase angle (Lamy et al. 2004). On the other hand, the Bond albedo refers to the portion of light scattered in all directions (e.g., over all phase angles), and is a fundamental parameter to evaluate the absorption of solar radiation, or insolation, by the nucleus surface. The determination of albedos using remote sensing data is often difficult and subject to considerable ambiguity in the case of distinctly irregular-shaped bodies. The analysis of the HST (R-band) observations by Lamy et al. (2007) revealed an geometric albedo between 0.05 and 0.06, although lower values could not be ruled out under somewhat restrictive observational condition (at low phase angle).

Thermal inertia Thermal inertia is among the thermo-physical properties that govern the distribution and transfer of heat inside the nucleus and hence the occurrence of activity therefrom. Before Rosetta, the thermal inertia of 67P nucleus was largely undetermined. The cometary nuclei are, however, known to be of low thermal inertia in general. By measuring the thermal lag, i.e., the time for surface temperature to adjust to changing insolation, near the morning terminator, Groussin et al. (2013) found that the thermal inertia at the nucleus surface of Tempel 1 should not exceed 45 $\mathrm{W\,K^{-1}m^{-2}s^{1/2}}$, while a higher upper limit of 250 $\mathrm{W\,K^{-1}m^{-2}s^{1/2}}$ was obtained for Hartley 2 from a similar analysis. It should also be noted that local variation of thermal inertia is expected for different morphologies (Davidsson et al. 2009).

Formation of dust mantle It has become increasingly clear that cometary nuclei are more dusty than previously assumed (Keller 1989). The formation of a dehydrated, refractory-dominant "dust mantle" over the surface, as a result of de-volatization when irradiated as well as accumulation of the non-escaping, heavy dust grains, is predicted by Whipple (1950), and largely substantiated both modelling and experimental studies (Brin and Mendis 1979, Brin 1980, Mekler et al. 1990, Grün et al. 1991, Kührt and Keller 1994). The presence of the dust mantle is consistent with the observation that comets are dark objects, which can be conveniently explained by scant exposure of (pure) water

ice over the surface. Build-up of the dust mantle yields an efficient mechanism to reduce volatile outgassing (Skorov and Rickman 1995, Gundlach et al. 2011, Skorov et al. 2011).

2.1.4 Dust and gas activities

The knowledge about the properties of the dust and gas comae of 67P was likewise derived from astronomical observations, performed with ground-based or space-borne telescopes from afar. Water production rates of 67P have been measured over a number of apparitions of 67P (Schleicher 2006, and references therein). The production of CN, a tentative proxy species for water (assuming a canonical ratio for CN/OH for short period comets), shows a distinct asymmetry before and after perihelion (Fulle et al. 2010). However, CN had not been detected beyond 2 AU pre-perihelion, making it unreliable reference to infer the water production from (other than its upper limit). On the other hand, dust ejection from the nucleus beyond 2 AU is confirmed (Fulle et al. 2004). The steep increase in dust production from 3.4 AU to 2.5 AU inbound suggests that water outgassing, rather than that of more volatile species, is the main driver of dust activity (Fulle et al. 2010). The agreement of simulated water production by thermo-physical models with the measured dust production indicates a dust-to-gas mass ratio for water of about 3 from 2.5 AU inbound. The ratio is confirmed by measurements at perihelion (Fulle et al. 2010). The coma is indistinguishable, indicating an overall dormant nucleus, when 67P is beyond about 4.9 AU from the Sun (Tubiana et al. 2008) (a more refined estimate of 4.6 AU is suggested by Tubiana 2008).

Concavity at pole The pre-perihelion images of 67P around two apparitions consistently indicate a strong anisotropy in the dust coma, with the tail veering towards the north. A possible explanation is the existence of a significant topographic concavity near the North Pole (Fulle et al. 2010), which effectively focuses or collimates the dust outflow, as demonstrated by Crifo et al. (2002).

Physical and compositional dichotomy between northern and southern hemispheres In order to account for (fit) the observations of the dust (outer-)coma, tail, and trail in the literature, an asymmetric size distribution of dust particles about perihelion seems necessary. Given the estimated orientation of the rotation axis (Tab. 2.2), the large particles, at least mm in size, dominated production from the northern hemisphere long illuminated before perihelion, while the south, which is briefly and intensely illuminated around perihelion, is releasing smaller grains on average (Fulle et al. 2010). It can be inferred that this dichotomy in dust size may be indicative of the “age" difference of the surfaces in the two hemispheres, with the south being younger and more pristine (Fulle et al. 2010).

Another complementary piece of evidence for the north-south dichotomy is the conformity of the ratio of CN and water to the canonical value around perihelion and the divergence beyond 2 AU pre-perihelion (Fulle et al. 2010). The northern hemisphere is depleted in CN relative to the south. However, the northern hemisphere is definitively active in terms of water outgassing (in order to explain pre-perihelion dust ejection beyond 2 AU), so that the distribution of water is more uniform than that of CN over the nucleus.

Link to local activity from nucleus While the volatile and dust productions from 67P have been observed and analyzed on many occasions, their connection with the nucleus activity had remained elusive. The obscurity can be largely attributed to the lack of or uncertainty in the knowledge about the shape, orientation, as well as the bulk physical properties of the nucleus. If nuclei are dirty "snowballs", the thermo-physical modeling analyses suggest that only a small fraction of the nucleus surface can be the source of water outgassing (Huebner et al. 2006); otherwise, the total production would far exceed measurements. If the estimate of ~50 km^2 for the total surface area of 67P nucleus is regarded as reasonable, then only ~5% of the surface is active (Lamy et al. 2007).

2.2 Rosetta exploration of 67P nucleus and activity

Launched in 2004, Rosetta would endure a ten-year journey in space before reaching its final destination, comet 67P. Four planet-gravity-assisted maneuvers were performed to vault the spacecraft into higher heliocentric orbits in the chase of 67P. Along the way, Rosetta would make repeated visits through the Main Asteroid Belt before and after the last maneuver around Earth. During the passages, they flung by and caught glimpses of two main belt asteroids, 2867 Šteins and 21 Lutetia, from some thousands of kilometers (Keller et al. 2010, Sierks et al. 2011). Rosetta dropped into a two-and-half-year slumber to minimize the energy consumption in the middle of 2011, before waking (and warming) up for the final braking maneuvers to synchronize its orbit with 67P in May 2014, marking the beginning of the long-awaited rendezvous with the comet.

2.2.1 Irregular shape and diverse morphology

When the high resolution camera of the Optical, Spectroscopic, and Infrared Remote Imaging System (OSIRIS) onboard the orbiter captured the first images that could resolve (the illuminated portion of) the nucleus of 67P from 10000 km afar, it became unmistakable that Rosetta was bound for an object far more irregular in shape than originally anticipated (Fig. 2.2). The nucleus is bi-lobed with a kilometer-wide concavity over the northern hemi-nucleus[iii] around the pole, thus confirming the prognosis by Fulle et al. (2010). The landforms are complex. Cuestas are prevalent and indicative of “onion-like” stratification on each of the two lobes, alluding to independent histories of their formation (Massironi et al. 2015). Depressions are among other prominent features to be first identified on the lobes during the arrival phase of Roseta at 67P (Fig. 2.3) (Vincent et al. 2015).

Shape model and coordinate system for nucleus From early September, 2014, the OSIRIS observations started to reveal topographic variations at the level of 1 m on the nucleus surface, surpassing the highest resolution achieved in previous missions by an order of magnitude (Thomas et al. 2015b). One of the finest products derived from OSIRIS imagery is the commensurately detailed shape models for 67P nucleus. In an elaborate effort,

[iii] The original term in this text is “hemisphere”, which is discarded hereafter in view of the highly irregular shape of 67P nucleus.

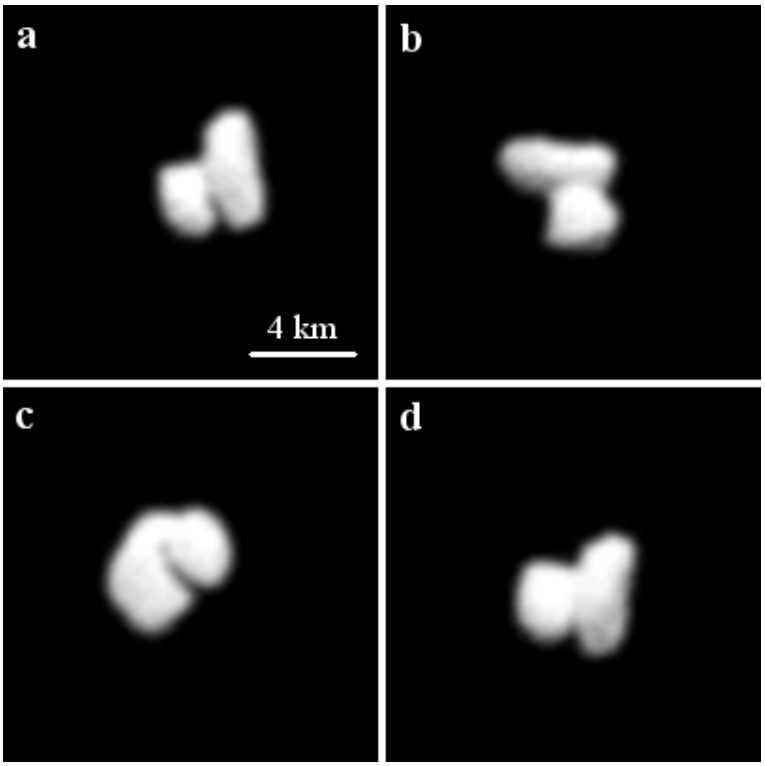

Figure 2.2: OSIRIS observations of 67P nucleus when Rosetta was approaching the comet at a distance of about 11710 km on Jul. 14, 2014. The four observations were taken roughly every three hours and almost covered a complete rotation of the nucleus. The nucleus appears distinctly bi-lobed in shape.

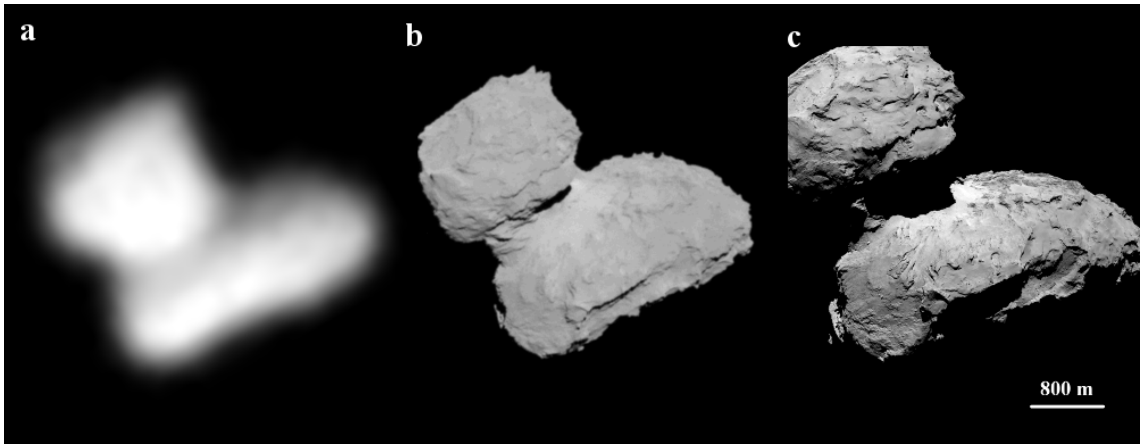

Figure 2.3: OSIRIS observations of 67P nucleus acquired at the descending distances of roughly 10000 km, 1000 km, and 100 km, respectively. The first two images are enlarged such that the dimensions of the nucleus therein are comparable to those in the last image. Note that the illumination conditions are different.

Preusker et al. (2015) performed shape reconstruction using the stereo-photogrammetric method (SPG), based on the principles of stereoscopy where surface points are determined via triangulation with respect to the viewing baselines formed by pairs of distinct observ-

ing points. The horizontal resolution of the resulting shape model is about 2 m, while the vertical uncertainties are an order of magnitude smaller (Preusker et al. 2015). A complementary shape model derived with an alternative method, stereo-photoclinometry (SPC), while assimilating a larger, growing dataset, is provided by Jorda et al. (2016).

Preusker et al. (2015) established a reference frame for the nucleus. The choice of the prime meridian is facilitated by the identification of a boulder-like monolith, named Cheops, located on the big lobe near the equator and defined to be located at 0.28°S and 142.35°E. However, due to the bi-lobed shape, the definition of the spherical coordinate system for 67P is ambiguous in latitudes. Two locations may share the same latitudes and longitudes, as revealed by the existence of multiple closed latitudinal contours (Fig. 2.4).

The bulk density of 67P nucleus is determined *in situ*[iv] by the ratio of the total mass and total volume of the body. An early estimate for the body mass was 1.0×10^{13} kg, derived from radio tracking measurements of the Radio Science Instrument (RSI) onboard the spacecraft sensitive to the gravitation of the nucleus (Pätzold et al. 2016). The total volume of the nucleus was initially estimated from the shape model to be around 21.4 km^3, with an overestimation of volume for the unilluminated southern hemi-nucleus at the time, yielding a bulk density of 470 $kg\,m^{-3}$ (Sierks et al. 2015). What turned out to be a better estimate was based on the assumption that south has the same volume as the north, in which case a slightly higher bulk density of about 535 $kg\,m^{-3}$ results (Preusker et al. 2015, Jorda et al. 2016).

Accurate shape modeling improves the determination of the nucleus orientation. The celestial pole on 67P is found to differ from previous estimates, an understandable consequence when the nucleus turned out far more concave than assumed (Tab. 2.3). More complex variations, namely precession and nutation, of the pole are revealed from OSIRIS observations (Preusker et al. 2015, Jorda et al. 2016). The rotation period matches the earlier estimate by Lamy et al. (2006), but exhibits clear temporal variations that can be partly explained by torques induced by activity of outgassing and dust flow (Keller et al. 2015b).

Smooth deposits and consolidated terrains The nucleus morphology is diverse. A most notable distinction is probably the smooth surface texture over ~80% of the northern hemi-nucleus, due to the existence of smooth cover formed, at least partly, by regolith or dust deposits. The thickness of the dust cover is not uniform across the nucleus. Morphological analyses of representative landforms, such as cratered structures and cliff edges, suggest that the dust cover may be on the order of 1 m in thickness, although variations are hard to assess. Where the dust cover runs out, consolidated, rugged terrains are revealed. The exposure mostly occurs over the steep surfaces less susceptible to dust accumulation (Fig. 2.5). The neck region of the nucleus, named Hapi, saddled between the two distinct lobes, is the most prominent reservoir.

The correlation of the dominant morphologies, i.e., the expanses of the dust cover and of the exposed rugged terrians, and the distribution of gravity[v] slope is illustrated in

[iv] "*In situ*" here refers to the measurements collected in the proximity of the nucleus, as opposed to those performed from afar such as ground-based observations. In a different context, some instruments, e.g., OSIRIS, RSI (introduced in the same paragraph), onboard Rosetta are classified as "remote sensing" instruments based on the measurement techniques that differ from *in situ* instruments collecting measurements in the proximity of the spacecraft.

[v] Following geodetic convention, gravity is defined with respect to the rotating, body-fixed frame, and

Figure 2.4: SPG Shape model and Cheops reference frame for the nucleus (Preusker et al. 2015). The latitudinal contours of the Equator, 20°N, 40°N, 60°N, and 80°N, are marked by green curves. The prime meridian (0°E) and the anti-meridian (180°W) are indicated by the red curves. The irregular shape of the nucleus gives rise to ambiguity in the use of the spherical coordinates, where multiple *closed* contours are present for the same latitude.

Table 2.3: Shape and orientation of 67P nucleus determined by the stereo-photogrammetry using OSIRIS images (Preusker et al. 2015).

Parameter		Value	
Semi-major axis*		2.40	km
First Semi-minor axis*		1.55	km
Second Semi-minor axis*		1.20	km
Total volume		18.7 ± 1.2	km^3
Mean bulk density**		535 ± 35	$kg\,m^{-3}$
Celestial pole***	Longitude	78.23°	
	Latitude	41.54°	
Obliquity		52°	
Rotation period****		12.40	hours

* For an approximating tri-axial ellipsoid.

** The total mass of the nucleus is adopted to be 1×10^{13} kg (Pätzold et al. 2016).

*** For comparative purposes, the angles are converted from the equatorial system, as adopted in the original publication, to the ecliptic system, with an approximate value of 23.4° for the obliquity of Earth.

**** For August and September, 2014, and subject to change.

Figs. 2.5 and 2.6. The gravity is that of a homogeneous nucleus, approximated by a shape model with reduced resolution (200,000 facets, Preusker et al. 2015), computed via the method proposed by Werner and Scheeres (1997). The distributions of the gravity slope are superposed on respective context images offering views of both lobes of the nucleus. The smooth, dust cover invariably coincides with the "flat" surfaces, e.g., with slopes less than 30°, whereas the rough terrains are dominantly associated with steeper areas. The flat areas in the vicinity of the abrupt topography, such as floors of cliffs and scarps, are often littered with boulder-like features. The debris field likely resulted from blocks breaking off the vertical surfaces and subsequently being deposited nearby.

North-South dichotomy in morphology While the dust deposits are a prevalent morphology in the northern hemi-nucleus, the southern hemi-nucleus tends to be more abrupt in topography and of higher surface roughness. This dichotomy was evident from early observations before the southern Spring equinox, but was only confirmed once the south was fully illuminated (the last two rows in Fig. 2.7). The smooth dust cover appears to run thin towards the south and finally gives way to the more exposed, craggy topography along the equator. It is worth noting that the morphology on the overall level far-side of the big lobe (where the Imhotep region is located) presents an exception, which is hardly inexplicable given the highly irregular-shaped nucleus.

It would seem too convenient a coincidence if the north-south dichotomy in morphology was unrelated to the seasonality on 67P, i.e., the long tepid northern summer in

therefore includes self-gravitation and centrifugal force due to rotation of the object (Heiskanen and Moritz 1967).

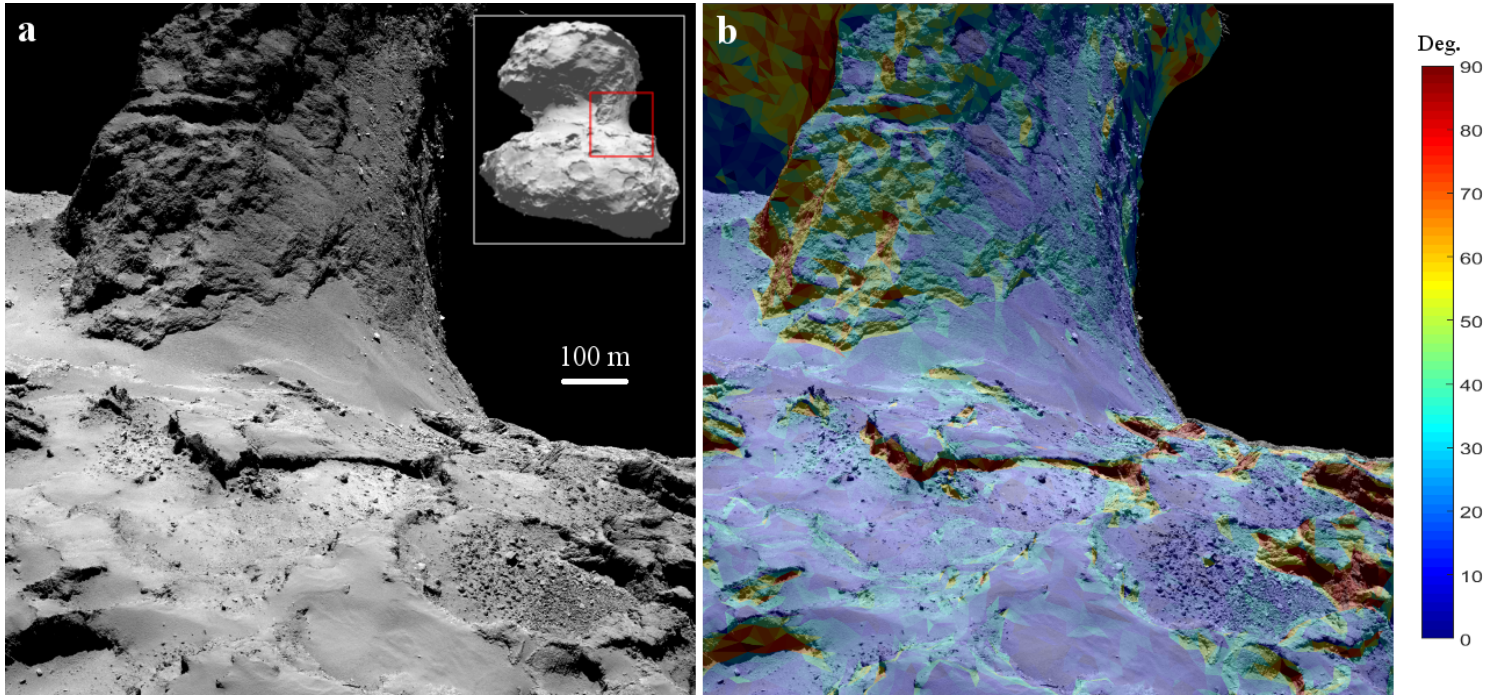

Figure 2.5: Morphology and gravity slope around the concavity of the northern hemi-nucleus. **a**. OSIRIS context image of the landscape; the field of view with respect to the nucleus is indicated by the red rectangle. **b**. Distribution of gravity slope superposed on the context image. The big lobe is in the foreground. The vertiginous, fractured wall across the valley belongs in the Harthor region (El-Maarry et al. 2015). The smooth areas are consistently correlated with slope less than 30°.

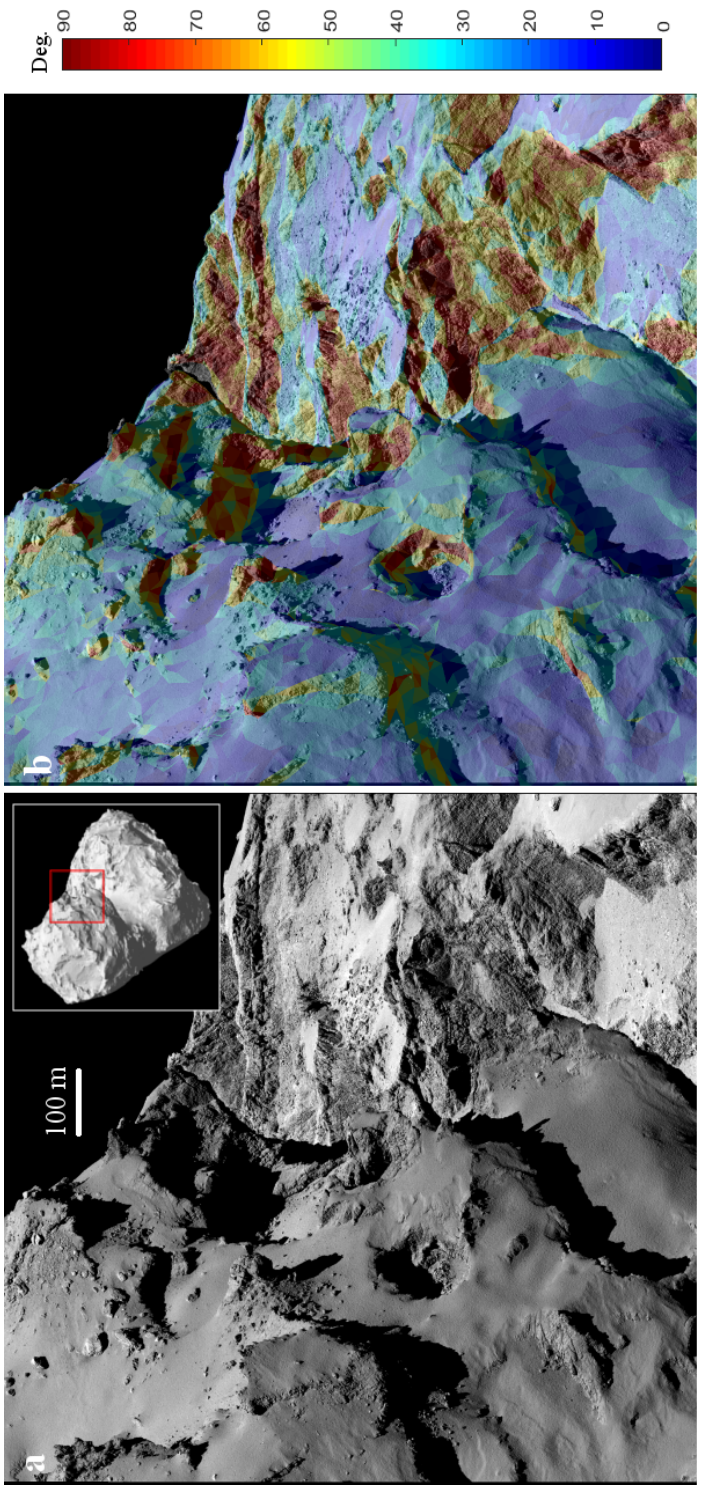

Figure 2.6: Morphology and gravity slope on the two lobes of the northern hemi-nucleus. **a**. OSIRIS context image of the landscape. the field of view with respect to the nucleus is indicated by the red rectangle. **b**. Distribution of gravity slope superposed on the context image. The small lobe is in the foreground. Complementary to the observation in Fig. 2.5, this figure accentuates the correlation of fractured terrains with steep surfaces, such as cliffs and crater walls.

contrast to the acute southern summer around perihelion. Keller et al. (2015a) considered it probable that the dust cover in the northern hemi-nucleus was sourced from dust ejected from the south undergoing strong erosion during the perihelion passage. Larger, more massive dust particles are less efficiently accelerated and, thus, less likely to escape the gravity of the nucleus in the gas flow. As a result of the selective process, some air-lifted dust particles will eventually fall back to the nucleus. The preferential site for the deposition of ejecta is the northern hemi-nucleus, where polar night occurs and (water) activity is at minimum during perihelion. An alternative scenario is also plausible, where the origins of the deposits in Hapi and of those over the two lobes differ (Thomas et al. 2015a). This can be argued from the fact that the total volume of deposits on the lobes could be tentatively explained by that of dust relocated from the neck region, with surface area of approximately 2.2×0.8 km^2 and dust removal by ~1 m in thickness by assumption.

.

Morphological regions A detailed examination of the surface morphology led to the division of the nucleus surface into a number of distinct morphological regions. The definition and naming of the regions, as well as the geological descriptions thereof, are provided in two consecutive papers by El-Maarry et al. (2015, 2016), focused on the northern and southern hemi-nuclei, respectively (Fig. 2.7).

The denomination of the morphological regions is provided in Fig. 2.8. The north-south morphological dichotomy is highlighted by color. The regions in blue correspond to the dusty terrains, further distinguished as either smooth areas, in dark blue, and dust-deposited areas, in light blue, according to El-Maarry et al. (2015). The Hapi region, on the saddle between the two lobes, and Imhotep, located on the far-side of the big lobe, are representative smooth regions. The dust deposits appear in many regions in the northern hemi-nucleus, such as Ash, Seth, Babi on the big lobe, and Ma'at, Serqet[vi] on the small lobe. The southern hemi-sphere appears more irregular in topography and overall consolidated.

2.2.2 Desiccated, organic-abundant, and insulating surface

The first observations by the Visible, Infrared and Thermal Imaging Spectrometer (VIRTIS) onboard Rosetta performed shortly after arrival at 67P suggest that the nucleus surface is nearly desiccated with little presence of volatile ices (Capaccioni et al. 2015). Overall, the surface is compositionally homogeneous, with clear indications of organic compounds likely in higher abundance than on other Jupiter Family comets. The low reflectance, as evidenced by the normal[vii] albedo of ~0.06 at the wavelength 550 nm (Capaccioni et al. 2015), could be attributed to the existence of opaque minerals associated with the refractory components.

The exposure of water ice, if any, is restricted to active areas. More conclusive evidence is the observed "frost" tracing the dawn or morning terminators, formed by water

[vi] Despite being categorized as a strongly consolidated region, a portion of the Serqet region displays smooth dust deposits.

[vii] Normal albedo is introduced in Sect. 3.3, and is defined, with more clarity and theoretical rigor, in the review by Shkuratov et al. (2011).

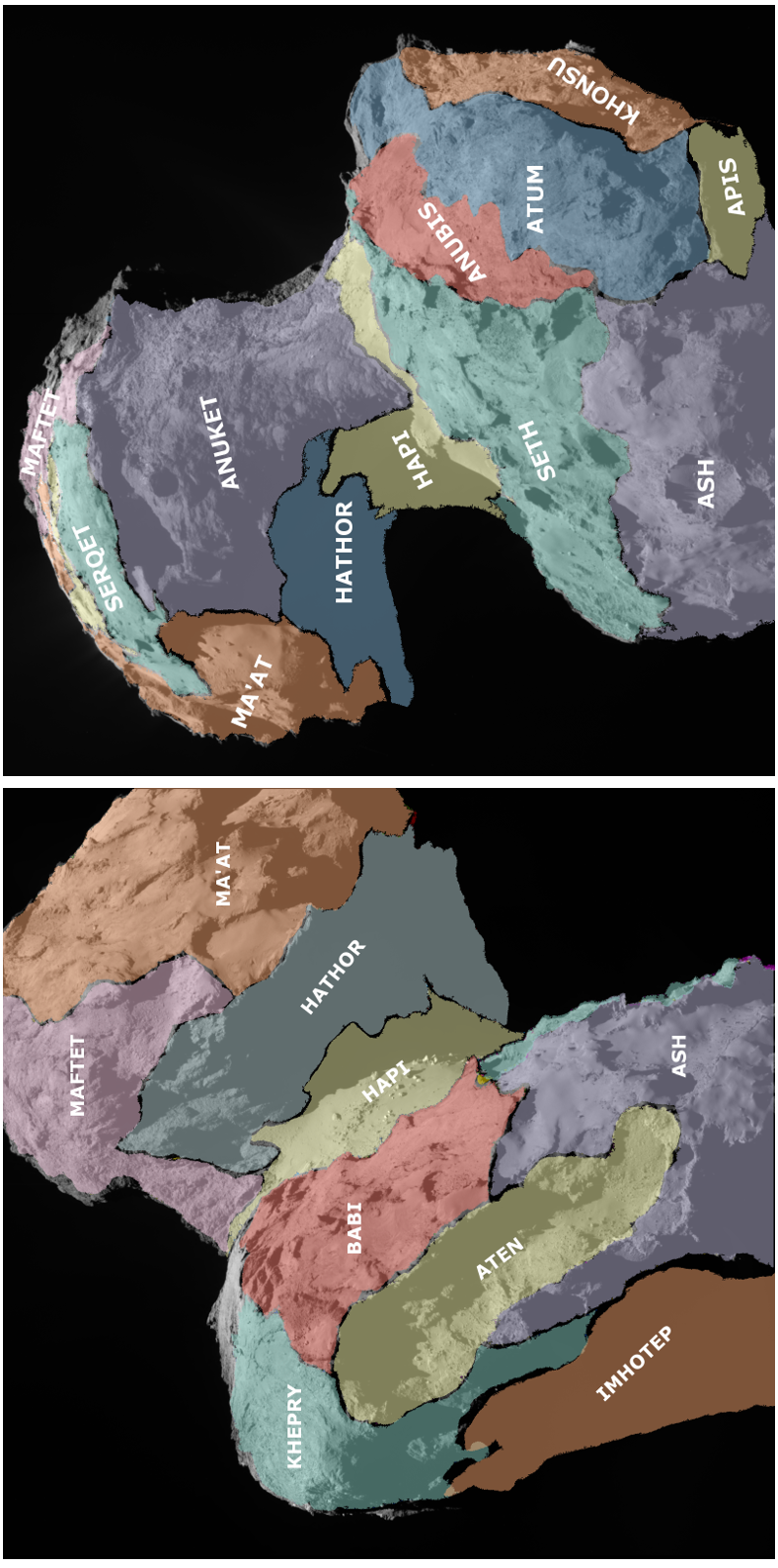

Figure 2.7: Geomorphological regions on 67P nucleus. The regions are distinguished by color with respect to two context OSIRIS images with complementary views of the nucleus as in Fig. 2.4. Detailed geological description is by El-Maarry et al. (2015, 2016).

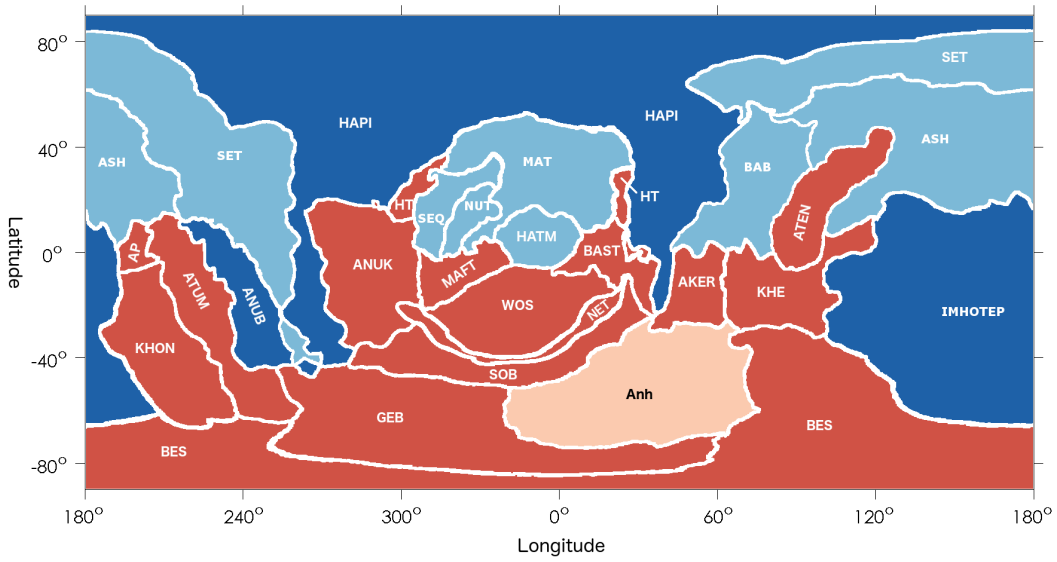

Figure 2.8: Map of geomorphological regions on 67P nucleus. Two dominant morphologies of dusty and consolidated terrains are colored in blue and red, respectively. The "smooth" terrains are in dark shade, while the dust deposits are in light blue. The consolidated terrains are in red. The abbreviation is as follows: ANH for Anhur; ANUB for Anubis; ANUK for Anuket; AP for Apis; BAB for Babi; BAST for Bastet; KHE for Khepry; KHON for Khonsu; HT for Hathor; HATM for Hatmehit; MAFT for Maftet; MAT for Ma'at; NET for Neith; SEQ for Serqet; SET for Seth; SOB for Sobek; WOS for Wosret. Note that not all region names are abbreviated.

vapor arising from the interior that remained warmer than the upper layers and subsequently recondensing near the cold surface during the night (De Sanctis et al. 2015). The frost would sublimate once illuminated, thus explaining its attenuation away from the terminator and disappearance into the long-sunlit area.

When detected, water ice is generally in scant amounts. The existence of pure water ice, probably millimeter in size, have been identified in Imhotep based on spectrum of VIRTIS observations (Filacchione et al. 2016). The surface abundance of such ice is no more than 5%, indicated by the occupied fraction of the pixel area. The fact that the ice grains are large and present more often in abrupt terrains, e.g., cliff walls and the adjacent debris field, likely suggests their formation in the subsurface due to re-condensation of diffusing vapor with subsequent exposure due to material collapse by gravity or due to surface erosion by activity (Filacchione et al. 2016). The detailed analysis of both OSIRIS and VIRTIS observations by Barucci et al. (2016) yielded consistent results, particularly regarding the ice abundance.

2.2.3 Dust-dominant, low-strength nucleus

It has been recognized, since Giotto's encounter with 1P/Halley, that cometary nuclei are composed predominantly of refractory materials or dust, with lesser amounts of volatile ices (see, e.g., Keller 1989, Küppers et al. 2005). In other words, the dust-to-ice mass

ratio of plurality is probably common. The characterization of cometary nuclei as icy "dirtballs", as advocated by Keller (1989), marked a paradigm shift from the former perception of them being (dusty) "snowballs", dominated by volatile components.

Dust-to-ice ratio The nucleus mass of 67P is dominated by dust, as first revealed *in situ* by the dust-to-gas ratio in the coma (Rotundi et al. 2015). The loss rate of dust is sampled *in situ* by the Grain Impact Analyzer and Dust Accumulator (GIADA) onboard the orbiter, while the abundance of large particles can be constrained by OSIRIS observations. The productions of volatile gases have been measured by various instruments, such as the Microwave Instrument for the Rosetta Orbiter (MIRO), the Rosetta Orbiter Spectrometer for Ion and Neutral Analysis (ROSINA), and VIRTIS. The dust-to-gas ratio averaged over the sunlit nucleus surface is around 4, that indicates a lower limit for the dust-to-*ice* ratios of the nucleus with the non-escaping fraction of the ejecta unaccounted for (Fulle et al. 2016a). The dust-to-water (gas) ratio is around 6, and may vary over time (Rotundi et al. 2015, Fulle et al. 2016a).

The low permittivity of the nucleus observed by the Comet Nucleus Sounding Experiment by Radio-wave Transmission (CONSERT) onboard the lander, Philae, reveals a dust-to-ice ratio ranging between 0.4 and 2.6 with the dust components being probably of carbonaceous chondrites (Kofman et al. 2015). It is not the intention, or in the interest, of the present work to discuss the apparent discrepancy between this lower value and those suggested in other studies. However, a dust-to-ice ratio greater than unity should not be surprising in the least.

Compact dust grains The dust ejected from 67P nucleus is dominantly compact, heavy grains. The density of the dust grains is 795^{+840}_{-65} kg m^{-3} on average, higher than the bulk density of the nucleus (Fulle et al. 2016b). The heaviness of the grains is congruous with the finding by VIRTIS that the nucleus surface is spectroscopically non-volatile, while organic- and mineral-like (Capaccioni et al. 2015). The dust particles are dry, or at least, do not contribute notably to the total (water) gas production from the nucleus (Fulle et al. 2016a). The single grain caught by the Dust Impact Monitor, being part of the Surface Electric Sounding and Acoustic Monitoring Experiment (SESAME), is inferred to have a density of 250 kg m^{-3} (Krüger et al. 2015), lower than that of the bulk nucleus but nonetheless belonging to the group of compact grains.

Fulle et al. (2016c) elaborated on another distinctive class of fluffy grains from GIADA collection of dust particles, that possesses ultra-low mass density on the order of 1 kg m^{-3} and thus yields a negligible contribution to the mass of the dust production. These grains are believed to be primitive and of interstellar origin, in comparison with the compact grains that have undergone processing in the pre-solar nebula (Fulle et al. 2016c).

Low material strength The structural strengths of the nucleus can be inferred from the (in)stability of landforms against gravity. Groussin et al. (2015a) analyzed various steep morphological structures, i.e., cliffs, overhangs, debris, etc., in OSIRIS images and derived tensile, shear, and compressional strengths for 67P nucleus. The results suggest that the nucleus is weak-structured, with tensile and shear strengths unlikely to far exceed

dozens of Pa, in agreement with previous observational, laboratory, and *in situ* findings (see, e.g., Asphaug and Benz 1996, A'Hearn et al. 2005, Blum et al. 2014). A more recent investigation is conducted by Basilevsky et al. (2016).

A suite of experiments was deployed onboard the lander, Philae, to investigate *in situ* nucleus properties at the landing site, decided as Agilkia on the far side of the small lobe shortly after the beginning of the rendezvous. On Nov. 12, 2014, in an unfortunate turn of fate, Philae was unable to anchor itself to the surface upon contact while attempting to land in Agilkia, and only came to a halt after a series of bounces off the nucleus surface (Fig. 2.9a). Traversing nearly half of the small lobe, Philae wound up shielded under a cliff in an awkwardly inclined position in the area named Abydos (Fig. 2.9b).

The final shelter of Philae is distinct from its designated landing site in terms of surface morphology and material properties. The first bounce of the lander off the surface produced several fresh depressions over the soft regolith layer prevalent in Agilkia (Fig. 2.9a). Even with a brief touch, the data registering the mechanical response of the landing equipment on Philae shed light on the material strengths of the surface layers. The compressive strength of the dust cover is on the order of a few kPa (Biele et al. 2015). The landscape at Abydos is more irregular and precipitous (Fig. 2.9b). A far higher compressive strength of ~2 MPa was derived for the exposed consolidated surface (Biele et al. 2015). Similar conclusions were drawn from measurements by the Multipurpose Sensors for Surface and Subsurface Science (MUPUS) on Philae that suggest a lower limit on the order of 1 MPa at Abydos (Spohn et al. 2015).

Low thermal inertia In addition to coma observations, the millimeter and sub-millimeter band receivers of MIRO are sensitive to temperatures in the shallow subsurface of the nucleus. By fitting the measured temperature variations with a thermo-physical model, Gulkis et al. (2015) derived a low thermal inertia in the range between 10 - 50 $\mathrm{W\,K^{-1}m^{-2}s^{1/2}}$ for the overall nucleus. This range falls below that derived by MUPUS between 50 and 120 $\mathrm{W\,K^{-1}m^{-2}s^{1/2}}$ (Spohn et al. 2015). Aside from uncertainties, the higher thermal inertia measured *in situ* at Abydos might be more representative of the thermal properties of the consolidated terrains.

2.2.4 Global outgassing and dust activity

The neck appeared to be the main source of dust activity in OSIRIS observations (Lara et al. 2015). Light scattered from concentrations of airborne dust grains along the line-of-sight in contrast with more rarefied surroundings in the coma gives rise to pale, hazy plumes, often overwhelmed against the illuminated nucleus but observable beyond the limb. These *visual* features are often vaguely termed dust jets, regardless of their actual dimensions or structures. The pronounced activity from the neck may have been in part due to convergence of gas and dust flows by the concavity.

Fine *visual* structures of jets are distinguished in observations at closer distance from the nucleus (Fig. 2.11). Dust activity is clearly insolation-driven and is prevalent over the sunlit portion of the nucleus (Keller et al. 2015a). The evolution of the activity appears to be correlated with variation of illumination conditions. The most pronounced (brightest) jets are usually associated with surface areas under direct illumination, e.g., around the sub-solar point, while activity from the night-side is less prominent (Vincent et al. 2016b).

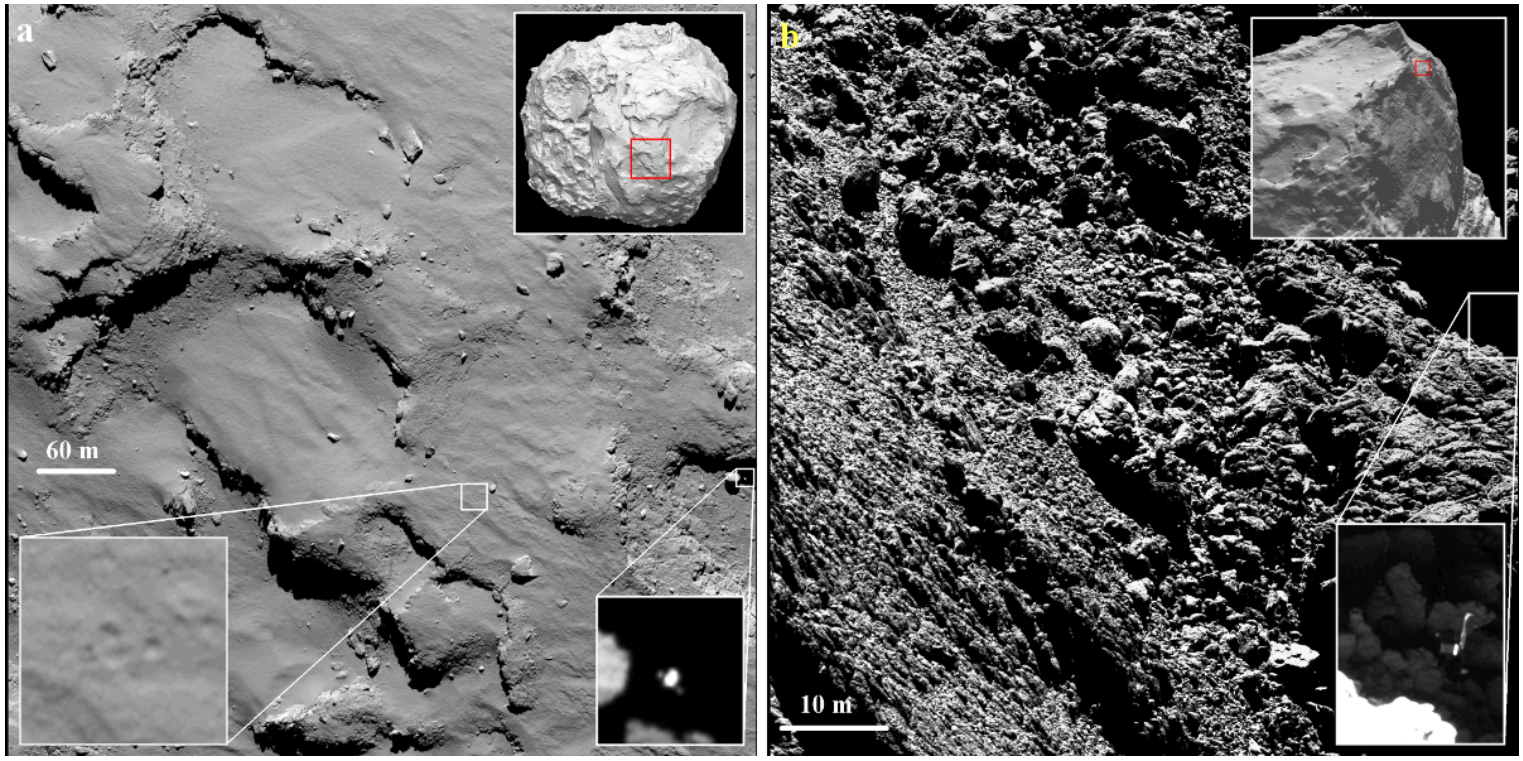

Figure 2.9: Distinction between general morphologies around Agilkia and Abydos. **a**. OSIRIS image taken shortly after the first landing attempt (bounce off the surface) of Philae, showing the prevalence of dust cover in Agilkia. The field of view with respect to the nucleus is indicated by the red rectangle. The footprints of Philae are noted as two small depressions within the white rectangle in the middle, with an enlarged view in the nested panel. Philae is seen here near the right edge of the image, (still) flying eastwards. **b**. Missing for nearly two years, Philae was finally confirmed to have settled in Abydos with predominantly abrupt, consolidated terrains. This OSIRIS image taken in Sep. 2016 shows the lander tilted against a cliff wall in shadow. The field of view with respect to (the small lobe of) the nucleus is indicated by the red rectangle.

Global water outgassing and dust ejection The actual sources of the dust jets on the nucleus are difficult to locate. Vincent et al. (2016b) suspect that the jets were associated exclusively with cliffs, where the steep surface prevents dust deposits to accumulate and thereby quench water outgassing. Prevalent fractures over the cliff walls may furnish an effective collimation mechanism. The main advantage of this scenario lies with its convenience to explain the overestimate of water production from 67P by a factor of nearly 20 in thermo-physical analyses (Keller et al. 2015a). The cliffs account for roughly 6% of the total surface area on 67P. It would be, therefore, a welcomed and comforting conclusion that water outgassing and dust flows are dominantly sourced from cliffs.

The investigation by Kramer and Noack (2015) proclaimed a counter scenario that was originally proposed by Crifo et al. (2002). By assuming homogeneous, insolation-driven outgassing from the nucleus, they performed simulations that suggest topography alone gives rise to complex, fine inner-coma structures that could account for the observed brightness fluctuations around the nucleus. Thus, with a general and, perhaps, minimal assumption the necessity of invoking strong inhomogeneity in activity is effectively obviated.

In two successive investigations, Fougere et al. (2016a,b) employed the Direct Simulation Monte Carlo (DSMC) to explain both the *in situ* gas measurements by ROSINA and the spectroscopic observations of coma patterns by VIRTIS. Their results suggest that while water outgassing is global, it is not uniform over the nucleus. Most notably, the neck region produces more water than can be explained by the effect of topographic concavity, that may be interpreted as resulting additionally from a higher water ice abundance (Capaccioni et al. 2015, De Sanctis et al. 2015).

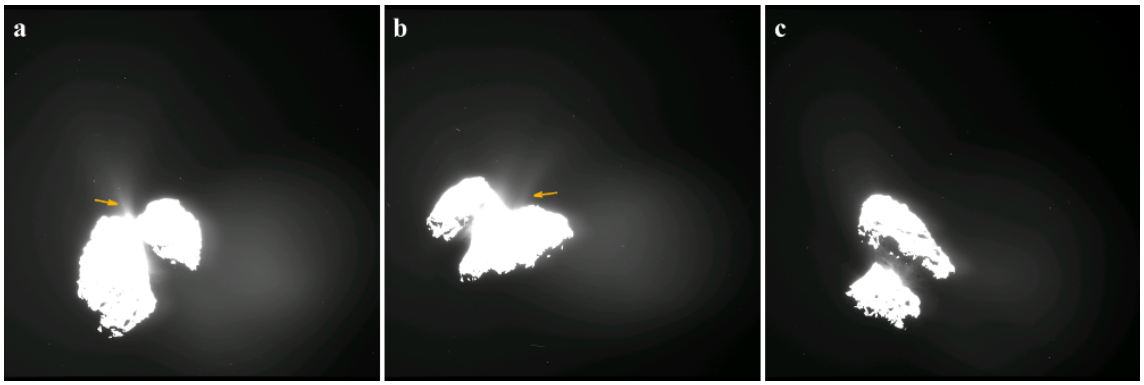

Figure 2.10: Early OSIRIS observations of dust jets arising from the nucleus against the dark background of the thin coma. The jets are highlighted by yellow arrows. The images are contrast-stretched to accentuate the brightness of the jets, thereby over-saturating the nucleus. The activity *appears* prominent over the concavity or the neck region (**a,b**). When the neck is shadowed, jets become less distinct (**c**), which, however, does not necessarily indicate inactivity. The roundish glimmer to the right of the nucleus and present in all three images is artifact.

Evolution of water production Even with *in situ* measurements offering unprecedented details of the coma, the production of volatiles from the irregular-shaped nucleus is difficult to determine. According to early observations by MIRO, the total water production

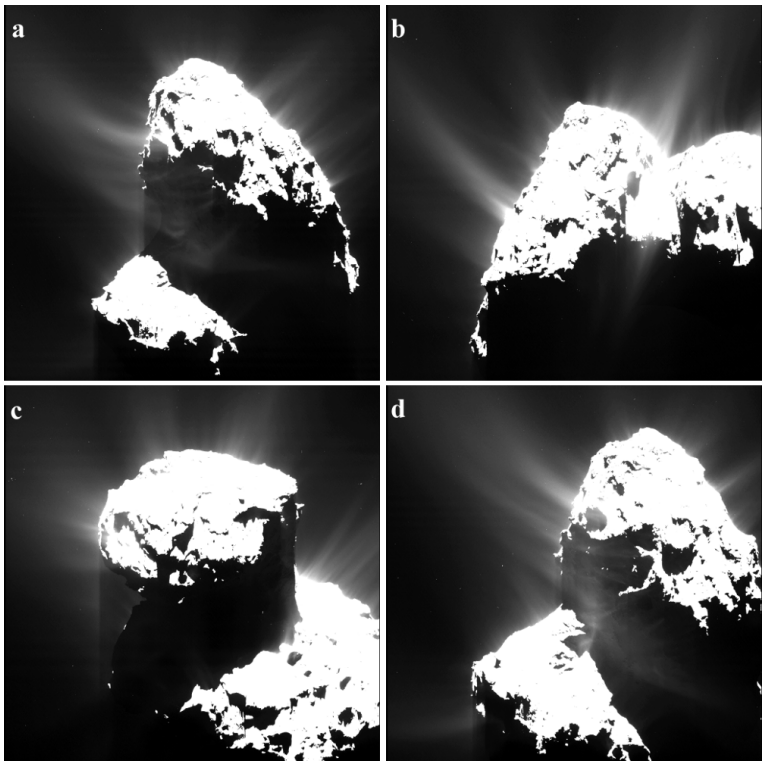

Figure 2.11: OSIRIS observations of dust jets over one comet rotation around midnight on April 23, 2015. The images are contrast-stretched to accentuate the brightness of the jets, thereby over-saturating the nucleus. Despite uneven distribution, jets appear to arise nearly everywhere from along the illuminated limb.

showed a clear increase from 0.3 $\mathrm{kg\,s^{-1}}$ to 1.2 $\mathrm{kg\,s^{-1}}$ between early June and late August, 2014, when the heliocentric distance of 67P decreased from around 3.9 AU to 3.5 AU (Gulkis et al. 2015). The results reported by Bockelée-Morvan et al. (2015) based on VIRTIS data show that the median of the diurnal water production, i.e., over one cometary rotation, is 2.5 $\mathrm{kg\,s^{-1}}$ for the period from November 2014 and January 2015 at around 2.5 AU. The water production increased steadily to 7.5 $\mathrm{kg\,s^{-1}}$ in February and 14 $\mathrm{kg\,s^{-1}}$ in April, 2015, at 2.2 and 1.8 AU, respectively (Fink et al. 2016).

The studies by Fougere et al. (2016a,b) suggest that the distribution of the activity over the nucleus applies to both pre- and post-perihelion periods. Meanwhile, their results represent a reliable assessment of the total gas productions calibrated by the *in situ* measurements of ROSINA. The evolution of water production around perihelion is illustrated in Fig. 2.12. While the production is clearly controlled by heliocentric distance, i.e., strength of insolation, the peak activity does not occur until 20 days after perihelion. The proposed reason for this lag is the non-uniform distribution of activity over the nucleus (Fougere et al. 2016b).

The production of more volatiles species, e.g., CO_2, CO, measures up to only a fraction of water outgassing, and varies less steeply with heliocentric distance, a typical behavior for ices sublimating from deeper layers effectively insulated from insolation. Before northern Autumn equinox, the activity of CO_2, CO is uncorrelated with that of water, and likely restricted to the unilluminated southern hemi-nucleus (Hässig et al. 2015), in

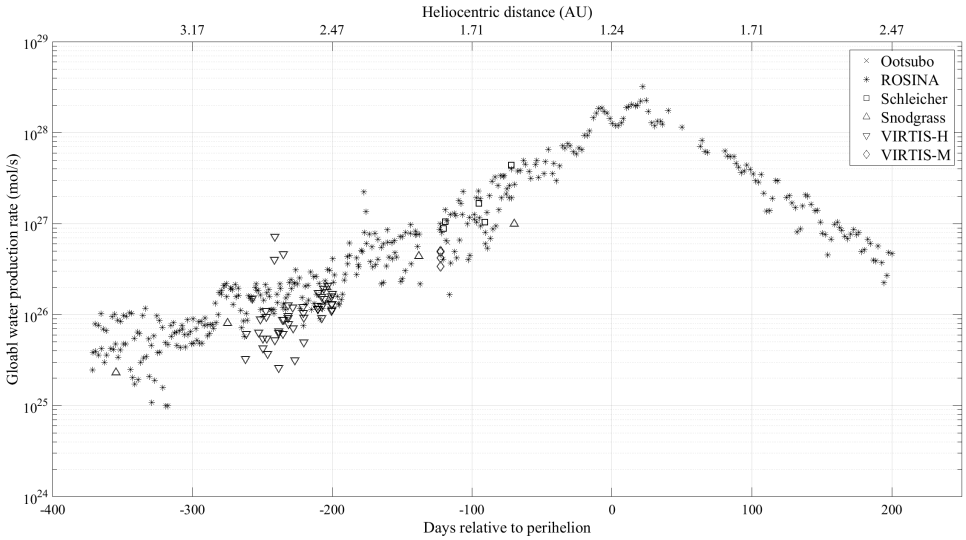

Figure 2.12: Evolution of total water production of 67P around perihelion as function of time or heliocentric distance. These data are adapted from Fougere et al. (2016a,b). The ROSINA data points are derived with the aid of the DSMC.

contrast to an evident correlation after the equinox (Fougere et al. 2016b).

Outbursts Another common form of cometary activity is outbursts, the more abrupt, short-lived events of gas and dust release. The observations were mostly collected in the three-month period around perihelion, starting from July 2015 (Vincent et al. 2016a), with an earlier detection in Mar. 2015 (Knollenberg et al. 2016). The outbursts around perihelion were largely sourced from rugged terrains, with an apparent concentration over the boundaries between morphological regions (Vincent et al. 2016a).

After a prominent outburst on July 29, 2015 (Fig. 2.13), roughly a fortnight before the perihelion passage of 67P, ROSINA measured a higher gas abundance for a variety of volatiles in the coma, with HCN nearly tripled, an increase in CH_4 by a factor of four, and almost sevenfold increase in H_2S. In contrast, the abundance of water vapor was nearly stable (ESA 2017a). These results *possibly* suggest that super-volatile species were responsible for the phenomenon.

One later event on Feb. 19 2016, when 67P was outbound at the heliocentric distance of 2.4 AU, was observed by multiple instruments onboard Rosetta (Grün et al. 2016). Occurring shortly after dawn, this outburst triggered a cloud rather than a collimated plume of dust, as seen from OSIRIS images. The authors concluded that driver was water, possibly in the amorphous form, exposed from the shallow subsurface that had been destablized by thermal stress or gravity.

2.2.5 Evolving morphology

Cometary activity modifies the nucleus, as confirmed by observations of Tempel 1 by Stardust-NExT in comparison with earlier images from the Deep Impact mission (Veverka et al. 2013). The changes took various forms such as retreat of cliffs, smoothing of

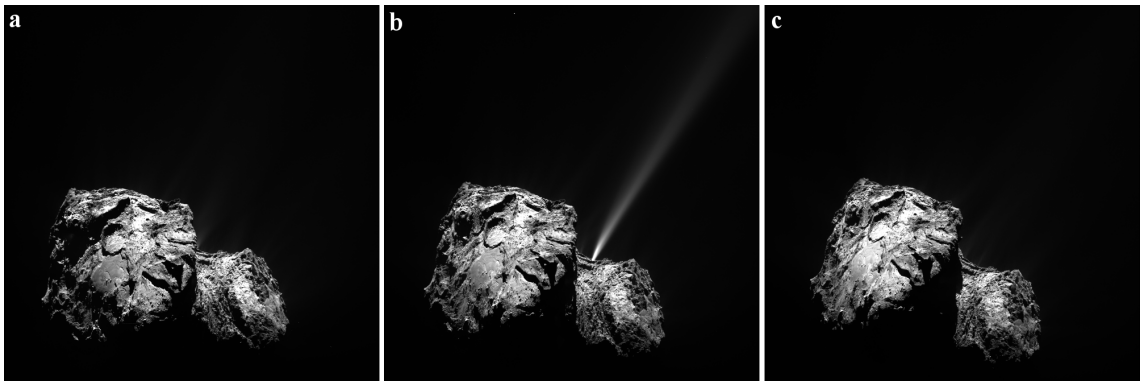

Figure 2.13: Outburst on July 29, 2015, observed by OSIRIS. The images were taken roughly 20 minutes apart. Partial views of this sequence have appeared in ESA article "Comet's firework display ahead of perihelioin".

craters, and possible variation of local contrast of surface albedo (Thomas et al. 2013). Accumulated over six years, the changes affected the nucleus surface on spatial scales of at least tens of meters. One of the main observational objectives of OSIRIS was to continuously survey the nucleus and monitor temporal evolution of the surface morphology (Keller et al. 2007). Morphological changes on 67P nucleus should amount to comparable magnitude as those detected on Tempel 1 over the course of the two-year rendezvous[viii].

Retreating scarps During the first half-year of rendezvous, the nucleus of 67P appeared somewhat quiescent in terms of surface transformation. This is hardly unexpected, since the highest resolution of OSIRIS observations before perihelion was around several decimeters on the nucleus surface, so that changes caused by surface erosion would only be recognizable after several months (Keller et al. 2015a). The first clear detection was reported by Groussin et al. (2015b) on the fast development of a series of circular features in Imhotep (Fig. 2.14) occurring from early May through early July 2015. These features appear to be receding scarps at least meters in height, and with a propagating speed of several meters each comet rotation that is too fast to be explained by surface erosion induced by volatile outgassing.

Erosion of dust cover A plethora of more subtle indications of surface changes, which turned out to have occurred earlier, were picked up only later and (had to be) verified at length. From a number of OSIRIS images acquired during the close fly-by of the nucleus in late March 2015, the surface texture at many locations over the originally dust-covered northern hemi-nuclues appeared to have roughened. The evolved surfaces are manifest as isles of indented patches (Fig. 2.15, Hu et al. 2017b). The small indentations are typically decimeters in width and (inferably) also in depth. In spite of a lack of strictly hexagonal cellular arrangement, some prominent patches are somewhat reminiscent of the honeycombed pattern. These features were subsequently named "honeycombs", if only for their visual distinction (Shi et al. 2016a). The distribution of the features shows a clear concentration over mid-latitudes, namely, between 20 and 40°N. Together with

[viii] Tempel 1 was visited by Deep Impact and Stardust-NExT around two successive perihelion passages.

many other changes in their vicinity, the honeycombs are interpreted as resulting from the surface erosion due to activity, given the curious timing of their occurrence in phase with the approach of 67P to the Sun as well as the southward movement of the sub-solar point on the nucleus. Chapter 7 will be dedicated to discussing the observation and the analysis of the changes.

Cliff collapse and other changes The changes discussed above are associated with the smooth terrains, i.e., flat or equipotential surfaces in terms of gravity. Changes over the steep areas likewise take a variety of forms. The cliffs are most likely places where materials are destablized by gravity and thus subject to collapse. This intuition is readily supported by the observation of nearly ubiquitous existence of debris fields at the foot of cliffs or scarps on 67P nucleus (Pajola et al. 2015). The aftermath of the long-anticipated event was observed in an area named Aswan, where a cliff was cloven along the edge from the top and was, therefore, one of the candidate sites to experience collapse later on. By June 2016, a chunk of the cliff measuring tens of meters long and roughly ten meters thick had broken and fallen off the wall where the inner layer was exposed (Pajola et al. 2017).

Among other changes are the growth of extensive fracture measuring hundreds of meters that had likely resulted from stresses induced by nucleus rotation, and the displacement of a decameter-sized boulder-like block having possibly slid down gravity slope. The reader is referred to the summary of OSIRIS-observed surface changes over the course of the mission by El-Maarry et al. (2017).

.

2.3 Motivation of this work

The activity of 67P is dominantly driven by water outgassing. Water ice was only occasionally found over the nucleus surface, and otherwise concealed by a dry dust mantle. The insulating nucleus surface layers (i.e., inclusive of the dust mantle) prohibit heat transport and, thereby, moderate the warming and cooling of the interior. The water ice must be present at such depths that it is not easily detectable in quantity over the nucleus surface but still effectively sublimates in response to the diurnal variation of insolation. Supervolatiles, such as CO_2 and CO, are present from deeper, cooler interiors than where the sublimation of water ice substantially occurs, and are even more sporadically exposed in, for instance, the long-frozen regions in (nearly) persistent shadows (Filacchione et al. 2016). Consequently, super-volatiles sublimate and seep from more insulated, inner layers, normally[ix] exhibiting less variability.

The strength of dust activity varies with the ebb and flow of water outgassing and, in doing so, follows ostensibly the exposure of the nucleus surface to insolation (Fig. 2.11). Specifically, once the gas pressure overcomes the material strengths of the dust(-dominant) structures and the gas drag exceeds the local gravity, dust is accelerated by the gas flow to be lifted from the nucleus (Skorov and Blum 2012, Blum et al. 2014). The over-pressurization may not necessarily occur at the bottom of the dust mantle, in which

[ix] Outbursts triggered by super-volatile outgassing are exceptions in this context.

case only dry fragments are ejected. It may also occur in the porous dust-ice mixtures underneath, in which case the ejecta would be icy (upon ejection). At first, it is arguably reasonable to adopt a working hypothesis that the dust mantle thickness remains constant, considering that the ice, if exposed, is usually in trace amount and, thus, vanishes quickly once illuminated, which in turn explains its shortage over the nucleus surface (Blum, personal communication). The assumption implies the occurrence of dust activity in near steady-state, and amounts to the stipulation that the ejected dust is proportionate to the loss of volatiles in mass; this proportion is governed by the dust-to-ice ratio.

2.3.1 Activity or dormancy of dust cover

The northern hemi-nucleus of 67P is covered in meter-thick dust. The sheer expanse of the dust cover suggests that its activity will significantly influence the overall activity and evolution of the entire nucleus. Conventional wisdom suggests that the dust deposits, if desiccated (or, indistinguishably, the dust mantle), would prevent water activity and, in a run-away process, build up and eventually suffocate any activity, thus limiting the active fraction of the nucleus surface. If this rationale would apply to 67P, then the majority of the northern hemi-nucleus would be dormant.

It would be tempting but groundless to assume that this dust *cover* is equivalent to the dust *mantle*. Only if the dust cover was completely desiccated would the equivalence hold. While little water had been detected over the nucleus surface, there is a lack of indication, if any at all, that the dust cover is depleted in water below the surface. On the other hand, the prominent activity was sourced from the Hapi region with the most abundant dust deposits and where water vapor diffusing from the subsurface re-condenses diurnally over the surface (De Sanctis et al. 2015). Visual perception of the near-nucleus coma based on OSIRIS images suggests that dust ejection takes place virtually everywhere over the (limbs of) illuminated nucleus (Fig. 2.11). The complex pattern of the inner coma such as the distinct jet structures can be produced by dust ejection from a homogeneous nucleus surface under illumination (Kramer and Noack 2015). For sure, a homogeneous nucleus is consistent with an overall *active* dust cover over the northern hemi-nucleus.

Whether the dust cover was active or dormant alludes to a more fundamental question regarding the distribution of active regions over cometary nuclei in general, to which an opinion had been entrenched and long prevailed[x] yet a definitive answer is still lacking. The expanse of activity over 67P nucleus can be constrained by OSIRIS observations of dust activity and distribution of surface changes.

2.3.2 Surface changes in relation to dust activity

The loss of volatiles and removal of dust transform the nucleus. The surface changes observed on 67P nucleus, some of which are introduced in Sect. 2.2.5, can be either transient or accumulative in nature (El-Maarry et al. 2017). The abrupt and sporadic changes, such as boulder movement and cliff collapse, probably necessitate a case-by-case investigation (Pajola et al. 2017). The accumulative changes, such as erosion, may

[x] That is, active areas are limited and localized over the nucleus; see the discussion in Sect. 2.1.4 and 2.2.4.

result from and thus be indicative of the nominal activity of outgassing and dust ejection, as had been continuingly observed in OSIRIS data over the course of the mission.

Sources of dust activity and magnitude of surface changes The distribution of sources of dust flows and that of surface changes reveal the expanse of active surface areas. The magnitude of changes, i.e., loss of materials in volume and mass, sheds light on the nucleus thermo-physical and compositional properties, such as structural strengths, gas pressure, and volatile abundance (i.e., dust-to-ice ratio), and potentially on the general mechanisms of cometary activity. The basis of this work is analysis of OSIRIS observations. Even for a preliminary attempt, some basic geometric and photometric techniques of imaging analysis are pre-requisite and instrumental (Sect. 3).

Describing the occurrence of activity and surface changes on the nucleus amounts to reconstruction observed spatial structures or events from their projections on images. Dust activity, in the form of jets, is rarely distinguishable against the background of illuminated nucleus surface (Fig. 2.11), and mostly observed above the nucleus. The source of a dust jet is the intersection of the line of jet (whose placement and direction are determined via triangulation) with the nucleus surface. While the locations of the surface changes are revealed from images based on the surrounding landscapes, the quantification of changes, e.g., volume loss of materials, requires the measurement and comparison of the surface levels or elevations at the specific nucleus position for different epochs.

The "inverse" projection from 2-D to 3-D space relies on the retrieval of information on depth between the camera and the observed feature. As introduced, the shape model of 67P nucleus can be reconstructed stereoscopically using multiple images (Preusker et al. 2015). The depth can also be estimated with the imposition of additional constraints. One possibility is to resort to a shape model of the nucleus with comparable resolution as the images. Then, the distance to a point on the nucleus surface in the field of view can be determined if the pointing and position of the camera with respect to the nucleus is known. Another possibility is to infer undulation of the surface from its brightness under illumination, provided the surface reflectance, illumination conditions, and pointing and position of the camera are known; the absolute distance between the surface and camera has to be further constrained (Rindfleisch 1966). This method, known as shape-from-shading, is the very principle of photoclinometry. In principle, the comparison of resulting surface elevations at different times enables verification and (volumetric) quantification of the surface changes.

2.3.3 Link between activity and nucleus thermal properties

The connection between the observed activity in the coma, surface changes, and the nucleus properties has to be established via thermo-physical, or more concisely, thermal modeling (Huebner et al. 2006). The OSIRIS observations necessitate realistic simulation of the distribution and variation of nucleus (sub-)surface temperatures and of the resulting sublimation flux of water ice in response to the energy input of insolation at high spatial and temporal resolutions.

That the nucleus of 67P is composed predominantly of dust and, not least of all, ice-depleted over the surface potentially invalidates an entire class of thermal models originally designed for the ice-dominant "snowball" nuclei (Fulle et al. 2016a). In fact, the

use of "snowball" thermal models would most likely contribute to misinterpretation of OSIRIS data and those from other Rosetta instruments. The formation of the dust mantle has long been proposed based on numerical and experimental studies, following the very insight of Whipple (1950). Even with a wealth of discussions and recommendations in the literature, what might not have garnered enough attention is the implications of the pervasive existence of the dust mantle on nuclei that is bound to significantly reduce the water sublimation over majority of the nucleus surface (Brin and Mendis 1979, Brin 1980, Kührt and Keller 1994, Davidsson and Gutiérrez 2005, Gundlach et al. 2011, Skorov and Blum 2012). It will be shown in this work that the over-estimation of water production from the unrealistic, "snowball" nucleus may be the main source of discrepancy when it comes to interpreting the global dust activity and distribution of surface changes displayed in OSIRIS imagery.

In this work, the thermal model based on the experiment by Gundlach et al. (2011), specifically designed for measuring the sublimation flux of water ice beneath the dust mantle and the diffusion of the vapor thereby, is employed to studying OSIRIS observations. Their results had previously been applied to predict the general dust activity of comets and the influence of various critical parameters, such as the mantle thickness, dust grain size, and heliocentric distance (Skorov and Blum 2012, Gundlach et al. 2015). Several thermal models presented by Keller et al. (2015a) adopt the formulas proposed by Gundlach et al. (2011) for evaluating the reduction of the sublimation flux by the dust mantle. The thermal models presented here involve a more rigorous numerical treatment for the solution of equation of heat transfer (Sect. 4), which is obviated in both Skorov and Blum (2012) and Keller et al. (2015a) neglecting thermal inertia over time scales up to ~1 hour for simplicity.

The application of the thermal models to 67P nucleus also relies on realistic description of energy absorption over the nucleus surface. Complex shape of the nucleus results in highly irregular local horizon and variable shadowing over the surface. On the other hand, the obstruction of local topography may enhance re-absorption of nucleus thermal radiation from the surroundings and, thus, prevent the nucleus cooling, especially over the concave, often-shadowed areas. The concept of a "landscape" database for 67P, extendable to other irregular-shaped objects, are beneficial for determining the illumination and nucleus thermal radiation (Lagerros 1997). The procedures and practical formulas for realizing such a database will be detailed in this work (Sect. 5).

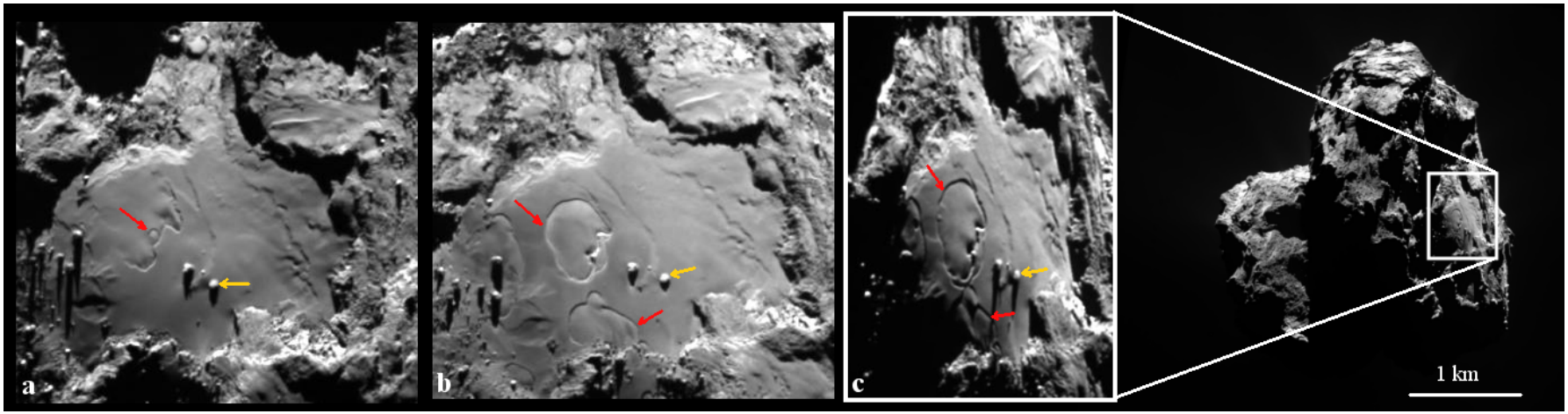

Figure 2.14: Surface changes in the Imhotep region taking place from late May till early July 2015, shortly before perihelion passage of 67P. The original, full figure that appears in Groussin et al. (2015b) is adapted (and abridged) here with a different context image for the last panel (outlined in white) offering a broad view of the entire nucleus. Two circular expanding features are indicated by red and yellow arrows. The angles in the upper-right corner of each panel indicate the approximate incidence angle of illumination at the locations of changes in the respective images.

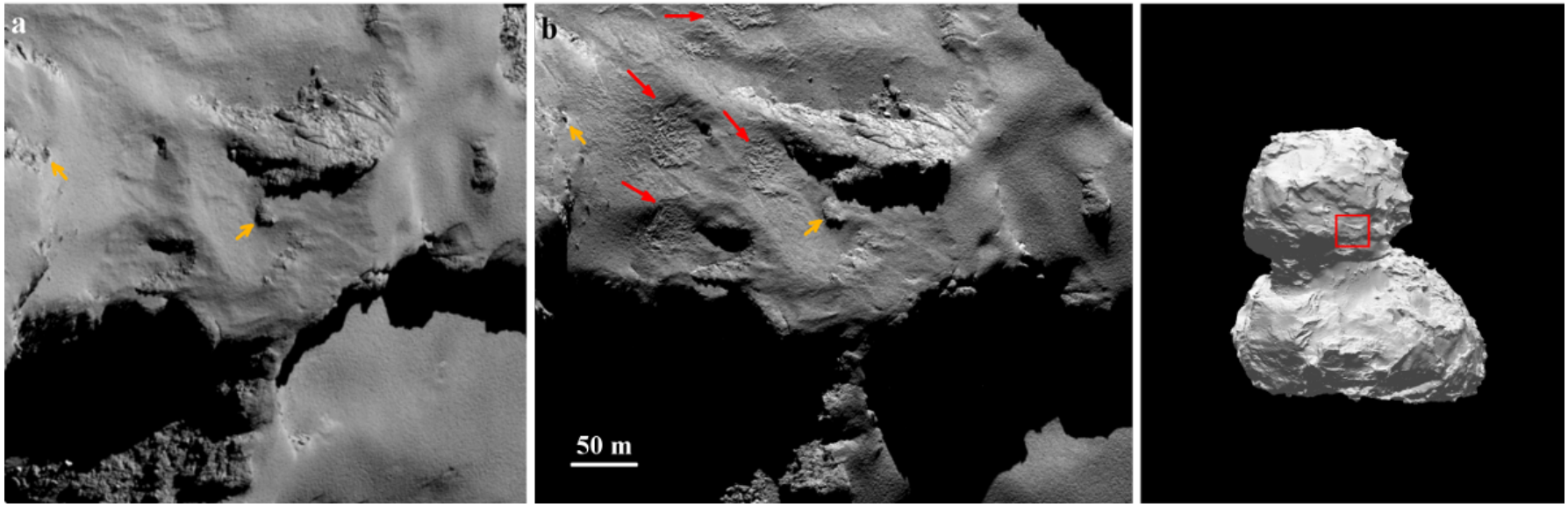

Figure 2.15: Increase of surface roughness observed in the Ma'at region that occurred before late March 2015. **a**. OSIRIS observation in Sep. 2014 showing smooth surface texture. **b**. OSIRIS image taken six months later showing enhanced roughness at various locations. Red arrows indicate detected changes; yellow arrows point to common landmarks in both images. The field of view with respect to the nucleus is that in the red rectangle in the right panel.

3 Methods for Analysis of Imaging Data

3.1 OSIRIS cameras and coordinate systems

The OSIRIS is a dual-camera system (Keller et al. 2007). A Narrow-Angle Camera (hereafter NAC) provides high-resolution observations aimed to enable detailed analysis on shape and rotation, morphology, composition, as well as activity from the nucleus. The Wide-Angle Camera (hereafter WAC), mounted abreast with NAC, commands a broader view of the nucleus and the inner coma (Fig. 3.1). The position and orientation of the OSIRIS cameras with respect to other instruments in the spacecraft frame are illustrated in Fig. 3.2; the key specifications of the camera system are provided in Tab. 3.1, adapted and updated from Keller et al. (2007). The bandpass filters of NAC were deployed for characterizing the spectral reflectance of the nucleus surface at a selection of wavelengths from ultraviolet to infrared and, in particular, detecting possible signatures of absorption by water and certain minerals. The WAC narrow-band filters were sensitive to the gas and radical emissions, e.g., from CN, NH, OH, etc. (Keller et al. 2007).

3.1.1 Camera coordinate system of OSIRIS

The definition of coordinate systems for the camera and the nucleus, as well as the realization of the respective coordinate frames, are requisite for describing the position and pointing of the cameras with respect to the nucleus. Let us first introduce a local Cartesian coordinate system associated with the OSIRIS cameras, hereafter referred to as the camera coordinate system. The origin of the system coincides with the focal point, while the z axis is aligned with the bore-sight of the camera. Hence, the x- and y-axes define

Table 3.1: Parameters of NAC and WAC observations*

	NAC	WAC
Focal length (mm)	717.3	135.7
Size of CCD (px)	2048×2048	2048×2048
Pixel length (μm)	13.5	13.5
Field of View ($^\circ$)	2.21×2.21	11.68×11.68
Wavelength range (nm)	250-1000	240-720
Number of filters	12	14

* After correction of geometric distortion.

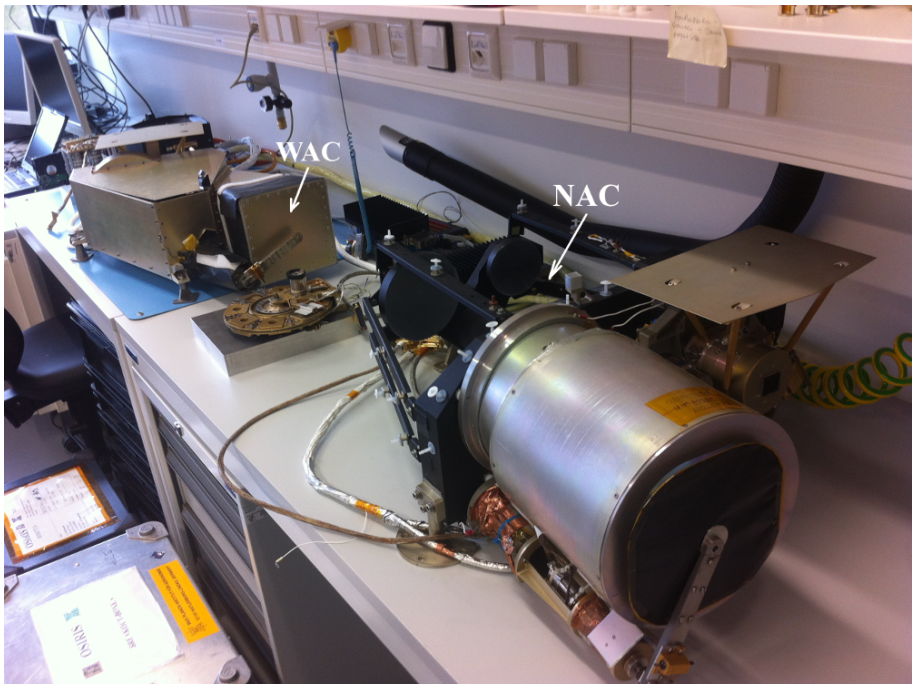

Figure 3.1: Models of OSIRIS NAC and WAC in the Laboratory.

the focal plane parallel with the image plane (or CCD detector). In particular, the x-axis points upward along the image plane; the y-axis points to the right of the image plane to form a right-handed coordinate system. Roughly speaking, the transformation from the spacecraft coordinate system to the camera system involves only translation of the origin.

Transformation from camera to body-fixed coordinate system of 67P The viewing geometry of observation, i.e., the position and orientation of the camera (spacecraft) with respect to those of the nucleus, is described by the transformation between the camera coordinate system and the body-fixed system of the nucleus. The body-fixed system is defined according to the Cheops reference frame whose realization is explained by Preusker et al. (2015).

Let $\mathbf{r}_\mathrm{C}$ denote the position vector of the focal point of the camera in the body-fixed coordinate system of 67P, i.e., the origin of the camera coordinates. Suppose the unit vectors of the camera coordinate axes in the body-fixed coordinate system are given by $\mathbf{u}_{\mathrm{C}\,x}$, $\mathbf{u}_{\mathrm{C}\,y}$, and $\mathbf{u}_{\mathrm{C}\,z}$. Denote the vector of a certain field point by $\mathbf{r}_\mathrm{P} = r_\mathrm{P}\hat{\mathbf{r}}_\mathrm{P}$, with $\hat{\mathbf{r}}_\mathrm{P}$ being the unit directional vector. The (re-)orientation of $\mathbf{r}_\mathrm{P}$, under a rotation from the body-fixed to the camera coordinate system can be expressed in the following form,

$$\hat{\mathbf{r}}_\mathrm{P}^{[\mathrm{C}]} = \mathbf{R}_{[\mathrm{BF}]}^{[\mathrm{C}]}\hat{\mathbf{r}}_\mathrm{P}\,, \tag{3.1}$$

where the superscript "[C]" explicates that the vector is expressed in camera coordinates. $\mathbf{R}_{[\mathrm{BF}]}^{[\mathrm{C}]}$ is a 3×3 matrix accounting for the rotation of the coordinate system. The rotation can be achieved by performing three successive rotations about the (instantaneous) coordinate axes. Alternatively, in case $\mathbf{u}_{\mathrm{C}\,x}$, $\mathbf{u}_{\mathrm{C}\,y}$, and $\mathbf{u}_{\mathrm{C}\,z}$ are known, $\mathbf{R}_{[\mathrm{BF}]}^{[\mathrm{C}]}$ can be formulated in terms of the three vectors as

Figure 3.2: Illustration of OSIRIS cameras onboard Rosetta spacecraft (model). The x-, y-, and z-axes refer to the coordinate system of the camera or the spacecraft. The lander is mounted over the *minus* x-axis (Keller et al. 2007). z axis points along the bore-sight of the cameras.

$$\mathbf{R}_{[\mathrm{BF}]}^{[\mathrm{C}]} = \begin{bmatrix} (\mathbf{u}_{\mathrm{C}\,x})^{\mathrm{T}} \\ (\mathbf{u}_{\mathrm{C}\,y})^{\mathrm{T}} \\ (\mathbf{u}_{\mathrm{C}\,z})^{\mathrm{T}} \end{bmatrix}, \tag{3.2}$$

where $\mathbf{u}_{\mathrm{C}}$ are assumed to be column vectors, and "T" denotes the transpose. It follows that the full transformation of $\mathbf{r}_{\mathrm{P}}$ from the body-fixed to the camera coordinate system is given by

$$\mathbf{r}_{\mathrm{P}}^{[\mathrm{C}]} = \mathbf{R}_{[\mathrm{BF}]}^{[\mathrm{C}]} \left(\mathbf{r}_{\mathrm{P}} - \mathbf{r}_{\mathrm{C}}\right) . \tag{3.3}$$

Transformation from camera coordinate system to pixel coordinate system of image
The projection of an object in 3-D space into the 2-D imaging plane is in effect the conversion from the camera coordinates into the pixel coordinates on the imaging plane, e.g., X, Y (Fig. 3.4). The imaging plane is located at a distance of r_{f} from the focal point, with

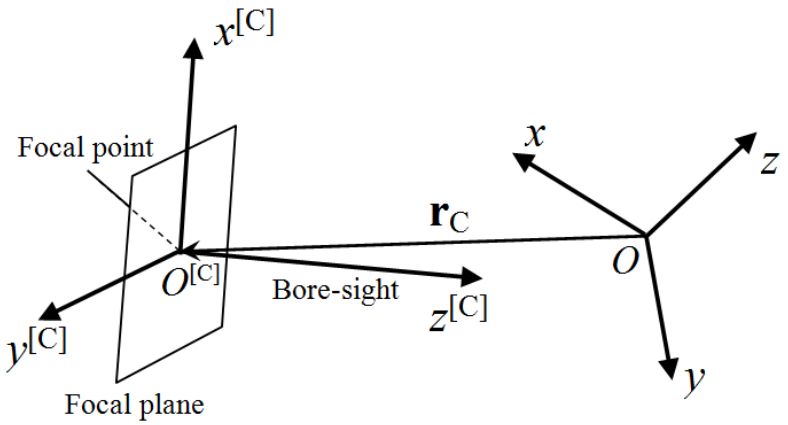

Figure 3.3: Camera coordinate system with respect to the body-fixed coordinate system of 67P

r_f being the focal length of the camera (Tab. 3.1). The axes of the planar coordinates X and Y are parallel to the x- and y-axes of the camera coordinates, respectively. Hence, the projection is given by,

$$\begin{pmatrix} X \\ Y \end{pmatrix} = \frac{1}{p} \frac{r_f}{z^{[C]}} \begin{pmatrix} x^{[C]} \\ y^{[C]} \end{pmatrix}, \tag{3.4}$$

where p indicates the pixel length (Tab. 3.1). The preceding factor "$1/p$" on the right-hand side of the above equation applies such that X, Y are in the units of pixels (px). Note that the origin of X, Y is at the center of the image, so that both X and $Y \in [-1024, 1024]$.

The inverse projection from 2-D to 3-D coordinates is underdetermined and, thus, not possible in general. It is nonetheless useful to derive the (unit) pointing vector to the imaged object from its image coordinates, such as,

$$\mathbf{u}^{[C]} = \begin{pmatrix} u_x^{[C]} \\ u_y^{[C]} \\ u_z^{[C]} \end{pmatrix} = \frac{1}{\sqrt{(pX)^2 + (pY)^2 + r_f^2}} \begin{pmatrix} pX \\ pY \\ r_f \end{pmatrix}. \tag{3.5}$$

3.2 Adjustment of viewing geometry

3.2.1 3-D positioning on nucleus using single image

As noted in Sect. 3.1.1, the two pixel coordinates underdetermine the position of a point in 3-D space, unless additional constraints are imposed. In case the extent along the line-of-sight is known, 3-D point-positioning becomes possible. Thus, if the position, orientation, and shape of the nucleus with respect to the camera are available, one may uniquely associate the pixel point from the image with a certain location on the nucleus.

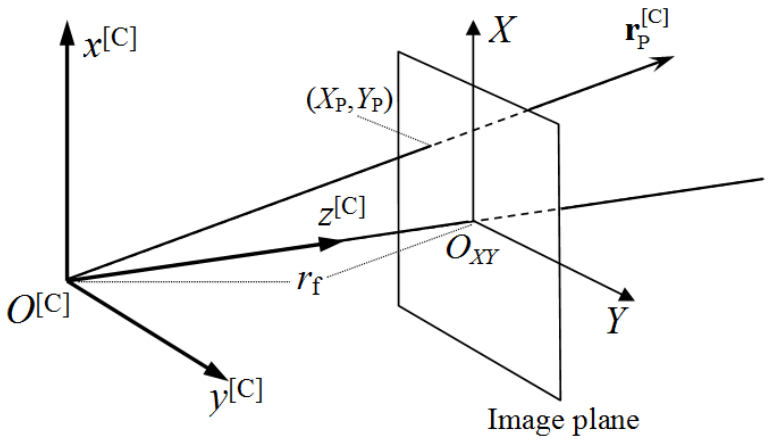

Figure 3.4: Image pixel coordinates associated with the camera coordinate system

For a certain pixel with coordinates (X_P, Y_P), the pointing vector along the line-of-sight is determined via Eq. (3.5) with respect to the camera coordinate system. The (orientation of) pointing vector is then transformed into the body-fixed coordinate system via

$$\mathbf{u}_P = \mathbf{R}_{[C]}^{[BF]} \mathbf{u}_P^{[C]} . \tag{3.6}$$

Hence, the equation of a ray parallel to the pointing vector and passing the focal point of the camera is given by,

$$\mathbf{l}_P = \mathbf{r}_C + l\,\mathbf{u}_P , \tag{3.7}$$

where $\mathbf{r}_C$ points to the camera, as in Eq. (3.3), and where $l \geq 0$ measures the displacement along $\mathbf{l}_P$ from $\mathbf{r}_C$. Be reminded that all quantities are referred to the body-fixed coordinate system.

In general, l is a free parameter, in which case point-positioning from the pixel coordinates is out of the question. However, if the nucleus, rather than the starry background, is in view along the line-of-sight, $\mathbf{l}_P$ intersects the nucleus surface and l is no longer ambiguous thereat. The shape model of 67P is applied to approximate the dimension of the nucleus. We utilize a function written by Legland (2009) that determines the intersections of a straight line given in the form of Eq. (3.7) and the polyhedral shape model. This function is hereafter denoted by $\Im$, namely,

$$\mathfrak{r} = \Im\,(\mathbf{l}; \mathfrak{v}, \mathfrak{f}) , \tag{3.8}$$

where $\mathfrak{v} = \{\mathbf{v}_n, n = 0, 1, \cdots\}$ and $\mathfrak{f} = \{\mathbf{f}_k, k = 0, 1, \cdots\}$ indicate the vector sets of vertices and of the facets of the shape model, respectively, and $\mathbf{l}$ denotes the straight line in the form of Eq. (3.7). The output of $\Im$ is a set of the position vectors of all the intersections, $\mathfrak{r} = \{\mathbf{r}_{\iota,\varkappa}, \iota = 1, 2, \cdots; \varkappa \in k\}$ where $\varkappa$ numbers the facet where intersection occurs. If there are no intersections, $\mathfrak{r} = \emptyset$.

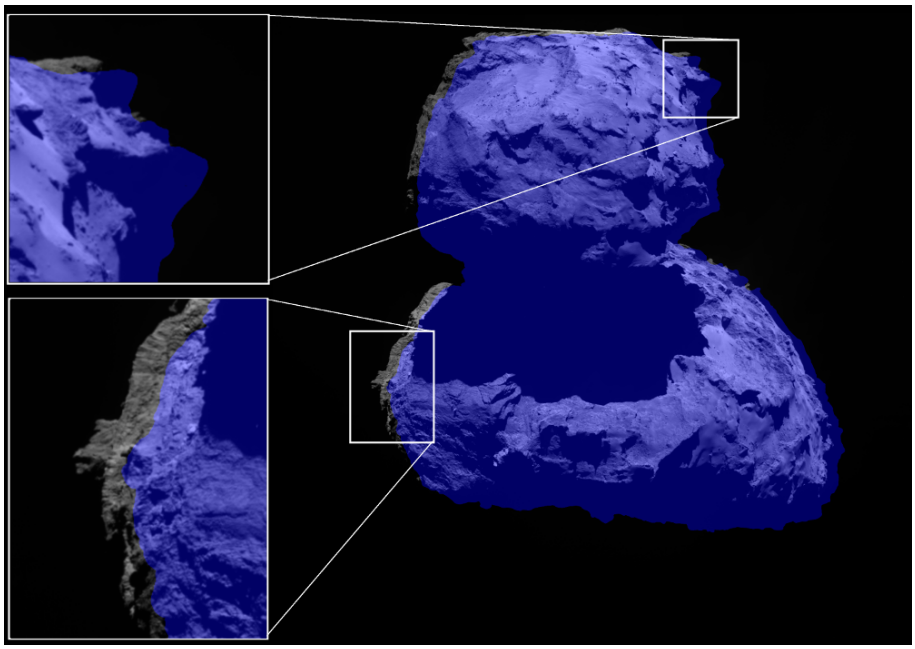

Figure 3.5: Misalignment between an OSIRIS image of 67P nucleus and the its silhouette from a synthetic image using a shape model (Preusker et al. 2015). The silhouette in blue in superposed on the OSIRIS image. The silhouette does not coincide with the limb of the nucleus but is offset towards the right of the image. The offset results from the erroneous estimates of spacecraft or camera position and orientation used for image simulation.

The first intersection along the line-of-sight, i.e., $\mathbf{r}_{1,\varkappa}$, which yields the the minimum l is located within the visible portion of the nucleus surface and, thus, corresponds to the pixel coordinates (X_P,Y_P) from the image.

3.2.2 Determination of position and orientation of spacecraft

Positioning on the nucleus using a single image requires *a priori* information about the position and pointing of the camera with respect to the nucleus. The transformation from the body-fixed to the camera coordinate system, i.e., the translational vector of the coordinate origin, $\mathbf{r}_\mathrm{C}$, and the rotation matrix, $\mathbf{R}^{[\mathrm{C}]}_{[\mathrm{BF}]}$, is derived directly from the SPICE kernels (Acton 1996). However, the quantities are subject to inevitable errors. The errors are often revealed by a clear mismatch between a synthetic or simulated image and the actual image (Fig. 3.5). The difference may be perceived as an offset, a misorientation, or unequal scales of the nucleus in the synthetic view compared with the actual image. Simply put, if the errors in the shape model are negligible (as is often the case), the discrepancy occurs only when the synthetic image is referred to some camera position and pointing other than that for the actual image.

Position and orientation errors of camera The goal is to align the synthetic image with the actual. Since the shape model used for simulation has a horizontal resolution of 2 m, which is close to the pixel resolution of the image, it is assumed here that the discrepancies between the synthetic and real images resulted from imperfect position and

attitude of the spacecraft and, thus, of the camera. The erroneous position vector is then denoted by

$$\tilde{\mathbf{r}}_{\mathrm{C}} = \mathbf{r}_{\mathrm{C}} + \delta\mathbf{r}_{\mathrm{C}}\,, \tag{3.9}$$

where $\delta\mathbf{r}_{\mathrm{C}} = (\delta x_{\mathrm{C}} \;\; \delta y_{\mathrm{C}} \;\; \delta z_{\mathrm{C}})^{\mathrm{T}}$ indicates the error vector.

The errors in the rotation matrix are considered to result in three additional (unnecessary) minute rotations of the true camera coordinate system, such as,

$$\tilde{\mathbf{R}}^{[\mathrm{C}]}_{[\mathrm{BF}]} = \boldsymbol{\delta}\mathbf{R}_{[\mathrm{C}]}\mathbf{R}^{[\mathrm{C}]}_{[\mathrm{BF}]}\,. \tag{3.10}$$

The error rotation matrix, $\boldsymbol{\delta}\mathbf{R}_{[\mathrm{C}]}$, is decomposed into three successive rotations around the instantaneous x-, y-, and z-axes, by the angles ψ_x, ψ_y, and ψ_z, respectively, i.e.,

$$\begin{aligned}\boldsymbol{\delta}\mathbf{R}_{[\mathrm{C}]} &= \mathbf{R}_z(\psi_z)\mathbf{R}_y(\psi_y)\mathbf{R}_x(\psi_x)\\ &= \begin{pmatrix} \cos\psi_z & \sin\psi_z & 0\\ -\sin\psi_z & \cos\psi_z & 0\\ 0 & 0 & 1\end{pmatrix}\begin{pmatrix} \cos\psi_y & 0 & -\sin\psi_y\\ 0 & 1 & 0\\ \sin\psi_y & 0 & \cos\psi_y\end{pmatrix}\begin{pmatrix}1 & 0 & 0\\ 0 & \cos\psi_x & \sin\psi_x\\ 0 & -\sin\psi_x & \cos\psi_x\end{pmatrix}.\end{aligned} \tag{3.11}$$

For small ψ, it is reasonable to neglect their products from the second order. With $\cos\psi \approx 1$ and $\sin\psi \approx \psi$, Eq. (3.11) is approximated as

$$\boldsymbol{\delta}\mathbf{R}_{[\mathrm{C}]} \approx \begin{pmatrix} 1 & \psi_z & -\psi_y\\ -\psi_z & 1 & \psi_x\\ \psi_y & -\psi_x & 1\end{pmatrix}, \tag{3.12}$$

irrespective of the order of rotations. Therefore, similar to the the position error vector, we may define a rotational error vector, $\boldsymbol{\psi} = (\psi_x \;\; \psi_y \;\; \psi_z)^{\mathrm{T}}$. It follows that Eq. (3.10) can be rewritten as

$$\tilde{\mathbf{R}}^{[\mathrm{C}]}_{[\mathrm{BF}]} = \boldsymbol{\delta}\mathbf{R}_{[\mathrm{C}]}\mathbf{R}^{[\mathrm{C}]}_{[\mathrm{BF}]} \approx (\mathbf{I} + [\boldsymbol{\psi}\times])\,\mathbf{R}^{[\mathrm{C}]}_{[\mathrm{BF}]}\,, \tag{3.13}$$

where $[\boldsymbol{\psi}\times]$ is a skew-symmetric matrix,

$$[\boldsymbol{\psi}\times] = \begin{pmatrix} 0 & \psi_z & -\psi_y\\ -\psi_z & 0 & \psi_x\\ \psi_y & -\psi_x & 0\end{pmatrix}. \tag{3.14}$$

Projection of misalignment error in image The errors in the camera position and orientation, i.e., $\boldsymbol{\delta}\mathbf{r}_{\mathrm{C}}$ and $\boldsymbol{\psi}$ (or $\boldsymbol{\delta}\mathbf{R}_{[\mathrm{C}]}$), will contaminate the position of a field point in the camera coordinate system as a result of erroneous transformation (i.e., even if its coordinates in the body-fixed system are accurate). In the presence of errors, Eq. (3.3) evaluating the transformation of a vector from the body-fixed to the camera coordinate system is revised as follows,

$$\tilde{\mathbf{r}}^{[\mathrm{C}]}_{\mathrm{P}} = \tilde{\mathbf{R}}^{[\mathrm{C}]}_{[\mathrm{BF}]}\,(\mathbf{r}_{\mathrm{P}} - \tilde{\mathbf{r}}_{\mathrm{C}})\;, \tag{3.15}$$

where $\mathbf{r}_\mathrm{P}$ is considered free of errors. With Eqs. (3.9) and (3.13), the above equation becomes,

$$\begin{aligned}\tilde{\mathbf{r}}_\mathrm{P}^{[\mathrm{C}]} &= \mathbf{r}_\mathrm{P}^{[\mathrm{C}]} + \boldsymbol{\delta}\mathbf{r}_\mathrm{P}^{[\mathrm{C}]} \\ &= \mathbf{r}_\mathrm{P}^{[\mathrm{C}]} - \mathbf{R}_{[\mathrm{BF}]}^{[\mathrm{C}]}\boldsymbol{\delta}\mathbf{r}_\mathrm{C} + [\boldsymbol{\psi}\times]\underbrace{\mathbf{R}_{[\mathrm{BF}]}^{[\mathrm{C}]}(\mathbf{r}_\mathrm{P} - \mathbf{r}_\mathrm{C})}_{\mathbf{r}_\mathrm{P}^{[\mathrm{C}]}} - [\boldsymbol{\psi}\times]\mathbf{R}_{[\mathrm{BF}]}^{[\mathrm{C}]}\boldsymbol{\delta}\mathbf{r}_\mathrm{C}\,. \end{aligned} \tag{3.16}$$

Hence, the error vector in the camera coordinate system is approximated to the first order of $\boldsymbol{\delta}\mathbf{r}_\mathrm{C}$ and $\boldsymbol{\psi}$ as

$$\boldsymbol{\delta}\mathbf{r}_\mathrm{P}^{[\mathrm{C}]} = -\mathbf{R}_{[\mathrm{BF}]}^{[\mathrm{C}]}\boldsymbol{\delta}\mathbf{r}_\mathrm{C} + [\boldsymbol{\psi}\times]\mathbf{r}_\mathrm{P}^{[\mathrm{C}]}\,. \tag{3.17}$$

where the second-order product, $-[\boldsymbol{\psi}\times]\mathbf{R}_{[\mathrm{BF}]}^{[\mathrm{C}]}\boldsymbol{\delta}\mathbf{r}_\mathrm{C}$, is neglected.

Let the coordinates of the field point with respect to the camera be denoted as

$$\tilde{\mathbf{r}}_\mathrm{P}^{[\mathrm{C}]} = \begin{pmatrix}\tilde{x}_\mathrm{P}^{[\mathrm{C}]}\\ \tilde{y}_\mathrm{P}^{[\mathrm{C}]}\\ \tilde{z}_\mathrm{P}^{[\mathrm{C}]}\end{pmatrix} = \begin{pmatrix}x_\mathrm{P}^{[\mathrm{C}]} + \delta x_\mathrm{P}^{[\mathrm{C}]}\\ y_\mathrm{P}^{[\mathrm{C}]} + \delta y_\mathrm{P}^{[\mathrm{C}]}\\ z_\mathrm{P}^{[\mathrm{C}]} + \delta z_\mathrm{P}^{[\mathrm{C}]}\end{pmatrix}. \tag{3.18}$$

In the synthetic image, $\boldsymbol{\delta}\mathbf{r}_\mathrm{P}^{[\mathrm{C}]} = (\delta x_\mathrm{P}^{[\mathrm{C}]} \quad \delta y_\mathrm{P}^{[\mathrm{C}]} \quad \delta z_\mathrm{P}^{[\mathrm{C}]})^\mathrm{T}$ manifests itself as "misalignment errors" in the simulated pixel coordinates, $(\tilde{X}_\mathrm{P}, \tilde{Y}_\mathrm{P})$, i.e.,

$$\begin{pmatrix}\tilde{X}_\mathrm{P}\\ \tilde{Y}_\mathrm{P}\end{pmatrix} = \frac{1}{p}\frac{r_\mathrm{f}}{\tilde{z}_\mathrm{P}}\begin{pmatrix}\tilde{x}_\mathrm{P}\\ \tilde{y}_\mathrm{P}\end{pmatrix} = \begin{pmatrix}X_\mathrm{P}\\ Y_\mathrm{P}\end{pmatrix} + \begin{pmatrix}\delta X_\mathrm{P}\\ \delta Y_\mathrm{P}\end{pmatrix}. \tag{3.19}$$

It can be shown that, as a first-order approximation,

$$\begin{aligned}\delta X_\mathrm{P} &= \frac{p^{-1}r_\mathrm{f}\,\delta x_\mathrm{P}^{[\mathrm{C}]} - X_\mathrm{P}\delta z_\mathrm{P}^{[\mathrm{C}]}}{z_\mathrm{P}^{[\mathrm{C}]}}\,,\\ \delta Y_\mathrm{P} &= \frac{p^{-1}r_\mathrm{f}\,\delta y_\mathrm{P}^{[\mathrm{C}]} - Y_\mathrm{P}\delta z_\mathrm{P}^{[\mathrm{C}]}}{z_\mathrm{P}^{[\mathrm{C}]}}\,.\end{aligned} \tag{3.20}$$

A task remains, however, to relate $(\delta X_\mathrm{P}, \delta Y_\mathrm{P})$ directly to the components of $\boldsymbol{\delta}\mathbf{r}_\mathrm{C}$ and $\boldsymbol{\psi}$ via Eq. (3.20). Referring to Eq. (3.17), it is found that

$$\begin{aligned}\delta x_\mathrm{P}^{[\mathrm{C}]} &= -R_{1,1}\delta x_\mathrm{C} - R_{1,2}\delta y_\mathrm{C} - R_{1,3}\delta z_\mathrm{C} + \psi_z y_\mathrm{P}^{[\mathrm{C}]} - \psi_y z_\mathrm{P}^{[\mathrm{C}]}\,,\\ \delta y_\mathrm{P}^{[\mathrm{C}]} &= -R_{2,1}\delta x_\mathrm{C} - R_{2,2}\delta y_\mathrm{C} - R_{2,3}\delta z_\mathrm{C} - \psi_z x_\mathrm{P}^{[\mathrm{C}]} + \psi_x z_\mathrm{P}^{[\mathrm{C}]}\,,\\ \delta z_\mathrm{P}^{[\mathrm{C}]} &= -R_{3,1}\delta x_\mathrm{C} - R_{3,2}\delta y_\mathrm{C} - R_{3,3}\delta z_\mathrm{C} + \psi_y x_\mathrm{P}^{[\mathrm{C}]} - \psi_x y_\mathrm{P}^{[\mathrm{C}]}\,,\end{aligned} \tag{3.21}$$

where $R_{i,j}$ indicates the element in row i and line j of the matrix $\mathbf{R}_{[\mathrm{BF}]}^{[\mathrm{C}]}$.

Substituting the expressions of Eq. (3.21) into (3.20), a set of linear equations is established that expresses the misalignment errors between a synthetic and real images in terms of the position and orientation errors of the camera with respect to the nucleus,

$$\begin{aligned}
&\mathbf{y}_\mathrm{P} = \mathbf{A}_\mathrm{P}\mathbf{x}\,,\\
&\mathbf{y}_\mathrm{P} = \begin{pmatrix}\delta X_\mathrm{P}\\ \delta Y_\mathrm{P}\end{pmatrix}, \quad \mathbf{x} = \begin{pmatrix}\boldsymbol{\delta}\mathbf{r}_\mathrm{C}\\ \boldsymbol{\psi}\end{pmatrix} = \begin{pmatrix}\delta x_\mathrm{C} & \delta y_\mathrm{C} & \delta z_\mathrm{C} & \psi_x & \psi_y & \psi_z\end{pmatrix}^\mathrm{T}.
\end{aligned} \tag{3.22}$$

The design matrix $\mathbf{A}_\mathrm{P}$ is given by,

$$\mathbf{A}_\mathrm{P} = \underbrace{\frac{1}{z_\mathrm{P}^{[\mathrm{C}]}}\begin{pmatrix}\frac{r_\mathrm{f}}{p} & 0 & -X_\mathrm{P}\\ 0 & \frac{r_\mathrm{f}}{p} & -Y_\mathrm{P}\end{pmatrix}}_{\mathbf{G}}\underbrace{\begin{pmatrix}-R_{1,1} & -R_{1,2} & -R_{1,3} & 0 & -z_\mathrm{P}^{[\mathrm{C}]} & y_\mathrm{P}^{[\mathrm{C}]}\\ -R_{2,1} & -R_{2,2} & -R_{2,3} & z_\mathrm{P}^{[\mathrm{C}]} & 0 & -x_\mathrm{P}^{[\mathrm{C}]}\\ -R_{3,1} & -R_{3,2} & -R_{3,3} & -y_\mathrm{P}^{[\mathrm{C}]} & x_\mathrm{P}^{[\mathrm{C}]} & 0\end{pmatrix}}_{\mathbf{H}}, \tag{3.23}$$

where $\mathbf{G}$ and $\mathbf{H}$ are derived from Eqs. (3.20) and (3.21), respectively.

Least-squares estimation of camera position and orientation errors Eq. (3.22) enables the estimation of $\boldsymbol{\delta}\mathbf{r}_\mathrm{C}$ and $\boldsymbol{\psi}$ from $(\delta X_\mathrm{P}, \delta Y_\mathrm{P})$ if measured. We use a high-resolution shape model to create the synthetic image, and select no less than three points on the shape model that correspond to some easily recognizable landmarks on the nucleus, such as monoliths, depressions. The initial estimates of the position and orientation of the camera are taken from the SPICE kernels (Acton 1996). The pixel coordinates of these landmarks, $\tilde{X}_\mathrm{P}$, $\tilde{Y}_\mathrm{P}$, in a image are computed via Eq. (3.15) and, then, Eq. (3.19) based on the initial estimates. The discrepancies between the pixel coordinates for all landmarks are arranged in a vector as,

$$\begin{aligned}
\mathbf{y}^\mathrm{T} &= \begin{pmatrix}\mathbf{y}_1^\mathrm{T} & \cdots & \mathbf{y}_i^\mathrm{T} & \cdots & \mathbf{y}_n^\mathrm{T}\end{pmatrix}\\
&= \begin{pmatrix}\delta X_1 & \delta Y_1 & \cdots & \delta X_i & \delta Y_i & \cdots & \delta X_n & \delta Y_n\end{pmatrix}^\mathrm{T},
\end{aligned} \tag{3.24}$$

where the integer index $i \in [1, n]$, replacing the letter subscript "P" (that indicates a general field point) in Eq. (3.22), distinguishes different landmarks.

Accounting for inevitable errors, $\boldsymbol{\upsilon}$, that arise from inaccurate measurement of (X_i, Y_i), shape model errors contaminating $\mathbf{r}_\mathrm{P}$ in Eq. (3.15), and so on, the linear system is expressed as

$$\mathbf{y} = \mathbf{A}\mathbf{x} + \boldsymbol{\upsilon}\,, \tag{3.25}$$

with

$$\mathbf{A}^\mathrm{T} = \begin{pmatrix}\mathbf{A}_1^\mathrm{T} & \cdots & \mathbf{A}_n^\mathrm{T}\end{pmatrix}, \tag{3.26}$$

according to Eq. (3.22), where all true (yet unknown) quantities can be approximated by the erroneous ones, e.g., $X_\mathrm{P} = \tilde{X}_\mathrm{P}$, $z_\mathrm{P}^{[\mathrm{C}]} = \tilde{z}_\mathrm{P}^{[\mathrm{C}]}$, and $\mathbf{R}_{[\mathrm{BF}]}^{[\mathrm{C}]} = \tilde{\mathbf{R}}_{[\mathrm{BF}]}^{[\mathrm{C}]}$.

If $n > 3$, the linear system of Eq. (3.25) is over-determined, and solved via least-squares methods. Suppose the measurement errors are unbiased, i.e., $E(\boldsymbol{\upsilon}) = \mathbf{0}$, and the weight matrix is given by

$$\mathbf{W} = \mathbf{\Sigma}^{-1}\,, \quad \mathbf{\Sigma} = E\left(\boldsymbol{\upsilon}\boldsymbol{\upsilon}^{\mathrm{T}}\right)\,, \tag{3.27}$$

with $\mathbf{\Sigma}$ denoting the covariance matrix for $\boldsymbol{\upsilon}$. Omitting the details, estimates are obtained as

$$\hat{\mathbf{x}} = \left(\mathbf{A}^{\mathrm{T}}\mathbf{W}\mathbf{A}\right)^{-1}\mathbf{A}^{\mathrm{T}}\mathbf{W}\mathbf{y}\,, \tag{3.28}$$

which minimize $(\mathbf{y} - \mathbf{A}\hat{\mathbf{x}})^{\mathrm{T}}\,\mathbf{W}\,(\mathbf{y} - \mathbf{A}\hat{\mathbf{x}})$ as a general weighted least-squares problem.

Because Eq. (3.25) (based on Eq. 3.22) is linearized with first-order approximation, the solution of Eq. (3.28) needs to be iterated and the error estimates, $\hat{\boldsymbol{\delta}}\mathbf{r}_{\mathrm{C}}$ and $\hat{\boldsymbol{\psi}}$, must be corrected from $\tilde{\mathbf{r}}_{\mathrm{C}}$ and $\tilde{\mathbf{R}}^{[\mathrm{C}]}_{[\mathrm{BF}]}$ after each iteration, namely,

$$\begin{aligned}\tilde{\mathbf{r}}_{\mathrm{C}}^{(k+1)} &= \tilde{\mathbf{r}}_{\mathrm{C}}^{(k)} - \hat{\boldsymbol{\delta}}\mathbf{r}_{\mathrm{C}}^{(k)}\,,\\ \tilde{\mathbf{R}}^{(k+1)} &= \left(\hat{\boldsymbol{\delta}}\mathbf{R}_{[\mathrm{C}]}^{(k)}\right)^{\mathrm{T}}\tilde{\mathbf{R}}^{(k)}\,,\end{aligned} \tag{3.29}$$

where the integer $k \geq 0$ increments with iterations. The lettered superscript and subscript, "[C]" and "[BF]", in $\tilde{\mathbf{R}}$ denoting the coordinate systems are omitted to reduce the clutter in notation. According to Eq. (3.10), $\hat{\boldsymbol{\delta}}\mathbf{R}^{\mathrm{T}}_{[\mathrm{C}]}$=$\mathbf{R}_x(-\hat{\psi}_x)\mathbf{R}_y(-\hat{\psi}_y)\mathbf{R}_z(-\hat{\psi}_z)$. In this case, the first-order approximation of Eq. (3.12) is discarded for the correction in order to prevent the violation of $\det(\mathbf{R}) = 1$ in numerical evaluation.

The iterations are terminated once $\|\hat{\boldsymbol{\delta}}\mathbf{r}_{\mathrm{C}}^{(k)}\|$ and $\|\hat{\boldsymbol{\psi}}^{(k)}\|$ both fall below the respective thresholds.

3.2.3 Application to OSIRIS observation of 67P nucleus

As an example, the adjustment method described above is applied to refine the initial estimates of camera position and pointing for the image in Fig. 3.5, clearly inaccurate with respect to the actual viewing geometry. In this particular case, six landmarks were identified, and their *actual* pixel coordinates, X_{P}, Y_{P}, were measured in the original image. The pixel coordinates of the landmarks in the synthetic image were measured as $\tilde{X}_{\mathrm{P}}$, $\tilde{Y}_{\mathrm{P}}$.

The observable for a *single* landmark was then formulated as $(\delta X_{\mathrm{P}}, \delta Y_{\mathrm{P}})^{\mathrm{T}} = (\tilde{X}_{\mathrm{P}}, \tilde{Y}_{\mathrm{P}})^{\mathrm{T}} - (X_{\mathrm{P}}, Y_{\mathrm{P}})^{\mathrm{T}}$ according to Eq. (3.19). The linear observation equation is specified by Eq. (3.22), where the error estimates, $\mathbf{x}^{\mathrm{T}} = (\boldsymbol{\delta}\mathbf{r}_{\mathrm{C}}^{\mathrm{T}}, \boldsymbol{\psi}^{\mathrm{T}})$, are connected to the observable via the design matrix evaluated by Eq. (3.23).

The full system is constructed via Eqs. (3.24)-(3.26) with $n = 6$ being the number of landmarks. The solution and correction of error estimates were performed iteratively according to Eqs. (3.28) and (3.29), respectively.

The corrected position of the camera differs from the initial estimate by nearly 80 m (Fig. 3.6). The synthetic image using the refined estimates shows a silhouette of the nucleus nearly coincident with the limbs of the illuminated nucleus from the actual image (Fig. 3.7), indicating a notable improvement on the estimation of viewing geometry of the camera and, thus, the spacecraft.

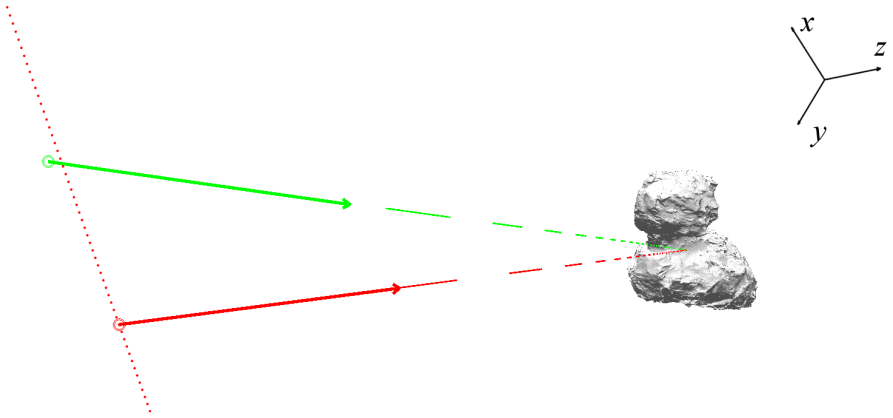

Figure 3.6: Improvement on estimation of viewing geometry for the OSIRIS image as shown in Fig. 3.5. The red arrow indicates the camera pointing vector (bore-sight) starting from the camera position based on initial estimates from SPICE. The dotted red curve indicates the SPICE-provided trajectory of the camera before and afterwards. The dashed line extends from the origin of body-fixed coordinate system towards the camera position. The initial estimate of the camera position is $(16.329,\ 14.421,\ 12.387)^{\mathrm{T}}$ km, as indicated by the double circles in red. The green arrow indicates the pointing vector based on refined estimates of camera position and orientation. The corrected camera position is at $(16.377,\ 14.382,\ 12.343)^{\mathrm{T}}$ km, as indicated by the double circles in green. Thus, the position errors are indicated by the deviation of the starting points of the two vectors. The coordinate axes are defined according to the body-fixed frame of 67P (Preusker et al. 2015).

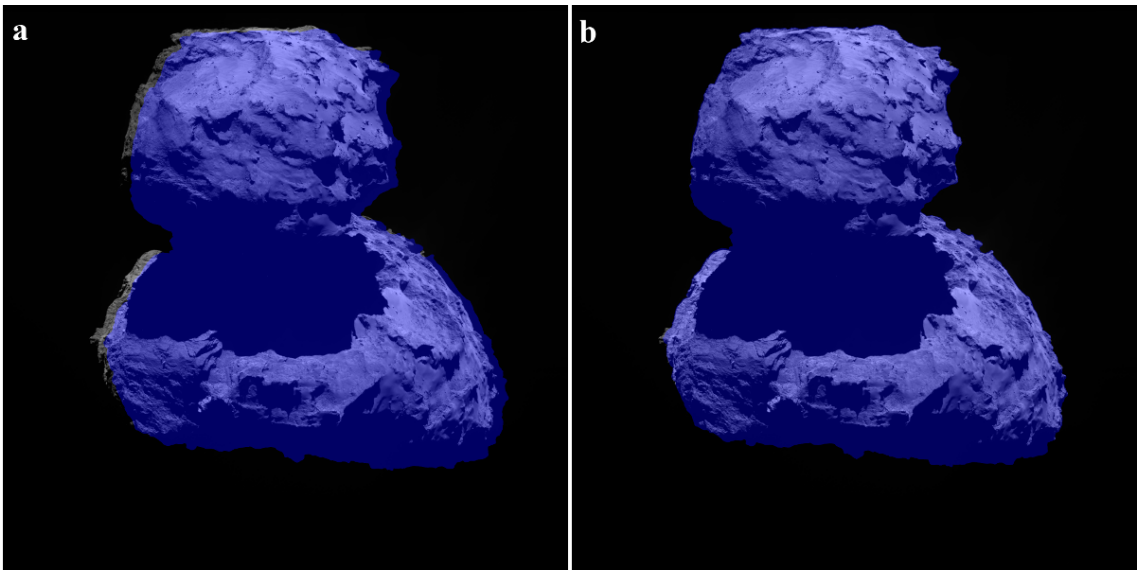

Figure 3.7: Comparison of synthetic and original image before and after correction of viewing geometry. The offset of the blue silhouette of the nucleus in the synthetic view (**a**, also highlighted in Fig. 3.5) is mostly corrected by procedure described in Sect. 3.2.2 (**b**).

3.3 Photometric method for shape modeling

The observations analyzed hereafter are radiometrically calibrated, optical-distortion corrected, "level-3" images (Tubiana et al. 2015). The pixel reading is the (scattered) spectral radiance, I_λ (in $\mathrm{W\,m^{-2}nm^{-1}sr^{-1}}$), collected by the camera through a certain filter at wavelength, λ (in nm). It is a common practice to derive the unitless radiance factor defined by

$$\mathcal{R}_\lambda = \frac{\pi I_\lambda}{F_\lambda}\,, \tag{3.30}$$

where F_λ is the solar radiance at λ. The radiance factor can be factorized into,

$$\mathcal{R}_\lambda = A_\lambda \mathcal{P}_\lambda(\alpha) D_\lambda(i,e)\,, \tag{3.31}$$

where A_λ is the wavelength-dependent normal albedo, the surface reflectance of the object at zero emission angle, $e = 0°$, relative to that of a Lambertian surface under overhead illumination, i.e., at incidence angle $i = 0°$. The phase function, $\mathcal{P}_\lambda$, and the disk function, D_λ, both of which are wavelength-dependent, will be introduced shortly. With little risk of confusion, the subscript, "λ", indicating the wavelength dependence of the quantity will be omitted in the notation hereafter.

A third angle can be introduced in addition to the incidence and emission angles, i, e, to define a practical set of photometric coordinates (Shkuratov et al. 2011). The photometric azimuth, φ, is the spherical angle between the two planes containing respectively the illumination and scattering vectors and intersecting at the surface normal (Fig. 3.8). These coordinates are conveniently converted into an equivalent set of coordinates of phase angle, α, photometric latitude, β, and longitude, γ, via (Shkuratov et al. 2011),

$$\begin{aligned}
\cos\alpha &= \cos i \cos e + \sin i \sin e \cos\varphi\,,\\
\cos\beta &= \left[\frac{\sin^2(i+e) - \cos^2\left(\frac{\varphi}{2}\right)\sin 2e \sin 2i}{\sin^2(i+e) - \cos^2\left(\frac{\varphi}{2}\right)\sin 2e \sin 2i + \sin^2 e \sin^2 i \sin^2\varphi}\right]^{\frac{1}{2}}\,,\\
\cos\gamma &= \frac{\cos e}{\cos\beta}\,.
\end{aligned} \tag{3.32}$$

The reverse conversion is given by,

$$\begin{aligned}
\cos i &= \cos\beta\cos(\alpha-\gamma)\,,\\
\cos e &= \cos\beta\cos\gamma\,,\\
\cos\varphi &= \frac{\cos\alpha - \cos i\cos e}{\sin i \sin e}\,.
\end{aligned} \tag{3.33}$$

Note, however, that the phase angle, α, can be defined alternatively as,

$$\alpha = \arccos\left(\mathbf{u}_\mathrm{O}\cdot\mathbf{u}_\odot\right)\,, \tag{3.34}$$

where $\mathbf{u}_\mathrm{O}{=}{-}\mathbf{u}_z^{[\mathrm{C}]}$ and $\mathbf{u}_\odot$ are the unit vectors of the observer and the Sun with respect to scattering location. The plane containing the two vectors is called the scattering plane, whose normal is along $\mathbf{u}_\mathrm{O}\times\mathbf{u}_\odot$, which is distinct from the local surface plane.

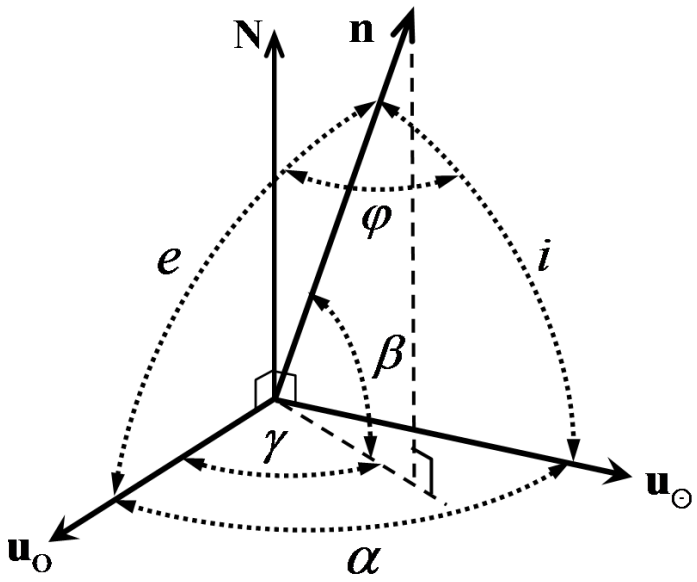

Figure 3.8: Angular coordinates for photometric analysis. The first set of photometric coordinates, i, e, and φ, are defined in reference to the the scattering surface. The second set consists of α, β, and γ, in reference to the scattering (light-travelling) plane. The normal to the scattering plane is indicated by **N**; the scattering plane contains the solar and scattering vectors indicated by $\mathbf{u}_\odot$ and $\mathbf{u}_\mathrm{O}$, respectively. The normal to the local surface plane is given by **n**.

Thus, the phase function is a measure of the angular distribution of the intensity of light scattering, and can be modeled by (Shkuratov et al. 2011),

$$\mathcal{P}(\alpha) = \sum_{k=0}^{k_{\max}} c_k \alpha^k \,, \tag{3.35}$$

for some integer k. c_k are coefficients and $c_0 = 1$ by definition.

The disk function, D, generally describes the variation of scattering intensity due to the macroscopic topography. An illustrative, though hardly rigorous, conception is that a change in the orientation of the local surface normal (e.g., **n** in Fig. 3.8) will induce a change in the incidence and emission angles. A very common yet, perhaps, sometimes too simplistic approximation of intensity variation is given by the Lommel-Seeliger Law, i.e.,

$$D(i, e) = \frac{2 \cos i}{\cos i + \cos e} \,, \tag{3.36}$$

which is unity at zero phase angle when $\cos i = \cos e$. Another instructive expression of D is obtained by substituting the expressions of $\cos i$ and $\cos e$ in terms of α, β, and γ, that yields,

$$D(\alpha, \gamma) = \frac{2\cos(\alpha - \gamma)}{\cos(\alpha - \gamma) + \cos\gamma}\,. \tag{3.37}$$

γ is the projection of the surface normal onto the scattering plane; therefore, it is a direct measure of the surface variation (in slope). In case the field-of-view of the camera is narrow (e.g., $\sim 2^\circ$ for NAC), the phase angle changes indistinctly over an image, and D is only dependent on γ.

3.3.1 Principles of Shape-from-Shading method

Shape modeling is a fundamental practice in image analysis. As expressed by Eq. (3.5), the inverse transformation from the image coordinates of an object to its 3-D position is prohibited by the lack of (or weak) constraint on distance or visual depth. The depth perception can be achieved by stereoscopy, or "binocular vision", where the object distance is determined via triangulation with respect to a baseline formed by two observers with known positions. In the context of shape modeling, the method is known as stereophotogrammetry (SPG) using pairs of images at respective conjugate locations. Alternatively, the topography and, in particular, slope of the object surface under illumination gives rise to variation in the radiance of scattered light that is measured by the brightness intensity of images of the object. Thus, the variation of brightness intensities of the image provides an indirect way to assess the *variation* of the visual depth of the object surface, though the absolute distance of the object from the camera remains undetermined without additional constraint. In the case of remote sensing observations at terrestrial bodies, where the distance of the camera (spacecraft) from the ground is known, the topographic variation can then be derived from the image brightness variations in reference to the known camera distance above the ground. This is the primitive principle of the Shape-from-Shading approach, or photoclinometry (Rindfleisch 1966).

Shape models for 67P nucleus The reconstruction of nucleus shape for 67P proved to be an exceedingly delicate task. The shape model produced by Preusker et al. (2015) employs the SPG method. The concave shape and abrupt topography give rise to highly variable illumination conditions that demand special care in the selection and analysis of datasets as well as the application of the method (Preusker et al. 2015). The photoclinometric techniques for shape reconstruction are adopted by Jorda et al. (2016). Specifically, the MPCD (multi-resolution photoclinometry by deformation) method is applied for a global reconstruction of the nucleus (Capanna et al. 2013), while the product is further refined by tiling of high-resolution, local topographic “maplets” produced by the stereophotogrammetry method (Gaskell et al. 2008). Both shape models of 67P achieved horizontal resolution at meter level, and can be expected to improve in future effort.

While elaborate shape modeling is beyond the scope of this work, it is instrumental to revisit the principles of the Shape-from-Shading method that has the potential to retrieve 3-D information from single images at virtually no cost.

Suppose the vector pointing from the focal point of the camera to an arbitary point on the object surface is given by $\mathbf{r} = r\hat{\mathbf{r}}$. For each image, a "zero-phase" point can be defined by the pixel where zero phase angle occurs, i.e., $\hat{\mathbf{r}}_\odot \times \hat{\mathbf{r}} = \mathbf{0}$. Not often are images

taken near the phase angle of 0° and, even less so, near 180° (pointing towards the Sun). In general, the zero-phase point lies outside the image frame (i.e., on the extended image coordinates). Rindfleisch (1966) was the first to show that the *variation* of the distance between the surface and the camera along the path radiating from the (projection of) zero-phase point is given by

$$\mathrm{d}r = \frac{r}{r_\mathrm{f}} \frac{(\hat{\mathbf{r}} \cdot \hat{\mathbf{z}})^2}{|\hat{\mathbf{z}} \times \hat{\mathbf{N}}|} \tan\gamma \, \mathrm{d}s \quad \text{(m)}\,, \tag{3.38}$$

where $\hat{\mathbf{z}}$ is aligned with the bore-sight of the camera, and where

$$\hat{\mathbf{N}} = \frac{\hat{\mathbf{r}}_\odot \times \hat{\mathbf{r}}}{|\hat{\mathbf{r}}_\odot \times \hat{\mathbf{r}}|}\,, \tag{3.39}$$

denotes the normal vector to the scattering plane (see Fig. 3.8). r_f is the focal length of the camera. s measures the distance along the path over the image plane. It can be shown that $\tan\gamma$ is expressible as (Rindfleisch 1966),

$$\tan\gamma = \left(\frac{\cos i}{\cos e} - \cos\alpha\right) \sin^{-1}\alpha = \left[\frac{\cos(\alpha-\gamma)}{\cos\gamma} - \cos\alpha\right] \sin^{-1}\alpha. \tag{3.40}$$

The unknown on the right-hand side of the equation, $\cos(\alpha-\gamma)/\cos\gamma$, can be derived from Eq. (3.37) as

$$\frac{\cos(\alpha-\gamma)}{\cos\gamma} = \frac{D}{2-D}\,, \tag{3.41}$$

where D can be obtained as

$$D = \frac{\mathcal{R}}{A\,\mathcal{P}(\alpha)}\,, \tag{3.42}$$

from the measured radiance factor, $\mathcal{R}$, provided that the phase function, $\mathcal{P}$, is known beforehand.

If the distance of a certain reference point, say P_0, from the camera is known as $r = r_0$, the distance of any other point, P, collinear with P_0 and the zero-phase point is formally obtainable by integrating Eq. (3.38) as

$$r(\mathrm{P}) = r_0 \exp\left(\frac{1}{r_\mathrm{f}} \int_{\mathrm{P}_0}^{\mathrm{P}} \frac{(\hat{\mathbf{r}} \cdot \hat{\mathbf{z}})^2}{|\hat{\mathbf{z}} \times \hat{\mathbf{N}}|} \tan\gamma \, \mathrm{d}s\right) \quad \text{(m)}\,. \tag{3.43}$$

Because the integration is along a straight line from the zero-phase point, the normal to the scattering plane, $\hat{\mathbf{N}}$, is a constant. In case the surface elevation varies negligibly with respect to the distance to the camera, i.e., $r = r_0 + \Delta r$ where $\Delta r \ll r_0$, it is legitimate to integrate Eq. (3.38) directly as,

$$\Delta r = \int_{\mathrm{P}_0}^{\mathrm{P}} \mathrm{d}r \quad \text{(m)}\,. \tag{3.44}$$

An even simpler but more restrictive approximation can be used in practice, by noting $(\hat{\mathbf{r}} \cdot \hat{\mathbf{z}})^2/|\hat{\mathbf{z}} \times \hat{\mathbf{N}}| \approx 1$ in Eq. (3.38) as long as image widths are small compared to the focal length of the camera, namely,

$$\Delta r \approx \frac{r_0}{r_\mathrm{f}} \int_{\mathrm{P}_0}^{\mathrm{P}} \tan\gamma \, \mathrm{d}s \quad (\mathrm{m}), \tag{3.45}$$

where $\tan\gamma$ is as measured via Eqs. (3.40)-(3.42). Eq. (3.45) reflects the essence of the basic Shape-from-Shading method that translates the brightness variation of the image into surface undulation rescaled by r_0/r_f (from the camera pixel length to the real-world distance).

3.3.2 Application of Shape-from-Shading to OSIRIS observation of 67P nucleus

A prerequisite for the application of the Shape-from-Shading method described above is the availability of the phase function of the object. Understandably, phase function is needed to derive the (tangent of) photometric longitude, i.e., the co-orientation of the scattering surface with respect to the Sun and the camera, from the radiance of the scattered light (Eq. 3.42). To obtain a function for 67P nucleus in the form of Eq. (3.35), the phase curve derived by Fornasier et al. (2015) is fitted to a maximum degree of $k_\mathrm{max} = 4$. Higher-degree polynomial change results only marginally.

In probably all OSIRIS images, the Sun is projected atop the image frame, i.e., shadows are always cast downwards, in which case the zero-phase point lies below the frame. To apply Eq. (3.45), the path for measurements of $\tan\gamma$ and integration thereon is a straight line from the bottom of the images along which the image coordinate X is fixed.

Strictly speaking, the value of r_0 is unknown and should be, whenever possible, determined by shape modeling. Under certain circumstances, it is viable to approximate r_0. One may resort to the method described in Sect. 3.2.1, where r_0 is determined by the distance from the camera to the point on the nucleus surface along line of sight, with the nucleus approximated by a shape model. In doing so, the product of the Shape-from-Shading does not improve the absolute accuracy of the shape model. The reason is the use of an imperfect shape model that leads to errors in the estimate, i.e., $\tilde{r}_0 = r_0 + \delta r_0$. However, if δr_0 is small compared with r_0, the topographic profiles offer details commensurate with the resolution of the images and, thus, may enhance the *local* resolution of the shape model. Thus, topographic profiles are useful where the macroscopic surface roughness, rather than the absolute surface height, is of interest.

As an example, the method is applied to reconstruct the roughness pattern of a local surface area as shown in Fig. 3.9. The image is a clip from the original larger image taken by the OSIRIS NAC. The integration starts from the bottom of the image and proceeds upward (Fig. 3.9a). The linear trend of the topographic profile is removed to accentuate the (deci-)meter-scale undulations due to surface roughness (Fig. 3.9b). Hereafter, such detrended profiles are referred as *roughness* profiles instead.

The integration of Eq. (3.45) along each path results in a roughness profile independent from others. The profiles can be connected to form a digital terrain model, or more suitably, roughness model if the initial values, r_0, of the profiles are known without errors. On the other hand, even if a unique strategy for "threading" initial points of the profiles exists, the errors accumulating along the path may give rise to erroneous undulations across profiles (Horn 1977). Therefore, a simple expedient approach is to impose some constraint on the smoothness across the profiles and, thus, on the resulting roughness model.

Here, it is stipulated that there is no abrupt and overall shift between adjacent profiles. Specifically, the difference between a pair of adjacent profiles is fitted by a polynomial as follows,

$$\Delta r' = \sum_{k=0}^{k_{\max}} a_k s^k \,, \tag{3.46}$$

where s is the distance from the initial point along the path, as in Eq. (3.45), and where $k_{\max}$ is the maximum degree of the polynomial. The *minuend* profile is then detrended by subtraction of the polynomial. The rule of thumb regarding the choice of $k_{\max}$ is the insignificant decrease of the fitting residual with degree of the polynomial. The roughness model assembled by individual profiles across the entire image is shown in Fig. 3.9c, where the elevation is magnified by three times to exhibit the undulations.

It is re-emphasized that the resulting roughness model does not yield improvement on the accuracy of the existing shape models; as will be shown in Sect. 7, the model will be used for measuring and comparing the roughness of the nucleus surface over time. It is desirable to refer the local roughness model to the global shape models (Preusker et al. 2015, Jorda et al. 2016). Fig. 3.10 shows a synthetic image of the surface roughness over the nucleus shape model under the same illumination condition and viewing geometry as the original image. Differences exist in the overall gradation of brightness, likely arising from the imperfect orientation of the facet of the shape model with respect to the nucleus: note an artificial crease slanting across the lower left corner of the synthetic image that corresponds to the boundary between two facets. Another general issue is that the method produces an ambiguous result over the shadowed areas. Nevertheless, the similarity between the images confirms the capability of Shape-from-Shading to capture the general roughness pattern of the local nucleus surface.

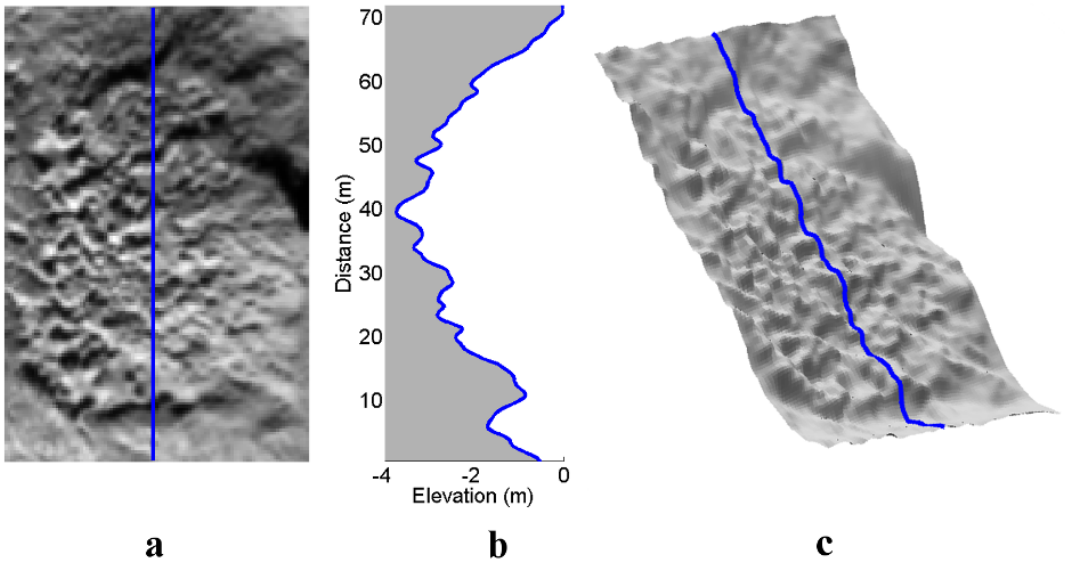

Figure 3.9: Application of Shape-from-Shading method to retrieve the surface roughness pattern from brightness intensities of a single image. **a**. Image of 150 by 100 pixels showing the "honeycomb" surface texture discovered on 67P (Shi et al. 2016a). **b**. Topographic (roughness) profile derived from the brightness variation of the image along the path indicated in **a**. The linear trend of the curve is discarded. Note that the "elevation", measured with respect to the camera rather than to some well-defined geodetic datum, is, strictly speaking, a misnomer. **c**. Full surface roughness model constructed by the assemblage of profiles. This figure is reproduced from Fig. 15 in Hu et al. (2017b), permission © ESO.

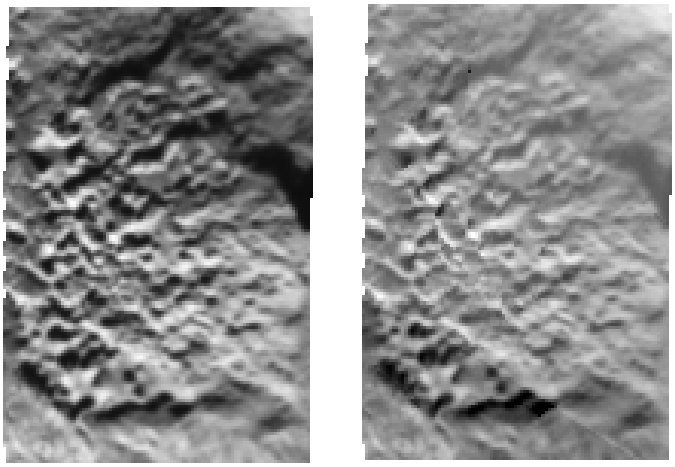

Figure 3.10: Comparison of the original image showing the honeycombed surface texture and the synthetic view using a reconstructed roughness model. The synthetic view is in the right panel.

4 Thermal Modeling: Concept and Numerical Approach

The essence of Chapters 4 and 5 is summarized in Hu et al. 2017, Monthly Notices of the Royal Astronomical Society, Vol. 469, S295-S311, published by Oxford University Press.

Cometary activity is manifest by the presence of extensive dust tail and coma shrouding the nucleus when observed from afar. Fine structures of the near-nucleus dust coma can only be revealed by *in situ* observations. Streams of dust particles that are often observed emanating from the nucleus are a source of replenishment of the dust coma. Sublimation and outgassing of volatile ices from the nucleus interior is the most probable mechanism to liberate and lift dust particles from the nucleus.

To understand cometary activity is to, above all, understand the activity of volatile species, i.e., their sublimation, transport from the nucleus and their interaction with dust particles. A great variety of volatiles have been found in comets, with H_2O, CO_2, CO, etc., among the most common species (Festou et al. 2004). The behaviors of volatilities and, more specifically, the thermo-physical conditions governing the phase change of different species can be vastly different. As a result, the abundance and activity of different species may vary substantially with depth inside the nucleus. Sublimation of (crystalline) water ice effectively occurs near 200 K. Such a temperature is usually found in the shallow subsurface of the sunlit nucleus when the comet is close enough to the Sun. Activity of water ice is expected to follow insolation on a diurnal basis. More volatile species, or supervolatiles such as CO_2, CO ices, sublimate strongly at lower temperatures. They can only be substantially preserved in deeper and cooler interiors of the nucleus. The activity of supervolatiles, i.e., sublimation, recondensation, and gas diffusion, is dependent on and influences the thermal and mechanical properties of the nucleus interior.

The occurrence of dust activity depends on the breakup of the surface layers and subsequent acceleration of the fragments to overcome local gravity. The dust cover prevalent in the northern hemi-nucleus of 67P had probably resulted from deposition of dust particles originating from the south. For simplicity, let us assume that the dust cover consists of spherical dust particles, each being an aggregate of smaller constituting particles. These particles were free-falling before being accreted over the nucleus surface by gravitation to form a loosely packed, porous layer at some low impact speed. The resistance of a dust particle to being separated from its surroundings is governed by the tensile strengths of the aggregates, i.e. (Skorov and Blum 2012, Blum et al. 2014),

$$P_\mathrm{t} = 1.6\phi r_\mathrm{d}^{-\frac{2}{3}} \quad \mathrm{(Pa)}\,, \tag{4.1}$$

where ϕ is the volume filling factor due to the packing structure of the dust cover. The particle radius, r_d, is in millimeters. Therefore, the dust aggregate can be mobilized if the pressure of the volatile gas overcomes the tensile strength of the aggregates, i.e.,

$$P_\mathrm{G} \geq P_\mathrm{t} \,. \tag{4.2}$$

Once the condition by Eq. (4.2) is fulfilled, the dust particle is subject to acceleration induced by the outgassing of volatiles. A spherical particle of radius r_d stationary on the nucleus surface will be set in motion if the drag force, F_G, exerted by the outward gas flow exceeds the gravity of the nucleus, namely,

$$F_\mathrm{G} \geq m_\mathrm{d} g = \frac{4}{3}\pi r_\mathrm{d}^3 \rho_\mathrm{d} g \,, \tag{4.3}$$

where g is the (magnitude of) gravity acceleration on the nucleus.

The drag force is given by (Weidenschilling 1977),

$$F_\mathrm{G} = \frac{1}{2} C_\mathrm{D} \pi r_\mathrm{d}^2 \rho_\mathrm{G} v^2 \,, \tag{4.4}$$

where ρ_G denotes density of the gas and C_D is the drag coefficient. v is the mean speed of uprising gas flow by the stationary particle,

$$v = \frac{\pi}{4} v_\mathrm{T} \,, \tag{4.5}$$

where the thermal speed of gas at temperature T is given by,

$$v_\mathrm{T} = \left(\frac{8 k_\mathrm{B} T}{\pi \hat{m}} \right)^{\frac{1}{2}} \,, \tag{4.6}$$

with k_B and $\hat{m}$ being the Boltzmann constant and molecular weight of the gas, respectively.

The mean free path of gas molecules is defined by,

$$\lambda_\mathrm{G} = \left(\sqrt{2} n \sigma \right)^{-1} \,, \tag{4.7}$$

where $n = \rho_\mathrm{G}/\hat{m}$ denotes the number density of gas and σ is the cross section of a molecule.

In case $\lambda_\mathrm{G} \gg r_\mathrm{d}$, the drag coefficient, C_D, is given by,

$$C_\mathrm{D} = \frac{8}{3} \frac{v_\mathrm{T}}{v} \,, \tag{4.8}$$

and Eq. (4.4) expresses the Epstein drag law (Weidenschilling 1977),

$$F_\mathrm{G} = \frac{4}{3} \pi r_\mathrm{p}^2 \rho_\mathrm{G} v v_\mathrm{T} \,, \tag{4.9}$$

The condition of Eq. (4.3) becomes,

$$\rho_\mathrm{G} v v_\mathrm{T} \geq \rho_\mathrm{d} r_\mathrm{d} g \,, \tag{4.10}$$

where Eq. (4.5) applied. Let Z denote the mass flux of outgassing and note that

$$\rho_{\mathrm{G}} = \frac{Z}{v}\,. \tag{4.11}$$

Then, Eq. (4.10) is expressed in terms of Z as follows,

$$Z \geq \frac{r_{\mathrm{d}}\rho_{\mathrm{d}}g}{v_{\mathrm{T}}} \quad (\mathrm{kg\,m^{-2}s^{-1}})\,. \tag{4.12}$$

Eq. (4.12) explicates the minimum outgassing flux for the ejection of a dust particle.

4.1 Model formulation

4.1.1 Dusty ice model

A basic approach of cometary thermal modeling is to assume that the nucleus is a uniform mixture of dust and ice (Fig. 4.1). This thermal model, hereafter referred to as the "dusty ice model", is described below. The nucleus surface absorbs solar energy once illuminated. Depending on the surface temperature, the nucleus cools off by thermal radiation back to space. The energy is partially consumed by the sublimation of water ice, in this case present at the surface, while the remainder is transported into the interior of the nucleus. The energy balance at the surface of the nucleus can therefore be formulated as follows,

$$Q_{(0)} = q_{\epsilon\,(0)} + q_{Z\,(0)} + q_{\kappa\,(0)} \quad (\mathrm{W\,m^{-2}}). \tag{4.13}$$

$Q_{(0)}$ on the left-hand side of the equation denotes the energy input, e.g., given by the absorbed flux of insolation. $q_{\epsilon\,(0)}$ indicates thermal radiation from the nucleus,

$$q_{\epsilon\,(0)} = \sigma\epsilon T_{(0)}^4\,, \tag{4.14}$$

where σ is the Stefan-Boltzmann constant and where $\epsilon \approx 1$ is the emissivity of the nucleus. $T_{(0)}$ denotes the surface temperature.

$q_{Z\,(0)}$ is the flux of energy consumed by the sublimation of water ice,

$$q_{Z\,(0)} = \ell Z_{(0)}\,, \tag{4.15}$$

with ℓ ($\mathrm{J\,kg^{-1}}$) being the latent heat of water ice. The sublimation flux of *pure* solid water ice is given by the Hertz-Knudsen formula,

$$Z^{\mathrm{H\text{-}K}} = \alpha P_V \sqrt{\frac{\hat{m}}{2\pi k_{\mathrm{B}} T}}\,. \tag{4.16}$$

The sublimation coefficient is given by (Gundlach et al. 2011),

$$\alpha = c_0 + \frac{c_1}{1 + \exp(c_2 - c_3/T)}\,, \tag{4.17}$$

where c_i for $i = 0, 1, 2, 3$ are constants. P_V is the temperature dependent saturation vapor pressure,

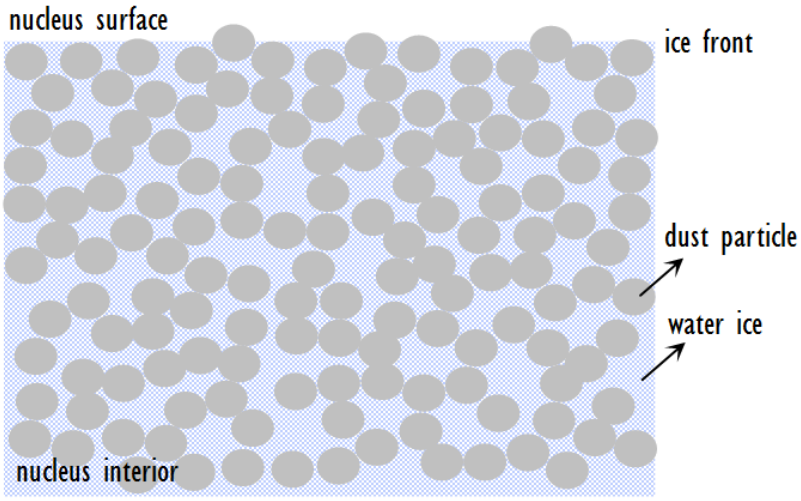

Figure 4.1: Illustration of 1-D structure of the nucleus subsurface for the dusty ice model.

$$P_V = a \exp\left(-\frac{b}{T}\right), \tag{4.18}$$

with constants a and b that can be located in such references as Fanale and Salvail (1984) and Gundlach et al. (2011).

Thus, the sublimation flux explicitly depends on the surface temperature of the nucleus, i.e., $T = T_{(0)}$ in Eq. (4.16). The presence of dust impurities result in a reduction of the icy area of the surface from which sublimation occurs. The sublimation flux of "dusty ice" can be expressed as,

$$Z_{(0)} = \mathscr{F} Z_{(0)}^{\text{H-K}}, \tag{4.19}$$

where $\mathscr{F} \in [0, 1]$ is the "icy area fraction". The expression and implications of $\mathscr{F}$ will be discussed later.

The heat transport inside the nucleus is determined by the temperature gradient,

$$q_\kappa = -\kappa \frac{\partial T}{\partial x}, \tag{4.20}$$

where x (m) measures the depth below the surface and κ (W K^{-1}m^{-1}) is the thermal conductivity of the constituting materials. Hence, the heat flux conducted from the surface downward is $q_{\kappa(0)} = q_\kappa|_{x=0^+}$.

Neglecting ice sublimation and gas diffusion that arise from the porosity of the nucleus, the heat transport in the interior is described by the 1-D heat equation,

$$c\rho \frac{\partial T}{\partial t} = \frac{\partial}{\partial x}\left(\kappa \frac{\partial T}{\partial x}\right), \tag{4.21}$$

where c (J K^{-1}) is the heat capacity and ρ (kg m^{-3}) the mass density of the material.

Depending on the timescale of insolation, the heat flux becomes negligible from a certain depth, i.e.,

$$q_{\kappa(\mathbb{X})} = q_{\kappa}|_{x=\mathbb{X}} = 0\,, \tag{4.22}$$

such that the nucleus becomes nearly isothermal underneath.

Evidently, even in the case of ice sublimating from the surface, Z is affected by not only the surface temperature but also heat flux into the nucleus. Therefore, Z must be evaluated by solving temperature profile inside the nucleus, particularly for $0 < x < \mathbb{X}$. Towards this end, Eq. (4.21) is solved by imposing surface and lower boundary conditions specified by Eqs. (4.13) and (4.22), respectively.

Icy Area Fraction The icy area fraction, $\mathscr{F}$ in Eq. (4.19), is reduced by the presence of non-volatile impurities, such as refractory dust particles, in the nucleus. To illustrate this, one may consider a unit area of the nucleus surface or a horizontal cross section of the nucleus subsurface at a certain depth. $\mathscr{F} = 1$ corresponds to a fully icy surface in which case sublimation may occur everywhere. In a dust-ice mixture, a certain portion of the area is occupied by dust where no sublimation may occur. The importance of $\mathscr{F}$ has long been recognized in previous works, such as Gutiérrez et al. (2001), Davidsson and Skorov (2002), Groussin and Lamy (2003). The correct general formula was suggested by Crifo (1997) as,

$$\mathscr{F} = \left(1 + \frac{\rho_{\mathrm{i}}}{\rho_{\mathrm{d}}}\mu\right)^{-1}\,, \tag{4.23}$$

with ρ_{i}, ρ_{d} indicating the densities of water ice and dust, respectively. μ is the mass ratio of dust and ice. Hence, outgassing from a dusty nucleus surface with higher μ is weaker than that from an icy nucleus.

4.1.2 Dust mantle model

The dusty ice model is valid if there is water ice prevalently exposed over the nucleus surface. Comet 67P is known to be overall desiccated at the surface with scarce exposure of water ice (Capaccioni et al. 2015). Hence, a more realistic characterization of the nucleus is a dust-ice mixture overlain by a dry dust mantle. Let us consider an alternative formulation to the dusty ice model presented above. This model is termed "dust mantle model", where the sublimation of water ice is assumed to occur underneath dry mantle (Fig. 4.2). In this case, the term for the heat consumption by sublimation, q_Z, should be omitted from the right-hand side of Eq. (4.13) for energy balance at the surface, namely,

$$Q_{(0)} = q_{\epsilon(0)} + q_{\kappa(0)} \quad (\mathrm{W\,m^{-2}}). \tag{4.24}$$

An additional boundary condition should be implemented that explicates the energy balance at the ice front at $x = X$, i.e.,

$$q_{\kappa\,(X^-)} = q_{\kappa\,(X^+)} + q_{Z(X)}. \tag{4.25}$$

Note that the dust mantle corresponds to $x \in (0, X)$. Eq. (4.25) suggests that part of the heat flux transported across the ice front is consumed by sublimation thereat. Specifically,

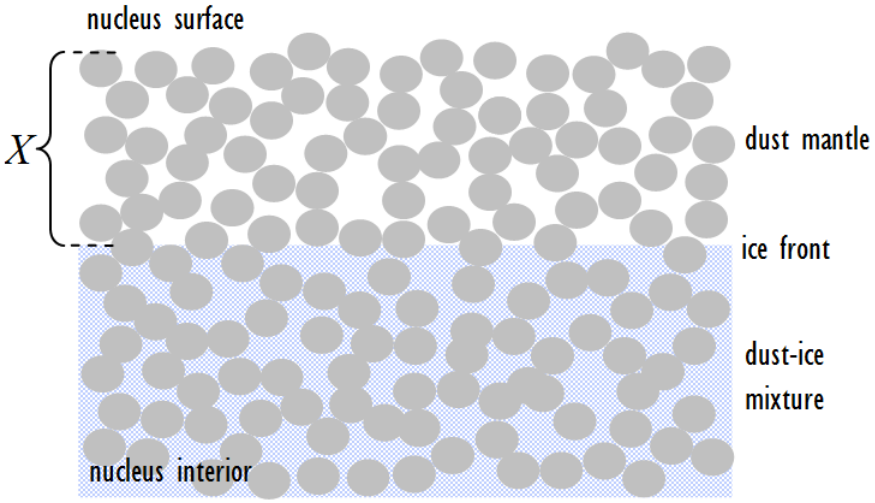

Figure 4.2: Illustration of 1-D structure of the nucleus subsurface for the dust mantle model. This figure appears as Fig. C.1 in Hu et al. (2017b), reused here with permission © ESO.

$$q_{\kappa\,(X^-)} = -\kappa_\mathrm{d} \left.\frac{\partial T}{\partial x}\right|_{x=X^-} , \tag{4.26}$$

$$q_{\kappa\,(X^+)} = -\kappa_\mathrm{i} \left.\frac{\partial T}{\partial x}\right|_{x=X^+} , \tag{4.27}$$

where κ_d and κ_i denote the thermal conductivities of the dry dust mantle and the icy interior, respectively.

As demonstrated by Gundlach et al. (2011), the presence of an overlying dust mantle significantly influences the sublimation of water ice underneath. First of all, the resistence of the dust mantle to gas tranport increases with the "height" of the layer measured in diameters of constituent particles, given by,

$$H = \frac{X}{2r_\mathrm{P}} . \tag{4.28}$$

The reduction or "quenching" factor is determined experimentally by the authors as,

$$\Psi = \frac{1}{1 + p\,H} , \tag{4.29}$$

where p is a constant.

The sublimation flux of *pure* solid water ice from below the dust mantle is given by,

$$\bar{Z}_{(X)} = \Psi Z^{\mathrm{H\text{-}K}}_{(X)} , \tag{4.30}$$

where $Z^{\mathrm{H\text{-}K}}$ is given by the Hertz-Knudsen formula of Eq. (4.16).

It should be stressed that the nucleus underneath the dust mantle is most certainly not pure ice. The same reduction factor, $\mathscr{F}$ in Eq. (4.19), should be applied to Eq. (4.30) to account for the "icy fraction area" less than unity below the dust mantle, i.e.,

$$Z_{(X)} = \Psi \mathscr{F} Z_{(X)}^{\text{H-K}}. \tag{4.31}$$

The heat flux consumed by sublimation is then

$$q_Z = \ell Z_{(X)}. \tag{4.32}$$

4.1.3 Other thermal models in literature

The dusty ice model can be intuitively associated with the characterization of comet nuclei as dusty "snowballs", even if Fred L. Whipple himself may never have actually described the problem in the form of Eq. (4.13) (Whipple 1950, 1951, 1955). Nonetheless, the dusty ice model has been widely adopted as an instructive and practical tool for describing the thermo-physics of comets. The discussions by Smoluchowski (1981), Weissman and Kieffer (1981), Froeschle et al. (1983), Kührt (1984), Kührt (1999) are among numerous references on the topic.

Our best knowledge at the time of writing is that the exposure of water ice on the nuclei is scanty in general (see Sect. 2 and references therein). That is, the sublimation of ice must take place beneath a dust mantle, where the temperature should differ from that on a bare icy nucleus. As noted, the dust mantle also restricts the diffusion of gas and, thus, regulates outgassing through the nucleus. On the other hand, the reduction of outgassing and energy consumption thereby will naturally enhance the heat flux across the ice front which in turn may compensate outgassing. Hence, the existence of dust mantle has complex and fundamental implications on the mechanisms and conditions of cometary activity. We refer the reader to the work by Mendis and Brin (1977), Brin and Mendis (1979), Brin (1980), Fanale and Salvail (1984), Kührt and Keller (1994), Skorov and Rickman (1995), Davidsson and Skorov (2002), Skorov et al. (2011), Gundlach et al. (2011), Gundlach and Blum (2012) whose discussions constitute a more comprehensive and in-depth discourse on the thermo-physics of a mantled nucleus.

There is a notable simplification with the dusty-ice and dust-mantle models described above, in that the sublimation is assumed to occur from a surface of solid ice. This is contrary to the fact that, in reality, comet nuclei are porous bodies. The porosity gives rise to bulk sublimation of ice from the voids, as well as gas diffusion into the nucleus. Consequently, the re-condensation of gas may take place upon cooling inside the nucleus. The mass transport complicates the heat transfer inside the nucleus, in which case Eq. (4.21) may be a poor or even invalid approximation. The reader can consult Spohn and Benkhoff (1990), Mekler et al. (1990), Prialnik and Mekler (1991), Enzian et al. (1997), de Sanctis et al. (1999), Capria et al. (2000), Gortsas et al. (2011) for more elaborate treatment of mass and heat transfer inside porous nuclei.

4.2 Numerical recipe

4.2.1 Crank-Nicolson method

The 1-D heat equation given by Eq. (4.21) can be solved by the Crank-Nicolson method with proper boundary conditions. The basics of this method are discussed below. Let us re-write Eq. (4.21) as follows,

$$\frac{\partial u}{\partial t} = -\frac{a}{\kappa}\frac{\partial q}{\partial x} = a\frac{\partial^2 u}{\partial x^2}\,, \tag{4.33}$$

where u, substituted for T as temperature, indicates an *unknown* to be solved numerically.

$$a = \frac{\kappa}{c\rho} \tag{4.34}$$

is the thermal diffusivity. Let the nucleus interior be spatially discretized into a number of layers at interval Δx, i.e.,

$$x_{j+1} = x_j + \Delta x\,, \tag{4.35}$$

with integer, $1 \leq j \leq j_{\max}$ and $x_1 = \frac{\Delta x}{2}$, such that x_j always refers to the center of each layer. For the sake of brevity, the collection of these discrete layers will be referred to as a "stack". And, let the system states be sampled temporally every Δt, i.e., at $t^{i+1} = t^i + \Delta t$. Then, the temperature of a certain layer *centered* at depth x_j and time t^i is expressed compactly as,

$$u_j^i = u(t^i, x_j)\,. \tag{4.36}$$

It is natural and convenient to refer heat flux to the boundary between each layer (Fig. 4.3), i.e.,

$$q_j^i = q(t^i, \underline{x}_j)\,. \tag{4.37}$$

where

$$\underline{x}_j = x_j + \frac{\Delta x}{2} \tag{4.38}$$

Note that, although x_0 is undefined, $\underline{x}_0 = 0$ refers to the upper boundary or surface of the stack (i.e., not necessarily the nucleus surface) so that q_0 is the heat flux conducted downward from the upper boundary.

The left-hand side of Eq. (4.33) is approximated via the central-difference scheme as,

$$\frac{\partial u_j^{i+1/2}}{\partial t} = \left.\frac{\partial u_j}{\partial t}\right|_{t^{i+1/2}} \approx \frac{u_j^{i+1} - u_j^i}{\Delta t}\,. \tag{4.39}$$

Similarly, the second-order partial derivative on the right-hand side of Eq. (4.33) becomes,

$$a\frac{\partial^2 u_j^i}{\partial x^2} \approx -\frac{a}{\kappa}\frac{q_j - q_{j-1}}{\Delta x} \approx a\frac{u_{j+1}^i - 2u_j^i + u_{j-1}^i}{\Delta x^2}\,. \tag{4.40}$$

Note that,

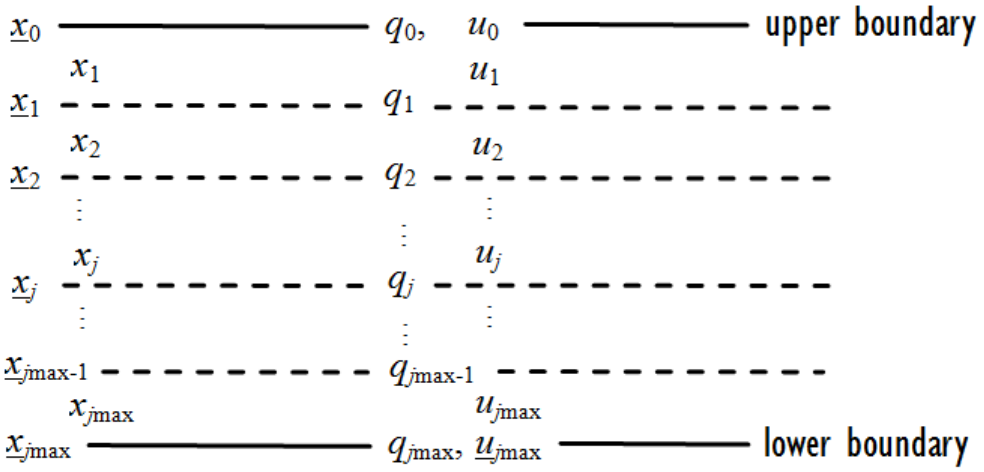

Figure 4.3: Stack is a spatial unit for the numerical solution via the Crank-Nicolson method. The nucleus interior is discretized along depth into a stack of layers. The upper and lower boundary conditions of each stack are specified by the temperatures and heat fluxes at the respective boundaries

$$\frac{\partial u_j^{i+1/2}}{\partial t} \approx \frac{1}{2}\left(\frac{\partial u_j^i}{\partial t} + \frac{\partial u_j^{i+1}}{\partial t}\right). \tag{4.41}$$

It follows from Eqs. (4.39), (4.40), and (4.41) that Eq. (4.33) can be discretized as,

$$u_j^{i+1} - u_j^i = \frac{a\Delta t}{2\Delta x^2}\left(u_{j+1}^i - 2u_j^i + u_{j-1}^i + u_{j+1}^{i+1} - 2u_j^{i+1} + u_{j-1}^{i+1}\right). \tag{4.42}$$

The Crank-Nicolson method is an implicit algorithm in that the unknowns, $u_{j(\pm1)}^{i+1}$, appear on both sides of the above equation. Assuming u^i is obtained at t^i , u^{i+1} should be solved via a system of linear equations at the following time step. Let us re-arrange Eq. (4.42) as,

$$ru_{j-1}^i + (1-2r)u_j^i + ru_{j+1}^i = -ru_{j-1}^{i+1} + (1+2r)u_j^{i+1} - ru_{j+1}^{i+1}, \tag{4.43}$$

with

$$r = \frac{a\Delta t}{2\Delta x^2}. \tag{4.44}$$

All quantities on the right-hand side of Eq. (4.43) are known at time t^i. Therefore, Eq. (4.43) constitutes a set of linear equations, i.e.,

$$\mathbf{Au} = \mathbf{y}, \tag{4.45}$$

where

$$\mathbf{u} = \left(u_0^{i+1}\ \ u_1^{i+1}\ \ldots\ u_j^{i+1}\ \ldots\ u_{j_{\max}}^{i+1}\right)^{\mathrm{T}} \qquad \mathbf{y} = \left(y_0\ \ y_1\ \ldots\ y_j\ \ldots\ y_{j_{\max}}\right)^{\mathrm{T}} \tag{4.46}$$

$$\mathbf{A} = \begin{pmatrix} b_1 & c_1 & & & & & \\ a_2 & b_2 & c_2 & & & & \\ & \ddots & \ddots & \ddots & & & \\ & & a_j & b_j & c_j & & \\ & & & \ddots & \ddots & \ddots & \\ & & & & a_{j_{\max}-1} & b_{j_{\max}-1} & c_{j_{\max}-1} \\ & & & & & a_{j_{\max}} & b_{j_{\max}} \end{pmatrix}. \tag{4.47}$$

According to Eq. (4.43), the elements in **y** are,

$$y_j = ru^i_{j-1} + (1-2r)u^i_j + ru^i_{j+1} \quad \text{for} \quad 1 < j < j_{\max}\,. \tag{4.48}$$

The coefficients along each row of the tridiagonal matrix, **A**, are given by,

$$a_j = -r\,, \quad b_j = 1+2r\,, \quad c_j = -r \quad \text{for} \quad 1 < j < j_{\max}\,. \tag{4.49}$$

The cases of $j = 1$ or $j_{\max}$ at the upper and lower boundaries must be specifically treated.

Upper boundary In the topmost layer, i.e., for $j = 1$, Eq. (4.33) is approximated as,

$$\frac{\partial u_1}{\partial t} \approx \frac{a}{\kappa}\frac{q_0 - q_1}{\Delta x}\,. \tag{4.50}$$

where

$$q_0 \approx -2\kappa\frac{u_1 - \underline{u}_0}{\Delta x}\,, \tag{4.51}$$

denotes the heat flux from the upper boundary into the layer. $\underline{u}_0$ is the temperature at the upper boundary (Fig. 4.3). The heat flux into the underlying layer is,

$$q_1 \approx -\kappa\frac{u_2 - u_1}{\Delta x}\,. \tag{4.52}$$

Therefore,

$$\frac{\partial u_1}{\partial t} \approx \frac{a}{\Delta x^2}\left(2\underline{u}_0 - 3u_1 + u_2\right). \tag{4.53}$$

Referring again to Eq. (4.41), we find that

$$u^{i+1}_1 - u^i_1 = r\left(2\underline{u}^i_0 - 3u^i_1 + u^i_2 + 2\underline{u}^{i+1}_0 - 3u^{i+1}_1 + u^{i+1}_2\right). \tag{4.54}$$

Therefore, the coeffcients, b_1, c_1, and y_1, in Eq. (4.45) are found as,

$$b_1 = 1+3r\,, \quad c_1 = -r\,, \quad y_1 = 2r\underline{u}^i_0 + 2r\underline{u}^{i+1}_0 + (1-3r)u^i_1 + ru^i_2\,. \tag{4.55}$$

It has to be noted that the temperatures at the upper boundary, $\underline{u}^i_0$, $\underline{u}^{i+1}_0$, are treated as known quantities that must be derived before applying the algorithm. In particular, $\underline{u}^{i+1}_0$ has to be predicted at t^i. This issue is discussed in Sect. 4.2.2.

Lower boundary Heat flux across the lower boundary is,

$$q_{j_{\max}} = -2\kappa \frac{\underline{u}_{j_{\max}} - u_{j_{\max}}}{\Delta x}\,, \tag{4.56}$$

where $\underline{u}_{j_{\max}}$ is the temperature at the lower boundary. The temperature variation of the bottom layer is,

$$\frac{\partial u_{j_{\max}}}{\partial t} \approx \frac{a}{\kappa}\frac{q_{j_{\max}-1} - q_{j_{\max}}}{\Delta x} = \frac{a}{\Delta x^2}\left(u_{j_{\max}-1} - 3u_{j_{\max}} + 2\underline{u}_{j_{\max}}\right). \tag{4.57}$$

Thus,

$$u^{i+1}_{j_{\max}} - u^{i}_{j_{\max}} = r\left(u^{i}_{j_{\max}-1} - 3u^{i}_{j_{\max}} + 2\underline{u}^{i}_{j_{\max}} + u^{i+1}_{j_{\max}-1} - 3u^{i+1}_{j_{\max}} + 2\underline{u}^{i+1}_{j_{\max}}\right). \tag{4.58}$$

Subsequently, the quantities, $a_{j_{\max}}$, $b_{j_{\max}}$, and $y_{j_{\max}}$, in Eq. (4.45) are,

$$a_{j_{\max}} = -r\,, \quad b_{j_{\max}} = 1 + 3r\,, \quad y_{j_{\max}} = ru^{i}_{j_{\max}-1} + (1-3r)u^{i}_{j_{\max}} + 2r\underline{u}^{i}_{j_{\max}} + 2r\underline{u}^{i+1}_{j_{\max}}\,. \tag{4.59}$$

As $\underline{u}_0$ at the upper boundary, $\underline{u}_{j_{\max}}$ must be known beforehand; and, $\underline{u}^{i+1}_{j_{\max}}$ needs to be predicted at t^i.

4.2.1.1 Condition of numerical stability

A condition of numerical stability of the Crank-Nicolson method can be generally expressed as

$$\frac{a\Delta t}{\Delta x^2} \le \frac{1}{2}\,, \quad \text{or} \quad r \le \frac{1}{4}\,. \tag{4.60}$$

Therefore, a high spatial resolution necessitates a fine temporal discretization, i.e., $\Delta t \le \frac{\Delta x^2}{2a}$. Violation of this criterion will cause large errors often in the form of artificial temporal variations in the solution.

4.2.1.2 Time derivative

While perhaps already evident, the time derivative of temperature, i.e.,

$$\dot{u}^{i+1}_j = \left.\frac{\partial u_j}{\partial t}\right|_{t=t^{i+1}}\,, \tag{4.61}$$

is output by the Crank-Nicolson method. The expressions are collected as follows. In case $1 < j < j_{\max}$, the solution is, according to Eq. (4.40),

$$\dot{u}^{i+1}_j = a\frac{u^{i+1}_{j+1} - 2u^{i+1}_j + u^{i+1}_{j-1}}{\Delta x^2}\,, \tag{4.62}$$

after u^{i+1} is available. Again, the temperatures at the boundaries need to be treated specifically. At the upper boundary, the time derivative is according to Eq. (4.53),

$$\dot{u}_1^{i+1} = a\frac{2\underline{u}_0^{i+1} - 3u_1^{i+1} + u_2^{i+1}}{\Delta x^2}\,. \tag{4.63}$$

At the lower boundary, it is given by

$$\dot{u}_{j_{\max}}^{i+1} = a\frac{u_{j_{\max}-1}^{i+1} - 3u_{j_{\max}}^{i+1} + 2\underline{u}_{j_{\max}}^{i+1}}{\Delta x^2}\,. \tag{4.64}$$

The solution of temperature at the upper and lower boundaries, $\underline{u}_0^{i+1}$ and $\underline{u}_{j_{\max}}^{i+1}$, is discussed in Sect. 4.2.2, distinguishing two thermal models. Eqs. (4.63) and (4.64) are applied only after $\underline{u}_0^{i+1}$ and $\underline{u}_{j_{\max}}^{i+1}$ are available.

From a numerical standpoint, the two models are essentially distinguished by different boundary conditions of energy balance. Most notably, the sublimation of water ice is assumed to occur beneath rather than at the nucleus surface in the dust mantle model, for which an alternative boundary condition needs to be established in the subsurface. This will be elaborated in the following section.

4.2.2 Treatment of boundary condition

4.2.2.1 Dusty ice model

The nucleus is a uniform mixture of dust and water ice. The upper and lower boundaries of the Crank-Nicolson algorithm correspond to the nucleus surface and the (minimum) depth from which the interior becomes isothermal, respectively. Therefore,

$$\begin{aligned} u_j^i &= T_j^i, \quad 1 \le j \le j_{\max}\,, \\ \underline{u}_j^i &= \underline{T}_j^i \quad 0 \le j \le j_{\max}\,. \end{aligned} \tag{4.65}$$

The temperature at the upper boundary, $\underline{T}_0$, and that at the lower boundary, $\underline{T}_{j_{\max}}$, are determined separately.

Surface The temperature at the upper boundary in Eq. (4.51) is given by the surface temperature, i.e.,

$$\underline{T}_0 = T_{(0)}\,. \tag{4.66}$$

Once T_j^i are known, $\underline{T}_0^i$ can be derived via the Newton-Raphson method. Define a function,

$$F = q_{\epsilon(0)} + q_{\kappa(0)} + q_{Z(0)} - Q_{(0)} = 0\,, \tag{4.67}$$

which is explicated as,

$$F(\underline{T}_0) = \sigma\epsilon\cdot(\underline{T}_0)^4 - 2\kappa\frac{T_1 - \underline{T}_0}{\Delta x} + \ell Z(\underline{T}_0) - Q_{(0)}\,. \tag{4.68}$$

Taking the partial derivative of the above function with respect to $\underline{T}_0$ yields,

$$F'(\underline{T}_0) = 4\sigma\epsilon\cdot(\underline{T}_0)^3 + \frac{2\kappa}{\Delta x} + \ell Z'(\underline{T}_0)\,, \tag{4.69}$$

with

$$Z'(\underline{T}_0) = \left(\frac{\alpha'}{\alpha} + \frac{P'_V}{P_V} - \frac{1}{2\underline{T}_0}\right) Z \,. \tag{4.70}$$

$\underline{T}_0$ is then solved recursively as,

$$\underline{T}_0^{(k+1)} = \underline{T}_0^{(k)} - \frac{F(\underline{T}_0^{(k)})}{F'(\underline{T}_0^{(k)})} \,, \tag{4.71}$$

with k as a non-negative integer. The solution can be initialized by $\underline{T}_0^{(k=0)} = T_1$, and is considered convergent, i.e., $\underline{T}_0 = \underline{T}_0^{(k)}$, once $\left|\underline{T}_0^{(k+1)} - \underline{T}_0^{(k)}\right| < \varepsilon$.

Bottom It is assumed by Eq. (4.22) that heat flux vanishes at the bottom, $x = \mathbb{X}$. In this case, the temperature at the bottom should be specified as,

$$\underline{T}_{j_{\max}} = T_{(\mathbb{X})} \,, \tag{4.72}$$

where $T_{(\mathbb{X})}$ is the *constant* interior temperature of the nucleus.

4.2.2.2 Dust mantle model

In the dust mantle model, two sets of equations (i.e., Eq. 4.45) are solved simultaneously for temperatures in the dust mantle and the underlying dust-ice mixture. Introduce an augmented index, J, for the discretization of the nucleus subsurface above the isothermal depth (while $1 \le j \le j_{\max}$ refers to an individual stack of Crank-Nicolson solutions). The dust mantle corresponds to the top stack of the first J layers, while the dust-ice mixture occupies the underlying stack of layers $J + 1 \le J \le J_{\max}$. Thus, for the dust mantle,

$$\begin{aligned} u_j &= T_{J=j} \,, \quad 1 \le J \le J \,, \\ \underline{u}_j &= \underline{T}_{J=j} \,, \quad 0 \le J \le J \,. \end{aligned} \tag{4.73}$$

For the dust-ice mixture,

$$\begin{aligned} u_j &= T_{J=j+J} \,, \quad J + 1 \le J \le J_{\max} \,, \\ \underline{u}_j &= \underline{T}_{J=j+J} \,, \quad J \le J \le J_{\max} \,. \end{aligned} \tag{4.74}$$

The boundary conditions can be treated in a similar manner to those in the dusty ice model. The main difference lies with the determination of the temperature at the ice front, $\underline{T}_J$, that governs the balance of energy transfer across the boundary between the dust mantle and the icy mixture.

Surface The temperature at the upper boundary of the first stack is given by the surface temperature of the nucleus or the dust mantle, i.e.,

$$\underline{T}_0 = T_{(0)} \,. \tag{4.75}$$

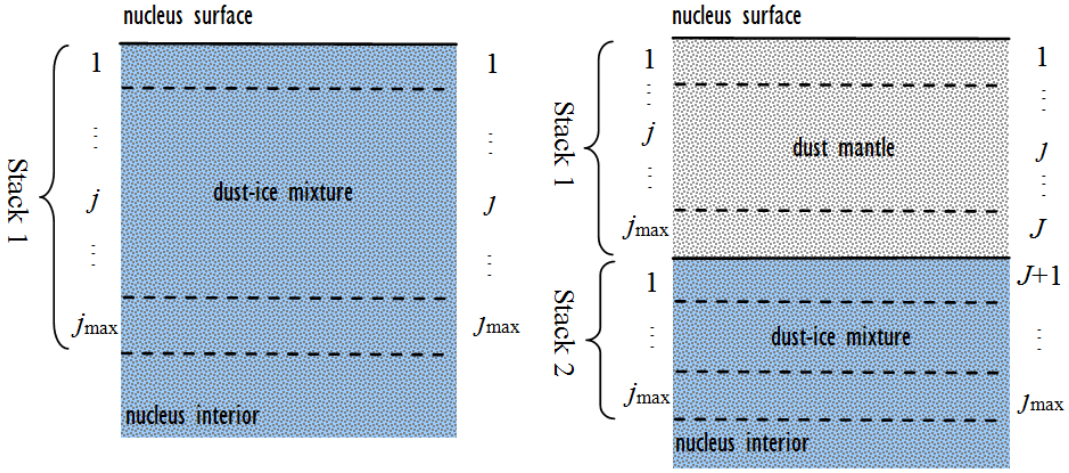

Figure 4.4: Numerical structure of the dusty-ice and dust-mantle models. **a**. A single stack is needed for the dusty ice model where the nucleus is assumed to be a uniform dust-ice mixture. **b**. Two stacks are used in the dust mantle model to distinguish between the dust mantle and the underlying dust-ice mixture.

which is solved by the Newton-Raphson method, as described by Eqs. (4.67)-(4.71). In this case, an alternative function to Eq. (4.67) should be used that omits the heat loss due to ice sublimation on the surface, i.e.,

$$F = q_{\epsilon(0)} + q_{\kappa(0)} - Q_{(0)} = 0\,, \tag{4.76}$$

Consequently, the last term on the right-hand side of Eq. (4.69) should be dropped.

Ice front The temperature at the lower boundary of the dust mantle, $\underline{T}_J$, is assumed to coincide with the temperature at the ice front, i.e., $\underline{T}_J = T_X$ where X indicates the depth of the ice front. Recall Eq. (4.25) which expresses the energy balance at the ice front,

$$-\kappa_\mathrm{d} \left.\frac{\partial T}{\partial x}\right|_{x=X^-} = -\kappa_\mathrm{i} \left.\frac{\partial T}{\partial x}\right|_{x=X^+} + \ell Z_{(X)}\,. \tag{4.77}$$

The above equation is approximated as,

$$-2\kappa_\mathrm{d}\frac{\underline{T}_J - T_J}{\Delta x} = -2\kappa_\mathrm{i}\frac{T_{J+1} - \underline{T}_J}{\Delta x} + \ell Z(\underline{T}_J)\,, \tag{4.78}$$

with T_{J+1} being the temperature (at the central depth) of the topmost icy layer. Again, the Newton-Raphson method is applied to solve for $\underline{T}_J$. In this case, a function similar to Eq. (4.67) is defined as,

$$F(\underline{T}_J) = 2\frac{\kappa_\mathrm{d} + \kappa_\mathrm{i}}{\Delta x}\underline{T}_J + \ell Z(\underline{T}_J) - \frac{2\kappa_\mathrm{d}}{\Delta x}T_J - \frac{2\kappa_\mathrm{i}}{\Delta x}T_{J+1} = 0\,, \tag{4.79}$$

whose partial derivative with respect to $\underline{T}_J$ is,

$$F'(\underline{T}_J) = 2\frac{\kappa_\mathrm{d} + \kappa_\mathrm{i}}{\Delta x} + \ell Z'(\underline{T}_J)\,. \tag{4.80}$$

Note that Eq. (4.70) is valid for deriving $Z'(\underline{T}_J)$; however, Eq. (4.31) should be applied to calculate $Z(\underline{T}_J)$. The initial value of $\underline{T}_J$ is set to T_{J+1}.

Bottom As with the dusty ice model, the adiabatic condition is usually imposed at the bottom boundary, i.e.,

$$\underline{T}_{J_{\max}} = T_{(\mathbb{X})}\,, \tag{4.81}$$

with $T_{(\mathbb{X})}$ being the interior temperature.

4.2.2.3 Prediction of boundary condition

The application of the Crank-Nicolson method requires *a priori* knowledge of the boundary conditions. The determination of the boundary conditions is, however, explicitly related to the temperatures on the boundary surfaces. In this case, a strategy is to predict boundary temperatures. The following discussion is based on the dust mantle model as an example.

Suppose the solution for time t^i has been finalized, i.e., the temperatures, T_j^i with $0 \leq j \leq J_{\max}$, are available. The surface boundary condition at time t^{i+1} is given by Eq. (4.24),

$$Q_{(0)}^{i+1} = q_{\varepsilon\,(0)}^{i+1} + q_{\kappa\,(0)}^{i+1}\,. \tag{4.82}$$

With no loss of generality, it is assumed that $Q_{(0)}^{i+1}$ is known. The surface temperature $\underline{T}_0^{i+1}$ then needs to be predicted to obtain $q_{\varepsilon\,(0)}^{i+1}$ and $q_{\kappa\,(0)}^{i+1}$. It has been shown in Sect. 4.2.2.2 that the surface temperature is affected by the temperature in the topmost layer, i.e., T_1. Therefore, the task boils down to predicting T_1^{i+1}. A feasible approximation is given by,

$$T_j^{i+1} \approx T_j^i + \dot{T}_j^i \Delta t + O(\Delta t^2)\,, \tag{4.83}$$

where $j = 1$ in this case, and $\dot{T}_1^i$ is calculated by Eq. (4.63). Once T_1^{i+1} is available, $\underline{T}_0^{i+1}$ can be calculated via the Newton-Raphson method as via Eq. (4.76).

The treatment for the ice front is similar. The boundary condition is given by Eq. (4.25) and, in the discrete form, by Eq. (4.78) as,

$$-2\kappa_{\mathrm{d}} \frac{\underline{T}_J^{i+1} - T_J^{i+1}}{\Delta x} = -2\kappa_{\mathrm{i}} \frac{T_{J+1}^{i+1} - \underline{T}_J^{i+1}}{\Delta x} + \ell Z(\underline{T}_J^{i+1})\,. \tag{4.84}$$

Therefore, the temperature at the ice front, $\underline{T}_J^{i+1}$, is determined by that in the lowermost layer of the dust mantle as well as the topmost layer of the dust-ice mixture. Thus, the temperatures in both layers need to be predicted via Eq. (4.83) for $j = J$ and $J + 1$, respectively. Eqs. (4.64) and (4.63) should be applied to evaluate $\dot{T}_J^i$ and $\dot{T}_{J+1}^i$, accordingly. Once T_J^{i+1} and T_{J+1}^{i+1} are derived, $\underline{T}_J^{i+1}$ is calculated via the Newton-Raphson method based on Eqs. (4.79) and (4.80).

Because the adiabatic condition is imposed at the bottom boundary for the dust mantle model, contant temperature is assumed, i.e., $\underline{T}_{J_{\max}}^{i+1} = \underline{T}_{J_{\max}}^i$.

4.3 Generic procedure of numerical solution

The 67P nucleus is subject to periodic heating of insolation[i] due to both rotation and orbital motion of the nucleus around the Sun. Hence, the periodicity of the surface energy input can be expressed by (recalling Eqs. 4.13 and 4.24),

$$Q_{(0)}(t) = Q_{(0)}(t \pm t_\mathrm{P})\,, \tag{4.85}$$

with t_P being the period of variation of insolation. It is then imperative to solve for periodic variations of temperatures and outgassing flux of the nucleus, such as,

$$T(t) = T(t \pm t_\mathrm{P})\,, \tag{4.86}$$

according to the physical timescale of the problem at hand.

The thermal skin depth of the nucleus can be defined by (Huebner et al. 2006),

$$X_S = \sqrt{\frac{t_\mathrm{P}\kappa}{\pi\rho c}}\,, \tag{4.87}$$

which approximates the depth at which the temperature variation decays by a factor of e^{-1} with respect to the surface temperature in response to periodic heating. With a rotation period of 12.4 hours, the diurnal variation of water activity is considered to be mostly affected by the top few centimeters of the subsurface. On the other hand, the temperatures and heat transport through the first few meters of the subsurface need to be resolved in order to describe the orbital behavior of water activity on 67P over ~6.5 years.

If the adiabatic condition is imposed at the bottom boundary as given by Eqs. (4.72) or (4.81), it must be ensured that the maximum depth of the numerical solution always exceeds the thermal skin depth, namely, $\underline{x}_{J\max} > X_S$, recalling that $\underline{x}_{J\max}$ is defined by Eq. (4.38).

At the initial epoch, t_0, the nucleus can be assumed to be isothermal with depth everywhere, e.g., $T_J(t_0) = T_{(\mathbb{X})}$. The temperatures and, depending on the depth of the ice front, the sublimation flux are propagated or solved at every step in time, Δt, until a full period, t_P, is reached. The amplitude of the temperature variation at depth x_J is given by

$$\left|\Delta T_J\right| = \max\left[T_J(t_0 \le t < t_0 + t_\mathrm{P})\right] - \min\left[T_J(t_0 \le t < t_0 + t_\mathrm{P})\right]\,. \tag{4.88}$$

The "numerical" thermal skin depth is then found as the first layer below the surface where

$$\left|\Delta T_J\right| < \varepsilon\,, \tag{4.89}$$

where ε indicates some small threshold value of choice. Let the numerical thermal skin be denoted by x_{Js}. The deviation between the temperature profiles one period apart can be evaluated by,

$$D_T = \sqrt{\frac{1}{J_\mathrm{max}}\sum_{J=1}^{J_\mathrm{max}}\left(T_J(t_0) - T_J(t_\mathrm{P})\right)^2}\,. \tag{4.90}$$

[i] It will be shown in Sect. 5.2.2 that the absorption of thermal radiation from the nucleus itself may yield a non-negligible contribution to the total energy input.

The solution is iterated over many periods until D_T becomes sufficiently small, suggesting that Eq. (4.86) is satisfied.

5 Thermal Modeling: Application to 67P

In Chapter 4, the formulation and numerical treatment of two cometary thermal models have been introduced. In principle, the models can be applied to simulate the surface and subsurface temperatures of the nucleus and water outgassing at any location of the nucleus for proper boundary conditions on the surface and at depths. While adiabatic condition is commonly (and reasonably) assumed for the bottom boundary, the establishment of surface boundary condition relies on proper evaluation of the energy input into the thermal model.

The primary source of energy is insolation. The flux density of sunlight is dependent on heliocentric distance, i.e., the orbital motion of the comet around the Sun. The energy flux incident on the nucleus is dependent on the orientation of the local surface with respect to the Sun, which is significantly controlled by the shape and the rotation of the nucleus in space. If the shape of the nucleus is complex, the shadowing of the topography needs to be taken into account. This is particularly true for the comet 67P whose nucleus is highly irregular-shaped.

The abrupt shape gives rise to additional complexity in modeling. For instance, while the nucleus loses heat via thermal radiation, this energy is partially intercepted by topography and, thus, absorbed by (other parts of) the nucleus. This phenomenon is usually referred to as the "self-heating" effect (Lagerros 1997). Self-heating is pronounced in the rugged landform, such as valleys, coves, cliffs, compensating for a deficiency of insolation due to shadowing.

The energy flux of solar irradiation on an open, unobstructed surface is

$$Q_\odot = \left(\frac{1\,\mathrm{AU}}{r_\odot}\right)^2 C_\odot (1 - \mathcal{A}) \max(\cos\theta_\odot, 0)\,, \tag{5.1}$$

where $\mathcal{A}$ is the surface Bond albedo and $C_\odot$ the solar constant. The time-varying solar incidence angle, $\theta_\odot$, and the heliocentric distance in units of AU, $r_\odot$, are derived from the ephemeris, rotation state, and the shape model of the nucleus. In the case of a highly irregular-shaped body such as 67P, special care is warranted to assess the illuminability of the surface, i.e., if the ray of sunlight can propagate to the local point unobstructed by topography. In a similar rationale, the evaluation of the self-heating requires the depiction of the surrounding landscape so as to determine local absorption of thermal radiation from all other visible surface areas.

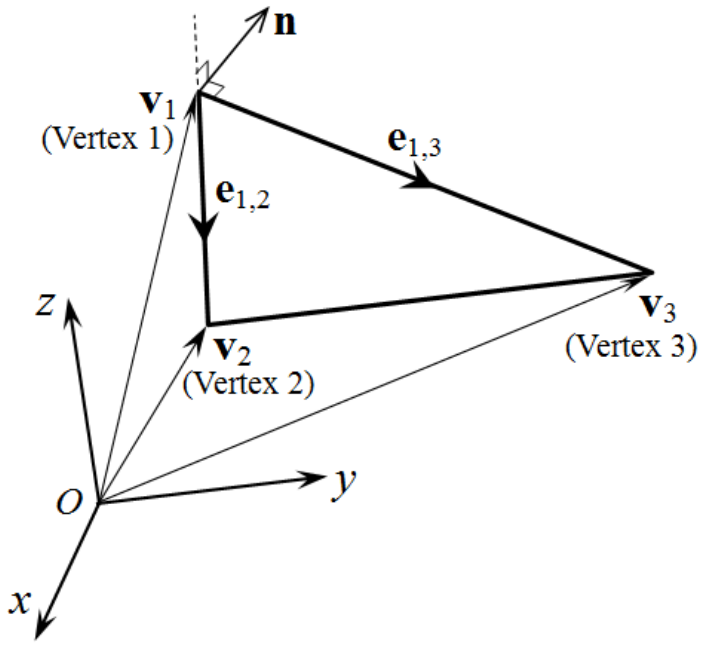

Figure 5.1: Facet of the shape model with respect to the body-fixed coordinate system

5.1 Landscape of 67P

5.1.1 Shape

Shape models of 67P have been by Preusker et al. (2015) and Jorda et al. (2016). The shape model is usually in the form of a polyhedron with a triangulated surface. The vertices of each triangular facet are ordered counterclock-wise with respect to an external observer. Let us denote the vectors of the respective three vertices as $\mathbf{v}_k$ with $k = 1, 2, 3$. Two edge vectors, $\mathbf{e}_{1,2}$, $\mathbf{e}_{1,3}$ are defined as pointing from vertex 1 to vertices 2 and 3, respectively, e.g., $\mathbf{e}_{1,2} = \mathbf{v}_2 - \mathbf{v}_1$ (Fig. 5.1). The surface normal is given by $\mathbf{n} = \mathbf{e}_{1,2} \times \mathbf{e}_{1,3}$ such that it always points outwards.

The original form of the shape model is augmented with some supplementary information in order to facilitate the thermal analysis, particularly the evaluation of energy input on the nucleus surface.

Centroid of facet The position vector for a given facet is defined as pointing to the centroid of the facet, i.e.,

$$\mathbf{r}_\mathrm{F} = \frac{1}{3}\left(\mathbf{v}_1 + \mathbf{v}_2 + \mathbf{v}_3\right) , \tag{5.2}$$

which uniquely locates the position of a facet, irrespective of its orientation in space. As will be discussed, $\mathbf{r}_\mathrm{F}$ is the defined origin for a local coordinate system associated with each facet.

Area of facet The area of the facet is useful for assessing the thermal radiation from the nucleus (see Sect. 5.2.2). Depending on the topography or, more exactly, concavity, thermal radiation can be re-absorbed by the nucleus at other locations. The facet area is computed by the Heron's formula,

$$A_{\rm F} = \sqrt{s(s-a)(s-b)(s-c)}\,, \tag{5.3}$$

where a, b, and c denote the lengths of the three triangular edges, and

$$s = \frac{1}{2}\,(a+b+c)\ . \tag{5.4}$$

5.1.2 Visibility

We first introduce a database providing the reciprocal "visibility" between two given locations on the surface. With a discrete shape model, the nucleus is sampled by a set of points at the (centroid of the) respective triangular facets. At a certain point on the nucleus, all other facets are either visible or invisible. Two facets can be visible only if they are oriented face-on. Invisibility may also result from obstruction of topography along line of sight between the facets.

The criterion of orientation for the mutual visibility of two facets can be simply established as follows. Denote the vector from the centroid of facet k towards that of facet l as

$$\mathbf{d}_{k,l} = \mathbf{r}_{{\rm F}l} - \mathbf{r}_{{\rm F}k}\,. \tag{5.5}$$

The two facets are visible only if

$$\begin{aligned} \mathbf{n}_k \cdot \mathbf{d}_{k,l} > 0\,, \\ \mathbf{n}_l \cdot \mathbf{d}_{l,k} > 0\,, \end{aligned} \tag{5.6}$$

where $\mathbf{n}_k$ and $\mathbf{n}_l$ are the surface normals to the facets k and l, respectively.

The topographic obstruction, on the other hand, can be evaluated via the strategy discussed by Lagerros (1997). For each pair of facets, a connecting line segment is found that passes the centroids of facets. Denote the position vector of a point along the connecting line by $\mathbf{r}_{\rm P} = r_{\rm P}\hat{\mathbf{r}}_{\rm P}$ where r is the radius. Let $\mathbf{r}_{\rm F} = r_{\rm F}\hat{\mathbf{r}}_{\rm F}$ be the position vector for a facet of the shape model. Assuming $\hat{\mathbf{r}}_{\rm P} \approx \hat{\mathbf{r}}_{\rm F}$, one may determine the visibility of the two facets by testing $r_{\rm P} > r_{\rm F}$ is violated anywhere along the connecting line in between.

Alternatively, the obstruction of topography to the mutual view of two facets can be tested directly as the intersection of topography with the connecting line. Towards this end, we adapt the function which identifies the points of intersection of a line and a polyhedron (Legland 2009). Suppose all intersections are found as $\mathbf{r}_{{\rm P}i}$. The centroid of each facet accounts for an intersection, i.e., $\mathbf{r}_{{\rm P}i} = \mathbf{r}_{{\rm F}k}$ or $\mathbf{r}_{{\rm F}l}$. Let the distance between an intersection and facet k as

$$d_{k,i} = \left|\mathbf{d}_{k,i}\right| = \left|\mathbf{r}_{{\rm P}i} - \mathbf{r}_{{\rm F}k}\right|\ , \tag{5.7}$$

and that to facet l as $d_{k,l} = \left|\mathbf{d}_{k,l}\right|$ (Eq. 5.5). The following equality holds for intersections between the two facets,

$$d_{k,\iota} + d_{l,\iota} = d_{k,l}\,. \tag{5.8}$$

We introduce the visibility factor, $v_{k,l}$, which is unity if facets k and l are visible from each other and zero otherwise (Lagerros 1997). Hence,

$$v_{k,l} = v_{l,k} = \begin{cases} 1\,, & \text{if Eq. (5.6) holds,} \quad \text{and } \iota = \emptyset\,, \\ 0\,, & \text{otherwise}\,. \end{cases} \tag{5.9}$$

In practice, it is probably more efficient to check the above criteria successively. Only those pairs of facets for which Eq. (5.6) holds are further tested against Eq. (5.8). The reason is that determining the intersections of a line and polyhedron is computationally cumbersome, especially when high-resolution shape models with a large number of facets are used.

The information is visualized in Fig. 5.2. The fraction of the nucleus surface visible from a given location varies notably across the nucleus. Concavities, such as the "neck" between the two lobes, result in large visible surface area (Fig. 5.2a-c), in contrast to the convex topographies, e.g., on the far sides of the lobes, that are less obstructed by the surrounding landscape (Fig. 5.2d). Additionally, it is worth noting that the distribution of the visible facets may be scattered, which likely results from the irregularity in topography reflected even in a low-resolution shape model (Fig. 5.2a,c).

Some auxiliary information can be derived from the above analysis with little additional cost.

Distance between facets Note that the distance between a pair of facets needs to be derived for determining their mutual visibility via Eq. (5.8). Therefore, for each pair of visible facets, k and l, the distance, $d_{k,l}$, should be stored, while the distance for the invisible pairs can be discarded.

Mutual view of facets Consider a pair of visible facets, k and l, and let $\theta_{k,l}$ denote the orientation of (the line-of-sight to) facet l with respect to the surface normal to facet k (Fig. 5.3), such that

$$\cos\theta_{k,l} = \frac{\mathbf{n}_k \cdot \mathbf{d}_{k,l}}{d_{k,l}}\,. \tag{5.10}$$

Note that $\theta_{k,l} \neq \theta_{l,k}$ in general. The product $\cos\theta_{k,l}\cos\theta_{l,k}$ is defined here as the mutual orientation of the facets, which is calculated and stored for all visible pairs.

A particularly useful quantity in practice, e.g., for evaluating self-heating of the nucleus, is,

$$w_{k,l} = v_{k,l}\frac{\cos\theta_{k,l}\cos\theta_{l,k}}{\pi d_{k,l}^2}\,, \tag{5.11}$$

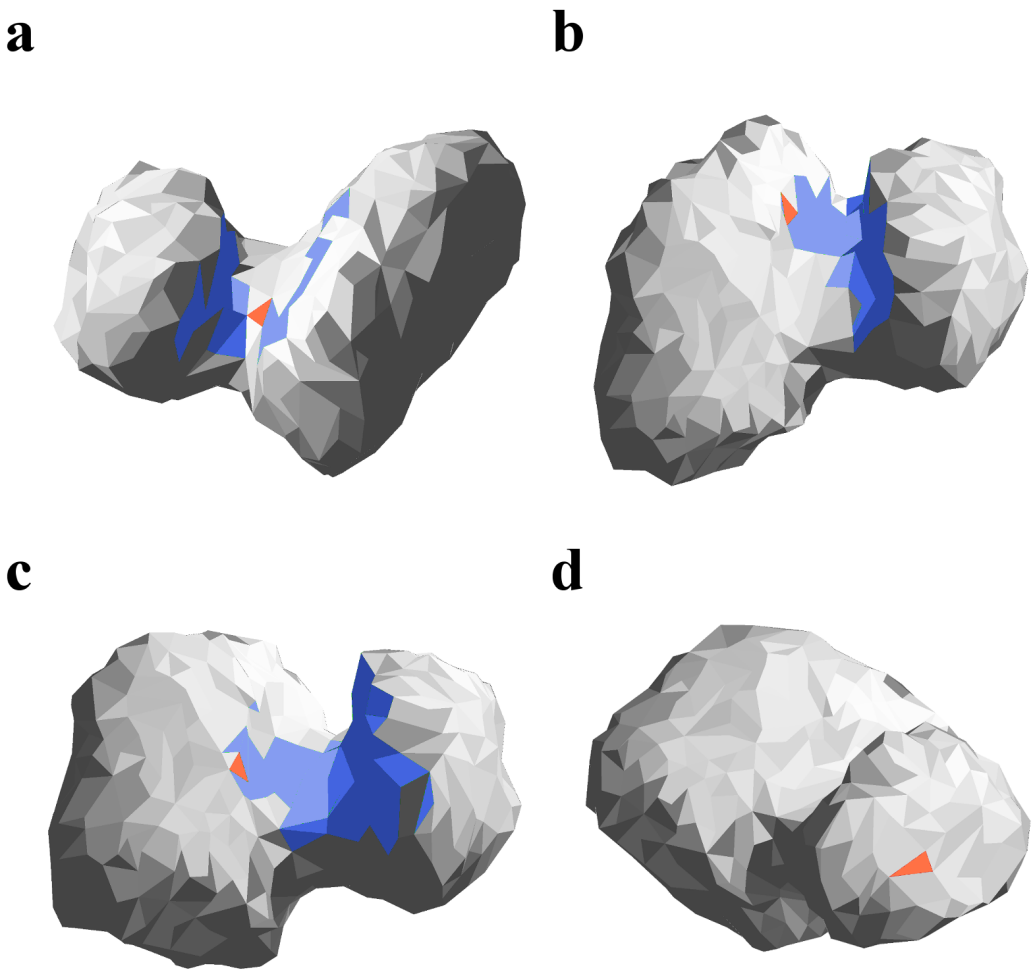

Figure 5.2: Visible portions of the surface from four different locations on the nucleus. The shape of the nucleus is represented by a SPC shape model with one thousand facets. The local facet is in orange; the visible facets thence are in blue. **a**. The local facet is at the floor of a valley between the two lobes, with visible facets distributed across the walls. **b,c**. The local facet is on the wall on the big lobe looking into the valley, but loses sight almost entirely of facets on the other side where topography bends below the horizon. **d**. The facet situated on the far side of the small lobe with nearly convex topography sees no other facets

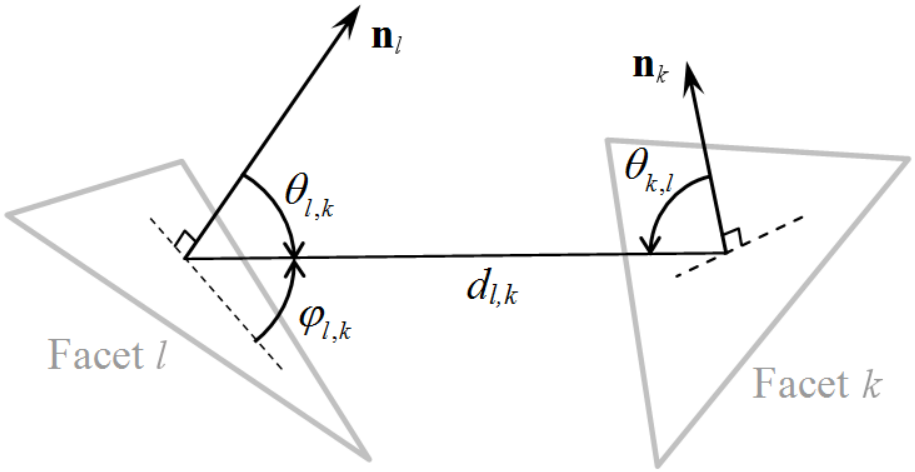

Figure 5.3: Mutual orientation of two facets. The orientation of one facet with respect to the other is given by the angle, θ, between the line-of-sight along the distant facet and the surface normal of the local facet. θ is complementary to the elevation angle φ. $\mathbf{n}$ indicates the surface normal.

We refer to $w_{k,l}$ as the "mutual viewing factor" considering the obvious reciprocality, i.e., $w_{k,l} = w_{l,k}$. $w_{k,l}$ differs subtly from the well-defined "view factor" (Özişik 1985), and is related to the latter via Eq. (5.36).

The results derived in Sect. 5.1.2 constitute a database named "Visibility". The database consists of two files. The first is a two-column table of integer indices for all pairs of mutually visible facets, i.e., $v_{k,l} = 1$ as in Eq. (5.9). The other file contains a single colume of real numbers indicating the mutual viewing factors, $w_{k,l}$, for each pair of visible facets. Row-to-row correspondence between the two files is ensured. A potential advantage for creating two separate files lies in the ease of storing and retrieving different data types in binary format.

5.1.3 Horizon

A certain location on a convex object, such as a sphere, is illuminated if

$$\cos\theta_\odot = \mathbf{n} \cdot \frac{\mathbf{r}_\odot - \mathbf{r}}{|\mathbf{r}_\odot - \mathbf{r}|} > 0\,, \tag{5.12}$$

where $\theta_\odot$ stands for the solar incidence angle and $\mathbf{r}_\odot$ is the solar vector. $\mathbf{r}$ is the position vector of the surface point and $\mathbf{n}$ is the unit vector of surface normal. Eq. (5.12) yields a trivial and minimal condition for illumination when the Sun rises above local horizon which in this case is the tangential plane of the surface.

More realistically, the visual horizon may be influenced by surface topography. In the case of 67P, the irregular landscape likely producing complicated shadowing effect casts doubt on the validity of Eq. (5.12) as a criterion for illumination. Determination of shadowing amounts to finding the intersection of a ray of sunlight with topography in

the foreground. However, this approach would require performing a search for intersections at every location on the nucleus and at each instant of analysis. The computation is exceedingly demanding when high temporal and spatial resolutions are desired.

A more cost-effective strategy is to trade memory for computational speed, i.e., by deriving and pre-storing the discrete variation of the local horizon as a function of azimuth. The open sky is specified as segments of the local upper meridian along each azimuthal direction. The surface point is illuminated when the Sun is projected within specified segments. This approach prevents the laborious search for intersections of a line and a polyhedron at the expense of pre-storage of horizon record for each facet.

Horizontal coordinate system We define a right-handed Cartesian coordinate system with its origin at a given point on the nucleus surface and z axis pointing upwards along the surface normal (Fig. 5.4). The definition of the x axis or that of the reference meridian is arbitrary. We approximate the nucleus by a shape model, the origin is then located at the centroid of the corresponding facet, $\mathbf{r}_{\mathrm{F}}$. Hence, the axes of a local horizontal coordinate system can be defined as follows,

$$\begin{aligned} \mathbf{u}_z &= \mathbf{n}\,, \\ \mathbf{u}_x &= \frac{\mathbf{v}_2 - \mathbf{v}_1}{|\mathbf{v}_2 - \mathbf{v}_1|}\,, \\ \mathbf{u}_y &= \frac{\mathbf{u}_z \times \mathbf{u}_x}{|\mathbf{u}_z \times \mathbf{u}_x|}\,, \end{aligned} \tag{5.13}$$

where $\mathbf{v}_1$ and $\mathbf{v}_2$ are the position vectors of the first and second vertices of the facet, respectively. $\mathbf{n}$ is the unit normal vector to the facet. It is convenient to refer all quantities to the body-fixed coordinate system of 67P. The transformation of a vector, $\mathbf{r}$, from the body-fixed system to the local horizontal system is,

$$\mathbf{r}^{[\mathrm{H}]} = \mathbf{R}^{[\mathrm{H}]}_{[\mathrm{BF}]} \left(\mathbf{r} - \mathbf{r}_{\mathrm{F}}\right)\,, \tag{5.14}$$

where the 3×3 rotation matrix is obtained as,

$$\mathbf{R}^{[\mathrm{H}]}_{[\mathrm{BF}]} = \begin{pmatrix} \mathbf{u}_x & \mathbf{u}_y & \mathbf{u}_z \end{pmatrix}^{\mathrm{T}}\,. \tag{5.15}$$

The superscript "[H]" indicates that the vector is with respect to the horizontal coordinate system.

To project the Sun onto the celestial sphere at the given location, we refer to a corresponding spherical coordinate system of radius, r, elevation, φ, and azimuth, α, namely,

$$\begin{aligned} r &= \sqrt{\left(x^{[\mathrm{H}]}\right)^2 + \left(y^{[\mathrm{H}]}\right)^2 + \left(z^{[\mathrm{H}]}\right)^2}\,, \\ \alpha &= \arctan\left(\frac{y^{[\mathrm{H}]}}{x^{[\mathrm{H}]}}\right)\,, \\ \varphi &= \arcsin\left(\frac{z^{[\mathrm{H}]}}{r}\right)\,. \end{aligned} \tag{5.16}$$

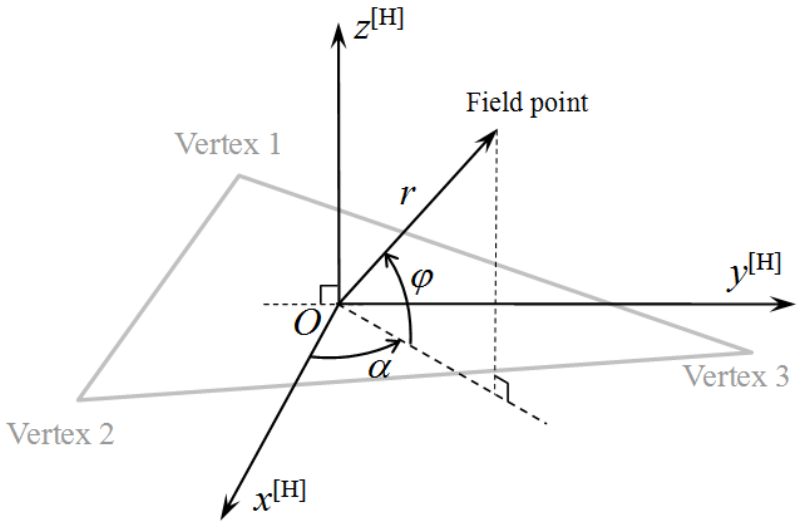

Figure 5.4: Local horizontal coordinate system defined for an individual facet

Note that, for numerical purposes, the two-argument function, $\text{atan2}(x, y) \in (-\pi, \pi]$, is used to calculate α, i.e.,

$$\alpha = \text{atan2}\left(x^{[H]}, y^{[H]}\right) = \begin{cases} \arctan\left(\frac{y^{[H]}}{x^{[H]}}\right), & \text{if} \quad x > 0\,, \\ \arctan\left(\frac{y^{[H]}}{x^{[H]}}\right) \pm \pi\,, & \text{if} \quad x < 0\,, \\ \text{sgn}\left(y^{[H]}\right)\frac{\pi}{2}\,, & \text{if} \quad x = 0\,, \end{cases} \tag{5.17}$$

with "sgn" being the sign function.

A survey is performed over the upper hemisphere of the horizontal coordinate system on each facet. The upper hemisphere is discretized in azimuth and elevation, such as,

$$\begin{aligned} \alpha_n &= n\Delta\alpha\,, \\ \varphi_m &= m\Delta\varphi\,, \end{aligned} \tag{5.18}$$

where $\Delta\alpha$, $\Delta\varphi$ are the azimuthal and elevation increments, respectively. Indices, n, m, are non-negative integers. The visual obstruction of topography is indicated by any intersections of a ray from the facet with the shape model in the direction specified by α_n and φ_m. Referring to Eq. (5.16), the ray is expressed in the horizontal coordinate system as,

$$\mathbf{r}^{[H]} = \mathbf{r}_0^{[H]} + r\mathbf{u}^{[H]}\,, \tag{5.19}$$

with $\mathbf{r}_0^{[H]} = (0\ 0\ 0)^{\mathrm{T}}$ and

$$\mathbf{u}^{[H]} = \begin{pmatrix} \cos\varphi\cos\alpha \\ \cos\varphi\sin\alpha \\ \sin\varphi \end{pmatrix}. \tag{5.20}$$

The radius coordinate of the ray, $r \geq 0$, is a free parameter. The equation is then converted into the body-fixed coordinate system by,

$$\mathbf{r} = \mathbf{r}_0 + r\mathbf{u}\,, \tag{5.21}$$

where

$$\begin{aligned} \mathbf{r}_0 &= \mathbf{r}_\mathrm{F}\,, \\ \mathbf{n} &= \mathbf{R}^{[\mathrm{BF}]}_{[\mathrm{H}]}\mathbf{u}^{[\mathrm{H}]}\,. \end{aligned} \tag{5.22}$$

As in Eq. (5.14), $\mathbf{r}_\mathrm{F}$ is the position vector of the origin of the horizontal coordinate system with respect to the body-fixed system. The intersections of the line and the shape model are found at $\mathbf{r}_{\mathrm{P}\,i}$ for non-negative index, i, via the algorithm of Eq. 3.8. Denote the intersection of the line with the local facet as $\mathbf{r}_{\mathrm{P}\,i} = \mathbf{r}_\mathrm{F}$. Other intersections beyond $\mathbf{r}_\mathrm{F}$ in the direction of $\mathbf{u}$ are verified by the following condition,

$$(\mathbf{r}_{\mathrm{P}\,\imath} - \mathbf{r}_\mathrm{F}) \cdot \mathbf{u} > 0\,. \tag{5.23}$$

If $\imath \neq \emptyset$, the line-of-sight along $\mathbf{u}$ from the local facet is obstructed by topography of the nucleus, i.e., illumination of the surface from the direction of α_n and φ_m is impossible.

The computations can be somewhat sped up by taking advantage of the Visibility database described in Sect. 5.1.2. Only those facets visible from the local spot need to be considered for determining the intersections. While the search for intersections has to be applied to all facets of the shape model, the whole procedure is carried out only once for each shape model.

The above analysis results in a point grid for every facet of the shape model, that samples the visual (non-)obstruction by topography in all directions, i.e., at each (discrete) azimuth, α, and elevation, φ, namely,

$$\delta(\alpha,\varphi) = \begin{cases} 1, & \text{if open sky is along line-of-sight,} \\ 0, & \text{if topography is along line-of-sight.} \end{cases} \tag{5.24}$$

The local surface within the facet can only be illuminated from (α,φ) for non-zero $\delta(\alpha,\varphi)$. The volume of data is stored as intervals of elevation, i.e., $(\varphi_\mathrm{a}, \varphi_\mathrm{b})$, such that $\delta(\alpha, \varphi_\mathrm{a} < \varphi < \varphi_\mathrm{b}) = 1$ for every azimuth at a given facet. Note that there might be multiple non-overlapping intervals of $(\varphi_\mathrm{a}, \varphi_\mathrm{b})$ at a certain azimuth.

Examples of use of the Horizon database are shown in Fig. 5.5. The panoramic view from a given facet is projected over the upper hemisphere with respect to the horizontal coordinate system. The upper hemisphere is discretized into a point grid at 5-degree interval in elevation and 4-degree interval in azimuth. The shape model consists of one thousand facets and is reduced from an original three-million-facet SPC shape model (Jorda et al. 2016). The black dots indicate nucleus topography along the line-of-sight while the unfilled areas correspond to the open sky. The complex shape of the nucleus significantly distorts the local horizon from a flat level. In the cases of Fig. 5.5a-c, the view of the facets is obstructed by the two lobes and confined along the valley in between.

In Fig. 5.5b, the facet is mostly ceiled by the Harthor cliff of the small lobe, with a view similar to the outlook from a cave. Open view is not uncommon, e.g., on the far side of the small lobe where global-scale topographic variation is absent, as in Fig. 5.5d. It is thus evident that the shadowing effect needs to be taken into account for at least a significant portion of the nucleus surface.

There are certain artifacts, mostly seen at low elevation angles, e.g., some open views occur at 0 degree in Fig. 5.5a and c. They are mostly due to the use of the imperfect Visibility database for the (de-)selection of facets in the search for intersections of the line-of-sight and the shape model. Because a triangular facet has always been treated as a point for simplicity, inconsistencies may result if the centroid of the target facet is out of sight while the edges are partially visible from the local facet. This issue, however, is alleviated when a higher resolution shape model is used.

5.2 Energy input

5.2.1 Insolation

The absorbed energy flux of insolation on a convex object is given by Eq. (5.1). In the case of concave topography, Eq. (5.1) is modified as follows,

$$Q_\odot = \left(\frac{1\,\mathrm{AU}}{r_\odot}\right)^2 C_\odot (1-\mathcal{A})\,\delta(\alpha_\odot, \varphi_\odot)\sin\varphi_\odot\,, \tag{5.25}$$

where $\alpha_\odot$, $\varphi_\odot$ are the solar azimuth and elevation at a given location of the nucleus. δ is as defined by Eq. (5.24).

Procedure of evaluation The calculation of $Q_\odot$ may proceed as follows. Suppose the solar vector in the body-fixed coordinate system of 67P is given by $\mathbf{r}_\odot = r_\odot \hat{\mathbf{r}}_\odot$. Solar irradiance is calculated at each epoch as,

$$\bar{Q}_\odot = \left(\frac{1\,\mathrm{AU}}{r_\odot}\right)^2 C_\odot\,. \tag{5.26}$$

An initial check of illuminability of the surface within a given facet can be performed via Eq. (5.12). In case $\cos\theta_\odot \le 0$, $Q_\odot = 0$.

Otherwise, if $\cos\theta_\odot > 0$, the unit solar vector is transformed into the horizontal coordinate system for each facet, such as $\hat{\mathbf{r}}_\odot^{[\mathrm{H}]} = \mathbf{R}_{[\mathrm{BF}]}^{[\mathrm{H}]} \hat{\mathbf{r}}_\odot$ (according to Eq. 5.14 where the translation between the coordinate systems can be ignored).

Subsequently, the instant azimuth of the Sun, $\alpha_\odot$, with respect to the local horizontal plane is derived via Eq. (5.16); whereas, the solar elevation is given by $\varphi_\odot = \frac{\pi}{2} - \theta_\odot$. Depending on the facet, the illumination of the local surface is determined by the condition $\varphi_\odot \in (\varphi_\mathrm{a}, \varphi_\mathrm{b})$ at the corresponding $\alpha_\odot$, where $\varphi_\mathrm{a}, \varphi_\mathrm{b}$ are from the Horizon database. If illuminated, the absorbed energy flux by the local facet is then calculated as

$$Q_\odot = \bar{Q}_\odot (1-\mathcal{A}) \sin\varphi_\odot\,. \tag{5.27}$$

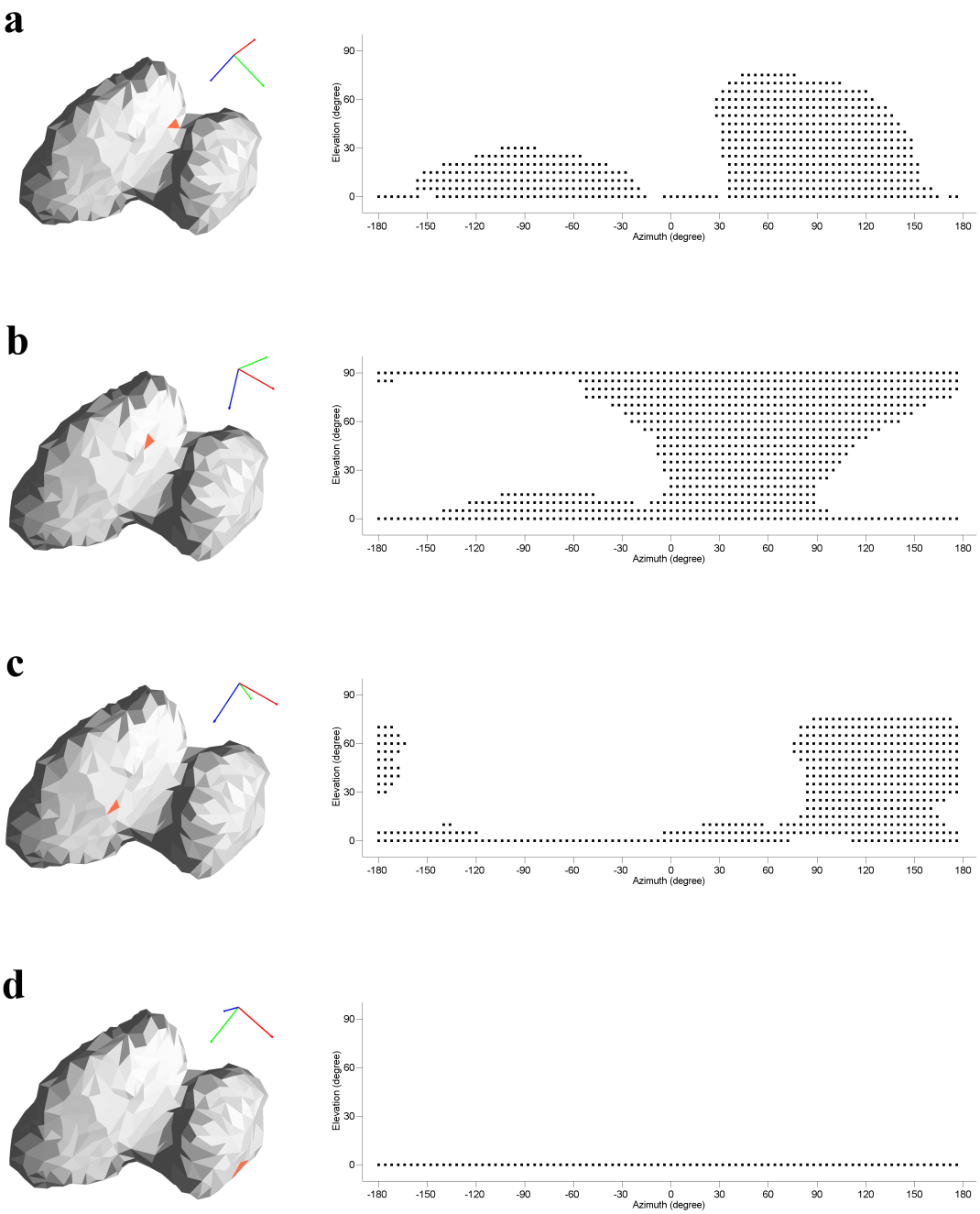

Figure 5.5: View of the upper celestial hemisphere at four locations of the nucleus as inferred from the Horizon Database. **a**. The horizon is distinctly rugged; the open and obstructed views alternate more than once along the same meridian, e.g., at around 30 degrees. **b**. Cave view with visual obstruction over zenith. **c**. Another case of multiple alternations of open and obstructed views along the meridian around 180 degrees. **d**. Open view on a convex topography. The location of the observer is within the triangle in orange on the shape model in the left panel. The x-, y-, and z-axes of the horizontal coordinate system are colored in blue, green, and red, respectively; the x-axis points to the prime meridian of zero azimuth.

5.2.2 Self-heating

It is assumed here that the surface reflectance is Lambertian, in which case the spectral radiance, I, of thermal radiation from the surface is constant in all directions. The radiant power from a fraction of the surface at F with area A_F is then calculated as,

$$\Phi = A_\mathrm{F} \int_0^{2\pi} \int_0^{\pi/2} I \cos\theta \sin\theta \mathrm{d}\theta \mathrm{d}\alpha = A_\mathrm{F}\, \pi I \,, \tag{5.28}$$

where α, θ indicate the azimuthal and emission angles, respectively. The solid angle subtended by the surface fraction from a point located at some great distance, d, can be approximated as,

$$\mathrm{d}\Omega = \frac{A_\mathrm{F} \cos\theta}{d^2} \,, \tag{5.29}$$

where θ is the angle between the surface normal of the facet and the line-of-sight to the distant point. Hence, the power emitted from the surface fraction and intercepted by a unit surface area at the distant point, say F', whose surface normal is inclined from the line-of-sight by θ' is,

$$\mathrm{d}\Phi = I \cos\theta' \mathrm{d}\Omega = I \cos\theta' \frac{\cos\theta}{d^2} A_\mathrm{F} \,. \tag{5.30}$$

Note that θ' is distinguished from θ by nature, since the former is the incidence angle of thermal *irradiation* at F'. Rearranging the above equation as follows,

$$\mathrm{d}\Phi = \Phi \frac{\cos\theta \cos\theta'}{\pi d^2} \,, \tag{5.31}$$

and recalling from Eq. (4.14) that

$$\Phi = A_\mathrm{F}\, q_\varepsilon = A_\mathrm{F}\, \varepsilon\sigma T_0^4 \,, \tag{5.32}$$

the specific power of thermal irradiation of a certain spatial point by a surface area on the nucleus is given by,

$$\mathrm{d}Q_\mathrm{F} = q_\varepsilon \frac{\cos\theta \cos\theta'}{\pi d^2} A_\mathrm{F} \,, \tag{5.33}$$

when there is no obstruction in between. The total thermal irradiation by the entire unobstructed nucleus surface, or self-heating, can be expressed as,

$$Q_\otimes = \int_{\mathrm{F}\in\otimes, \mathrm{F}\neq\mathrm{F}'} \mathrm{d}Q_\mathrm{F} \,. \tag{5.34}$$

Procedure of evaluation When a shape model is used in practice, the thermal irradiation of facet l by a visible facet k is given by,

$$\mathrm{d}Q_{\mathrm{F}k,l} = q_{\varepsilon k}\, v_{k,l} \frac{\cos\theta_{k,l} \cos\theta_{l,k}}{\pi d_{k,l}^2} A_{\mathrm{F}k} = q_{\varepsilon k} w_{k,l} A_{\mathrm{F}k} \,, \tag{5.35}$$

where the mutual viewing factor, $w_{k,l}$, as defined by Eq. (5.11) is obtained from the Visibility database, and $A_{\mathrm{F}k}$, the area of facet k, is obtained from the shape database.

Alternatively, one may introduce the view factor as (Özişik 1985),

$$\mathscr{F}_{k,l} = w_{k,l}\, A_{\mathrm{F}k} = v_{k,l} \frac{\cos\theta_{k,l} \cos\theta_{l,k}}{\pi d_{k,l}^2} A_{\mathrm{F}k}\,, \tag{5.36}$$

in which case the reciprocality relation is expressed by

$$\mathscr{F}_{k,l} A_{\mathrm{F}l} = \mathscr{F}_{l,k} A_{\mathrm{F}k}\,, \tag{5.37}$$

whereas $\mathscr{F}_{k,l} \neq \mathscr{F}_{l,k}$ in general.

The total thermal irradiation at facet l by all other facets visible therefrom is evaluated as,

$$Q_{\otimes l} = \sum_{k \neq l} \mathrm{d}Q_{\mathrm{F}k,l} = \sum_{k \neq l} q_{\varepsilon k} w_{k,l} A_{\mathrm{F}k}\,, \tag{5.38}$$

with summation over all k such that $v_{k,l} = 1$. It is assumed here that the energy flux of self-heating is entirely re-absorbed.

Neglecting other minor, indirect sources of energy, such as the reflected fluxes of solar and thermal radiation from the low-albedo cometary surface, the total energy input of the surface is collected as,

$$Q_{(0)} = Q_{\odot} + Q_{\otimes}\,. \tag{5.39}$$

5.3 Thermal model solution

In this section, the solutions of the dusty-ice and dust-mantle thermal models are illustrated with basic simulations for the water production of 67P. Some mandatory tests on the numerical consistency of the model solutions will be performed. The results of these benchmark tests are instructive on the general behavior of the thermal models simulating the distribution and evolution of water activity over the irregular-shaped nucleus in response to insolation while resolving parametrically the influence of nucleus properties.

5.3.1 Model parameterization

The parameterization of model is a crucial task and rarely unique with respect to model solutions. Some properties, such as low reflectance, high porosity, poor conductivity, and so on, are likely general among comet nuclei (Huebner et al. 2006). Others are associated with greater uncertainties and, in some cases, neglected in the model parameterization of previous thermal analyses. In the present simulations, the parameter space can be constrained by the multi-instrumental Rosetta observations of the nucleus and coma of 67P.

Albedo The dimness of 67P nucleus surface can be attributed to the presence of opaque minerals and organic materials and little exposure of water ice (Capaccioni et al. 2015). The normal albedo, as introduced in Eq. (3.31), is ~0.06 (Capaccioni et al. 2015). The

Bond albedo, which measures the fraction of power scattered off the irradiated object at all wavelengths and phase angles, may be somewhat lower (Fornasier et al. 2015). In this work, an approximate value of $\mathcal{A} = 0.05$ is adopted for the Bond albedo to evaluate the absorption of sunlight incident on the object via Eq. (5.1). The uncertainty of this approximation should not exceed 5%.

Density The bulk density of the nucleus was derived as $\rho = 470 \pm 45\,\mathrm{kg\,m^{-3}}$ shortly after the arrival of Rosetta at 67P (Sierks et al. 2015). This value turned out to be an underestimate due to an overestimation of the total volume, especially for the concave southern hemi-nucleus which was largely unilluminated at the time. Using a refined shape model (Preusker et al. 2015) and the estimate of the total mass of the nucleus based on measurements of the Radio Science Instrument onboard Rosetta, the updated bulk density is $\rho = 533 \pm 6\,\mathrm{kg\,m^{-3}}$ (Pätzold et al. 2016).

Thermal inertia Thermal inertia measures the resistance of material to change in temperature and is an intrinsic parameter that reflects the structural, compositional properties of the planetary surface. For instance, material of high thermal inertia warms and cools more slowly and less drastically than low thermal inertia material does subject to periodic heating. Thermal inertia is defined as

$$\mathcal{I} = \sqrt{\kappa c \rho} \quad \mathrm{W K^{-1} m^{-2} s^{1/2}}\,. \tag{5.40}$$

The Microwave Instrument for the Rosetta Orbiter (MIRO) measured an overall low thermal inertia the nucleus in the range between 10 and 50 $\mathrm{W\,K^{-1} m^{-2} s^{1/2}}$ in the early phase of the rendezvous. The estimate appeared representative of the unilluminated southern hemi-nucleus, as well (Choukroun et al. 2015). Spohn et al. (2015) derived a value of $85 \pm 35\ \mathrm{W\,K^{-1} m^{-2} s^{1/2}}$ based on the measurements of the Multi-Purpose Sensors for Surface and Subsurface Science (MUPUS) onboard the Rosetta lander Philae at the final landing site of Abydos. It is possible that the slightly increased estimate might result from the measurement uncertainties (Spohn et al. 2015). Alternatively, the difference might be due to variation of (sub)surface properties across the nucleus, considering that the local morphology at Abydos is dominantly consolidated terrains (Biele et al. 2015).

Icy area fraction As noted in Sect. 4.1, if the nucleus has a high dust content relative to the ice component, the reduction in the icy area of the (sub)surface from which sublimation may occur is inevitable. Consequently, the factor of icy area fraction, $0 \leq \mathscr{F} \leq 1$, is introduced when evaluating the sublimation flux in both the dusty-ice and dust-mantle models (Eqs. 4.19 and 4.31). The formula suggested by Crifo (1997) is adopted for evaluation such that $\mathscr{F}$ is related explicitly to the dust-to-ice ratio (Eq. 4.23).

Various *in situ* measurements provide constraints on $\mathscr{F}$. The spectroscopic observation of 67P by VIRTIS in August 2014 indicated less than 1% of water ice exposed over the nucleus surface. Hapi appeared to be the most water-abundant region of the nucleus, where exposed, transient water ice has been observed by the dawn terminator that would disappear instantly upon illumination (De Sanctis et al. 2015). Such recurring water ice was probably formed by water vapor diffusing from the deeper, warmer interiors and having recondensed near the cooler surface layers during the night. The exposed ice amounts

to no more than 15% of the surface area with respect to the refractory materials. The exposure of large pure water ice grains has been confirmed by Filacchione et al. (2016). Detected in the debris fields in the Imhotep region, these millimeter-sized grains had probably originated from the more ice-rich or sintered layers often buried underneath the dust mantle. In total, the water ice accounts for less than 5% of the observed area. A similar conclusion was drawn by Barucci et al. (2016).

Therefore, it is reasonable to consider an icy area fraction in the range between $\mathscr{F} \in [0.01,\ 0.1]$, i.e., only a few percent of the (sub)surface is icy. Let it be made clear that this icy area fraction does not indicate the presence of macroscopic dormant or inactive areas over the nucleus. For instance, the homogeneous thermal models applied by Keller et al. (2015a) tend to overestimate the total water production of 67P compared with the coma measurements. The modeled overproduction was interpreted as possibly indicating a limited nucleus surface being active (~6%). In this scenario, the nucleus surface is inhomogeneous, e.g., with significant portions where $\mathscr{F} = 0$ or where dust mantle is thick enough to effectively quench (any) water outgassing. In this work, it is always assumed that the nucleus surface is homogeneous with constant icy area fraction and dust mantle thickness everywhere. The icy fraction corresponds to the microscopic inhomogeneity on spatial scales lower than 10 m that is unresolved in the shape model used for the thermal analysis.

Dust mantle thickness The thickness of the dust mantle, X, introduced in Eq. (4.25), is a crucial parameter for the thermal models. As discussed in Sect. 4.1.2, not only does a thick dust mantle restrict diffusion of gas flow (Eq. 4.31), it also moderates the heat flow across the ice front (Eq. 4.25). As a result, the sublimation flux is strongly influenced by the mantle thickness.

Unfortunately, while it is clear that the nucleus surface is overall desiccated, the exact thickness of the dust mantle is difficult to determine. It is indicated by several studies, such as Bockelée-Morvan et al. (2015), Fougere et al. (2016a), and Fink et al. (2016), that the activity level varied across the nucleus, possibly suggesting a non-uniform mantle thickness. The mantle thickness also appeared to vary over time, as inferred from the decrease in spectral slope of the nucleus before perihelion (Fornasier et al. 2016). The physical meaning of the dust mantle may be obscured by the fact that the icy layers underneath are probably porous rather than a solid mixture of dust and ice (Biele et al. 2015). As discussed in Sect. 4.1.3, the porosity gives rise to diffusion of water vapor as well as concurrent recondensation and sublimation of molecules throughout the subsurface. The mechanism has been substantiated in many numerical and experimental investigations. The reader is referred to the discussions by Mekler et al. (1990), Prialnik and Mekler (1991), Kochan et al. (1989), Grün et al. (1991), and Spohn and Benkhoff (1990), the last three of which were among the studies dedicated to the KOSI experiment. The diurnal cycle of water ice observed by De Sanctis et al. (2015) supports the validity of the mechanism in general. Additionally, it suggests that the structural and compositional variation of the subsurface with depth is more complex than can be described by a uniform dust-ice mixture overlain by a dust mantle. At least, the depth of the ice front and, therefore, the thickness of the dust mantle probably varies on a diurnal basis.

All the aforementioned complexities render the mantled solid-mixture an *ad hoc* simplification of the subsurface structure. Hence, the mantle thickness needs to be treated as

Table 5.1: Parameters of thermal models for diurnal solutions in Sect. 5.3

Parameters	Symbols	Values	
Step in depth	Δx	1	mm
Step in time	Δt	$t_{\rm P}/1200$	
Rotation period	$t_{\rm P}$	44650	s
Bond albedo	$\mathcal{A}$	0.05	
Emissivity	ε	1	
Heat conductivity	κ	2×10^{-3}	$\mathrm{W\,m^{-1}K^{-1}}$
Specific heat capacity	c	1000	$\mathrm{J\,kg^{-1}K^{-1}}$
Density	ρ	500	$\mathrm{kg\,m^{-3}}$
Radius of dust particle	$r_{\rm d}$	0.5	mm
Latent heat of water ice	ℓ	2.3×10^{6}	$\mathrm{J\,kg^{-1}}$
Quenching factor*	p	0.14	
Sublimation coefficient**	c_0	0.146	
	c_1	0.854	
	c_2	57.78	
	c_3	11580	K
Saturation vapor pressure***	a	3.23×10^{12}	Pa
	b	6134.6	K
Bottom depth****	$\mathbb{X}$	1	m
Interior temperature****	$T_{\mathbb{X}}$	100	K

* Eq. (4.29) (Gundlach et al. 2011).
** Eq. (4.17) (Gundlach et al. 2011).
*** Eq. (4.18) (Gundlach et al. 2011).
**** Obtained by the orbital solution.

an adjustable empirical parameter. As will be shown, the choice of this parameter is not arbitrary and can be effectively constrained by observations.

Additional model parameters Other parameters of the thermal models are provided in Tab. 5.1.

5.3.2 Diurnal solution of nucleus temperature and water outgassing

As the first illustration, the subsurface temperature profiles and sublimation flux over the nucleus of 67P over one comet rotation on June 15, 2014 are derived via the two thermal models, according to the computational procedure described in Sect. 4.3.

5.3.2.1 Dusty ice model

The temperature profiles at two locations of the nucleus at midnight of Jun. 15, 2014, are shown in Fig. 5.6. For the sake of brevity, the epoch is referred to as t_0. With a low thermal inertia in the nucleus subsurface, it may be assumed that only the temperatures in the topmost centimeters of the nucleus affect diurnal variation of the water activity.

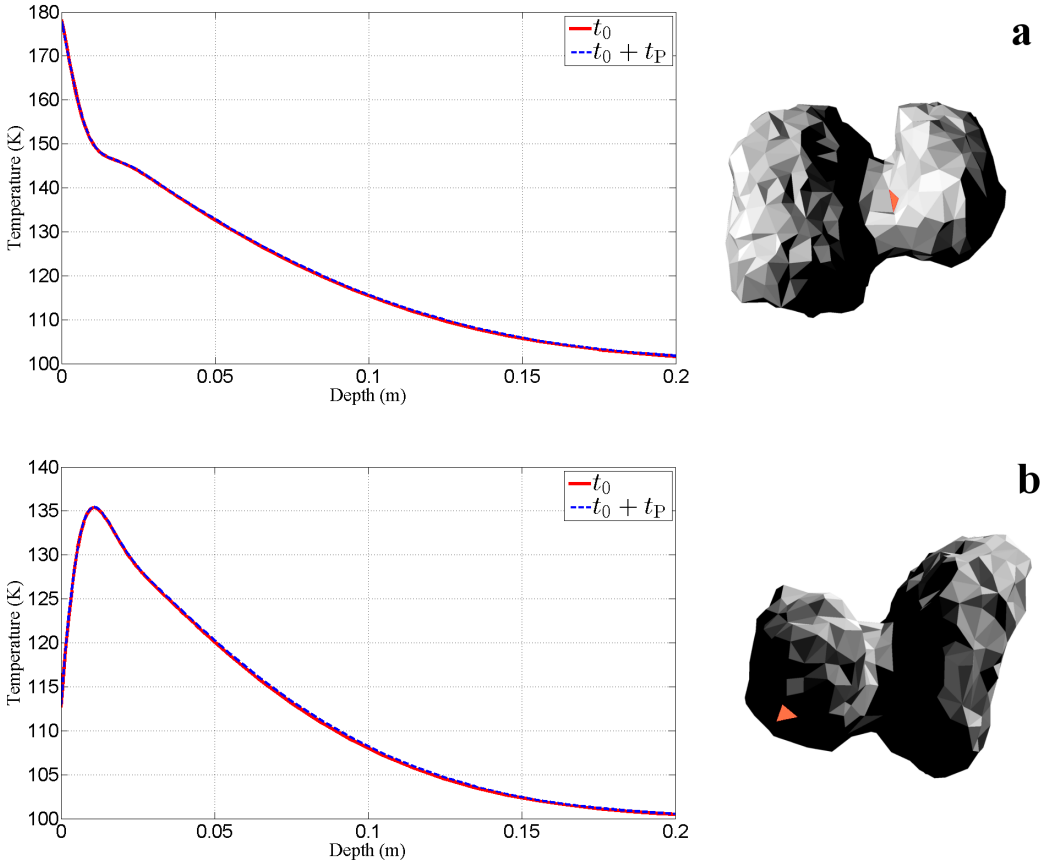

Figure 5.6: Profiles of temperature as a function of depth at two different locations on 67P as derived via the dusty ice thermal model. Profile at epoch t_0, at mid-night on Jun. 15, 2014, is indicated by the solid red curve. The dashed blue curve indicates the temperatures after one rotation period, t_P. The results are for a location in the neck region (**a**) and the other on the small lobe (**b**) of the nucleus, as marked by a triangle in orange on the shape model in the respective panels. Realistic illumination condition at $t_0(+t_P)$ is shown according to Eq. (5.25).

In Fig. 5.6, the temperatures down to the depth of 0.2 m are shown. The overlap of the profile at t_0 with that after a full comet rotation at $t_0 + t_P$ suggests that convergence of the numerical solution is achieved. The location in the neck region (Fig. 5.6a) was illuminated at t_0, as reflected by steep negative temperature gradient in the top centimeters below the surface. The profile starts to flatten at the depth of around 1.5 cm marking a pivot point of the curve. Correspondingly, the temperature profile at another location in shadow at t_0 shows a maximum at roughly the same depth (Fig. 5.6b). It can be inferred that diurnal variations of temperatures nearly vanish below this layer; instead, a steady heat flux is directed towards the nucleus interior underneath.

Conservation of energy It is a prerequisite to ensure that energy is conserved in the thermal analysis, i.e., energy input must be balanced by consumption. The conservation of energy for the dusty ice model can be expressed as follows,

$$Q_{(0)} = q_{\epsilon(0)} + q_{Z(0)} + \dot{U} \,, \tag{5.41}$$

where $Q_{(0)}$ denotes the energy input of insolation, and if applicable, of self-heating, and where $q_{\epsilon(0)}$ is the thermal radiation as defined by Eq. (4.14). $q_{Z(0)}$ is the energy flux consumed by sublimation of water ice. U is, loosely speaking, the internal energy of the system, which varies with temperature, i.e.,

$$\Delta U = c\rho \cdot \Delta T \,. \tag{5.42}$$

At a particular location on the nucleus, the *change* of internal energy in the subsurface is expressed by

$$\Delta U = \int_0^{\mathbb{X}} c\rho \Delta T \, \mathrm{d}x \,, \tag{5.43}$$

where the integration is carried out formally from the surface down to the isothermal depth, $\mathbb{X}$, where the heat flux vanishes, according to Eq. (4.22).

It is worth pointing out that, while Eq. (5.41) can be easily shown to be tantamount to Eq. (4.13) indicating the surface energy balance for the dusty ice model, it is not a mere repetition of the latter. Eq. (5.41) expresses the conservation of energy, which can be applied to test the consistency of the numerical solution. The density and specific heat capacity are assumed to be constant as a simplification in this work. The rate of change of the internal energy is evaluated numerically by summing up contributions from discrete layers, i.e.,

$$\dot{U} = \sum_{j=1}^{j\max} c\rho \dot{T}_j \Delta x_j \tag{5.44}$$

where $\dot{T}_j$ denotes the rate of temperature variation of the jth layer with thickness Δx_j. In the case of uniform discretization, Δx_j is a constant.

The energy fluxes, $Q_{(0)}$, $q_{\epsilon(0)}$, $q_{Z(0)}$, and $\dot{U}$, at the two locations indicated in Fig. 5.6 at t_0 are shown in Fig. 5.7. Note that $-Q_{(0)}$ is shown to allow for easy comparison with other sources of energy consumption. The energy input differs at the two locations with dissimilar landscapes. The area in the saddle between the two lobes (Fig. 5.6a) experiences abrupt exposure to strong illumination peering into the valley at high solar elevation (at ~8 hours in Fig. 5.7a). On the top of the small lobe with little elevation in the surroundings (Fig. 5.6b), the variation of insolation is distinctly sinusoidal on the dayside as given by Eq. (5.1).

At the heliocentric distance of 3.9 AU, thermal radiation is the dominant source of energy consumption from the dayside. The maximum thermal radiation trails the peak of insolation. That the maximum surface temperature occurs only after peak insolation results from thermal inertia of the nucleus. While surface temperature responds to the variation of insolation instantly, part of the heat flux is transported into the cooler interior (e.g., before midday). Indeed, the subsurface begins to warm up instantly at the onset of insolation. The *warming* intensifies and starts to decrease before insolation peaks. The subsurface starts to cool down in the late afternoon, e.g., from ~2 hours in Fig. 5.7a and

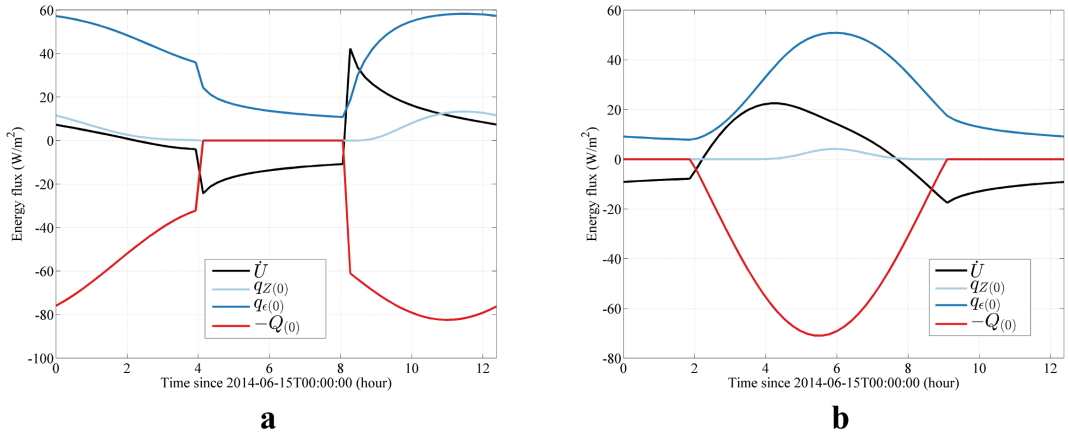

Figure 5.7: Energy fluxes over one comet rotation on Jun. 15, 2014, as estimated by the dusty ice thermal model. Results are for two locations on the nucleus as indicated in Fig. 5.6. Energy input of insolation is indicated by the red curve; negative flux is presented for comparison with other curves for energy consumption. Thermal radiation is indicated by the dark blue curve. The energy flux consumed by sublimation corresponds to the light blue curve. The change rate of internal energy of the nucleus is given by the black curve.

from ~8 hours in Fig. 5.7b. The energy flux consumed by sublimation coincides with thermal radiation, since both are governed by the surface temperature. Overall, however, the energy consumed by sublimation is insignificant at large heliocentric distances, a conclusion also drawn in previous studies (Gortsas 2010).

Diurnal skin depth Fig. 5.8 shows the diurnal variation of temperature at different depths starting from t_0 for the two locations in Fig. 5.6. As a result of low thermal inertia, the range of temperature variation attenuates with depth. The diurnal skin depth is estimated by the simple formula of Eq. (4.87). With $\kappa = 0.002\ \mathrm{W\,K^{-1}m^{-1}}$, $\rho = 500\ \mathrm{kg\,m^{-3}}$, and $c = 1000\ \mathrm{J\,K^{-1}kg^{-1}}$, a decay of temperature variation by $1/e$ relative to the range at the surface is expected to occur at a depth of ~8 mm. In comparison, the model results indicate attenuation factors of ~0.5 and ~0.3 at depths of 5 mm and 1 cm, respectively. Therefore, the numerical solution is in agreement with the analytic approximation.

The temperature variation becomes progressively delayed with depth relative to upper layers (Fig. 5.8), which is attributed to inefficient heat transport through the low thermal inertia medium. The surface temperature responds immediately to the energy input (the variation of insolation is indicated by the red curve in Fig. 5.7). At the depth of 1 cm, for instance, the temperature peaks more than one hour after the maximum surface temperature appears. Thus, the thermal lag may shed light on the subsurface thermal properties. As will be shown in Sect. 6, the variation of water activity in response to insolation provides constraint on the depth from which activity arises.

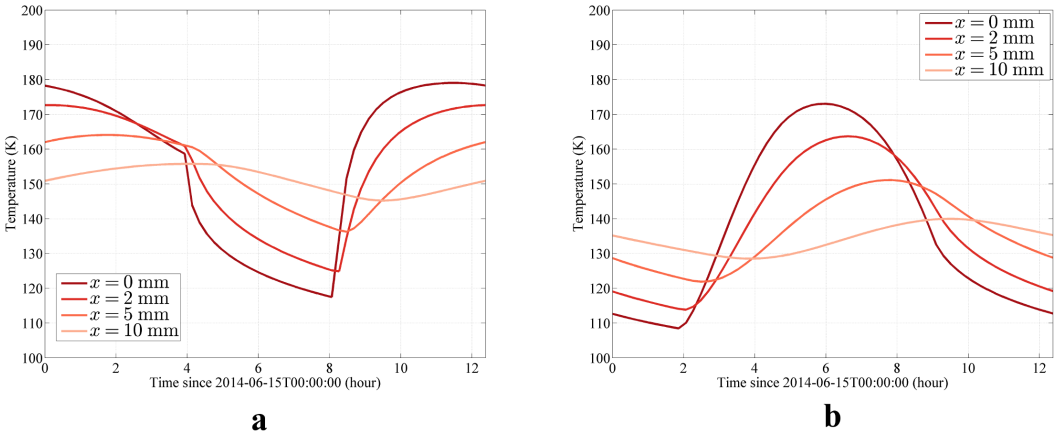

Figure 5.8: Diurnal temperature variations at different depths below the surface on Jun. 15, 2014, as estimated by the dusty ice model. Results are for two locations on the nucleus as indicated in the corresponding panels of Fig. 5.6. At both locations, the surface temperature varies by ~60 K (x=0 mm). The range of variation decays by one half at the depth of 5 mm. At 10 mm, temperature varies by less than 20 K. The diurnal skin depth lies between 5 mm and 10 mm.

5.3.2.2 Dust mantle model

For comparison, the solutions of the dust mantle thermal model, as described in Sect. 4.1.2 are obtained over the same comet rotation starting from midnight on Jun. 15, 2014, as the solutions of the dusty ice model in the previous section. The parameters of the model are found in Table 7.2.

The temperature profiles at locations A and B show a similar trend as those derived via the dusty ice model (Fig. 5.9). The surface temperature of the dust-mantled nucleus is higher by ~10 K than that for an icy surface at A on the dayside (Fig. 5.9a). The increase is due to the reduction of sublimation flux from below the air-resistant dust mantle and, thus, the excess of energy heating the subsurface. The surface temperature at location B in shadow is lower than that derived by the dusty ice model by ~10 K (Fig. 5.9b). In this case, the lower temperature at night is related to higher sublimation rate from the warmer subsurface than the sublimation from the colder icy surface, so that less energy is absorbed in the dust mantle. The diurnal insulation depth, i.e., the trough along the temperature profile in the daytime or the crest during the night, is slightly larger than that in the dusty ice model. The reason is, again, that reduced sublimation enables more energy to be transported into the interior and, thus, enlarges temperature variations in deeper layers. This is substantiated by the observation that the interior of a dust-mantled nucleus is significantly warmer than the interior of a bare, icy nucleus. Note, however, that greater insolation depth does not necessarily indicate deeper diurnal skin; as noted, the latter indicates where temperature range decays by the factor of $1/e$ *relative* to the temperature range at the surface.

Conservation of energy In the dust mantle model, energy balance must be numerically evaluated for both the nucleus surface and the ice front. Eq. (5.41) is revised as

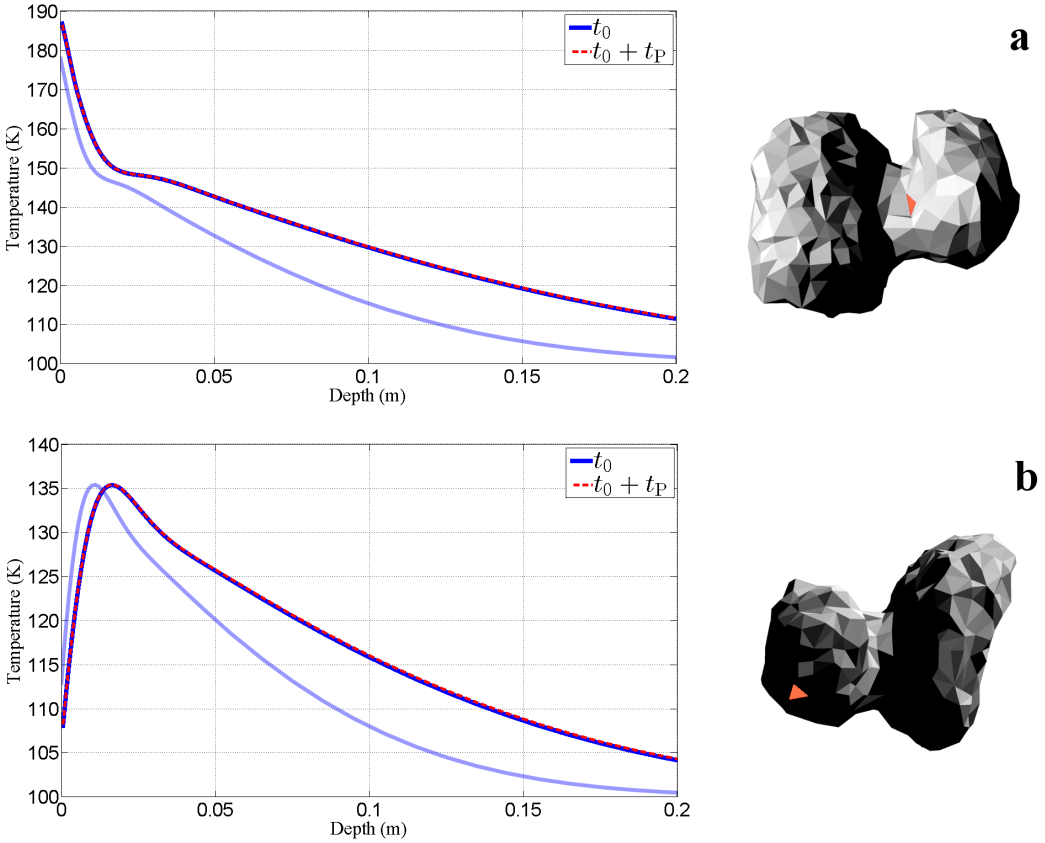

Figure 5.9: Profiles of temperature as a function of depth at two different locations on 67P as derived via the dust mantle thermal model. The mantle thickness is 5 mm. Profile at epoch t_0, at mid-night on Jun. 15, 2014, is indicated by the solid blue curve. The dashed red curve indicates the temperatures after one rotation period, t_P. The light blue profiles are as presented in Fig. 5.6 for the dusty ice model. The results are for a location in the neck region (**a**) and the other on the small lobe (**b**) of the nucleus, as marked by a triangle in orange on the shape model in the respective panels. Realistic illumination condition at $t_0(+t_P)$ is shown according to Eq. (5.25).

$$Q_{(0)} = q_{\epsilon(0)} + q_{Z(X)} + \dot{U} \,, \tag{5.45}$$

where $q_{Z(X)}$ refers to the sublimation from beneath the dust mantle, i.e., at depth X (Eq. 4.32), rather than at the surface, thus replacing $q_{Z(0)}$ in Eq. (5.41).

The diurnal variation of energy fluxes at the locations A,B, recalled in Fig. 5.9, on Jun. 15, 2014 is shown in Fig. 5.10. The flux of insolation is the same as in Fig. 5.7 (red curve). The energy fluxes estimated by the dust mantle model are similar to those by the dusty ice model on the night side, when the energy consumed by water sublimation is negligible in which case $q_{Z(0)} \approx q_{Z(X)}$ nearly vanish. On the dayside, the thermal radiation from the nucleus with a dust mantle is stronger than that from an icy surface by about 10 W m^{-2} (comparing the blue curves in Figs. 5.7 and 5.10), that results from the reduced sublimation below a quenching dust mantle (light blue curves in Figs. 5.7. The energy consumption by sublimation is imperceptible in Fig. 5.10.

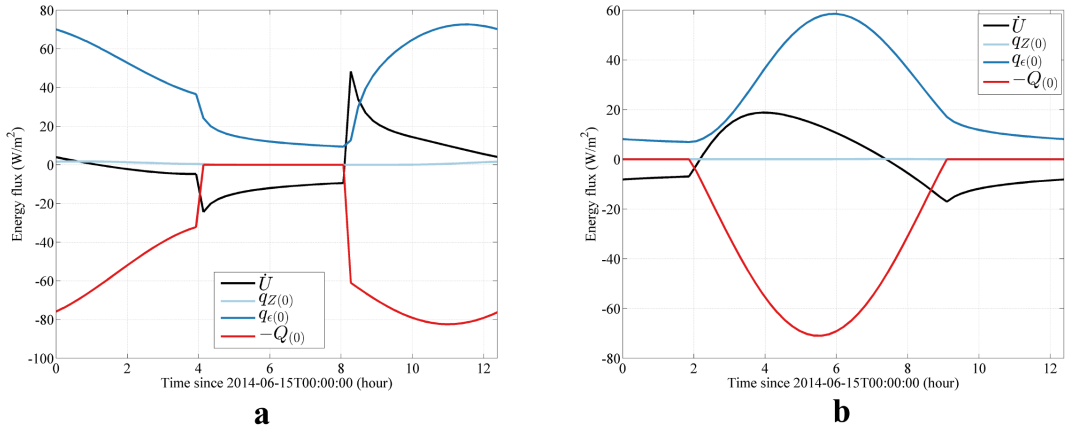

Figure 5.10: Energy fluxes over one comet rotation on Jun. 15, 2014, as estimated by the dust mantle thermal model. The mantle thickness is 5 mm. Results are for two locations on the nucleus as indicated in Fig. 5.9. Energy input of insolation is indicated by the red curve; negative flux is presented for comparison with other curves for energy consumption. Thermal radiation is indicated by the dark blue curve. The energy flux consumed by sublimation corresponds to the light blue curve. The change rate of internal energy of the nucleus is given by the dark curve.

Diurnal skin depth As revealed in Fig. 5.9, the 80 K variation of surface temperature on the dust-mantled nucleus is larger than that on the icy nucleus surface. During the daytime, more energy is used to warm up the nucleus interior when the sublimation rate is reduced by the dust mantle; conversely, in the night, higher temperature below the dust mantle maintains stronger sublimation than that from the icy surface, in which case less energy from the interior can escape from the surface. As in the dusty ice model, the temperature variation decays with depth. The sublimation temperature (x = 5 mm) varies by roughly 1/2 of the range at the surface. At the depth of 10 mm, the temperature range attenuates to 1/4. Therefore, the diurnal skin depth for the dust-mantled nucleus lies in between 5 mm and 10 mm, and is thus comparable to that in the case of a bare, icy nucleus.

5.3.3 Diurnal solution of global water activity

The water production rate of the nucleus is obtained by integrating the contribution from all facets of the shape model, such as,

$$\iint_A Z \cdot \mathrm{d}A = \sum_k Z_k \cdot A_{\mathrm{F}k} \,, \tag{5.46}$$

where A denotes the surface area over the nucleus and where Z_k indicates the sublimation flux from the kth facet of the shape model with surface area $A_{\mathrm{F}k}$. To simplify the notation, the expression of summation over the shape model is hereafter contracted as

$$\Sigma Z = \sum_k Z_k \cdot A_{\mathrm{F}k} \,. \tag{5.47}$$

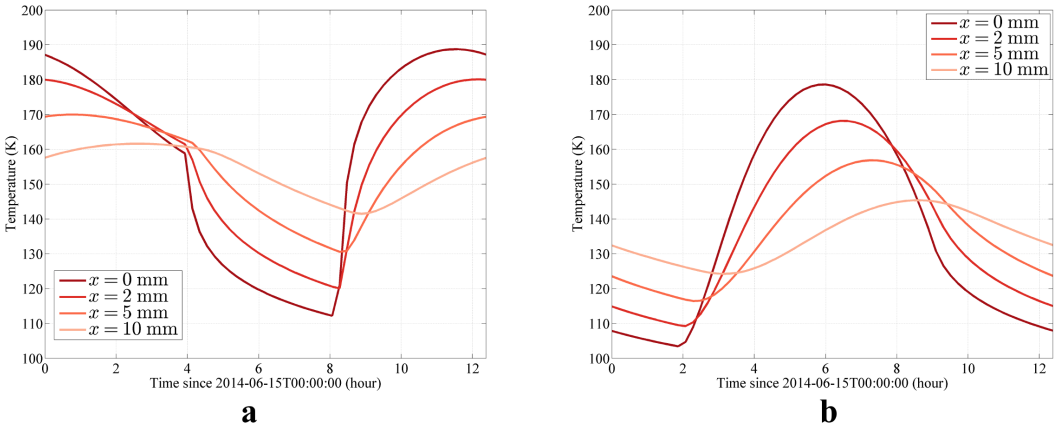

Figure 5.11: Diurnal variation of temperatures at different depths on Jun. 15, 2014, as estimated by the dust mantle thermal model. The results in **a** and **b** are for two locations as indicated in the corresponding panels in Fig. 5.9. At both locations, the surface temperature varies by nearly 80 K, exceeding the temperature range in the dusty ice model. The larger variation is attributed to the reduced sublimation flux below a dust mantle with respect to an icy nucleus surface. The diurnal skin lies between 5 mm and 10 mm in depth.

The notation applies to other quantities, e.g., $\Sigma q_{Z(0)} = \sum_k q_{Z(0)\,k} A_{\mathrm{F}\,k}$ denotes the total expense of energy for water ice sublimation from the nucleus.

Fig. 5.12 presents the diurnal variation of total energy input and consumption of the nucleus on Jun. 15, 2014. Consistent with the conclusion for single facets, the total energy consumption, $\Sigma Q_{(0)}$, is dominated by thermal radiation, $\Sigma q_{\epsilon(0)}$, at the large heliocentric distance of 3.9 AU. Thermal radiation from the nucleus with a dust mantle is higher than that from an icy surface, resulting from a lower sublimation rate and smaller $\Sigma q_{Z(0)}$ therewith.

As 67P approached perihelion, the water activity of the comet increased with intensifying insolation. Because this period of time spans but less than one fifths of the entire orbit period, the diurnal solutions of the thermal models for different heliocentric distances are expected to represent the increase of water activity over time. On Dec. 15, 2014, when 67P reached the heliocentric distance of 2.8 AU, the share of $\Sigma q_{Z(0)}$ would become notable with respect to $\Sigma Q_{(0)}$ for an icy nucleus surface (Fig. 5.13a). Around perihelion, sublimation dominates the energy consumption (Fig. 5.14a). In contrast, the nucleus covered by a dust mantle dissipates most of its heat via thermal radiation at all heliocentric distances (Figs. 5.13b, 5.14b).

5.3.4 Sensitivity of solution to model parameterization

5.3.4.1 Nucleus shape

Without detailed knowledge on the shape of the nucleus, it has been a common practice to consider a spherical nucleus. The evaluation of solar irradiation is straightforward on a spherical object, where the incidence angle is directly calculated by Eq. (5.12). Shadow-

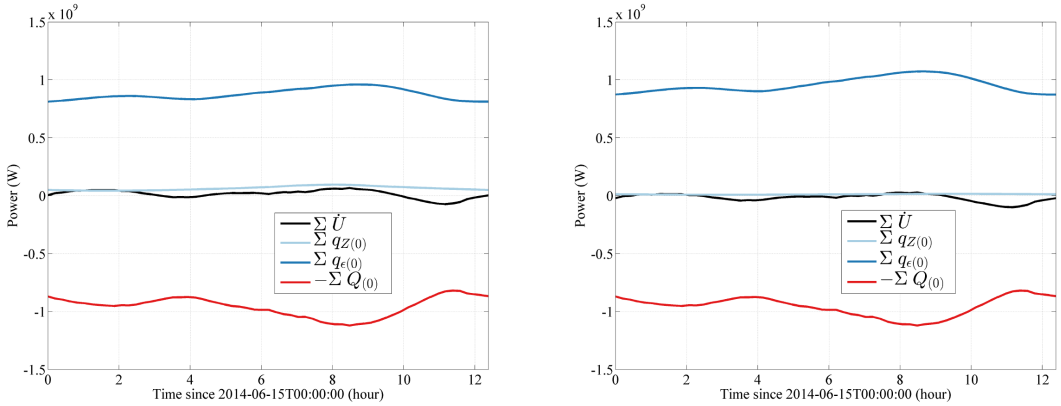

Figure 5.12: Diurnal variation of energy fluxes integrated over the nucleus surface on Jun. 15, 2014. The red curve indicates the *negative* total energy input of insolation. The blue curve indicates the flux of thermal radiation. The light blue curve marks the energy flux consumed by water sublimation. The dark curve indicates the change rate of internal energy of the nucleus. **a**. Results are for icy nucleus surface, derived by the dusty ice model. **b**. Results are for the nucleus with a dust mantle of 5 mm thick, derived by the dust mantle model.

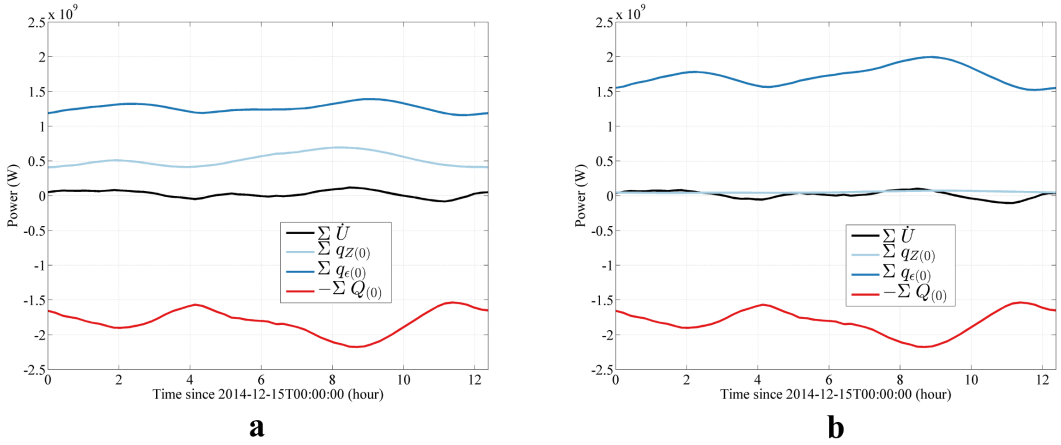

Figure 5.13: Diurnal variation of energy fluxes integrated over the nucleus surface on Dec. 15, 2014. The variables are as defined in Fig. 5.12. **a**. Results are for icy nucleus surface, derived by the dusty ice model. **b**. Results are for the nucleus with a dust mantle of 5 mm thick, derived by the dust mantle model.

ing does not occur on a convex surface and illumination is determined by the altitude of the Sun. The shape of the 67P nucleus is highly irregular, with bi-lobed silhouette deviating from a circle. Thus, the amount of solar radiation intercepted by 67P likely differs from that incident on a spherical nucleus.

Fig. 5.15 shows the comparison of the variation of the insolation flux across a 2-km radius sphere and the realistic shape of the nucleus on June 15, 2014. The tessellated shape models are used for approximation. The insolation varies continuously across a sphere,

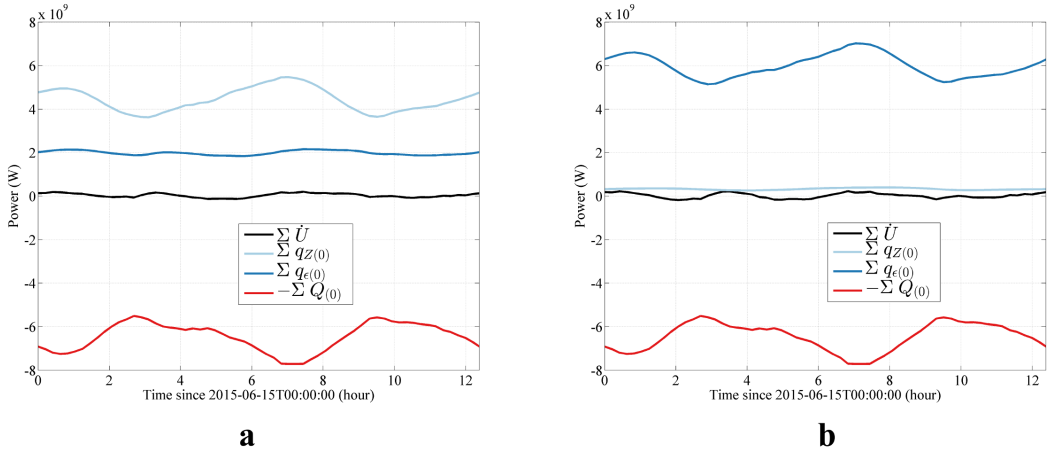

Figure 5.14: Diurnal variation of energy fluxes integrated over the nucleus surface on Jun. 15, 2015, at the heliocentric distance of 1.43 AU. The variables are as defined in Fig. 5.12. **a**. Results are for icy nucleus surface, derived by the dusty ice model. **b**. Results are for the nucleus with a dust mantle of 5 mm thick, derived by the dust mantle model.

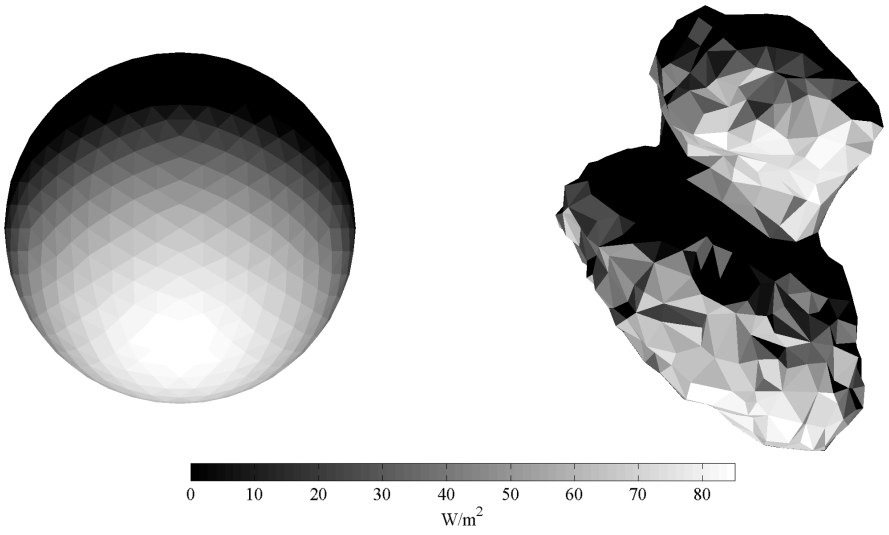

Figure 5.15: Insolation over the irregular-shaped nucleus in comparison with that over a sphere on June 15, 2014, at midnight. The radius of the sphere is 2 km. The nucleus is approximated by a 1000-facet shape model.

and peaks at the sub-solar point (left, Fig. 5.15). When the large scale topographies are taken into account (width of a facet is on the order of 100 m), the variations of insolation on the nucleus are more significant and irregular across abrupt topography (right panel, Fig. 5.15). Fig. 5.16 shows the variations of the total insolation on the sphere and the irregular nucleus. Because the cross section of a sphere does not change with rotation, the total insolation does not vary diurnally. This is in contrast to the cyclic variation of insolation over the rotating, irregular-shaped nucleus.

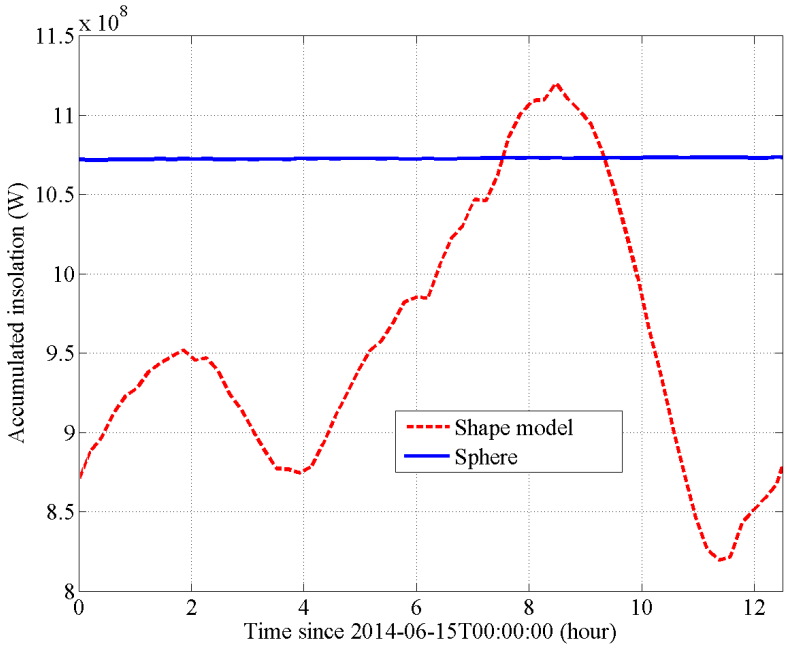

Figure 5.16: Diurnal variation of insolation over a sphere in comparison with that over the irregular-shaped nucleus. The radius of the sphere is 2 km. The nucleus is approximated by a 1000-facet shape model.

It is desirable to also compare the water production over the sphere and from the irregular nucleus in response to insolation. Here, let us assume for simplicity that the water ice sublimates from the surface in which case the dusty ice model is applicable. The surface temperature and the water production over the spherical and irregular nuclei exhibit a pattern similar to that of insolation (Fig. 5.17). As shown in Fig. 5.18, the production rate over the sphere is invariant with constant total insolation over a nucleus rotation. The production rate over the irregular nucleus, on the other hand, shows a distinct diurnal variation, that peaks with maximum insolation. However, another lower peak in insolation (that occurs at 2 hours into the midnight) corresponds to the minimum of total production. This indicates that the water production varies non-linearly with insolation.

5.3.4.2 Dust mantle thickness

The thickness of dust mantle significantly influences the water activity over the nucleus. Simply put, the dust mantle reduces the outgassing flux with respect to free sublimation of ice on the surface; in addition, it overlies the ice front and moderates the temperature at which sublimation occurs.

Fig. 5.19 illustrates that the total water production rate of the nucleus covered by a uniform dust mantle of varying thicknesses over one cometary rotation. Water sublimation rate from below a dust mantle of 2 mm is less than half of that from an icy nucleus surface; an even thicker mantle of 5 mm restricts the production rate to less than 20% of the surface sublimation rate. The range of diurnal variation attenuates with increasing mantle thickness. For instance, the production varies by less than 5 kg s^{-1} under a 5-mm

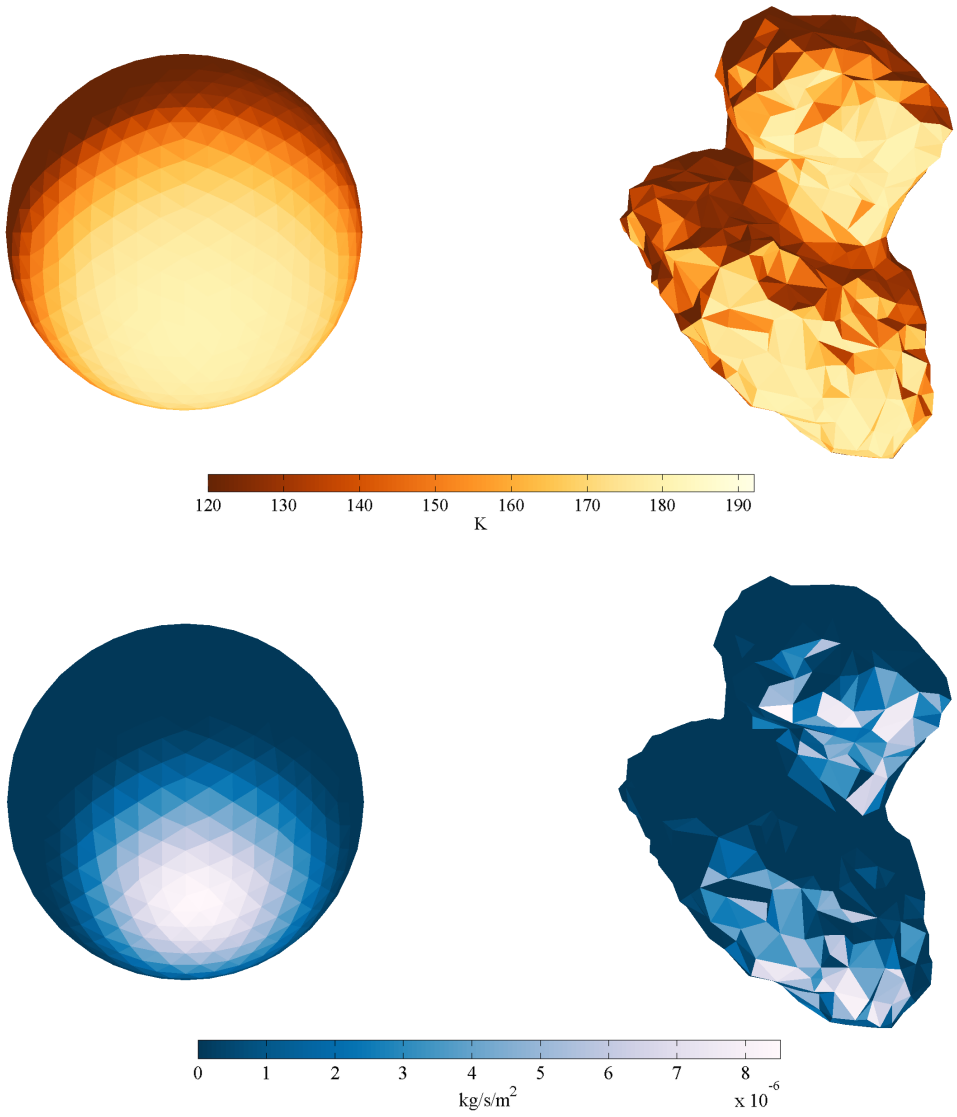

Figure 5.17: Modeled water production rate from a 2-km radius spherical nucleus in comparison with that from the irregular-shaped nucleus on June 15, 2014, at midnight.

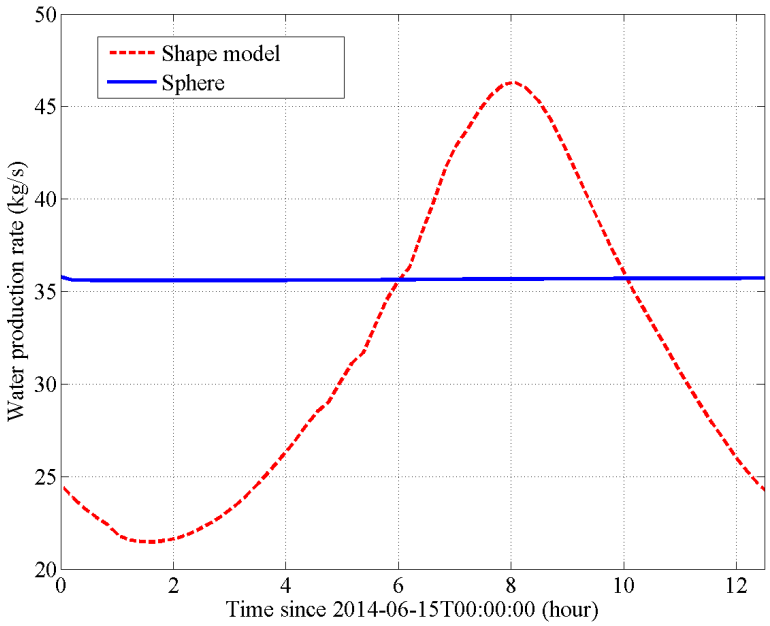

Figure 5.18: Diurnal variation of modeled total water production of 67P approximated by a realistic 1000-facet shape model (dashed red line) in comparison with that from a spherical nucleus with 2-km radius (solid blue line).

thick mantle, in contrast to the variation of ~20 kg s^{-1} in the case of ice sublimation from the surface.

The maximum water production rate below the dust mantle of 2 mm thick lags behind the peak production of the icy nucleus by nearly half an hour (Fig. 5.19); whereas, the lag in the case of a 5-mm thick mantle increases to over one and half hours. This delay results from the propogation time of thermal wave through the dust mantle that increases with mantle thickness. If observed, the delay of water activity with respect to varying insolation provides a constraint on the mantle thickness.

5.3.4.3 Icy area fraction

The parameter of the icy area fraction, $\mathscr{F}$, is likely non-negligible for a refractory nucleus. The reduction of the sublimation flux arises from the decrease of icy (sub)surface area from which sublimation occurs with other areas occupied by non-volatile components. Eq. (4.31) suggests that $\mathscr{F}$ and the quenching factor, Ψ, of the gas flow are not separable. In this work, an experimentally determined formula is adopted for Ψ (Gundlach et al. 2011). For a dust-to-ice ratio of 10, a reduction of the icy area fraction to ~10% is expected (Eq. 4.23).

It remains to be investigated how icy area fraction impacts the water production. The moderation of the production rate is unlikely given strictly by $\mathscr{F}$. Only when the nucleus is assumed to be locally active, i.e., with substantial dormant areas, does $\mathscr{F}$ *macroscopically* proportion the total water production with the icy fraction which is, in effect, the active fraction. On the contrary, because the nucleus is assumed to be globally active in

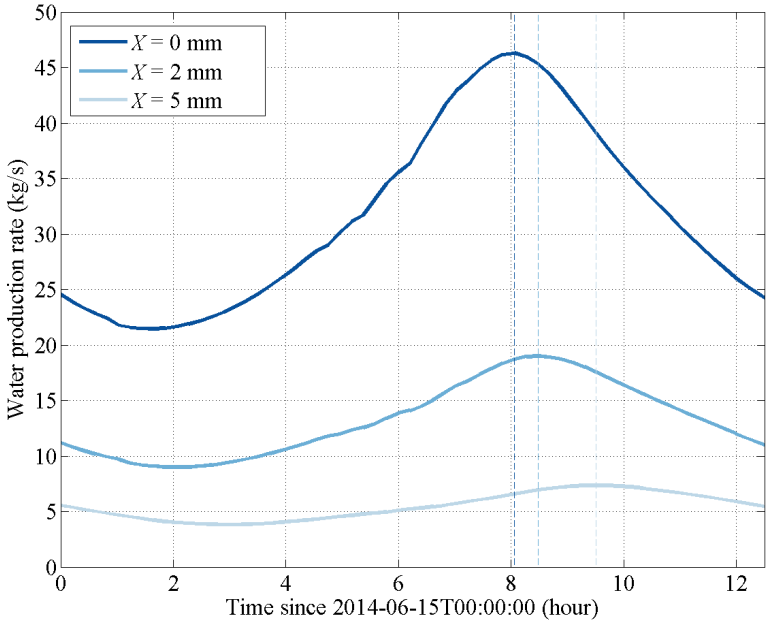

Figure 5.19: Modeled water production of 67P over one nucleus rotation on Jun. 15, 2014. The dark blue curve indicates the water production over an icy nucleus without a dust mantle. The medium and light blue curves correspond to the dust mantle thickness of 2 mm and 5 mm, respectively.

this study, $\mathscr{F}$ indicates a microscopic quantity regulating the water production from an areally homogeneous surface.

In Fig. 5.20, the total water productions of 67P nucleus with respective icy area fractions of 100%, 10%, and 1% are derived via the dusty ice thermal model. $\mathscr{F} = 0.1$ results in a reduction to ~20% of the production in comparison with the fully icy subsurface. The reduced production in the case of 1% is larger than $\mathscr{F}$ itself.

The under-reduction of the water production with respect to $\mathscr{F}$ is due to the compensation by increasing sublimation temperature. Referring to the energy balance given by Eq. (4.13) (or Eq. 4.25 in the case of dust mantle model), one sees that a reduction by $\mathscr{F}$ will result in a decrease of energy consumption by ice sublimation. Hence, more heat will be transported into the icy interiors, raising the temperatures at the ice front and in deeper layers. As a result of such negative feedback, sublimation will intensify somewhat. Although the warming of the subsurface will counter the reduction of the sublimation rate, it does not over-compensate sublimation rate so that the net result is still a decrease in production.

5.3.4.4 Self-heating

Self-heating is irrelevant for convex objects such as spherical nuclei. This may not be the case for irregular-shaped objects, however; in particular, 67P nucleus is bi-lobal in shape with strong concavity which is liable to reabsorption of thermal radiation. Self-heating is evaluated via the procedure described in Sect. 5.2.2. The effect of multiscattering, such as

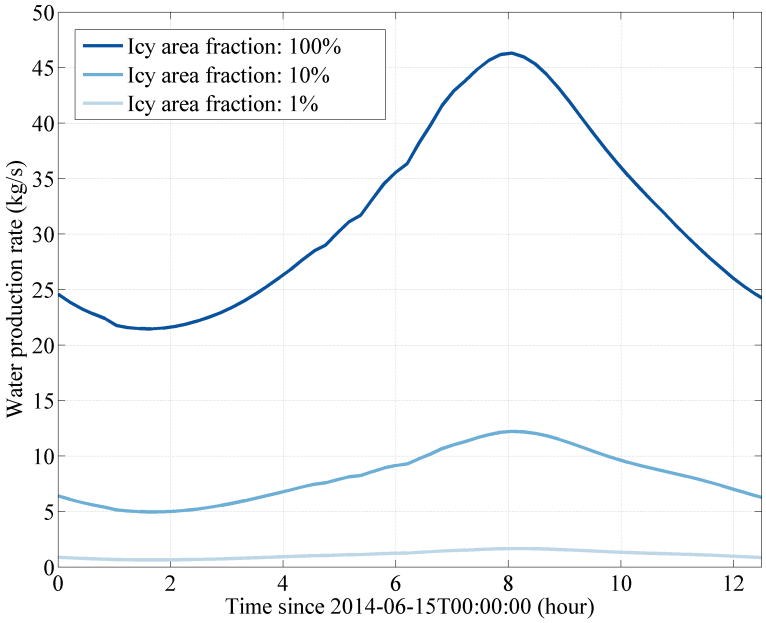

Figure 5.20: Diurnal variation of total water production of 67P influenced by the icy area fraction of the nucleus Three values are considered, i.e., 100%, 10%, and 1%. The dusty ice thermal model is applied for analysis. The input of insolation is as indicated in Fig. 5.16.

reflection of sunlight and re-absorption of nucleus thermal radiation, is neglected in this study. Arguably, this simplification should be reasonable for low-albedo objects.

To assess the impact of self-heating, a shape model of higher resolution than in Fig. 5.17 is used for analysis such that the size of an individual facet is negligible with respect to the dimension of the nucleus. The "neck" region is overall poorly illuminated due to obstruction of towering topography of the two lobes; however, it is where the effect of self-heating becomes most palpable since topographic obstruction also restricts the loss of heat. Self-heating accounts for up to 20% of additional energy input relative to the maximum insolation over the concavity (Fig. 5.21). The maximum increase coincides with abrupt topographic variations, e.g., scarps, recesses, and depressions. The walls along the deep valley between the two lobes are subject to strong self-heating. On the big lobe, the energy increase probably results from irradiation by the illuminated area on the opposite wall; self-heating on the small lobe is likely governed by absorption of local radiation from the illuminated surroundings (Fig. 5.21, right panel).

The increase in surface temperature due to self-heating of the nucleus is shown in Fig. 5.22. Self-heating accounts for the warming by as much as 40 K over the shadowed areas that probably absorb strong thermal radiation from the illuminated areas across the concavity (Fig. 5.22, right panel).

The enhancement of water production shows a different pattern (Fig. 5.23). The maximum enhancement still occurs within the concavity, but over the illuminated area (Fig. 5.23, right panel). The contrast results from the high temperature for substantial water sublimation (e.g., above 180 K) and the exponential dependence of water sublimation on

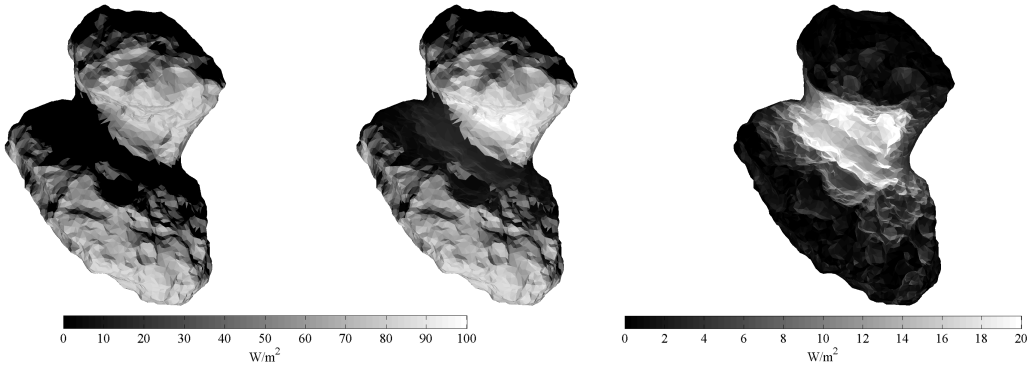

Figure 5.21: Energy input over the nucleus due to self-heating. The first panel (from the left) shows the absorbed energy flux of insolation at midnight on Jun. 15, 2014. The second panel shows increase of energy over the nucleus when the absorption of thermal radiation from the nucleus is considered. The right panel indicates the net increase of energy input due to self-heating. Note that different colorbars are adopted.

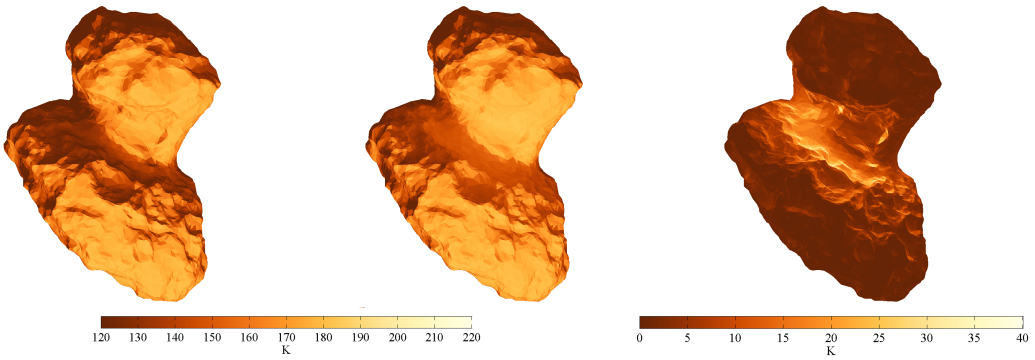

Figure 5.22: Increase of surface temperature due to self-heating of the nucleus. The first two panels show the nucleus surface temperatures derived via the dusty ice thermal model with energy input shown in the corresponding panels in Fig. 5.21. The right panel indicates the net increase of temperature as a result of self-heating. Note that different colorbars are adopted.

temperature (Eq. 4.18). Thus, while the surface temperature could be increased by ~40 K in the shadow, it would contribute little to the water production. On the other hand, even a small increase of a few K would significantly enhance water production over illuminated areas with high surface temperatures.

Fig. 5.24 shows the diurnal variations of total energy input and water production over the nucleus in the comparative cases of insolation with thermal irradiation and of pure insolation. Self-heating accounts for a steady contribution of about 10% of the total energy input at a heliocentric distance of 3.9 AU. The enhancement of water production is about 50%. The more significant increase reflects the nonlinear variation of the water sublimation rate with temperature, as also revealed by the comparison between Figs. 5.22 and 5.23. The effect of self-heating becomes less distinct as the heliocentric distance

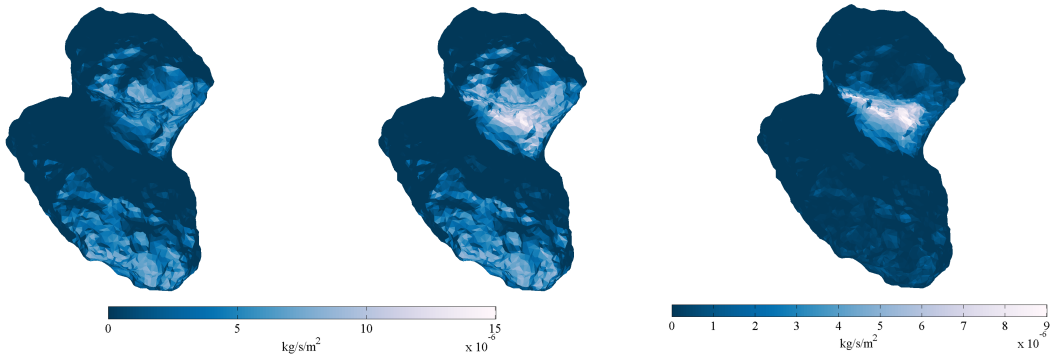

Figure 5.23: Enhancement of water production due to self-heating of the nucleus. The first two panels show the water production rates according to the modeled surface temperatures in the corresponding panels in Fig. 5.22. The right panel shows the net increase of production rate due to self-heating. Note that different colorbars are adopted.

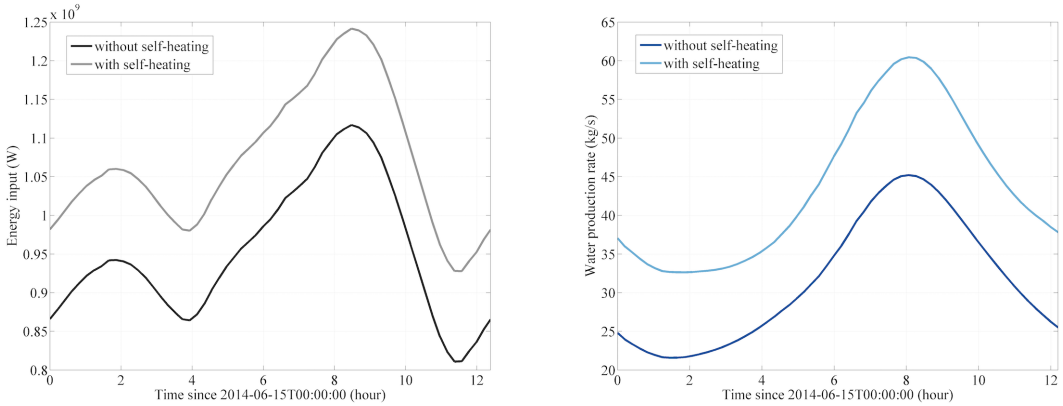

Figure 5.24: Contribution of self-heating to energy input and water production of the nucleus over one rotation. Results refer to Jun. 15, 2014 when 67P was at a heliocentric distance of 3.88 AU. Water production (right panel) is derived via the dusty ice model.

decreases (Fig. 5.25). In mid December, 2014, self-heating yields a contribution of only 10% to the total water production at a distance of about 2.8 AU from the Sun. At 1.4 AU, the enhancement is less than 1% and the water production is dominated by strong insolation close to perihelion .

Though the results presented above are derived via the dusty ice thermal model, i.e., for a "snowball" nucleus, the conclusions apply to the dust mantle model as well. To briefly sum up, self-heating plays a noticeable role in warming the shadowed nucleus. A temperature increase of tens of K should not be unexpected for an irregular object such as 67P. Self-heating may raise the temperature by a few K over the sunlit surface. However, this moderate warming may significantly enhance water production of the nucleus, because of the sharp increase of water ice sublimation with temperature from 180 K. Overall, self-heating enhances but does not dominate total water production of 67P from a heliocentric distance of ~4 AU inwards. Its role likely diminishes once the comet approaches perihelion.

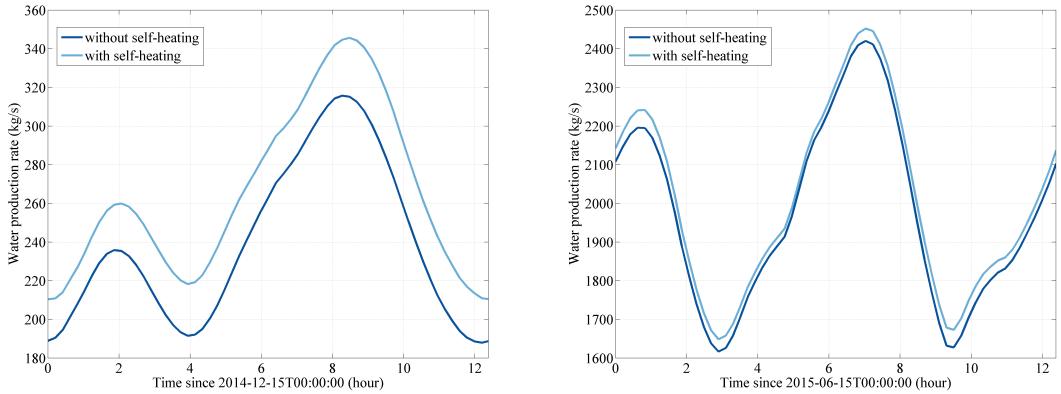

Figure 5.25: Enhancement of water production of the nucleus over one rotation. 67P was at a heliocentric distance of 2.77 AU on Dec. 15, 2014 (left panel) and 1.43 AU on Jun. 15. 2015 (right panel). Water production is derived via the dusty ice model.

6 Sunset Jets Revealing the Presence of Water Ice Near the Surface

This chapter recapitulates the discussion in Shi et al. 2016, Astronomy & Astrophysics, 586, A7. Figures 6.2, 6.3, 6.4, 6.6, 6.7, and 6.8 herein are reproduced from the counterparts in the original article, with permission .

The *in situ* and remote sensing measurements by Rosetta instruments suggest that water is the most abundant volatile species in the coma of 67P (Hässig et al. 2015, Bockelée-Morvan et al. 2015). The strongest water outgassing on the nucleus seemed to originate from the Hapi region on the saddle between the two lobes, which was the source of prominent dust jet structures observed as early as mid 2014 at a heliocentric distance of 3.5 AU (Lara et al. 2015). The water activity from Hapi dominated the total production of the nucleus at least up to the autumnal equinox in the northern hemi-nucleus (in early May 2015) (Bockelée-Morvan et al. 2015). During roughly the same period, it is over the high latitudes in the north where the highest concentration of dust particles in mass was measured *in situ*, probably sourced predominantly from Hapi (Della Corte et al. 2015). While Hapi is the dominant source of water production, the activity is prevalent, if not uniform, across the nucleus (Fougere et al. 2016a, Fink et al. 2016).

In OSIRIS observations, dust activities are, most of all, manifest as fuzzy, translucent plumes composed of light-scattering dust arising from the nucleus, often too faint to be distinguished against the illuminated nucleus surface but contrasted against the dark background of the tenuous coma beyond the limb of the nucleus. With the *visual* dimensions ranging from some meters, restricted by the resolution of observations, up to hundreds of meters, these distinctly concentrated structures are broadly termed dust jets, implicitly beams of dust flows sourced from the nucleus. The evolution of the dust jets, i.e., their onset and cutoff, follows the diurnal variation of insolation, with activity always prominent over the directly illuminated portions of the nucleus. The diurnal variation of dust activity with insolation, probably affecting the topmost few centimeters of the insulating nucleus subsurface, alludes to the importance of water sublimation in enabling the release of the dust from the shallow depths. The diurnal cycle of water ice discovered by VIRTIS observations is evidence for the presence of water ice above the diurnal skin depth in the subsurface (De Sanctis et al. 2015); in fact, dust emission was observed simultaneously with water ice sublimation along the dawn terminator by VIRTIS as well as OSIRIS (Shi et al. 2016b).

In a diurnal cycle, sublimation of water ice leads to the retreat of the ice front during the daytime, thus explaining the absence of exposed water ice over the illuminated sur-

face. With the cease of illumination after sunset, the surface layers cool down quickly. As a result of low thermal inertia, residual warmth allows the water sublimation to continue from the subsurface. The vapor may not diffuse out and escape from the nucleus but, rather, recondense[i] in the cold upper layers and, in particular, at the surface. The surface ice formed overnight sublimates quickly once illuminated, but could be observed temporarily as a frost-line tracing the dawn terminator and attenuates towards the sunlit areas.

While it is clear that water ice must be present close to the surface layers, the depth of the ice front, characterized by the thickness of the dust mantle, during the daytime has yet to be determined. As shown in Sect. 5.3.4.2, the mantle thickness strongly influences the water sublimation in that it does not only restrict the diffusion of the vapor and hence the sublimation flux but also moderates the temperature of sublimation.

6.1 Observation

Dust activity originating from the night side of the nucleus has been observed on several comets in previous missions, such as 81P/Wild 2 (Sekanina et al. 2004), 9P/Tempel 1 (Belton et al. 2008, Farnham et al. 2013), and 103P/Hartley 2 (A'Hearn et al. 2011, Bruck Syal et al. 2013). It has been speculated that water outgassing could be responsible for the dust emissions close to the terminator (Farnham et al. 2013), while those deep into the night side were likely triggered by activity of more volatile species (Belton et al. 2008).

Night-side dust activity on 67P had been captured by OSIRIS on multiple occasions since February 2015 from a heliocentric distance of about 2.5 AU inwards. One mini-outburst in the Imhotep region hours before dawn on March 12, 2015 probably involved the sudden release of super-volatiles, such as CO or CO_2 (Knollenberg et al. 2016). More frequently, the activity was detected near the dusk terminator. Fig. 6.1a shows the first detection of such dust emission from the shodowed nucleus surface in Ma'at (Shi et al. 2016a). Dust jets manifest themselves as faint plume(s) of enhanced brightness against dark background, either (optically) thin dust coma or nucleus surface in shadow.

Source of jets The dust jets shown in Fig. 6.1 arising from the shadowed nucleus cannot have originated from the illuminated foreground. The apparent source or origin of the jet is the point along the plume from which the dust particles are illuminated by sunlight. That is, the apparent source corresponds to the minumum altitude of illumination from the shadowed nucleus surface (Fig. 6.2). For simplicity, let us assume that a jet is projected as a straight ray emanating from the apparent source on the image. The determination of the jet source can be accomplished by determining

- position of the apparent source, and
- direction of the jet (passing the apparent source).

[i]The rigorous term describing the phase change from gas to solid states of materials is "deposition"; however, the phenomenon is referred to as "recondensation" here with little risk of confusion on account of its popularity in cometary science.

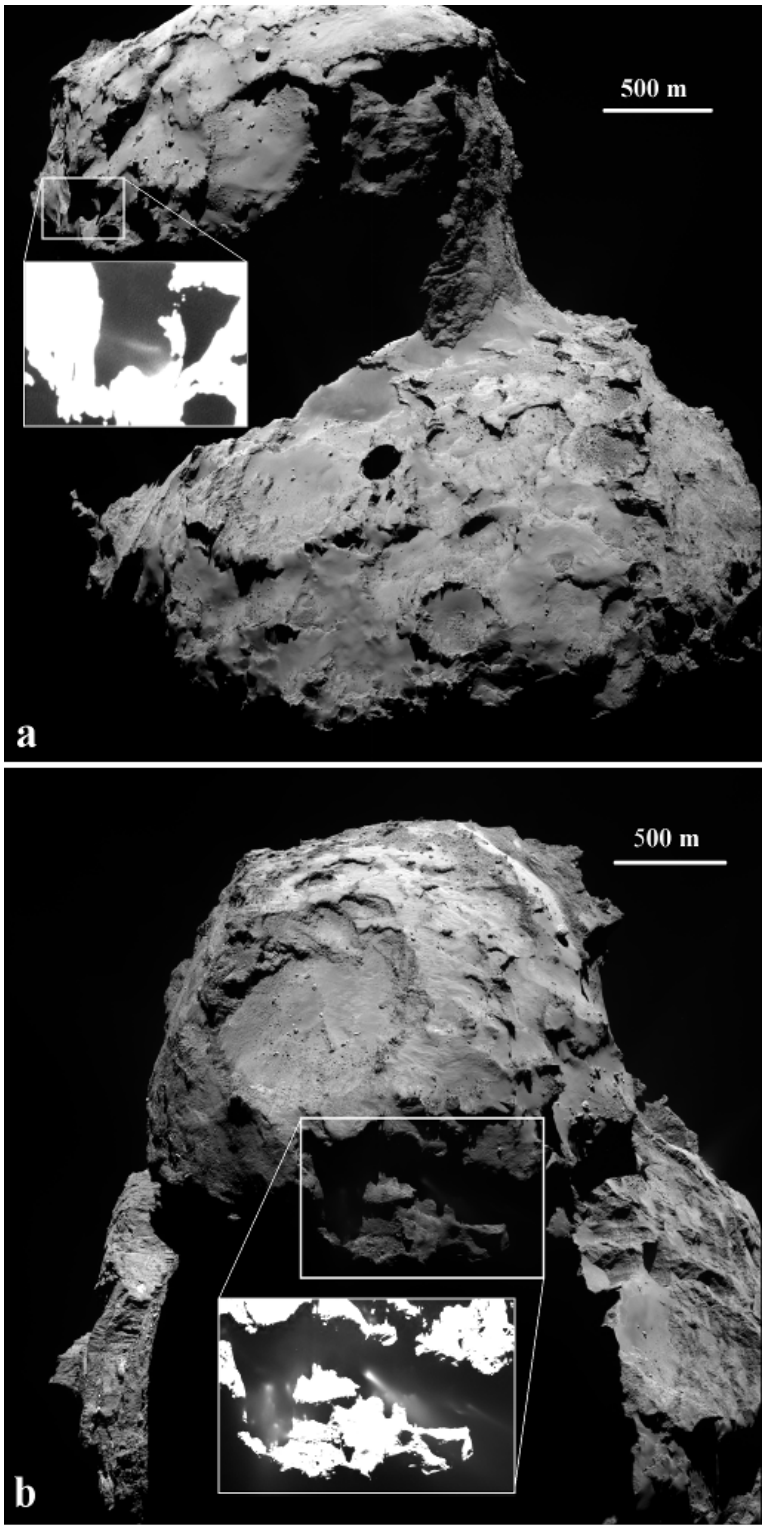

Figure 6.1: Observations of sunset jets. **a**. The earliest observation of a sunset jet from the Ma'at region captured by OSIRIS NAC on Feb. 28, 2015, at the heliocentric distance of ~2.2 AU. **b**. Clusters of sunset jets from the Ma'at region observed by NAC on Apr. 25, 2015, at the heliocentric distance of ~1.8 AU.

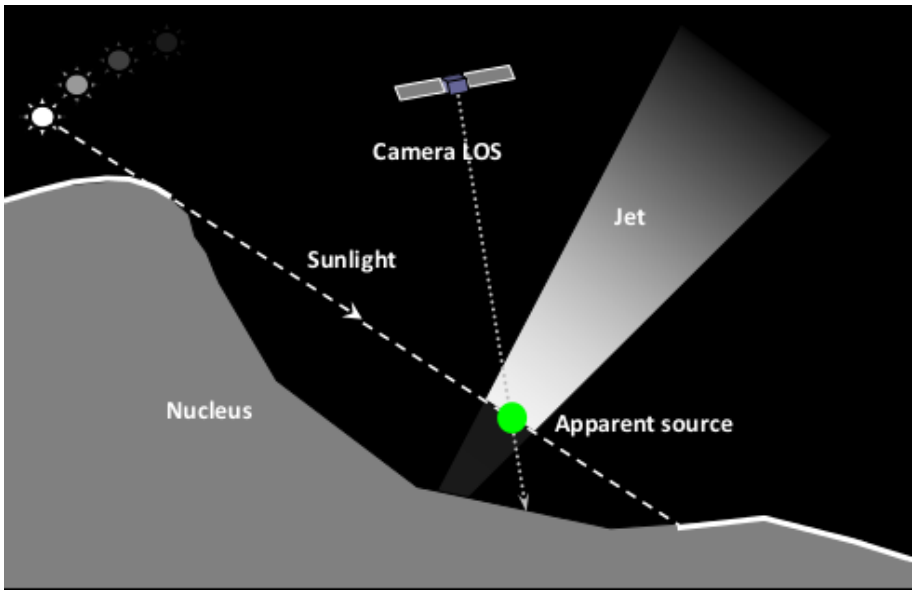

Figure 6.2: Schematic illustration of the observational condition for a sunset jet originating from the shadowed nucleus. This figure is reproduced from Fig. 4 in Shi et al. (2016a).

The position and orientation of the camera is known. The directional vector from the camera to the apparent source is given by Eq. (3.5), i.e.,

$$\mathbf{u}_{\mathrm{S}}^{[\mathrm{C}]} = \frac{1}{\sqrt{(pX_{\mathrm{S}})^2 + (pY_{\mathrm{S}})^2 + r_{\mathrm{f}}^2}} \begin{pmatrix} pX_{\mathrm{S}} \\ pY_{\mathrm{S}} \\ r_{\mathrm{f}} \end{pmatrix} , \tag{6.1}$$

with $X_{\mathrm{S}}, Y_{\mathrm{S}}$ being the pixel coordinates of the apparent source in the image. According to Eqs. (3.6) and (3.7), the equation of the line of sight towards the apparent source in the body-fixed frame of 67P is

$$\mathbf{l}_{\mathrm{S}} = \mathbf{r}_{\mathrm{C}} + l\,\mathbf{u}_{\mathrm{S}} , \quad \mathbf{u}_{\mathrm{S}} = \mathbf{R}_{[\mathrm{C}]}^{[\mathrm{BF}]} \mathbf{u}_{\mathrm{S}}^{[\mathrm{C}]} , \tag{6.2}$$

where l measures the distance from the camera. The distance of the apparent source, l_{S}, has yet to be determined. The intersection of the line of sight with the visible nucleus surface is subsequently determined by Eq. (3.8) as $r_{1,\varkappa}$. Recall that the apparent source corresponds to the minimum altitude from the nucleus surface above which the jet is illuminated. Therefore, l_{S} can be determined by locating decrementally from $r_{1,\varkappa}$ the first point along $\mathbf{l}_{\mathrm{S}}$ out of the shadow. Therefore, the position of the apparent source with respect to the body-fixed frame of 67P is obtained as,

$$\mathbf{r}_{\mathrm{S}} = \mathbf{r}_{\mathrm{C}} + l_{\mathrm{S}}\,\mathbf{u}_{\mathrm{S}} . \tag{6.3}$$

The sunset jets in the image of Fig. 6.1b are denoted in Fig. 6.3a in reference to a local shape model (Preusker et al. 2015). The apparent sources are assumed to correspond to the peak intensity along the jet profile or the projected orientation of the jet. All apparent sources are close to the ground with altitudes lower than 40 m (see Fig. 6.3d for a

sideview of the source area illustrating the low altitudes of apparent sources). The height of the shadows results from the topographic variations of the adjacent landscape. For example, a cluster of jets are located within a valley shadowed by a mild ridge along the western rim (Fig. 6.3c). In addition, the altitude of the apparent source increases locally with the elapse of time after sunset; for example, the latest [ii] jet to be distinguishable by the time of observation originated in a small shallow concavity immediately after sunset (#8 in Fig. 6.3a). The apparent source was about ~2 m from the nucleus, the lowest for all sunset jets identified in Fig. 6.3 (Shi et al. 2016a).

At first glance, the direction of a jet is difficult to resolve. Each jet (any two distinct points thereat) specifies a plane of sight, or jet plane, that encompasses the focal point of the camera (Fig. 6.3b). With minimum constraint, the direction of the jet varies about the apparent source within the jet plane and rotates from the observer (camera) to the line of sight towards the apparent source. The intersection of the jet plane with the nucleus indicates a trail of *possible* jet sources. Other constraints can be introduced to refine the orientation of the jet, however. Firstly, it is assumed that the jet is not intercepted or disconnected by topography; secondly, the jet should not be partially illuminated, i.e., shadowed along its trajectory. The imposition of the constraints rules out portions of the trails as possible sources for the jet (Fig. 6.3b,c).

With extended trail of possible sources on the ground (Fig. 6.3c,d), the actual source of a jet is still ambiguous. Nevertheless, the ground sources are unlikely to wander far from the vicinity below the apparent source. This speculation can be statistically confirmed. The distribution of inclinations of the jet planes with respect to the nucleus surface is shown in Fig. 6.4 based on all observations analyzed in Shi et al. (2016a). The jet planes are predominantly perpendicular to the nucleus surface, and nearly none is strongly tilted ($< 50°$ or $> 120°$). The results are derived from observations under different viewing geometries that can be considered arbitrary with respect to the orientations of the jets. It follows that the jets are unlikely strongly tilted but nearly perpendicular to the nucleus surface in general.

The reader is referred to Shi et al. (2016a) for more details regarding the determination of the jet sources. For many observations, particularly those overlooking the nucleus, it is legitimate to assume that the ground sources are indicated by the apparent sources of the jets.

6.2 Observational constraint on depth of ice front

The eventual subsidence of sunset jets suggests a distinct diurnal variation of dust activity where water is the main candidate volatile species. As suggested in Fig. 5.19, while the surface temperature varies promptly with insolation, the temperatures in deeper layers change more moderately and inertly. If water ice is present in the subsurface, the sublimation flux and, thus, the dust activity might be sustained by warmths from the depths even when the surface has cooled off after dark. A critical constraint on the depth of water ice

[ii] "Latest" does not refer to the physical occurrence or evolution of a jet, but to its visual detectability against the shadowed nucleus.

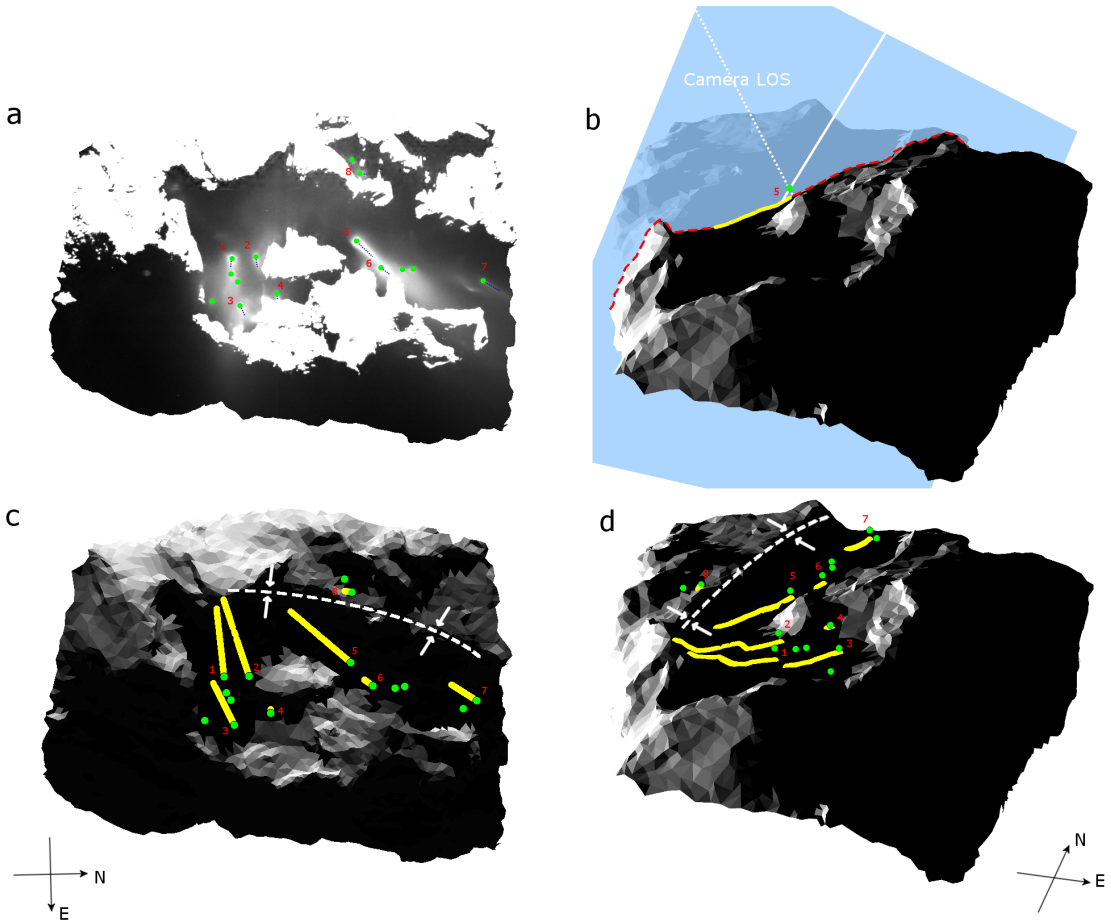

Figure 6.3: Apparent sources and corresponding trails of possible ground sources for the sunset jets shown in Fig. 6.1b. **a**. Apparent sources and projected directions of sunset jets are denoted by the green dots and dashed blue lines, respectively, in the original image. Jets are identified by numbers. **b**. Simulated oblique view of the local source area showing the altitude of the apparent source above the nucleus under realistic illumination condition. The camera line-of-sight towards the apparent source for jet #5 is indicated by the dashed white line. A possible direction of the jet is given by the solid white line. The yellow line indicates the trail of possible sources of the jet over the nucleus surface. **c**. Trails of possible sources for all jets with discernible projected directions are marked on the shape model. The dashed white curve delineates a ridge along the western rim of the valley where multiple jets were revealed by shadowing. **d**. The apparent sources and trails of possible ground sources of the jets in the same view as in panel **b**. This figure is reproduced from Fig. 5 in Shi et al. (2016a).

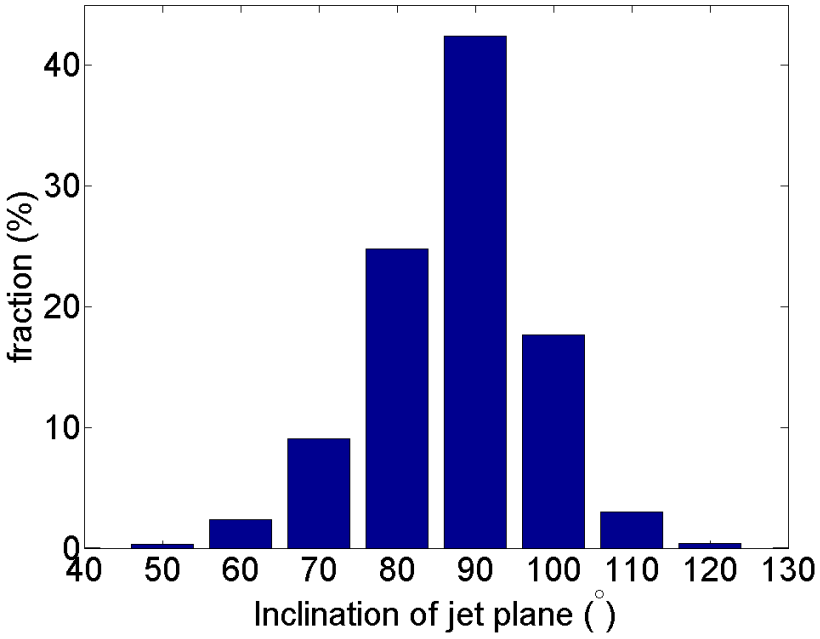

Figure 6.4: Distribution of the inclinations of the jet planes with respect to the nucleus surface along the trails of possible sources. This figure is reproduced from Fig. 6 in Shi et al. (2016a), using all observations of sunset jets.

in the nucleus subsurface lies with the duration of the dust activity and water sublimation beyond sunset.

6.2.1 Duration of dust activity beyond sunset

The jets in Fig. 6.1 had lasted for around 30 minutes after local sunset by the time of observations. A sequence of three images in Fig. 6.5 shows the attenuation of dust activity after sunset over the same area as in Fig. 6.1. When the source area is broadly illuminated and few sunset jets could be identified from the sporadic shadows. Two concentrations of jets become prominent about 40 minutes later arising from the valley out of sunlight. The jets have largely dissipated after another 40 minutes, by which time the entire source area had sunk into the night. These observations suggest that the dust activity in Ma'at could be sustained by at least half an hour but likely no more than one and half hours after sunset.

6.2.2 Timescale of heat propagation

It can be shown that the timescale of thermal diffusion, i.e., the time needed for the temperature variation to propagate to and from a certain depth, x, is given by,

$$\tau = \frac{x^2}{a}, \tag{6.4}$$

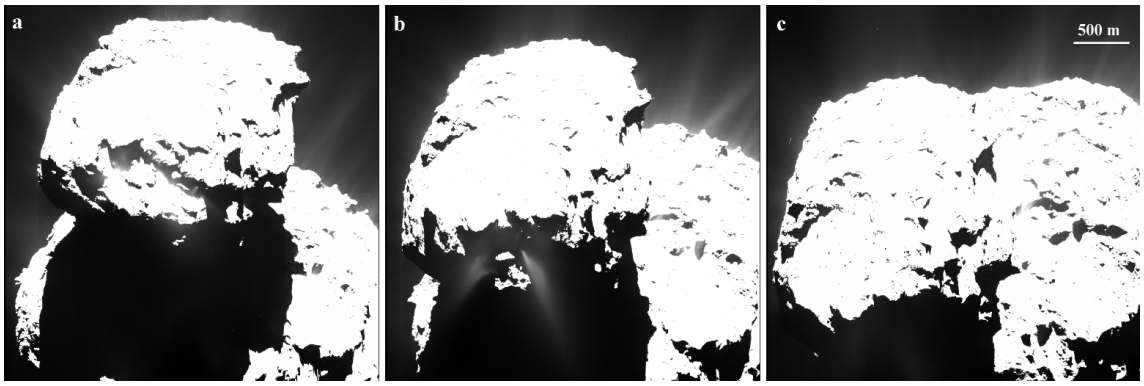

Figure 6.5: Sequence of three observations showing the attenuation of brightness of the sunset jets from the Ma'at region. The images were acquired every 40 minutes starting from UTC 05:07:07 on Apr. 25, 2015, at the heliocentric distance of 1.78 AU.

where a is the thermal diffusivity defined by Eq. (4.34). In order for the sublimation flux to respond to the diurnal heat wave of insolation, it is assumed here that the thermal timescale is similar to that of the (brightness) variation of the dust jets after sunset.

Although the thermal inertia over 67P was measured between 10 and 50 $\mathrm{W\,K^{-1}m^{-2}s^{1/2}}$ around September 2014, it is probably reasonable to consider a slightly higher value. This is justifiable because the sunset jets were observed later and from a heliocentric distance of less than 2.3 AU. The increase in temperature near the nucleus surface will likely contribute to the heat transport through the pore spaces via radiative heat transfer. The enhancement in the *effective* heat conductivity is temperature dependent and can be expressed as

$$\kappa_\epsilon = 8\sigma\epsilon\,\Lambda\,T^3\,, \tag{6.5}$$

where Λ is the mean free path of the photons. In case the porous medium comprises uniform, spherical particles, Λ can be evaluated as (Gundlach and Blum 2012)

$$\Lambda = 1.34\frac{1-\phi}{\phi}r_\mathrm{P}\,. \tag{6.6}$$

with r_d being the radius of the particles and ϕ the volume filling factor of the medium. For millimeter-sized particles (i.e., $r_\mathrm{d} = 0.5$mm) and a filling factor of ~0.5, the radiative component of the conductivity varies between 0.001 and 0.01 $\mathrm{W\,K^{-1}m^{-1}}$ for temperature ranging between 150 and 300 K, and thus could dominate the heat transport in the subsurface. In the simulation for the sunset jets, a median value of 0.005 $\mathrm{W\,K^{-1}m^{-1}}$ will be adopted.

According to Eq. (4.34), $\kappa = 0.005$ $\mathrm{W\,K^{-1}m^{-1}}$, $\rho = 500$ $\mathrm{kg\,m^{-3}}$, and $c = 1000$ $\mathrm{J\,kg^{-1}K^{-1}}$ yields $a = 1\times10^{-8}$ $\mathrm{m^2s^{-1}}$. Letting $\tau = 1$ hour, one finds that water sublimation from $x \sim 6$ mm could potentially be sustained one hour after cutoff of insolation at the surface. Evidently, when the intensities of water sublimation and the induced dust activity exhibit diurnal variations, water ice should be present above the diurnal skin depth of $\sqrt{at_\mathrm{P}/\pi} \approx 1$ cm for the rotation period of $t_\mathrm{P} \approx 45000$ s of the nucleus (Huebner et al. 2006).

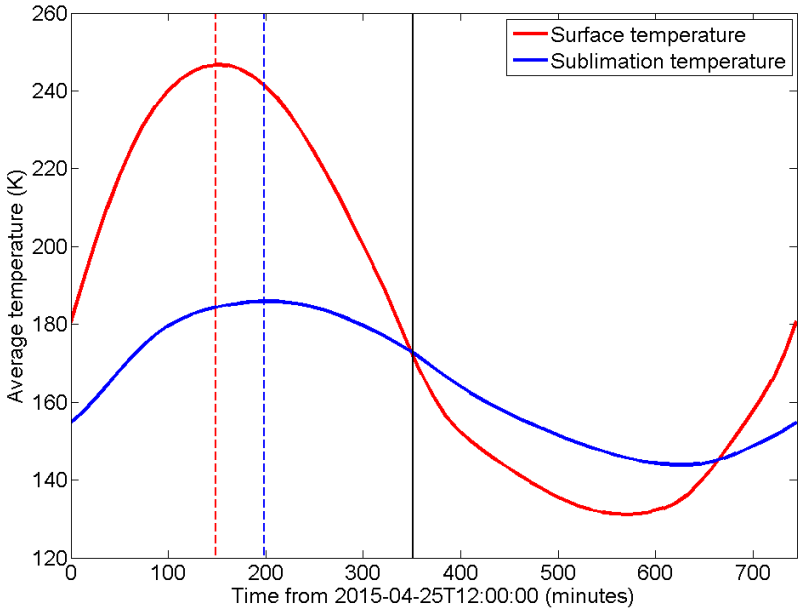

Figure 6.6: Diurnal variation of surface and subsurface temperatures over the source area of the subset jets observed in Fig. 6.1b. The red curve traces the variation of the area-averaged surface temperature; the blue curve is for the average temperature at the depth of 6 mm where we assume water sublimation occurs. The dashed red and blue lines mark the epochs of the respective maximal temperatures. The black line marks the time when the temperatures are equal. This figure is reproduced from Fig. 8 in Shi et al. (2016a).

Hereafter, $X = 6$ mm is adopted for the depth of the water ice front in Eq. (4.25) for the dust mantle thermal model. As a preliminary validation of the model parameterization, the diurnal variations of temperatures at the surface and the ice front averaged over the source area where the sunsets in Fig. 6.1b were observed on Apr. 25, 2015 are presented in Fig. 6.6. In general accordance with the result in Fig. 5.19, the comparison reveals that the temperature variation at a depth of 6 mm is more moderate than and lags behind the variation of the surface temperature. The delay of ~50 minutes as indicated by the offset between the peaks of the respective curves is consistent with the analytic approximation of 1 hour.

6.3 Effect of thermal lag and terminator of inactivity in subsurface

The distributions of surface temperature and the subsurface temperature at the depth of 6 mm over the source area of sunset jets in Fig. 6.1b at the time of observation are derived via the dust mantle model. The sharp variation of the surface temperature from below 140 K in the nightside to about 280 K under illumination compares to a more subdued range between 160 K and 190 K in the subsurface beneath the insulating dust mantle (Fig. 6.7a,b). In the nightside, the subsurface temperature decreases with distance (and, hence,

time) into the shadow and could remain warmer than the surface layers by ~20 K in the vicinity of the terminators (Fig. 6.7c,d). Indeed, all sunset jets were sourced from the vicinity of terminators, more likely from the subsurface than the surface.

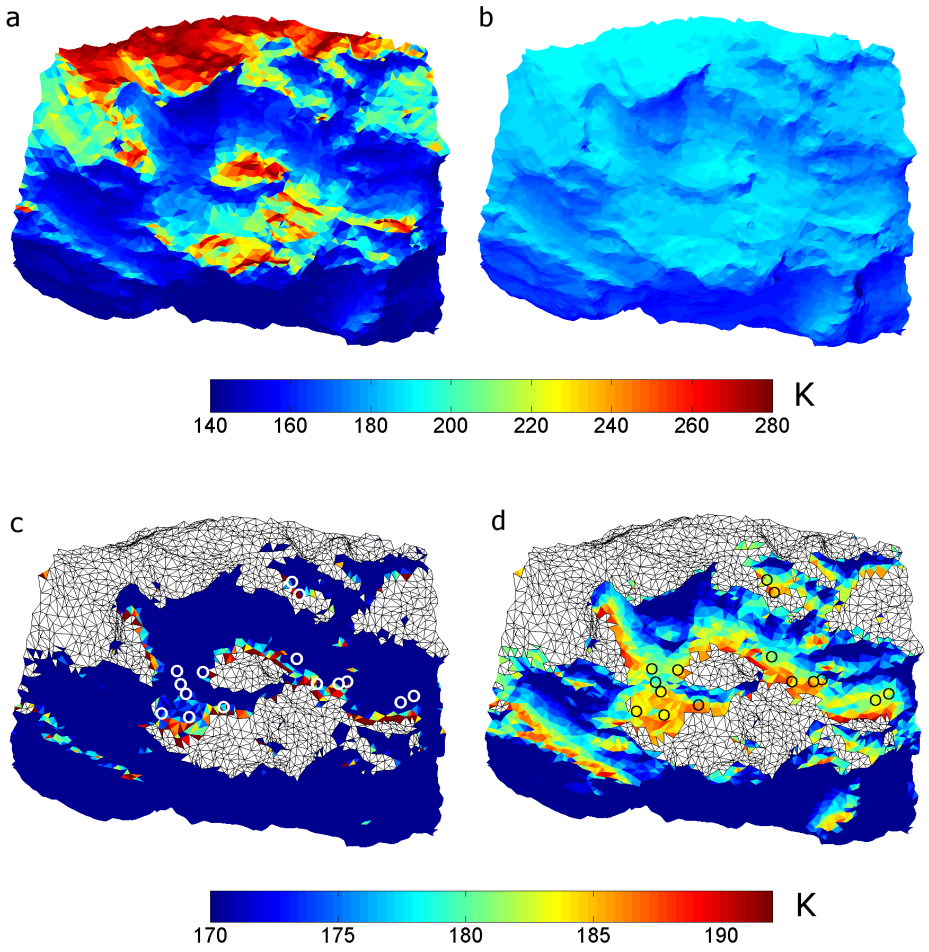

Figure 6.7: Distribution of surface and subsurface temperatures over the source area of sunset jets in Fig. 6.1b at time of observation. **a**. Surface temperature. **b**. Temperature at the sublimating ice front at depth of 6 mm. **c**. Surface temperature from the nightside as in panel **a** but with a confined colorbar. The illuminated portions are marked by white facets; the sunset jet sources are indicated by white empty circles. **d**. Subsurface temperature from the nightside as in panel **b** but with a confined colorbar. The sunset jet sources are marked by dark circles filled in white. This figure is reproduced from Fig. 9 in Shi et al. (2016a).

6.3.1 Necessary condition for dust activity driven by sublimation of water ice

The conditions of dust activity are introduced in Ch. 4. On the one hand, the minimum sublimation flux to lift a dust particle against gravity is recalled (and adapted) from Eq. (4.12) as

$$\underline{Z} = \frac{X}{2}\frac{\rho_\mathrm{d} g}{v_\mathrm{T}} \quad (\mathrm{kg\,m^{-2}s^{-1}})\,, \tag{6.7}$$

with ρ_d and v_T denoting respectively the density of the particle and the thermal speed of the escaping vapor. The particle radius, r_d, in the original expression is substituted by the half-thickness of the dust mantle, $X/2$, to roughly accommodate the ejection of the entire mantle. Adopting $g = 2 \times 10^{-4}$ m s^{-2} for local gravity and $v_\mathrm{T} = 400$ m s^{-1}, one finds $\underline{Z} = 1 \times 10^{-6}$ kg m^{-2}s^{-1}.

The sublimation flux underneath the dust mantle given by Eq. (4.31) is used to derive the minimum temperature of water sublimation, $\underline{T}$, that enables dust ejection against gravity, i.e.,

$$\underline{Z} = \Psi \mathscr{F} Z^{\text{H-K}}_{(X)}(\underline{T})\,. \tag{6.8}$$

The above equation constitutes an implicit function that is solved via the Newton-Raphson method to yield a minimum temperature of $\underline{T} \approx 175$ K.

The cohesion between the dust particles is much more difficult to overcome than is gravity. Recalling Eq. (4.1), the minimum vapor pressure to exceed the tensile strengths between aggregates is (Skorov and Blum 2012),

$$\underline{P} = P_\mathrm{t} = 1.6 \phi r_\mathrm{d}^{-\frac{2}{3}} \quad (\mathrm{Pa})\,, \tag{6.9}$$

with ϕ being the volume filling factor of the dust mantle and r_d the radius of dust particles in millimeters (Eq. 4.1). The tensile strength thus decreases with particle size. For millimeter-sized dust aggregates packed with $\phi = 0.5$, the tensile strength is about 1 Pa. It is reasonable to assume that the state of local equilibrium is achieved where the real gas pressure traces the saturation vapor pressure defined by Eq. (4.18), i.e., $P \approx P_\mathrm{V}$. The maximum subsurface temperature from the nightside is ~190 K that corresponds to a maximum vapor pressure of ~0.5 Pa, which is insufficient to overcome the cohesion between aggregates. The deficiency of vapor pressure exists for smaller dust particles. Decreasing the particle size in the simulation via the dust mantle model decreases the sublimation flux and, therefore, increases the subsurface temperature. However, the increasing tensile strength between the smaller aggregates invariably exceeds the saturation vapor pressure.

As it turns out, the mechanisms to break off cohering dust particles remain largely unresolved. The solution to this open question is far out of scope of this work. It seems that the constructive approach is to neglect the obstacle of cohesion, but consider only the effect of gravity on the condition of dust activity. In doing so, Eq. (6.7) constitutes a necessary condition for dust ejection.

6.3.2 Terminator of inactivity

In effect, $\underline{T}$ (or $\underline{Z}$) defines the border between two regions in the subsurface: one where $T \gtrsim \underline{T}$ so that dust activity is *possible*, and elsewhere with $T < \underline{T}$, too low a temperature to enable any dust ejection from the nucleus. This border can be conceptualized as a terminator of *inactivity* (TOI) in the subsurface to be distinguished from the terminator of illumination on the surface.

A sequence of six images in Fig. 6.8 shows the evolution of the TOI defined by $\underline{T}$ = 175 K and that of observed jet activities during the sunset process. The data analysis are described in detail in Shi et al. (2016a). The observations, obtained during the same week of Apr. 25, 2015, spanned multiple comet rotations with similar sub-solar latitude. They are ordered in Fig. 6.8 according the local time, and show the successive decrease of the illuminated surface areas. The sunset jets were scarce when the shadowed area was limited (Fig. 6.8a), but gradually increased in number as the shadow expanded (Fig. 6.8b,c). The jets were always sourced from within the TOI (and beyond the terminator of illumination), i.e., in the region of possible activity where the subsurface temperatures remained above 175 K. Over time, the jet sources migrated with the possibly active region as the TOI trailed the illumination terminator (Fig. 6.8b,c,d,e). After more than one and half hours after sunset, the possibly active region nearly diminished trailing the cease of illumination, and sunset jets became indistinguishable (Fig. 6.8f).

The determination of TOI illustrated in Fig. 6.8 is model dependent. In particular, different $\underline{T}$ would result for different particle sizes and mantle thickness that govern the sublimation rate. However, the thermal lag has been constrained by observed duration of the sunset jets that determines distance of the TOI from (behind) the illumination terminator and, hence, the breadth of the possibly active region. It is expected that the demonstrated co-evolution of the sunset jets and the region of possible activity is qualitatively authentic.

6.4 Summary

Observing and characterizing the diurnal evolution of activity and, in particular, that from the night side was among the specific scientific objectives of OSIRIS (see Sect. 4.1.10 and Sect. 4.2.2.3 in Keller et al. 2007). The sunset jets had been frequently observed on 67P inbound from 2 AU. These dust jets were consistently sourced from the dust covered terrains, rather than the fractured surfaces, and were in most cases detected near the dusk terminators and rarely far into the night side. The temporal evolution of the dust emissions exhibited a pattern associated with activity of water ice gradually subsiding after illumination had ceased. The dust mantle thermal model (Sect. 4.1.2) was applied to examine the effect of thermal lag in the nucleus subsurface on water ice sublimation and dust ejection. It is assumed that the duration of the dust jets after sunset, roughly one hour, should be comparable to the time it would take for heat wave from insolation to propagate to the depth of the ice front. With a low thermal inertia of 50 $\mathrm{W\,K^{-1}m^{-2}s^{1/2}}$ of the subsurface, it is estimated that the sublimation of water ice occurred from about 6 mm below the surface. Therefore, water ice must be present from a very shallow depth inside the nucleus and respond to the change of insolation on a diurnal basis.

There exists an alternative dusk terminator in the subsurface that defines the boundary between active and latent portions of the surface. The shape of this *terminator of inactivity*, or TOI, is essentially determined by the distribution, or more exactly, the contours of subsurface temperatures. The TOI always trails the terminator of insolation at the surface. The sublimation of water ice at temperature of 175 K would sustain an outgassing flux sufficient to eject dust particles up to a few millimeters in size against gravity of the 67P nucleus. It is found that the ground sources of the sunset jets never strayed beyond the

Figure 6.8: Evolution of the TOI and observed jets along the sunset process illustrated on the shape model. The illuminated surface is masked by white facets. The region of possible activity is in red; the region of inactivity is in dark gray. The TOI is the border between the two regions and corresponds to $\underline{T}$ = 175 K. This figure is adapted from Fig. 10 in Shi et al. (2016a).

TOI, where the water outgassing had effectively ceased to occur.

The role of tensile strength on the condition of dust activity is unknown and could not be resolved by this analysis. The pressure of water vapor in the subsurface clearly fell below the cohesive forces between the dust grains, as estimated by Skorov and Blum (2012), Blum et al. (2014). Although it would be convenient to resort to the activity of supervolatiles that might enhance vapor pressure (Shi et al. 2016a), the evidence of their presence over the northern hemi-nucleus is almost absent. The possibility of diurnal outgassing of supervolatiles (in order to explain the evolution of sunset jets) would by itself require a dedicated thermal analysis that is far beyond the scope of this study.

7 Seasonal Erosion and Restoration of Dust Cover on 67P

This chapter is a concise summary of material presented in Hu et al. 2017, Astronomy & Astrophysics, 604, A114. Figures herein are reproduced from those in the original publication, with permission © ESO.

Prior to the advent of Rosetta rendezvous with 67P, the first and only clear evidence of surface evolution of the cometary nucleus was on 9P/Tempel 1, the target of the Deep Impact mission that was later revisited by the Stardust spacecraft during its extended mission (Stardust-NExT) (A'Hearn et al. 2005, Thomas et al. 2013, Veverka et al. 2013). In more than six years between the flybys, both of which took place around the perihelion passage of the comet, a number of scarps had receded visibly and the rims of several depressions had been smoothed out. These hitherto unique observations of surface changes signify the role of cometary activity in reshaping the appearance of the nucleus.

Capturing surface changes on 67P and understanding the mechanisms of their occurrence was at the heart of mission for OSIRIS (Keller et al. 2007, Sierks et al. 2015). Thanks to the high resolution of the cameras and duration of the exploration, most of the nucleus surface had been recurrently observed in great detail. Surface changes had been noted before the perihelion passage of 67P. A prominent event occurred in the smooth basin of Imhotep between the end of May and early July, 2015, roughly two months before the perihelion, when several near-circular scarps emerged and expanded due to either collapse or removal of the surface layers at least several meters in thickness (Groussin et al. 2015b). Escarpments exhibiting similar development had been noticed earlier on in the Hapi region (Davidsson et al. 2016a), which appeared to be the source area of the strongest dust activity until northern autumn equinox (Lara et al. 2015).

7.1 Observation

7.1.1 Erosion of dust cover before perihelion

Hints of nucleus evolution were noted more frequently after 67P reached a heliocentric distance of 2.5 AU in early 2015. Most of the observed (and, in some cases, suspected) surface changes before perihelion occurred over the dust deposits covering roughly 80% of the total surface area in the northern hemi-nucleus of 67P.

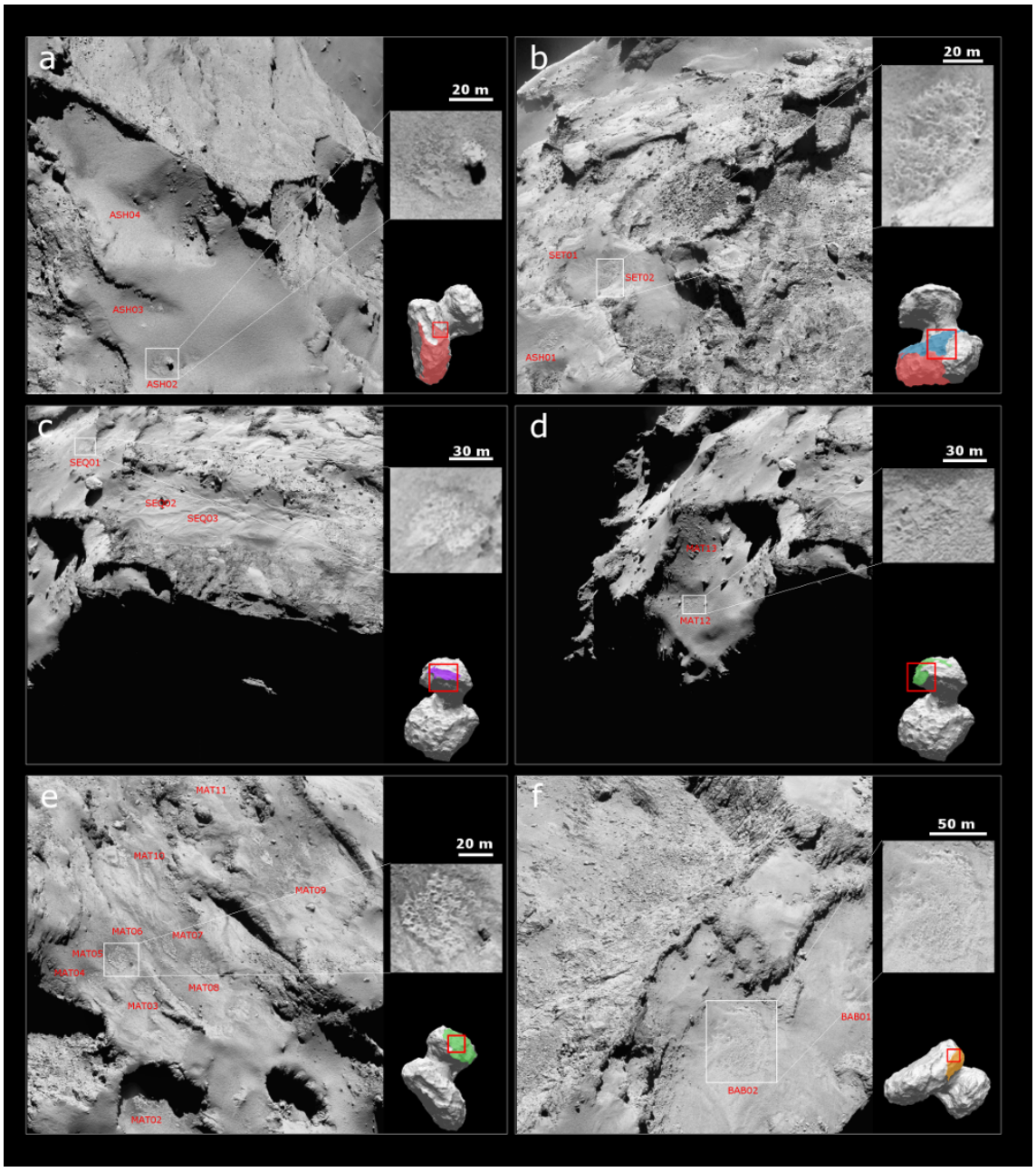

Figure 7.1: Honeycomb features observed by OSIRIS during the Rosetta flyby of 67P on March 28, 2015, in Ash (**a**); at the border between Ash and Seth (**b**); at the border between Serqet and Ma'at (**c,d**); in Ma'at (**e**); and in Babi (**f**). The view of each image is indicated by the red rectangle with respect to the nucleus. Regions are distinguished by color, i.e., Ash in red, Seth in blue, Serqet in purple, Ma'at in green, and Babi in orange. Nomenclature is according to Tab. 7.1.

7.1.1.1 Honeycombed surface textures

During a flyby of Rosetta that reached as close as 15 km from 67P nucleus on March 28, 2015, the NAC of OSIRIS collected a series of images with pixel resolutions of 0.5 m or better over the nucleus surface. Despite the often dissimilar observing conditions in

illumination and viewing geometry, the images in comparison with earlier observations revealed numerous fresh features over the entire northern hemi-nucleus. As shown in Fig. 7.1, many features are distinguished as rough or pitted surface patches, somewhat resembling the honeycombed pattern, typically several tens up to hundreds of meters in expanse (Shi et al. 2016a). The locations of some distinct "honeycomb" features are provided in Tab. 7.1.

Table 7.1: Nonexhaustive list of honeycomb features detected in OSIRIS images

Name	Region	Latitude (°)*	Longitude (°)*
ASH01	Ash	27.1	212.2
ASH02		46.6	110.2
ASH03		45.4	105.9
ASH04		42.7	99.0
BAB01	Babi	15.4	74.7
BAB02		20.9	80.9
MAT01	Ma'at	33.6	25.5
MAT02		32.5	19.5
MAT03		28.2	15.9
MAT04		26.3	18.1
MAT05		26.2	16.1
MAT06		26.5	13.7
MAT07		27.2	12.6
MAT08		28.8	11.3
MAT09		27.6	3.8
MAT10		21.8	11.4
MAT11		17.8	3.8
MAT12		41.3	328.4
MAT13		34.7	328.2
SEQ01	Serqet	26.3	335.1
SEQ02		21.2	321.9
SEQ03		18.3	318.7
SET01	Seth	25.4	219.2
SET02		23.2	219.1

* Defined with respect to the Cheops reference frame (Preusker et al. 2015).

Ma'at The earliest appearance of honeycombs was in January 2015. Two features, MAT01 and MAT02, emerged on the floors of two adjacent shallow depressions that had been covered by a smooth layer of deposits six months earlier (Fig. 7.2). It can be ruled out that the contrast in the images was due to difference in observing conditions. Because several boulder-like blocks nearby, roughly comparable to the newly discovered pits in size, can be easily identified in both images, the emergence of the honeycombed texture should not be a visual coincidence.

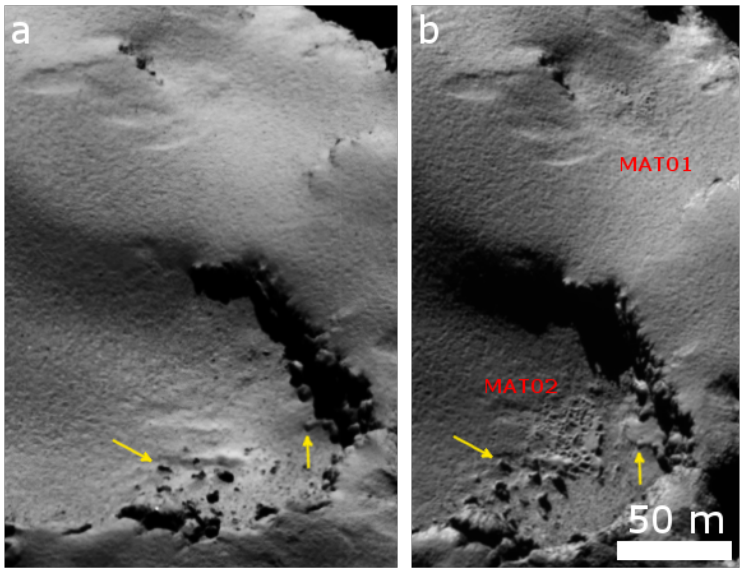

Figure 7.2: Comparison of surface texture around honeycombs MAT01 and MAT02 between September 2014 (**a**) and January 2015 (**b**). Some common features are marked by yellow arrows as landmarks. The dust deposits located between MAT02 and the cliff has been partially removed, forming a distinct valley. The scale bar applies to both panels. Nomenclature is as given in Tab 7.1.

The three observations in Fig. 7.3 span six months from late September 2014, and exemplify the development of surface roughness in the area around features MAT03-07. In September 2014, the dust deposits were prevalent, giving rise to a uniform and granular surface texture, except for some large consolidated outcrops (Fig. 7.3a). By mid-February 2015, the area appeared widely but unevenly eroded (Fig. 7.3b). The excavation of the material was particularly evident within some gentle-sloped depressions where the local surface textures would further evolve and roughen to form the honeycombs (Fig. 7.3c).

Border of Ash and Seth Similar evolution of the surface roughness was observed in other regions. Some prominent changes occurred at the border between the Ash and Seth regions. The extensive, undulating dust deposits masking the substrate topography in September 2014 started to display more varied surface textures by mid-February 2015 which were clearly still in development (Fig. 7.4a,b). Numerous shallow concavities had taken shape as indicated by the lower brightness of various scattered surface patches, some of which were marked by shaded edges or rims. By March 2015, the honeycomb features, ASH01, SET01 and SET02, had become distinguishable by their irregular, heavily pitted texture, accompanied by many other changes such as depressions that probably had evolved from the formerly more shallow concavities (Fig. 7.4c).

Babi Two honeycombs in the Babi region, BAB01 and BAB02, also emerged from the previously dust-covered terrains (Fig. 7.5). The area had not experienced perceptible changes, e.g., of more than 0.5 m in dimension (or the pixel resolution of the images), by December 2014. Some localized excavation or erosion of material, however, must have

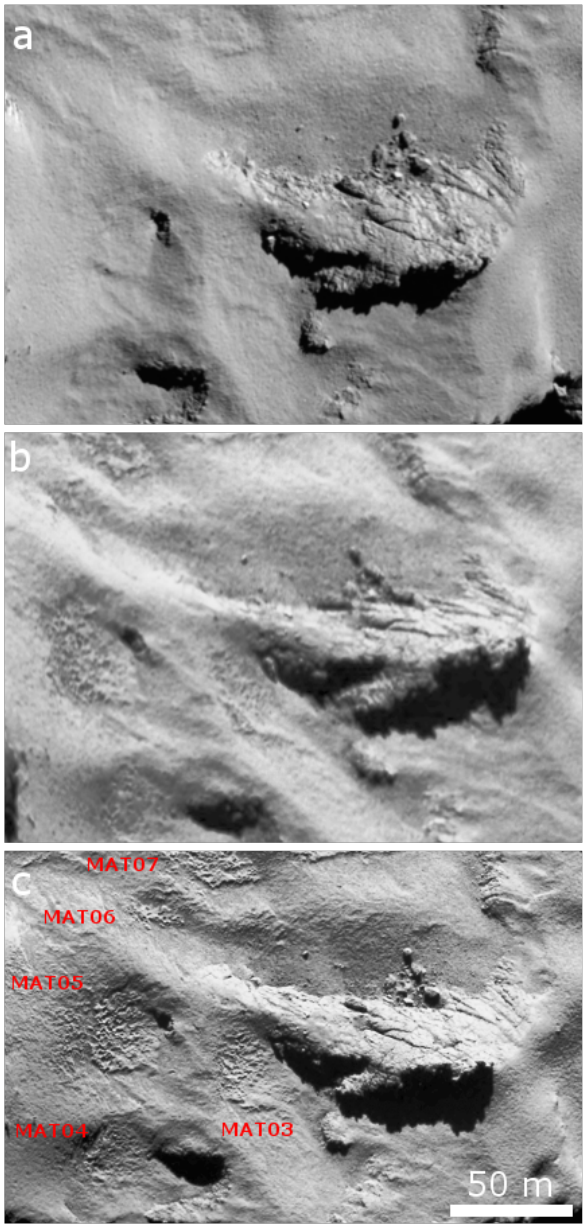

Figure 7.3: Comparison of surface texture around MAT03-07 from September 2014 through March 2015. **a.** Smooth deposits were prevalent on September 20, 2014. **b.** Surface roughness had increased at various locations by February 14, 2015. **c.** Honeycomb features were distinguishable on March 28, 2015. Nomenclature is as given in Table 7.1.

occurred before mid-February 2015, when several concavities of from decimeters up to meters in size had appeared (Fig. 7.5c,d). Significant surface changes had not occurred by this time. BAB01 and BAB02 probably developed quickly only afterwards.

Tri-border area of Serqet, Ma'at, and Nut Fig. 7.6 shows the erosion of the dust cover in the morphologically diverse area at the borders of the Serqet, Ma'at, and Nut

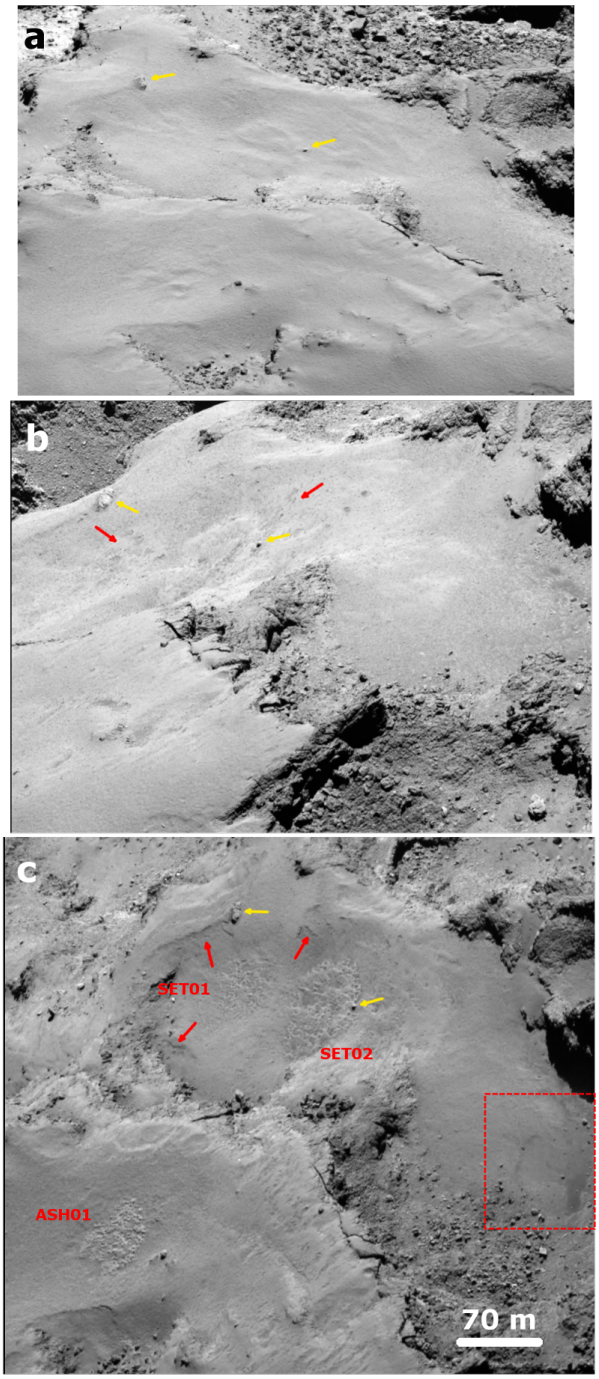

Figure 7.4: Comparison of surface texture around ASH01, SET01 and SET02 between November 2014 and the end of March 2015. **a.** Smooth deposits showed dune-like corrugations on November 11, 2014. **b.** Depressions had appeared in scatter over the area by February 14, 2015. **c.** Mature honeycombs were observed on March 28. 2015. Nomenclature is as given in Table 7.1. Several fresh scarps (red arrows) and a wide shallow depression (dashed red rectangle) represent other potential changes in the vicinity.

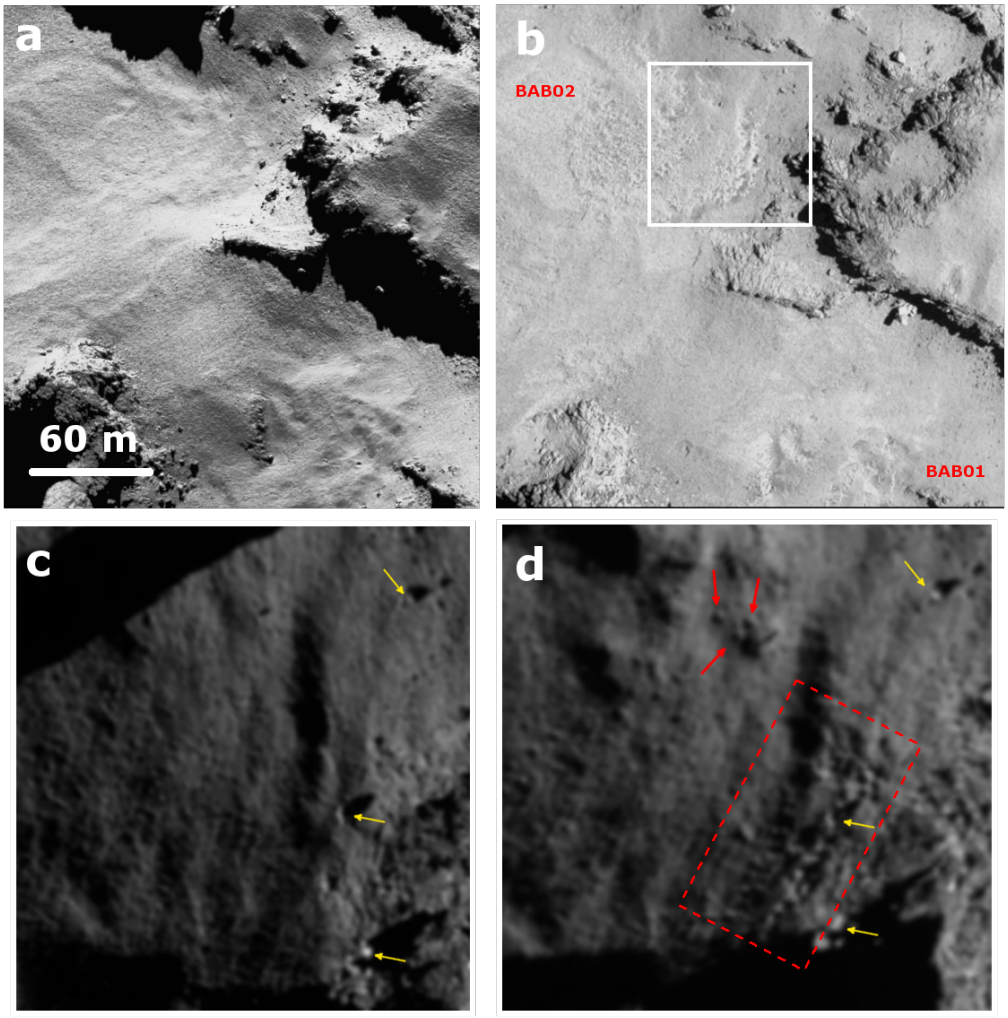

Figure 7.5: Comparison of surface texture around BAB01 and BAB02 between early October 2014 and late March 2015. **a.** Smooth dust deposits were prevalent over the area on October 4, 2014. **b.** Honeycombs were observed on March 28, 2015. **c,d.** Images taken on December 30, 2014, and February 14, 2015, show changes occurring on the perimeter of BAB02. The Sun is projected onto the lower left of the image plane in **c**,**d**. Some newly-formed depressions are indicated by red arrows. The surface texture within the rectangle of dashed red outline is rougher in the latter image. Yellow arrows indicate common boulder-like features as landmarks. Nomenclature is as in Tab. 7.1.

regions before late March 2015. A distinct honeycomb feature, SEQ02, was apparently formed over the previously undulating, dune-like dust deposits. The boundary of SEQ02 was difficult to delineate, as the pitted texture of the feature seemed to disperse away (the same is true with SEQ03 in Fig. 7.1c). It is also worth noting that these changes were close to where the honeycombs MAT12 and MAT13 were located (Fig. 7.1d), suggesting that the erosion was anything but localized.

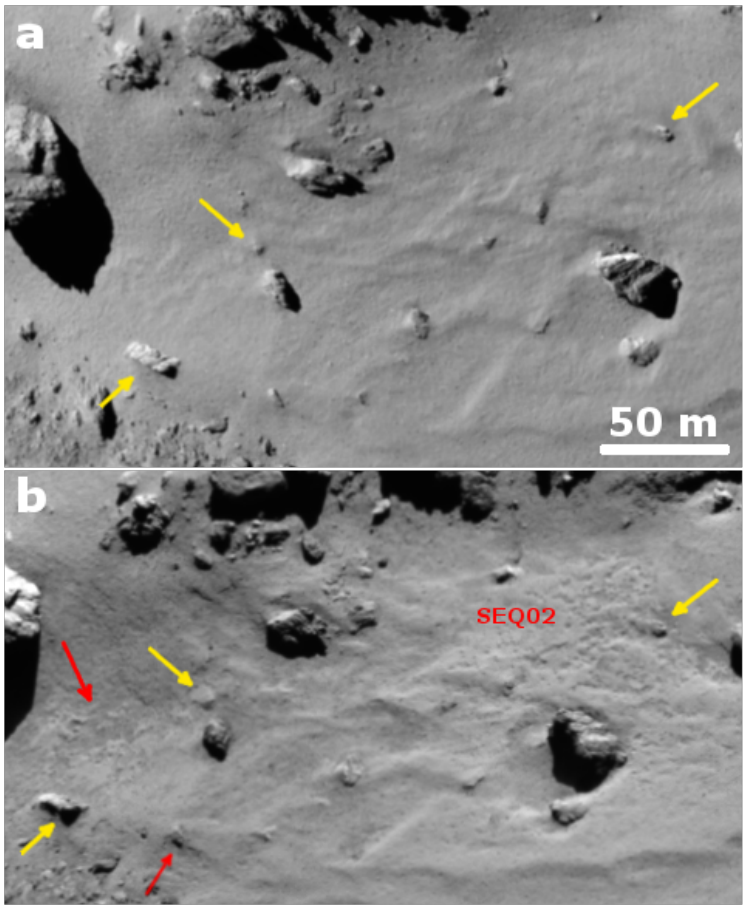

Figure 7.6: Comparison of surface texture around SEQ01 and SEQ02 between September 30, 2014 (**a**) and February 14, 2015 **b**. Nomenclature is as given in Table 7.1.

7.1.1.2 Evolving pitted deposits

While the honeycombs in Fig. 7.1 signified surface evolution between September 2014 and late March 2015, similar features, such as the pitted dust deposits, had already been present in many areas that may or may not be of the same origin (Thomas et al. 2015a, Mottola et al. 2015). The pitted deposits near the border of Ma'at and Maftet seemed to have persisted at least until late March 2015 (Fig. 7.7a). The area had undergone significant changes during perihelion, as several patches of deposits had been visibly removed or displaced one year later (Fig. 7.7b,c,d,e). The changes most likely occurred shortly before perihelion, months after the development of the honeycombs, because this area is at far lower latitudes where insolation peaked later.

7.1.1.3 Exposed sharp substrate

The erosion of the dust deposits was also indicated by the exposure of abrupt, sharp substrate. The emergence of some rugged outcrops before late March 2015 shown in Fig. 7.8 had resulted from the exhaustion of the overlying dust deposits. Around the same time, the previously dust-covered area surrounding the honeycomb feature MAT05 displayed a

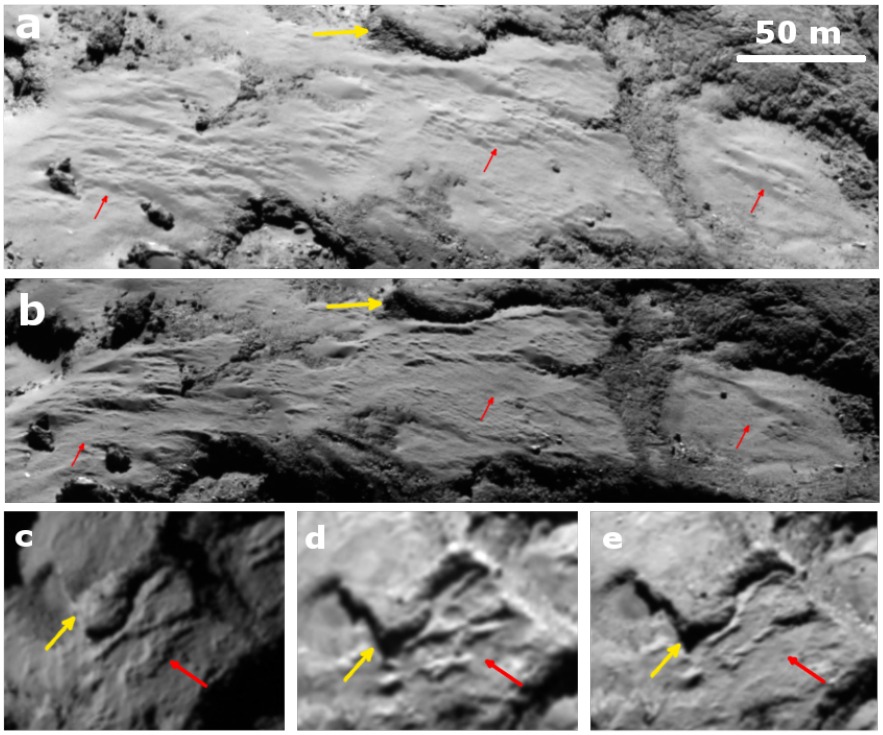

Figure 7.7: Changes in the pitted dust deposits in Ma'at bordered by Maftet. **a.** Pitted deposits distinct at the end of March 2015. **b.** Several pitted patches had been smoothed out by May 2016. **c, d, e.** Sequence of three images taken in January, July, and November 2015, respectively, showing the evolution of pitted deposits (indicated by the red arrow)

rutted texture probably indicating subsurface topography (Fig. 7.9). The removal of the surface layers also left behind a trench tracing the edge of an escarpment that had been previously veiled by the dust cover. The retreat of the surface in another area in the Ma'at region revealed a substrate scarp and the edges of various boulder-like blocks nearby (Fig. 7.10).

7.1.1.4 Scattered depressions

As probably evident from the changes around SEQ02 (Fig. 7.6), it may be difficult to distinguish a honeycomb feature from its surroundings by the pitted textures. The formation of decimeter to meter-sized depressions occurred prevalently over the nucleus and can be regarded as representing a distinct type of surface changes. These depressions were often formed more randomly and, therefore, did not result in clear-cut pitted patches as the honeycombs (Fig. 7.11). In most cases, the depressions emerged together with other types of changes noted above, such as uncovering of boulders and rough substrate (Fig. 7.12 and 7.13), and development of honeycombs (Fig. 7.14).

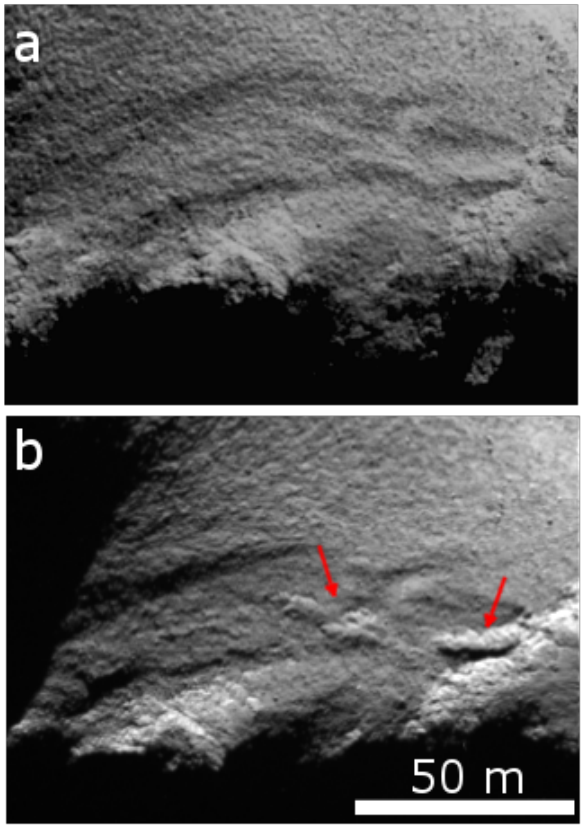

Figure 7.8: Emergence of an outcropping structure in Ma'at. Smooth dust deposits observed in early October 2014 (**a**) had thinned out, occasionally exposing the rugged surface (indicated by the red arrow) in late March 2015 (**b**).

7.1.1.5 Fresh scarps

Not all changes over the dust cover before perihelion manifested themselves as an increase of surface roughness. An illustrative example occurred in the Seth region (Fig. 7.15). In January 2015, two escarpments appeared over the terraces that had exhibited distinct smooth dust deposits until one month earlier. In less than two weeks, one of the scarps migrated by more than 10 m, whereas the other nearly disappeared. The phenomenon was comparable to the retreat of scarps observed in Imhotep shortly before perihelion and those in Hapi earlier on (Groussin et al. 2015b, Davidsson et al. 2016a). Similar changes, or the aftermaths thereof, were also detected in other areas of the nucleus around the same time (Fig. 7.16-7.18). In the Seth region close to the honeycombs SET01 and SET02, the dust cover around the debris field below a cliff had undergone a textural change over what could later be distinguished as a shallow depression with scarped boundaries (Fig. 7.16). A boulder-like feature in this area had disappeared. The mechanisms for the formation of scarps are debatable, as they may have resulted from either sinking or ejection of the surface layers. In one case, the formation of a scarp in the Nut region probably indicates the removal of dust deposits which exposed the boulder-like features nearby previously buried under dust (Fig. 7.18).

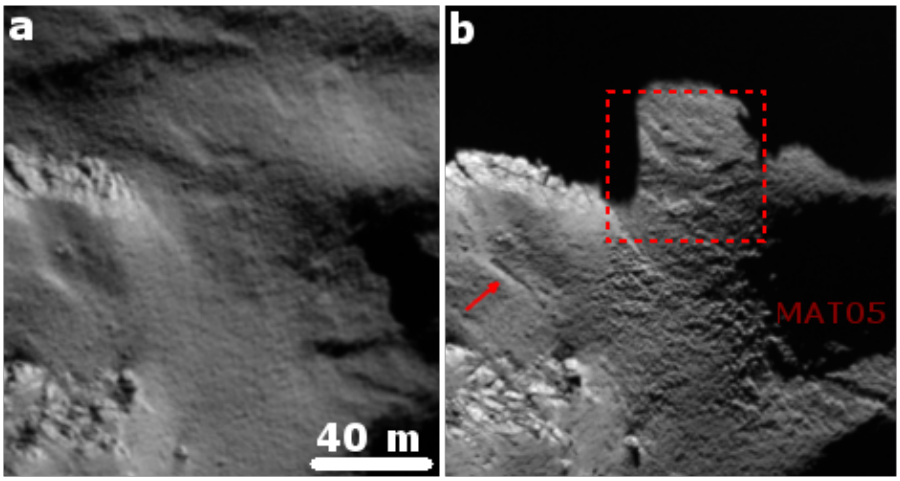

Figure 7.9: Rugged substrate topography exposed by the exhaustion of overlying dust cover between mid-November 2014 (**a**) and late March 2015 (**b**). The area in the red rectangle showed clearcut furrow-like structures indistinct earlier on. The roughness had increased around the honeycomb MAT05 (in shadow in **b**). A trench, indicated by the red arrow, had emerged along the foot of a scarp previously veiled by the dust deposits.

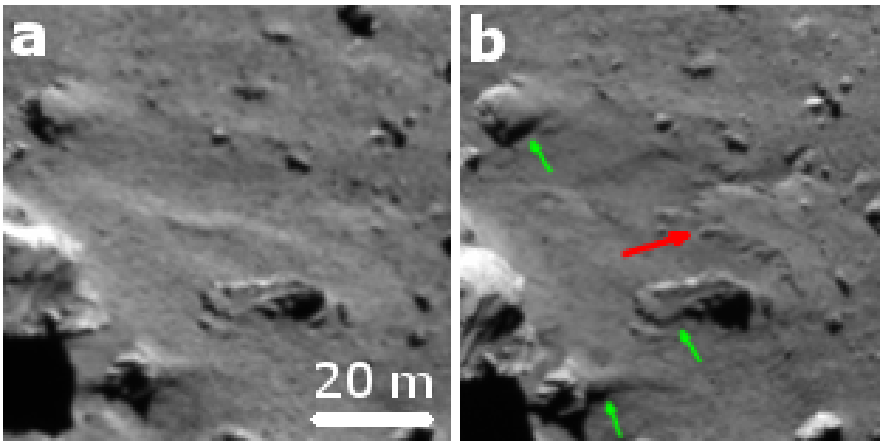

Figure 7.10: Scarp (indicated by the red arrow) in Ma'at occurred between early December 2014 (**a**) and late March 2015 (**b**). The sharp edges (indicated by the green arrows) of a few semi-buried boulders had been exposed by the retreat of the surrounding dust deposits.

7.1.2 Restoration of dust cover after perihelion

If the dust cover was formed by deposition of ejecta from elsewhere, it was probably composed predominantly of "large" dust particles, e.g., those at least one millimeter in size. Larger, heavier particles are less likely to be accelerated enough to escape from the nucleus and therefore more susceptible to deposition over the nucleus. Thomas et al. (2015a) showed that it was plausible that the northern dust deposits had originated from the Hapi region close to the North Pole, a prominently active area (Fougere et al. 2016a,b). An alternative scenario was described by Keller et al. (2015a) where the northern deposits

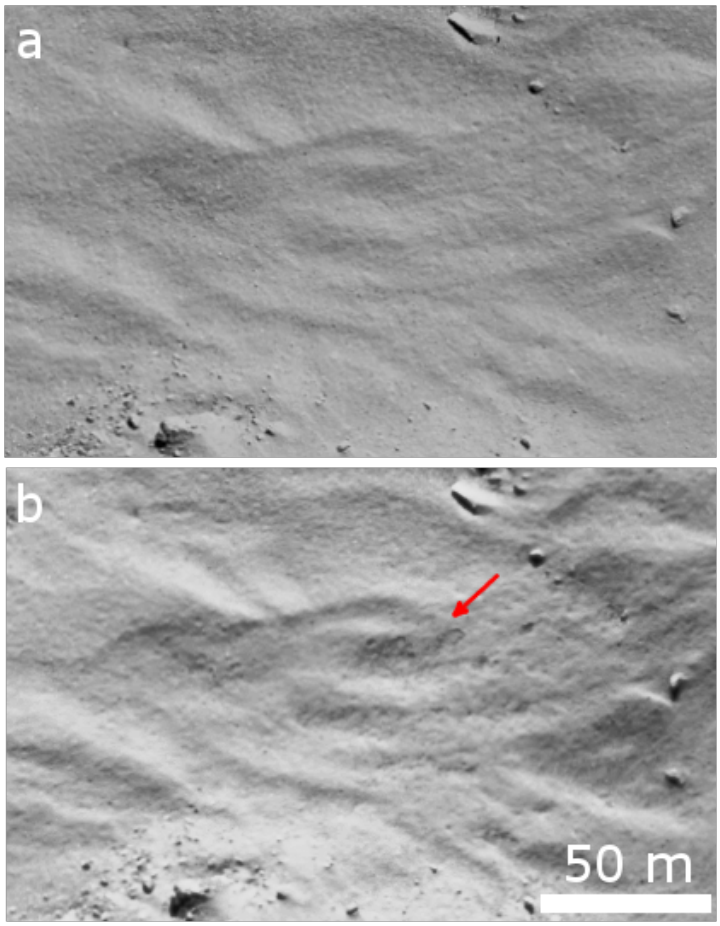

Figure 7.11: Emergence of scattered depressions (indicated by the red arrow) over the dune-like dust deposits located in Ma'at close to the border with Hatmehit. The earlier image was taken in November 2014 (**a**); the later image was from the end of March 2015 (**b**).

had been formed by ejecta from the south, always briefly but intensely illuminated every perihelion when the north was in polar night.

The honeycomb features that started to emerge from early 2015 vanished in OSIRIS observations after perihelion. The disappearance of some pronounced features in Ma'at is shown in Fig. 7.19. While the locations of many features could still be identified by the relief of the surface, the formerly distinct pitted pattern in contrast to the often more smooth surroundings gave way to the uniform, speckled texture that is reminiscent of the unaltered dust cover before perihelion. The observations indicate that the features most likely had been blanketed by renewed dust deposits that had been widely distributed over the flat terrains. The restoration of the dust deposits was a global phenomenon. The three large honeycombs, ASH01, SET01, and SET02, near the border between Ash and Seth regions had undergone the same transformation with pitted texture largely smoothed out (Fig. 7.20). Not far from the features, some small concavities along the foot of the higher terrace, revealed by the thinning of the dust before perihelion, were leveled with the surroundings exhibiting a uniform surface roughness.

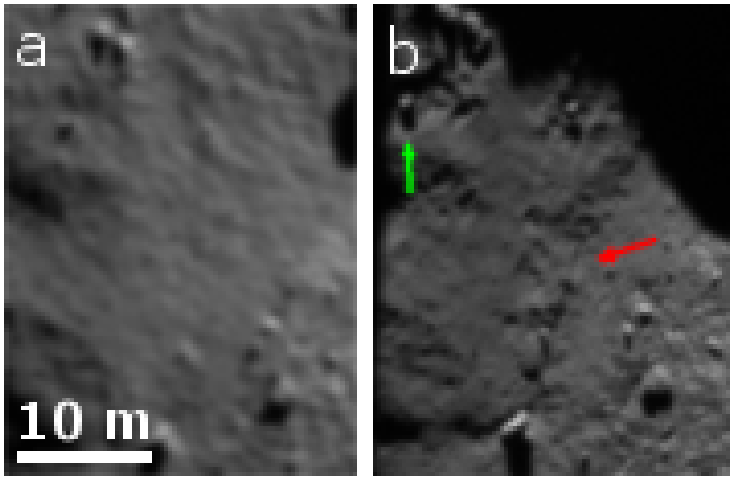

Figure 7.12: A chain of decimeter- to meter-wide depressions (indicated by the red arrow) emerged in Ma'at. **a** is from an image taken in November 2014; **b** is from the end of March 2015. Some boulder-like blocks had become more distinct. Dust deposits around the boulder (indicated by the green arrow) in the upper-left corner of the image(s) may have been excavated, with the boulder isolated at the bottom of the depression.

The scarps in Seth that showed significant development in early 2015 (Fig. 7.15) were masked by the new dust deposits after perihelion (Fig. 7.21). Several meter-sized monoliths protruded from the renewed dust and were probably displaced from the consolidated terrace walls and the adjacent talus field. Another convincing observation indicative of dust deposition during perihelion is in Fig. 7.22, showing a substrate scarp in Ma'at exposed in March 2014 veiled again by deposits one year later. The shape of the scarp had become obscure but still discernible, suggesting that the thickness of the new deposits should not exceed the order of one or a few meters.

7.1.3 Global distribution and timeline of surface changes

The locations of the surface changes described in Sect. 7.1.1 and 7.1.2 are indicated in Fig. 7.23 where the smooth, dusty regions and the more consolidated, rugged regions are marked in blue and red, respectively. The retreating scarps in the Imhotep region reported by Groussin et al. (2015b) are also included in the map. Evidently, the erosion had affected the entire northern hemi-nucleus of 67P before perihelion. The changes were concentrated at mid-latitudes between 20°N and 40°N. In particular, their distribution roughly outlines the global boundary between the northern dust-covered and the southern consolidated terrains (except for changes in Imhotep). Therefore, it is not surprising that the signs of erosion were most abundant where the northern dust cover thinned out towards the south and where the rugged substrate was easily uncovered.

The fact that all the erosive changes before perihelion had occurred (been detected) from early 2015 onwards suggests that they were essentially caused by intensifying insolation as 67P approached perihelion. A more detailed timeline for the detections of some changes is gathered as follows:

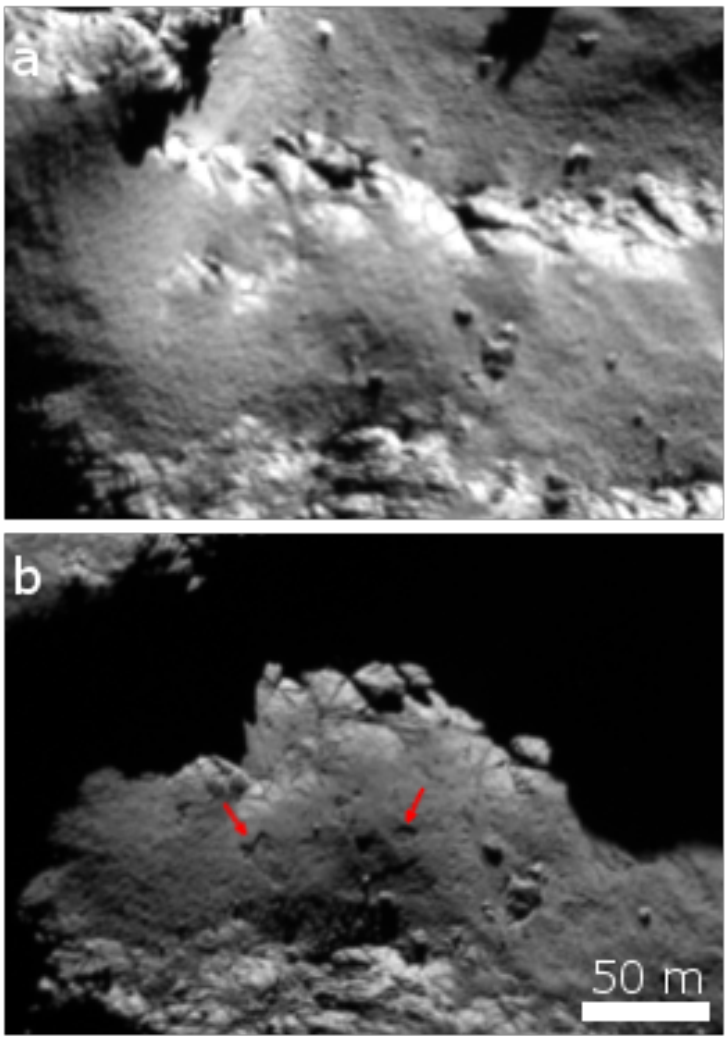

Figure 7.13: Emergence of scattered depressions (indicated by the red arrows) over the dust-covered terrace. Earlier image was taken in November 2014 (**a**); later image was from the end of March 2015 (**b**). Dust deposits appeared to thin out towards the edge of the terrace where underlying fractured materials were revealed.

1 The honeycombs MAT01 and MAT02 had occurred before late January 2015 (Fig. 7.2b), while the features MAT03-08 had taken shape by mid-February (Fig. 7.3b).

2 The honeycombs ASH01, SET01, and SET02 as well as some other changes in the surrounding area were visible by mid-February 2015 (Fig. 7.4b).

3 The area around BAB01 and BAB02 started to show visible development in February (Fig. 7.5c,d).

4 The removal of the pitted dust deposits at the border between Ma'at and Maftet occurred after the northern autumn equinox in early May 2015 (Fig. 7.7).

Referring back to Fig. 7.23, we find that:

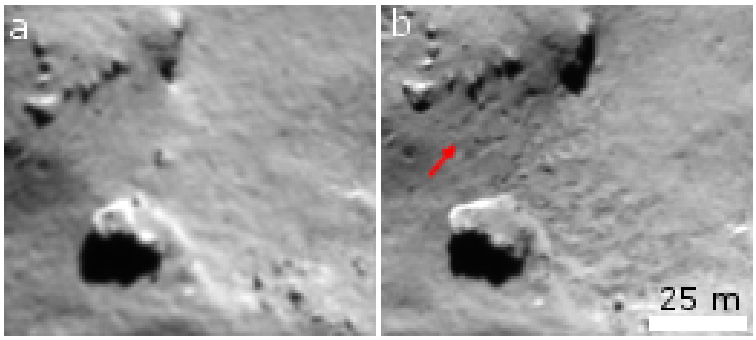

Figure 7.14: Scattered depressions (indicated by the red arrow) occurred next to what appeared to be a honeycomb feature in Ma'at. The earlier image was taken in November 2014 (**a**); the later image was from the end of March 2015 (**b**).

i MAT01, MAT02 were at ~33° N; MAT03-08 were at slightly lower latitudes of 25 ± 5° N.

ii ASH01, SET01, and SET02 were at the same latitudes as MAT03-08.

iii BAB01 and BAB02 were further south, at ~21°N and ~15°N, respectively.

iv The pitted deposits at the southernmost edge of Ma'at displaced shortly before perihelion were located near the equator.

Though the precise timing of the development of changes proved difficult, a comparison of the timeline and the distribution of changes suggests that they likely developed in succession, with the changes further south occurring later. Thus, it is conceivable that the observed surface erosion had been driven by insolation as the sub-solar point moved towards the south.

7.2 Quantification of surface changes

All the observed (suspected) surface changes, namely, the excavation of pits, the exposure of substrate, etc., can be interpreted generally as variations of resolved surface roughness. In order to mitigate the impacts of illumination and viewing conditions on the detection of changes, the Shape-from-Shading technique, introduced by Rindfleisch (1966) which is reviewed in Sect. 3.3.1, can be applied to infer the local surface topographies from the images for comparison. It was shown in Sect. 3.3.2 that the roughness model derived via Shape-from-Shading could capture the essential roughness pattern of the surface. In general, it is difficult to compare directly two models due to inevitable errors in the absolute elevation determined from the variation of image brightness. However, there is little restriction on using the roughness model to simulate views of the surface texture under arbitrary illumination. Thus, the difficulty of comparing surface textures from different images can be alleviated by comparing a real image with the simulated view of the surface roughness model derived from a different image.

As an example, the change of surface roughness over the honeycomb feature MAT05 is illustrated in Fig. 7.24. The feature was articulate from an image taken on Mar. 28,

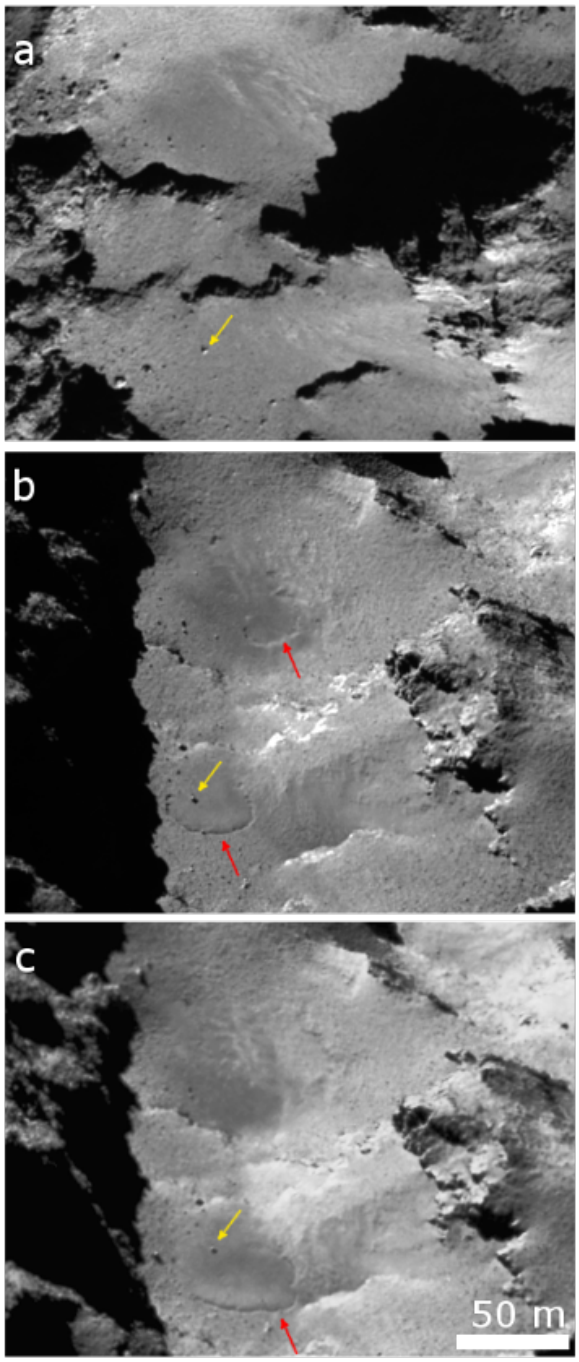

Figure 7.15: Development of scarps in Seth. **a.** Scarps were imperceptible in early December 2014. **b.** Two scarps (indicated by red arrows) were observed on January 23, 2015. **c.** One scarp had retreated by more than 10 m in the following two weeks; the other feature had become less distinguishable. The yellow arrows point to a common boulder in all images as landmark.

2015 (Fig. 7.3c). The surface roughness modeled via Shape-from-Shading can reproduce the overall shading pattern in the original image (the comparison of Fig. 7.24a,b is reproduced from Fig. 3.10). The feature could not be distinguished from an earlier image of

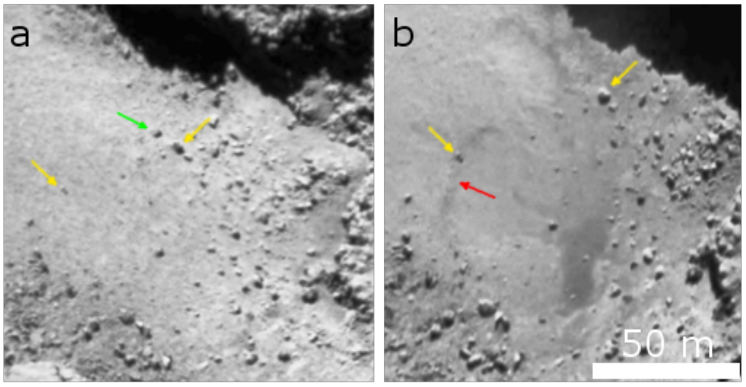

Figure 7.16: Scarp (indicated by the red arrow) in Seth occurred from November 2014 (**a**) until late March 2015 (**b**). The previously stippled texture gave way to the smoother texture over the floor of the scarp. One meter-sized boulder (indicated by the green arrow) appeared to have been removed. The yellow arrows point to common features in both images as landmarks.

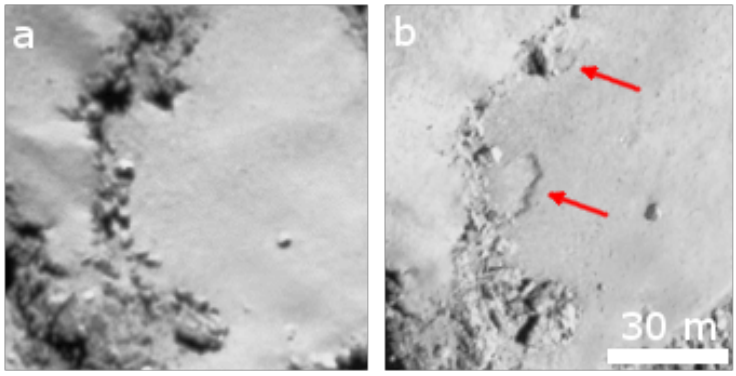

Figure 7.17: Scarps (indicated by the red arrows) in Babi emerged between October 2014 (**a**) and late March 2015 (**b**).

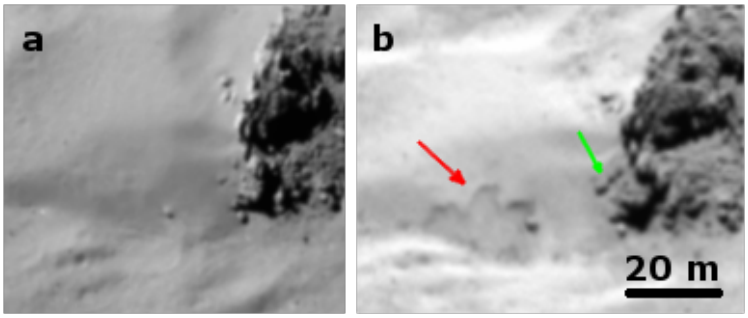

Figure 7.18: Paw-print scarp (indicated by the red arrow) in Nut occurred between mid-September 2014 (**a**) and late March 2015 (**b**). Note also a string of boulder-like blocks (indicated by the green arrow) that were apparently semi-buried by smooth deposits.

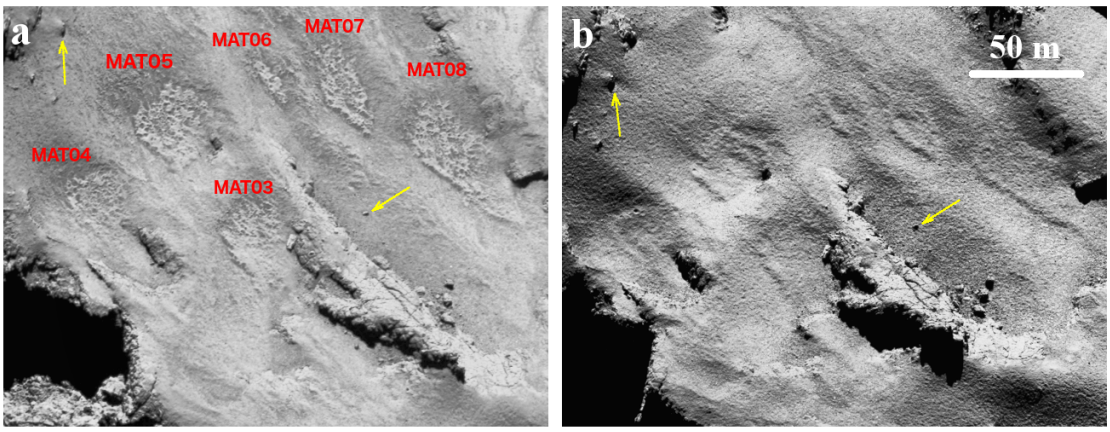

Figure 7.19: Renewed dust deposits covering the honeycombs MAT03-08 after perihelion. Image in panel **a** showing the features was obtained on Mar. 28, 2015, at the heliocentric distance of 2 AU inbounds; the one in **b** was taken on Mar. 14, 2016, at 2.6 AU outbounds. The honeycomb features are labeled in red; the yellow arrows indicate common landmarks in both panels.

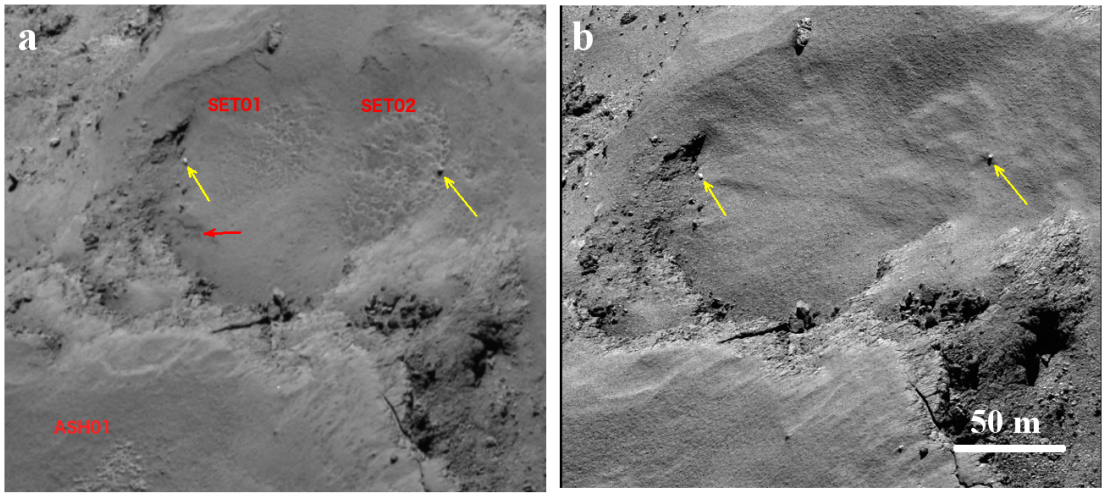

Figure 7.20: Renewed dust deposits covering the honeycombs ASH01, SET01 and SET02 after perihelion. Image in panel **a** showing the features is as in Fig. 7.4c, taken on Mar. 28, 2015, at the heliocentric distance of 2 AU inbounds. Image in **b** was taken on May 20, 2016, at the heliocentric distance of 3 AU outbounds. The honeycomb features are labeled in red; the yellow arrows indicate common landmarks in both panels.

the local area (Fig. 7.24c, cropped from Fig. 7.3a). However, the indication of surface change may be still not conclusive because the viewing and illumination conditions differ in the two images. The roughness model was used to simulate the appearance of the feature in the same view as in the earlier image under identical illumination (Fig. 7.24d). Because the simulated image clearly differs from the observation (Fig. 7.24c), the surface texture must have evolved in the time frame between the observations. Fig. 7.25 shows the results for feature ASH01 by the same analysis, confirming that the surface roughness

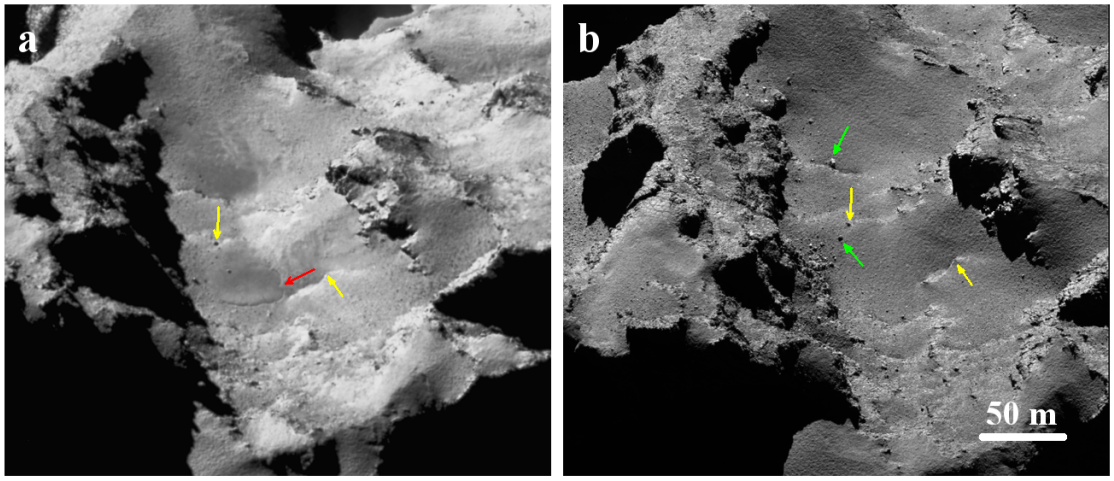

Figure 7.21: Renewed dust deposits obscuring the evolving scarp in Seth after perihelion. Image in panel **a** showing the feature is as in Fig. 7.15c, taken on Feb. 4, 2015, at the heliocentric distance of 2.4 AU inbounds. Image in **b** was taken on Apr. 28, 2016, at the heliocentric distance of 2.9 AU outbounds. The red arrow points to the scarp that had vanished, while the green arrows highlight fresh boulder-like structures; the yellow arrows indicate common landmarks in both panels.

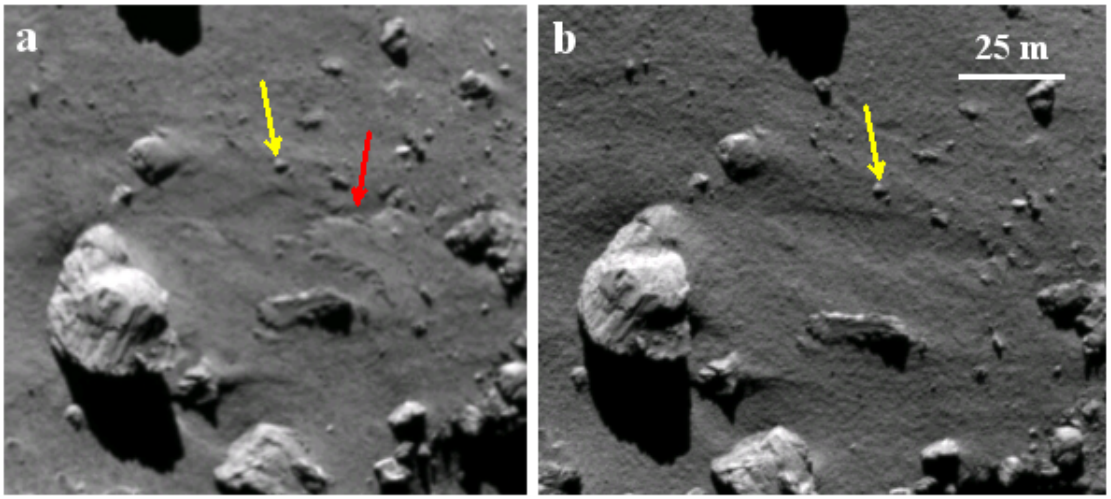

Figure 7.22: Renewed dust deposits obscuring the substrate scarp in Ma'at after perihelion. Image in panel **a** showing the feature is as in Fig. 7.10b, taken on Mar. 28, 2015, at the heliocentric distance of 2 AU inbounds. Image in **b** was taken on Jun. 6, 2016, at the heliocentric distance of ~3.2 AU outbounds. The red arrow points to the change; the yellow arrow indicates a common landmark in both panels.

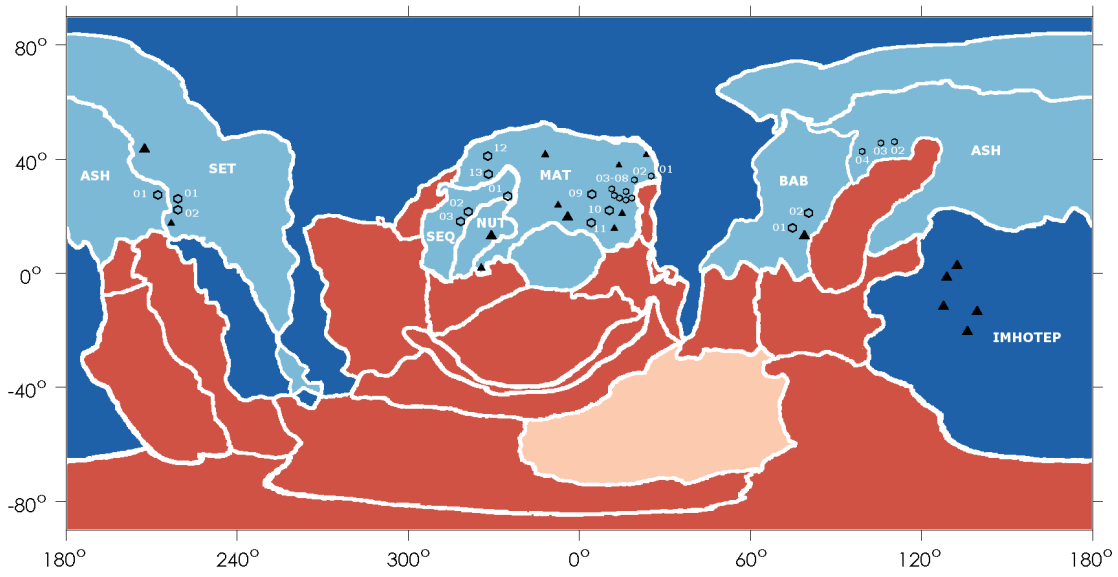

Figure 7.23: Map of surface changes in cylindrical projection. Morphological regions are defined according to El-Maarry et al. (2015, 2016). Dark blue regions correspond to smooth terrains; light blue regions contain distinct dust deposits; regions in dark or light red are consolidated. Note that dust deposits were present in Serqet (SEQ) which was diverse in morphology but categorized generally as weakly consolidated by El-Maarry et al. (2015). Honeycombs are indicated by hexagons. Other surface changes are marked by triangles.

had increased notably between November 2014 and March 2015.

7.2.1 Thickness of surface erosion

The amount of surface erosion at the locations of observed changes is of special interest to this study. Even though the detailed mechanisms of material loss are unclear, the activity of volatiles, and in particular, the sublimation of water ice is the most probable trigger for the dust ejection and thereby the surface erosion. This scenario is supported by the timeline and the distribution of the changes which had clearly responded to the intensifying insolation as well as the southward movement of the sub-solar point (Sect. 7.1.3).

With considerable uncertainty in the absolute elevation of the roughness model (which is difficult to assess), a direct comparison between two models (before and after the change had occurred) is not possible. However, provided that the changes before perihelion were (most probably) erosive in nature, in which case the surface had lowered, it is possible to quantify the *minimum* thickness of erosion reflected by the increase of surface roughness. The dashed red curve and the solid blue curve in Fig. 7.26 are the roughness profiles showing the undulations of the surface before and after erosion along the same path (as indicated by the blue line in Fig. 3.9a). The roughness profile before the change was assumed to *overlie* the one afterwards. The profiles were detrended to a certain degree to suppress any systematic variations. Note that the surface elevation before the erosion

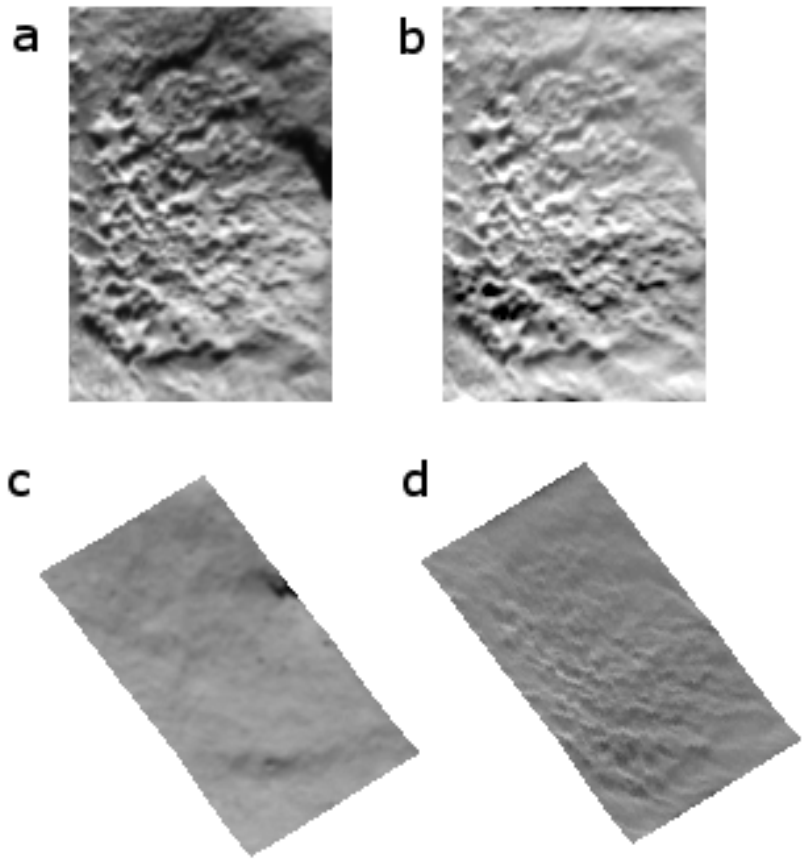

Figure 7.24: Synthetic views of the roughness model for feature MAT05 in comparison with the real images. **a.** Real image of the feature. **b.** Synthetic image of the feature in the same view and illumination as in **a**. **c.** Real image of the feature location before the feature was detected. **d.** Synthetic image of the feature in the same view and illumination as in **c**. The same brightness scale is used for the real and synthetic images for each comparison.

might be higher, which however could not be resolved in the present analysis. The mean difference between the two curves detrended up to degree four is about 0.5 m, which can be regarded as a robust yet conservative estimate for the minimum thickness of erosion.

Fig. 7.27 show the results for two other changes, namely the emergence of the outcrop and an underlying scarp in the Ma'at region (as shown in Fig. 7.8 and 7.10, respectively). The minimum thickness of erosion at both locations was similar to that in Fig. 7.26. It is indeed a necessary result of the analysis that at least the top (half-)meter of the surface had been eroded before perihelion in terms of order-of-magnitude, as this estimate must exceed the resolutions of the images used for change detection, i.e., 0.5 m per pixel (for the changes would not have been detectable otherwise).

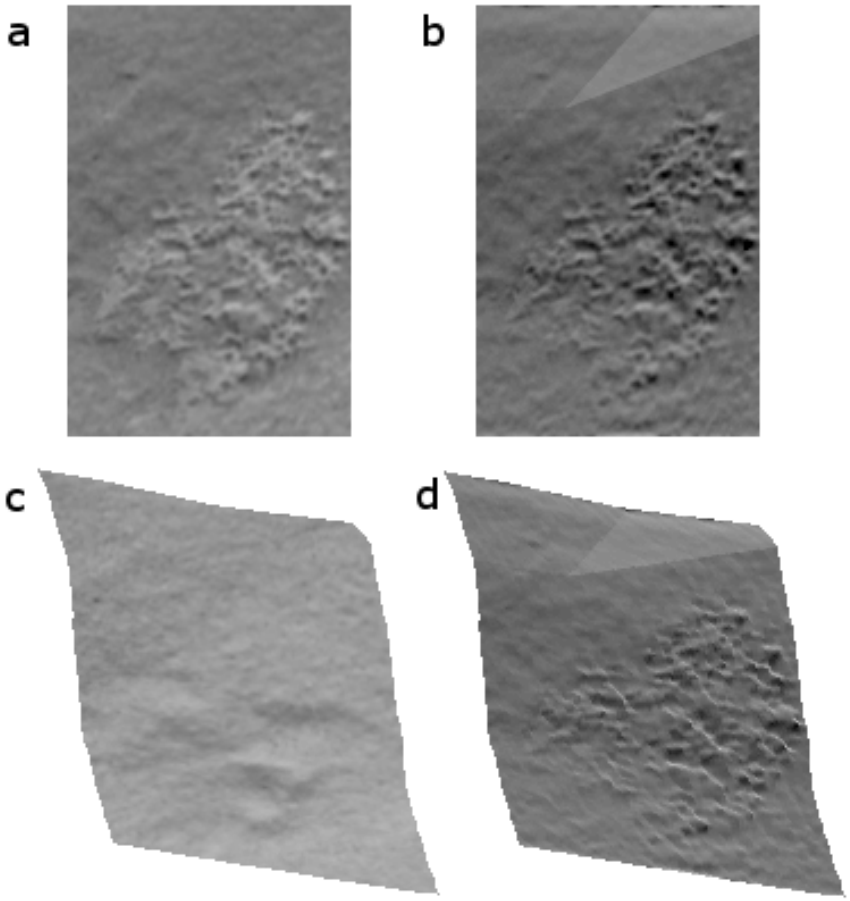

Figure 7.25: Synthetic views of the roughness model for feature ASH01 in comparison with the real images. **a.** Real image of the feature. **b.** Synthetic image of the feature in the same view and illumination as in **a**. **c.** Real image of the feature location before the feature was detected. **d.** Synthetic image of the feature in the same view and illumination as in **c**. The same brightness scale is used for the real and synthetic images for each comparison.

7.3 Thermal modeling of surface erosion around perihelion

Although it remains unclear how water ice sublimation could drive the surface erosion via dust ejection, e.g., the tensile strengths of the nucleus seem to be too strong to be overcome by vapor pressure of water (Skorov and Blum 2012, Shi et al. 2016a), water activity is the most likely, if not the only, candidate to have induced the changes. Hence, quantifying the strength of water activity in response to intensifying insolation before perihelion during the period in which surface erosion was observed is of vital importance to understanding the evolution of the nucleus.

An attempt to estimate the volume of the surface erosion was discussed in Sect. 7.2. Assuming that the mass density of the eroded material is known, e.g., $\sim 500\,\mathrm{kg\,m^{-3}}$ as for the bulk nucleus, we then have a reasonable estimate of the total mass loss for the

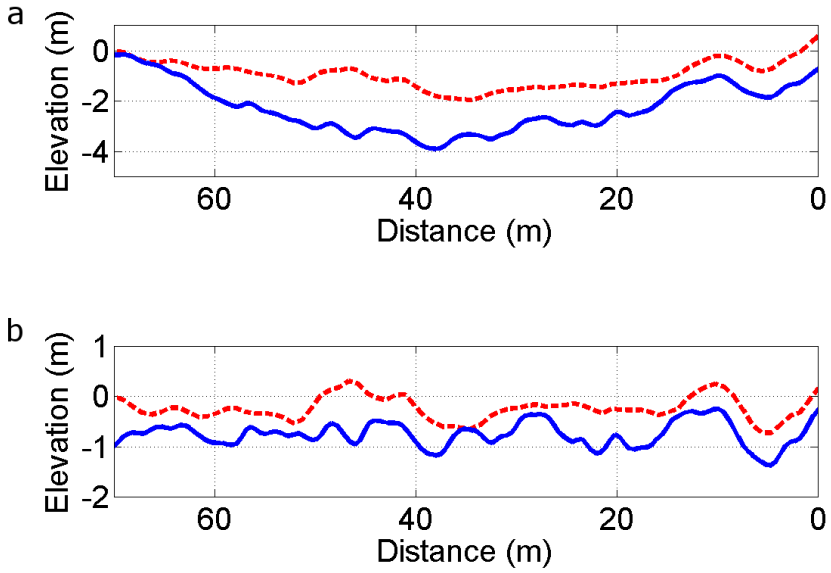

Figure 7.26: Roughness profiles over the honeycomb feature MAT05 on Septemper 20, 2014 (dashed red curve) and March 28, 2015 (solid blue curve), respectively. The path is as indicated in Fig. 3.9a. It is assumed that the red curve must overlie the blue curve. **a.** Profiles directly produced by shape-from-shading. The end points of both curves are registered to the shape model (Jorda et al. 2016), thereby removing the respective linear trends. The mean elevation difference is 1.3 m. **b.** Profiles detrended up to degree four. The mean elevation difference is 0.51 m.

observed surface changes. The objective of this section is to quantify the amount of water ice sublimation or water erosion using a thermal model as described in Sect. 5. The modeled water ice erosion in comparison with the observed total mass loss will permit constraining the abundance of water ice in the dust deposits on 67P.

7.3.1 Accumulated insolation over 67P nucleus

The insolation at a certain location of the nucleus accumulated from t_0 to t_1 is calculated as,

$$E_\odot(t_0, t_1) = \int_{t_0}^{t_1} Q_\odot(t)\mathrm{d}t \quad (\mathrm{J\,m^{-2}})\,, \tag{7.1}$$

where $Q_\odot(t)$ is given by Eq. (5.25),

$$Q_\odot(t) = \left(\frac{1\ \mathrm{AU}}{r_\odot(t)}\right)^2 C_\odot(1-\mathcal{A})\,\delta(\alpha_\odot, \varphi_\odot)\sin\varphi_\odot \quad (\mathrm{W\,m^{-2}}). \tag{7.2}$$

The heliocentric distance of the comet, $r_\odot$, the azimuth and the elevation of the Sun, $\alpha_\odot, \delta_\odot$, and the illuminability of the local surface, $\delta(\alpha_\odot, \varphi_\odot)$, are derived from the Horizon database implemented with the SPICE kernels, as described in Sect. 5.1.3.

A local shape model truncated from a global SPG model with a 10 m spatial resolution was used to calculate the accumulated insolation September 1, 2014 to the end of

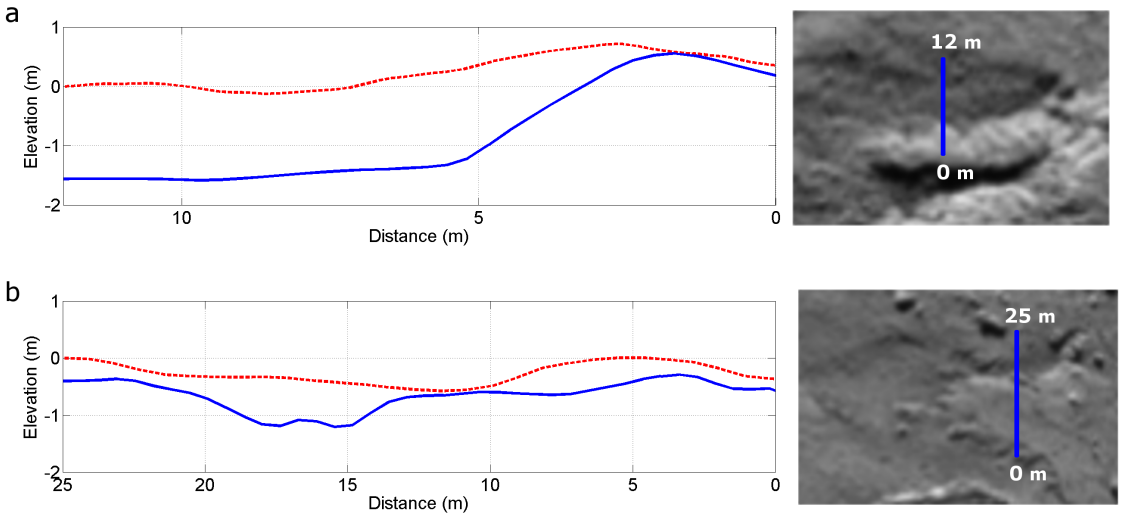

Figure 7.27: Comparison of roughness profiles before and after the surface change. **a.** The solid blue curve corresponds to the path over an exposed outcrop indicated in the right-panel image (cropped from Fig. 7.8b) on March 28, 2015, the dashed red curve is for October 1, 2014. **b.** The solid blue curve follows the path over a fresh scarp indicated in the right-panel image (cropped from Fig. 7.10b) on March 28, 2015. The dashed red curve refers to December 2, 2014.

February, 2015, as shown in Fig. 7.28 and 7.29. The results are color-coded superimposed on context images. In particular, we examine closely two areas at similar latitudes: the area in Ma'at where the cluster of honeycombs, MAT02-11, were observed at the end of March, 2015 (Fig. 7.28); and another area surrounding ASH01, SET01, and SET02 at the border of the Ash and Seth regions (7.29a). The pattern of insolation is governed by topographic variations. The locations of the changes in open, unobstructed areas had received ample insolation of about 10^9 J m^{-2} over this period. The energy over the cliffs varies: the north-facing walls were subject to peak accumulated insolation in clear excess of 10^9 J m^{-2}, while those looking to the south were least energized areas where insolation was below 6×10^8 J m^{-2}.

On a global scale (Fig. 7.28b and 7.29b), the maximum insolation occurs at high latitudes, e.g., above 40°N. The energy decreases towards lower latitudes, which had been illuminated for shorter period of time as the sub-solar point moved southward. Most of the southern hemi-nucleus had not been illuminated by late February, still two months before the southern vernal equinox.

7.3.2 Improvement on parameterization of thermal models

The validity of application of the thermal model to estimate water erosion rests upon reasonable parameterization of the model. It is, above all, imperative that the modeled water production of 67P (defined by Eq. 7.3 below) is in agreement with estimates based on remote observations and *in situ* measurements collected by Rosetta. The key nucleus properties impacting the behavior of the water activity are the depth of the water ice and ice abundance therein, as represented by the dust mantle thickness and icy area fraction,

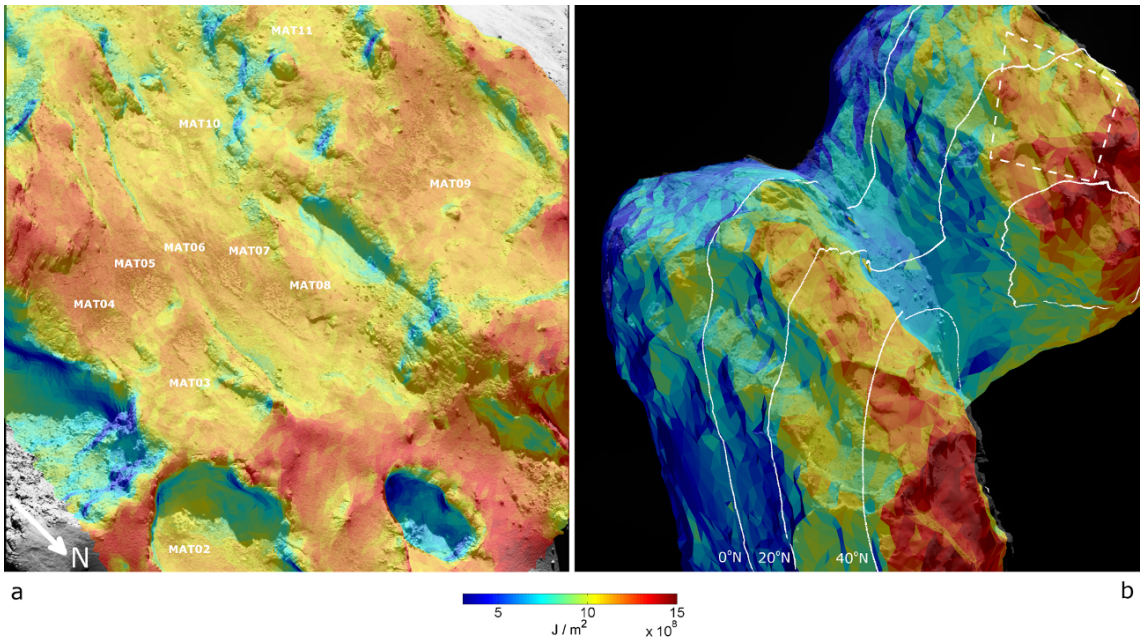

Figure 7.28: Accumulated insolation from September 1, 2014 through February 28, 2015. **a.** Local accumulation in Ma'at superimposed on the context image of Fig. 7.1e showing honeycombs MAT02-10. **b.** Global accumulation over the nucleus from a more distant view than **a**. The field of view of **a** is indicated by the quadrilateral of dashed white outline in **b**.

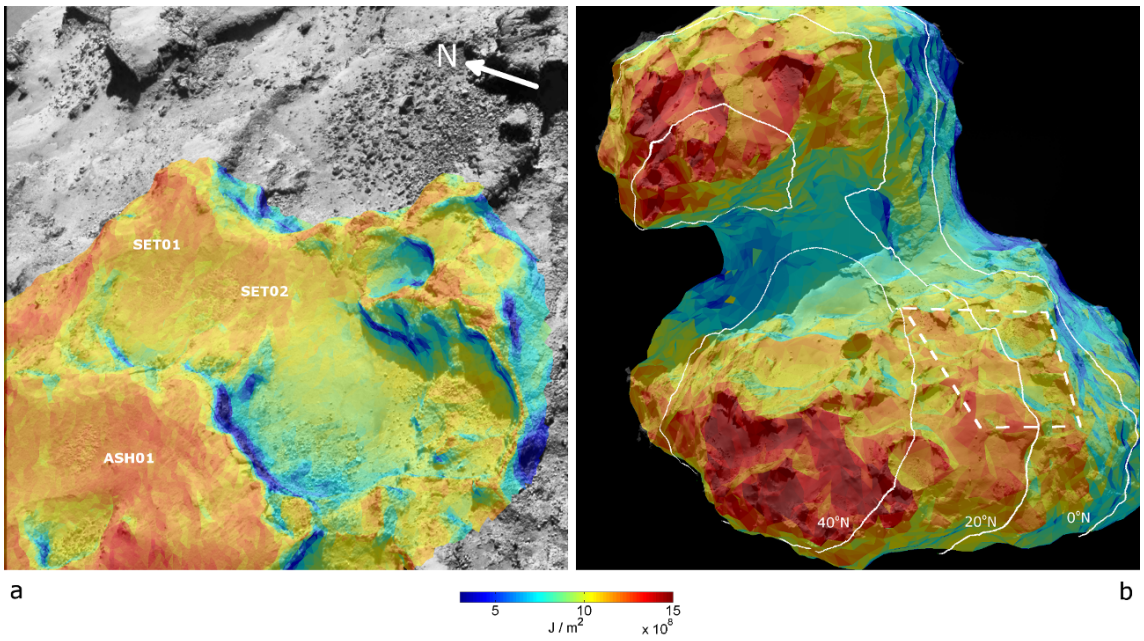

Figure 7.29: Accumulated insolation from September 1, 2014 through February 28, 2015. **a.** Local accumulation at the border between Ash and Seth superimposed on the context image of Fig. 7.1b. **b.** Global accumulation over the nucleus from a more distant view than **a**. The field of view of **a** is indicated by the quadrilateral of dashed white outline in **b**.

respectively (Sect. 4.1).

We specify the water production as the time-average over one rotation period of the comet,

$$\zeta = \frac{1}{t_\mathrm{P}} \int_{t_0}^{t_0+t_\mathrm{P}} \Sigma Z \, \mathrm{d}t \quad (\mathrm{kg\,s^{-1}}), \tag{7.3}$$

Note that this definition differs but is related to that of the (instantaneous) sublimation flux (Eq. 4.19 or 4.31). For instance, $\Sigma Z(t)$ denotes the time-varying total flux of water sublimation from 67P as defined by Eq. (5.47). $t_\mathrm{P} \approx 12.5$ hours is the rotation period of 67P. Although the rotation of 67P slowed down somewhat before perihelion (Keller et al. 2015a), this change does not affect the evaluation of ζ.

To test the influence of the dust mantle thickness, X in Eq. (4.28), we first fix the icy area fraction as $\mathscr{F} = 0.1$, which corresponds to the observed ice areal abundance of the "morning frost" over the surface in the Hapi region (De Sanctis et al. 2015). Fig. 7.30 shows the modeled water production as a function of heliocentric distance for three dust mantle thicknesses, namely, 5 mm, 10 mm, and 15 mm. The mantle thickness is assumed to be uniform over the nucleus. Evidently, an increase of mantle thickness consistently reduces the water production. The model results are plotted against measurements of water production, most of which are collected by Fougere et al. (2016a). It seems that the best approximation resulted from the mantle thickness of 10 mm over the nucleus, while thinner and thicker dust mantles led to an over-estimation and a slight under-estimation compared with measurements, respectively.

It is also found that a different parameterization of $X = 5$ mm and $\mathscr{F} = 0.01$ also yielded reasonable results in comparison with measurements (Fig. 7.30). It is not realistic to evaluate the improvement or degradation of this parameterization or to quantify the exact mantle thickness and icy area fraction of the nucleus, when the assumptions of uniform mantle thickness and ice abundance are ideal. However, the model results indicate that the water activity is significantly influenced by the dust mantle and ice abundance. Moreover, the bulk of the activity does not occur from the bare, pure-icy surface but from some depths of several millimeters where only a few percent of the subsurface area is icy. Hereafter, the results are for $X = 10$ mm and $\mathscr{F} = 0.1$.

7.3.3 Correlation between modeled water erosion and observed surface change

Once the thermal model is parameterized with reference to the measurements, it can be integrated to quantify the erosion of water ice at any given location between t_0 and t_1 as,

$$\Delta m_{\mathrm{H_2O}} = \int_{t_0}^{t_1} Z \mathrm{d}t \quad (\mathrm{kg\,m^{-2}}). \tag{7.4}$$

The amount of water erosion between September 1, 2014 and February 28, 2015 over the area encompassing the honeycombs MAT02-11 is shown in Fig. 7.31. As in Fig. 7.28 showing the pattern of accumulated insolation, the results are coded in color and superimposed on a context image exemplifying the changes. As expected, the pattern of water erosion resembles that of accumulated insolation, because water sublimation occurs from

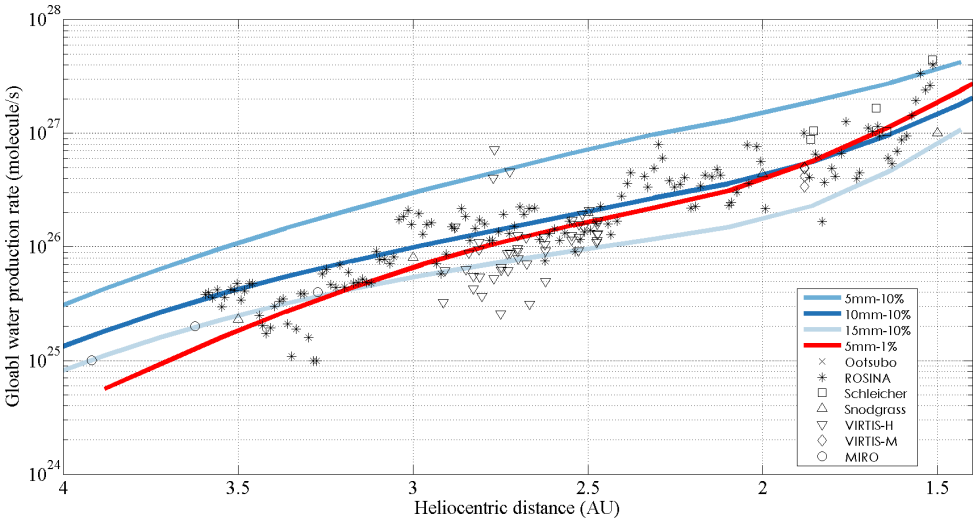

Figure 7.30: Modeled water production rate as a function of heliocentric distance from 4 AU inbounds in comparison with measurements. Measurements are marked by discrete symbols. MIRO data are given by Gulkis et al. (2015). All other data are adapted from Fig. 15 in Fougere et al. (2016a). Model results assuming different thickness of the overlying dust mantle for $\mathscr{F} = 0.1$ are indicated by solid blue lines. The solid red curve corresponds to $\mathscr{F} = 0.01$ with a mantle thickness of 5 mm.

a shallow depth from the surface so that activity always varies with insolation. The water erosion generally ranged between 5 kg m^{-2} and 10 kg m^{-2} over the flat areas where the features were present having received ample insolation over six months. The same amount of erosion had probably occurred over the other area around features ASH01, SET01, and SET02 (Fig. 7.32) on the different lobe, located at similar latitudes as MAT02-11 and thus having absorbed a comparable amount of insolation.

As shown in Fig. 7.23, the observed surface changes were distributed between about 20° and 40°N. According to the model results, these latitudes correspond to an equal-erosion strip along the nucleus. The absence of observations of surface changes towards the south can be easily attributed to less erosion with a dearth of insolation before the approach of the sub-solar point (Fig. 7.31b and 7.32b). The reason that fewer changes were detected further north *on the two lobes*[i] with higher accumulation of energy is less straightforward. Possible explanations are presented below.

[i]The earliest changes appeared in the Hapi region near the North Pole situated between the two lobes.

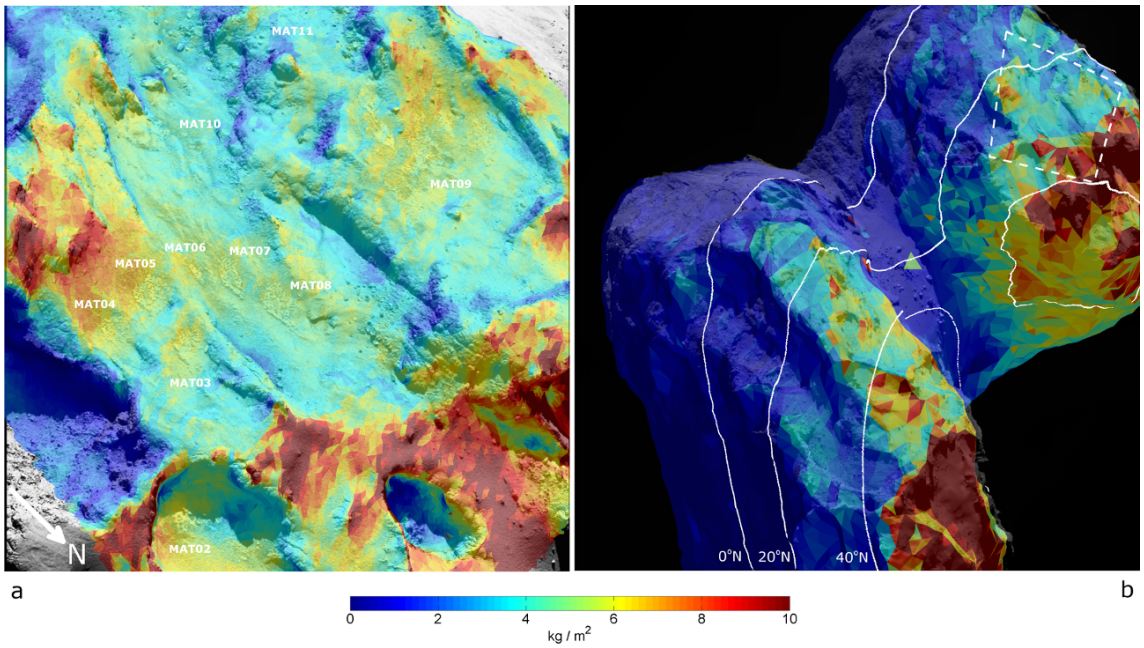

Figure 7.31: Total erosion of water ice from September 1, 2014 through February 28, 2015. **a.** Local erosion in Ma'at superimposed on the context image of Fig. 7.1e showing honeycombs MAT02-10. **b.** Global erosion over the nucleus from a more distant view than **a**. The field of view of **a** is indicated by the quadrilateral of dashed white outline in **b**.

7.4 Discussion: morphological expression of seasonality on 67P

7.4.1 Transition strip of global morphology

There is an obvious explanation for the plethora of surface changes affecting the nucleus between 20°N and 40°N. As discussed by Gundlach et al. (2015), the water activity on 67P probably did not begin until the comet had reached ~ 2.5 AU inbound. From then on, it was probable that large particles, e.g., several centimeters in size or even larger, comprised the bulk of the ejecta. The onset of strong water erosion and release of large particles would accelerate the erosion of the surface, which may be reflected in the timeline of the observed changes.

In addition, we interpret the apparent lack of detections of surface erosions at latitudes higher than 40°N as indicating thicker cover of deposits. Thicker deposits do *not* indicate quenched or reduced activity because the dust deposits were most likely icy. Rather, the erosion probably had not exhausted the deposits or exposed the abrupt substrate topography, so that the surface textures remained smooth. The strip between 20°N and 40°N marked a transition of global morphology from the northern dust cover towards the southern rugged terrains (Fig. 7.33). Within the *transition strip*, the thickness of dust deposits gradually decreased southwards and started to run out occasionally. Hence, the aftermaths of surface erosion before perihelion were most remarkable over the transition strip.

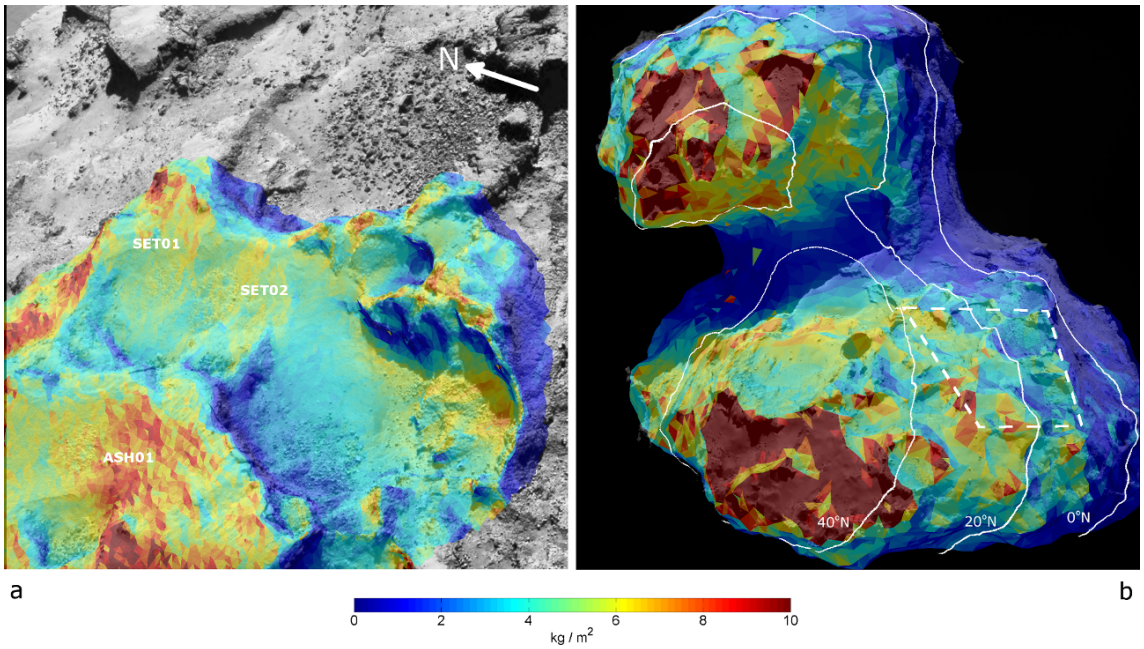

Figure 7.32: Total erosion of water ice from September 1, 2014 through February 28, 2015. **a.** Local erosion at the border between Ash and Seth superimposed on the context image of Fig. 7.1e. **b.** Global erosion over the nucleus from a more distant view than **a**. The field of view of **a** is indicated by the quadrilateral of dashed white outline in **b**.

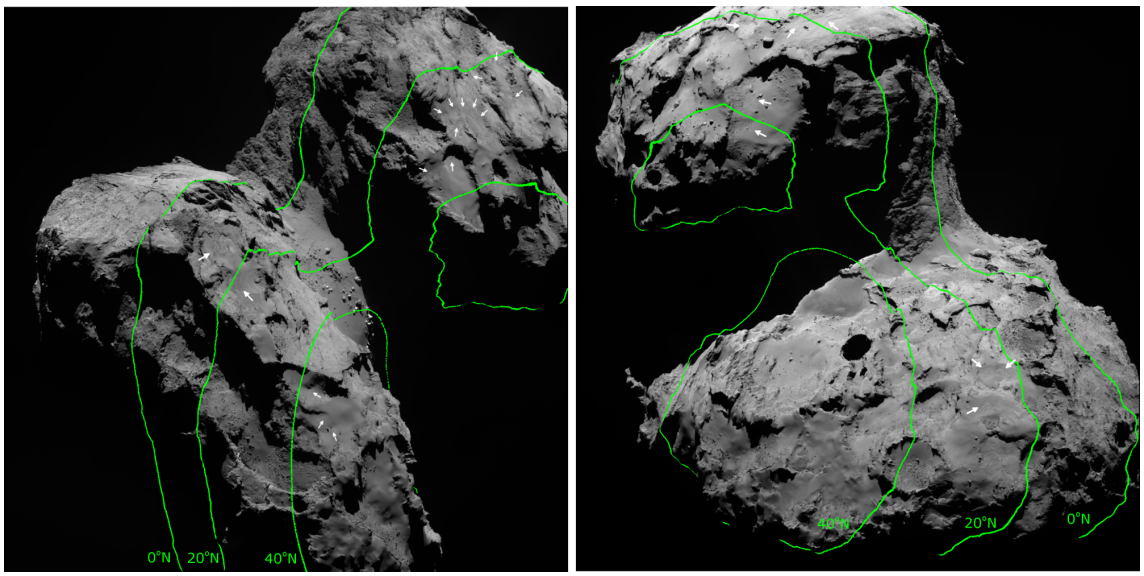

Figure 7.33: Distribution of honeycombs on 67P indicated on two context images with complementary views of the nucleus. Honeycombs are marked by white arrows. Three lines of latitudes, the equator, 20° N, and 40° N, are denoted by green lines. The latitudinal line at 40° N is disconnected, i.e., circumscribing each lobe, which arises from the ambiguity of the latitude-longitude system (Preusker et al. 2015).

7.4.2 Seasonal retreat and expansion of dust cover

The erosion before perihelion had depleted dust deposits at numerous places along the transition strip. This caused the edges of the dust covers on the respective lobes to retreat, and the coverage of the deposits to shrink. During perihelion, the northern deposits had been restored or replenished by the deposition of icy ejecta from the south undergoing maximum activity, stretching the dust covers southwards beyond (further below) 20°N. Therefore, the conspicuous, locally distinctive changes on 67P around perihelion were glimpses of a global, cyclic retreat and expansion of the icy dust deposits (for as long as the present-day orbit and rotation of the comet will last). On the one hand, this morphological expression of seasonality on exists because of the eccentric orbit together with oblique rotational axis of the nucleus. On the other hand, it manifests itself on an active body such as comet 67P where global transport of material takes place.

7.5 Discussion: water ice abundance in dust cover

7.5.1 Mass ratio of dust and water ice in the dust cover

That the deposits contained water ice, even if of trace amount, has important implications for the cyclic activity of 67P as well as nucleus evolution over time. The outcome of this investigation provides a direct constraint on the scale of ice abundance in the dust deposits.

We express the total mass of surface erosion over a unit of surface area as

$$\Delta M = \Delta m_{\mathrm{dust}} + \Delta m_{\mathrm{H_2O}},\ (\mathrm{kg\,m^{-2}}), \tag{7.5}$$

with Δm_{dust} and $\Delta m_{\mathrm{H_2O}}$ being the mass of dust component and that of water ice, respectively. The dust-to-ice (mass) ratio is defined by $\mu = \Delta m_{\mathrm{dust}}/\Delta m_{\mathrm{H_2O}}$. Let the total erosion be denoted by $\Delta M = (1+\mu)\Delta m_{\mathrm{H_2O}}$. It follows that the dust-to-ice ratio is evaluated by

$$\mu = \frac{\Delta M}{\Delta m_{\mathrm{H_2O}}} - 1 = \frac{\rho \Delta x}{\Delta m_{\mathrm{H_2O}}} - 1\,, \tag{7.6}$$

where ρ indicates the mass density of the icy dust deposits, assumed to be $530\,\mathrm{kg\,m^{-3}}$ (Pätzold et al. 2016). Note that the thickness of surface erosion, Δx, has been derived from the (photometric analysis of) observations (Sect. 7.2), and that $\Delta m_{\mathrm{H_2O}}$ was determined by thermal modeling (Sect. 7.3). We adopt $\Delta x = 1\,\mathrm{m}$ as a rough estimate for the order of magnitude of erosion thickness. Subsequently, the total mass of erosion is obtained as $\Delta M = 530\,\mathrm{kg\,m^{-2}}$.

7.5.1.1 Case A: $50 \leq \mu \leq 100$ for a homogeneous dust cover

Without concrete evidence or indication for the spatial variation of dust-to-ice ratio over the nucleus (dust deposits), it is reasonable to assume that the dust cover was homogeneous and that the dust-to-ice ratio thereof was constant. Support for this assumption comes from at least the observational evidence for the global renewal of the dust cover around perihelion, when the redistribution of dust from the south to the north

had likely homogenized the ice abundance in the deposits. It can then be argued that $5 \leq \Delta m_{\mathrm{H_2O}} \leq 10\,\mathrm{kg\,m^{-2}}$ derived via the dust mantle model (Fig. 7.31) will be representative of water ice loss at the "sample" locations where surface erosion had been observed. In this case, we obtained $50 \leq \mu \leq 100$ that indicates a nearly dry dust cover with only 1-2% of water ice below a completely desiccated dust mantle (Capaccioni et al. 2015). We note that this conclusion also justifies the choice of $\mathscr{F} = 0.1$ or 0.01 for the icy area fraction of the nucleus subsurface when modeling the water erosion (Sect. 7.3.2).

7.5.1.2 Case B: $\mu \geq 4$ for any location

It is helpful to admit the possibility of a (highly) non-uniform dust cover with a spatially varying ice abundance and understand the consequence thereof. In this case, the lower limit of the dust-to-ice ratio, or the upper limit of ice abundance, can be determined.

Because most of the surface changes were concentrated at mid-latitudes and driven by intensifying insolation, it suffices to examine one example of the honeycomb feature MAT05 (Fig. 7.2) which should be representative of all changes. Let us first consider an extreme case in which the local nucleus surface consists of pure water ice, i.e., $\mathscr{F} = 1$ or $\mu = 0$. Applying the dusty-ice thermal model, we found that the water erosion between early September 2014 and late February 2015 is $\Delta m_{\mathrm{H_2O}} = 175\,\mathrm{kg\,m^{-2}}$. However, there arises an inconsistency as such $\Delta m_{\mathrm{H_2O}}$ yields a dust-to-ice ratio of two instead of zero (as for a purely icy surface).

A consistent estimate for the lower limit of the dust-to-ice ratio is obtained via a trial-and-error approach. We adopted a number of discrete values for the icy area fraction, $\mathscr{F}_{(k)}$ for $k = 1, 2, ...$, each of which represents a distinct dust-to-ice ratio by $\mu_{(k)} \approx \mathscr{F}_{(k)}^{-1} - 1$ (Eq. 4.23). For each $\mathscr{F}_{(k)}$ we applied the dusty-ice thermal model and derived the water erosion $\Delta \hat{m}_{\mathrm{H_2O}\,(k)}$. This estimate then yields a model estimate of $\hat{\mu}_{(k)}$ according to Eq. (7.6). If $\hat{\mu}_{(k)}$ is close enough to $\mu_{(k)}$, i.e., the derived dust-to-ice ratio conforms to the assumed value and therefore indicates a consistent estimate.

Fig. 7.34 shows the solutions of $\hat{\mu}$ for different $\mathscr{F}$ in comparison with μ related algebraically to $\mathscr{F}$. The intersection of the two curves is at $\mathscr{F} \approx 0.2$ or $\mu \approx 4$. Note that the dust-to-ice ratio of four indicates the absolute minimum at *any* location of surface erosion. If $\mu = 4$ would hold for the entire nucleus surface, then the water production of 67P would exceed the measurements by a factor of about 20. Therefore, this ice abundance of 20% cannot exist everywhere (Capaccioni et al. 2015). Furthermore, if a dust mantle is present on the nucleus, the water erosion will invariably be reduced. In this case, the curve of $\hat{\mu}$ in Fig. 7.34 will be elevated as a whole and the dust-to-ice ratio (below the dust mantle) in excess of four must result.

We note that, while $\mu = 4$ indicates the minimum of the dust-to-ice ratio in a highly inhomogeneous dust cover, $\mu \in [50, 100]$ as derived for the homogeneous deposits should *not* be regarded as the upper limit. In fact, the upper limit is always $\mu = \infty$ that would indicate a completed desiccated dust cover.

7.5.1.3 Checkerboard scenario of spatially varying dust-to-ice ratio

It is plausible, or perhaps even necessary, that the reality is intermediate between the two extreme scenarios described above. The fact that the dust cover had been formed by the

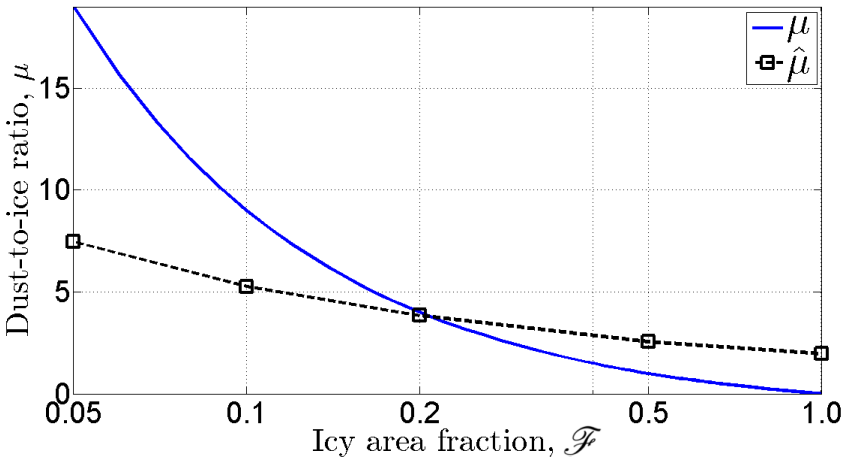

Figure 7.34: Lower limit of dust-to-ice ratio. The blue curve describes the icy area fraction related to the dust-to-ice ratio via Eq. (4.23). The black squares indicate the modeled dust-to-ice ratios according to Eq. (7.6). The intersection of the two curves indicates a consistent estimate of the minimum dust-to-ice ratio.

global deposition of ejecta originating from the southern hemi-nucleus suggests that the deposits were likely compositionally homogenized to a certain extent. This is evidenced by the global, latitudinal distribution of the observed surface erosions before perihelion, suggesting that there was no strong contrast of ice abundance over the nucleus on a global scale. On the other hand, the dust cover may be non-uniform on local scales, e.g., below 10 m. This can be argued from the uneven thickness of erosion, such as the development of the densely pitted textures; it may also have been revealed by the observed activity of the sunset jets arising from the dust covered areas (Sect. 6). However, such small-scale inhomogeneities cannot be resolved by the present analysis.

Therefore, we should consider a "checkerboard" scenario, in which higher ice abundance may occur on local scales while the dust cover is more or less uniform on a global scale. In effect, this can be conceptualized as a uniform distribution of locally enhanced ice concentrations over the dust cover.

7.5.2 Non-escaping dust

Based on the dust and water productions measured in the coma, (Rotundi et al. 2015, Fulle et al. 2016c) derived an average dust-to-ice ratio of 4(±2) for 67P up to perihelion, always referred to the sunlit portion of nucleus surface. In other words, this ratio is related to the *mass loss* of 67P, i.e., material escaping entirely from the nucleus. OSIRIS observations show that a fraction of the dust ejected from the nucleus definitely did not escape but were redeposited. The non-escaping fraction of the ejecta in mass is defined as follows,

$$\eta = \frac{[\Delta m_{\mathrm{dust}}] - [\Delta m'_{\mathrm{dust}}]}{[\Delta m_{\mathrm{dust}}]} \times 100\%\,, \tag{7.7}$$

where $[\Delta m_{\mathrm{dust}}] = \int_S \Delta m \, \mathrm{d}S\,\mathrm{kg}$ indicates the mass ejected from the surface. $[\Delta m'_{\mathrm{dust}}]$ indicates the mass of the escaping dust. $\eta[\Delta m_{\mathrm{dust}}]$ then denotes the dust that is still bound by

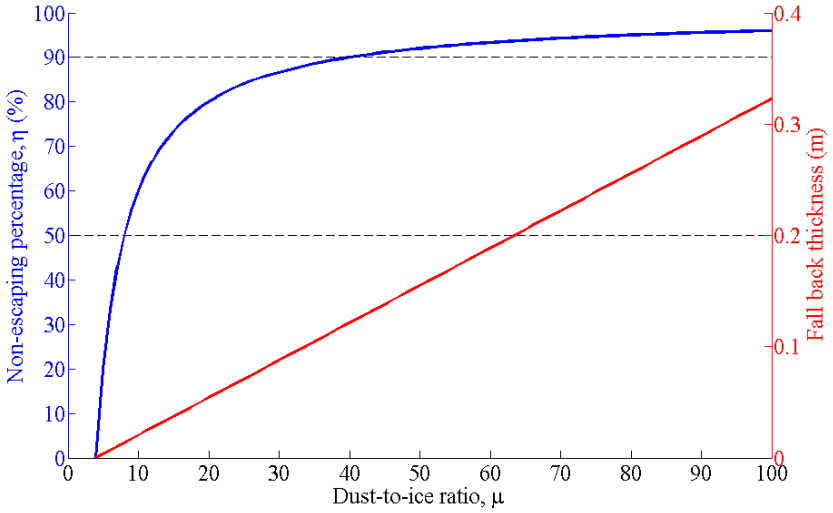

Figure 7.35: Non-escaping fraction in mass of dust ejected from the northern dust cover (blue curve) and the thickness of redistributed or fall-back dust deposits (red curve) as a function of average dust-to-ice ratio of the dust cover. The surface area of the dust cover is ~8 km^2 including Ash, Babi, Seth, and Ma'at regions, excluding Hapi and Imhotep. The site of redeposition of fall-back dust is the southern hemi-nucleus and Hapi.

the gravity of the nucleus (Agarwal et al. 2016).

If the nucleus is nearly homogeneous on scales >10 m, then $[\Delta m'_{\rm dust}] = 4[\dot{\Delta} m_{\rm H_2O}]$. Here, let μ be a variable denoting the average dust-to-ice ratio over the *entire* nucleus, the non-escaping fraction is then $\eta = 1 - 4\mu^{-1}$ (blue curve in Fig. 7.35).

7.5.2.1 Case A: Dust ejected from exposed ice: full-escaping

An extreme case in which dust all escapes is $\eta = 0$ (η cannot be negative). We note that this is related to the scenario described in Sect. 7.5.1.2, in which the ejection of dust was driven by sublimation of exposed dusty water ice scattered on the nucleus surface (Filacchione et al. 2016, Barucci et al. 2016). The dust-to-ice ratio at these locations is four. However, it can be argued that this situation does not occur, because $\mu = 4$ can only exist at scattered locations and therefore the average dust-to-ice ratio over the nucleus must be higher.

7.5.2.2 Case B: Dust ejected from the south: half-escaping

Fulle et al. (2016b) derived a dust-to-ice ratio of 8.5 for the bulk nucleus. Because the southern hemi-nucleus experiences peak activity during perihelion, when fresh material in the nucleus interior is constantly exposed, the ratio may therefore represent the composition of dust ejected therefrom. Then, we may infer that a little more than 50% of the ejecta from the south are still bound by the nucleus gravity. A part of these must have been accumulated over the northern hemi-nucleus, which explains the renewed dust cover observed after perihelion.

7.5.2.3 Case C: Dust ejected from the northern dust cover: limited-escaping

The dust-to-ice ratio of a homogeneous dust cover is $50 \leq \mu \leq 100$ (Sect. 7.5.1.1). This much higher ratio than that derived from coma measurements suggests that only a very small fraction, e.g., <10% of the ejecta would escape. The surface area of the dust cover, excluding Hapi and Imhotep, is roughly 8 km^2 (Thomas et al. 2015b). For instance, if the average thickness of erosion was $\Delta\bar{x} = 1$ m, the escaping mass was 4×10^9 kg between September 2014 and February 2015. Then, the average mass flux of ejecta would be larger than 250 $kg\,s^{-1}$. Combining GIADA and OSIRIS observations, Fulle et al. (2016c) calculated a mass flux of 70 $kg\,s^{-1}$ at the end of March 2015 for dust particles ≤ 0.1 kg. The value of 35 $kg\,s^{-1}$ averaged over six months was less than 15% of the dust flux from the dust cover. On the other hand, we may consider $\Delta\bar{x} = 0.1$ m, which would result from $\mu = 8.5$ (Fulle et al. 2016b). The erosion of water ice averaged over the dust cover is ~ 5.5 $kg\,m^{-2}$ (derived by the dust mantle thermal model; see Sect. 7.3.3). Thus, the total mass loss over a unit surface area is $5.5 \times (1 + 8.5) \approx 52$ $kg\,m^{-2}$. The average dust flux would be 25 $kg\,s^{-1}$. Then, no more than half of the ejecta from the dust cover had escaped from the nucleus.

7.5.2.4 Global re-distribution of dust

We suspect that a large amount of the ejecta from the dust cover may not have escaped from 67P, but were redeposited over the nucleus or afloat in the coma. These nucleus-bound, often large particles were likely not accounted for in the dust production derived from measurements by the onboard instruments of Rosetta. This is especially plausible when these particles were being transported in the inner-coma below the altitude of the spacecraft. In light of this situation, the dust-to-water ratio of 4(±2) reported by Rotundi et al. (2015) must only be considered as a lower limit (Fulle et al. 2016a). A consequence is that the dust-to-gas ratio based on coma observations must be clearly distinguished from and, indeed, will always be lower than the dust-to-ice ratio from the nucleus.

Probably, the transport and (re-)deposition of dust is a prevalent phenomenon (Thomas et al. 2015a, Kramer and Noack 2015). The south-to-north transport was significant during perihelion (Keller et al. 2015a), where about half of the mass was redistributed over the northern hemi-nucleus. The non-escaping fraction may be even greater for ejecta from the dust cover in the north eroded before perihelion. The dust may have fallen back onto other parts of the nucleus surface, such as the shadowed southern hemi-nucleus and Hapi. If the non-escaping dust must all fall back, the thickness of deposition varies linearly with the average erosion thickness, i.e., $\Delta\bar{x}$, and thus with the average dust-to-ice ratio, as well (red curve in Fig. 7.35). Note that the exact average thickness of erosion cannot be determined here, which needs to be constrained via a dedicated analysis in the future.

8 Summary of Conclusions

Of six comet nuclei that had been visited *in situ* by spacecraft to date, 67P was the fourth to display a highly elongated nucleus with global concavities (Sect. 1.2 and 2.2). The bi-lobed shape of the nucleus had probably resulted from the merger of two independently-formed objects (Sierks et al. 2015, Massironi et al. 2015, Davidsson et al. 2016b). The nucleus is desiccated over the surface, with limited exposure of water ice (Capaccioni et al. 2015). The orientation of the rotation axis of 67P nucleus coupled with its orbital motion gives rise to strong asymmetry in the lengths of seasons. At present, the north is being heated enduringly but mildly by the Sun when the comet is withdrawn from perihelion for much of the six-year orbit; whereas, the south experiences vigorous summer heat around perihelion that lasts only several months.

The nucleus morphology is diverse and, intriguingly, dichotomous over the two hemi-nuclei (Thomas et al. 2015b). The northern hemi-nucleus is overall covered by a layer of dust deposits, with rugged, consolidated substrate revealed over the steep or abrupt surfaces. This morphology is in sharp contrast to that in the south, where the dust deposits are far less significant and consolidated terrains prevail. The dust activity of comet 67P is overall driven by water outgassing. Water activity from the nucleus is prevalent, even if non-uniform, and shows a distinct diurnal variation. In the northern hemi-nucleus, water production exceeds that of any other volatile by a factor of ten. The productions of super-volatiles, such as CO_2 and CO, were anti-correlated with water outgassing and showed less variability, suggesting their reservoirs from the more or less diurnally iso-thermal interior (Bockelée-Morvan et al. 2015). Around perihelion, the productions of water and super-volatile species from the southern hemi-nucleus became correlated, possibly suggesting more significant roles of super-volatiles in driving the dust activity (Fougere et al. 2016b).

Activity from underneath the prevalent dust mantle The nearly ubiquitous dust mantle over comet nuclei (Capaccioni et al. 2015) had been predicted by both experiments (Grün et al. 1991) and theoretical modeling (Grün et al. 1989, Mekler et al. 1990), and could be inferred from the low-reflectance of comet nuclei in general (see, e.g., Sect. 1.2 and references therein). The water production of the nucleus with a dust mantle, even a few millimeters in thickness, would be drastically reduced with respect to that of a bare icy nucleus, or "snowball" (Gundlach et al. 2011) (Sect. 5.3.4.2). As introduced in Sect. 2.3.1, application of thermal models designed for the bare nucleus invariably yielded over-estimation of the water production that, in turn, led to the intuition that the nucleus must be locally active from the limited exposure of icy surfaces. The expanse of observed dust activity (Sect. 6) and the detected surface changes (Sect. 7), in agreement with the global

water outgassing from the 67P nucleus, suggest that this intuition is misleading at best and, perhaps, simply false. It is, therefore, imperative that all thermal models must be able to explicitly account for the influence of a *global* dust mantle over the nucleus. An immediate consequence is that the assumption of localized water activity from scarce water exposure, for the sole purpose of scaling down the over-production of a "snowball" nucleus, can be effectively obviated (Hu et al. 2017a).

Dry dust mantle and icy dust cover The sunset jets on 67P frequently observed by OSIRIS (Sect. 6) exhibited a characteristic diurnal pattern of water sublimation from shallow depths of the nucleus. The results of thermal analysis indicate that the water ice should be present at the depth of 6 mm, where the residual warmth of the subsurface could sustain substantial water sublimation ~1 hour after dark. The sublimation flux is well sufficient to eject millimeter-sized dust grains from the nucleus against gravity, while the mechanisms to overcome cohesive forces between particles could not be resolved.

The distribution of ground sources of the sunset jets showed no morphological association. Most of the jets arose from the dust covered areas, more expansive than the consolidated terrains. This result calls for an *urgent* distinction between the *dust cover* as a prevalent morphology and the *dust mantle* as a volatile-free coating of insulation and gas pressurization. The thickness of the dust cover could well exceed several meters on each lobe and, conceivably, thicker in the neck of the nucleus. With the top few (six) millimeters desiccated, forming the prevalent dust mantle, the dust cover is icy underneath.

Seasonal morphology of dust cover Multitudes of surface changes detected from OSIRIS observations suggested that the dust cover had been widely eroded when 67P approached ~2 AU inbound (Sect. 7). These changes in the form of increase of surface roughness as dust cover thinned unevenly over time were concentrated at latitudes between 20°N and 40°N. The dust cover is overall depleted further south, while the deposits to the north may be perennial. During perihelion, the dust cover thickened with a significant deposition of ejecta from the southern hemi-nucleus experiencing peak activity. These mid-latitudes correspond to a "transition strip" of global morphology, where the edges of the dust cover retract and expand seasonally.

Dust-to-ice ratio of nucleus greater than dust-to-gas ratio in coma The outcome of photometric and thermal-modeling analysis of the observed erosion and restoration revealed an *average* dust-to-ice ratio of over 50 in the dust cover, substantially larger than the dust-to-gas ratio of around 4 measured in the coma (Rotundi et al. 2015). Here, another distinction, namely, between the dust-to-*ice* and the dust-to-*gas* ratios, must be clarified. In fact, the latter, referred to the mass fluxes of gas production and dust *escaping* from the nucleus, always indicates a lower limit of the dust-to-ice ratio of the nucleus (Fulle et al. 2016a). To the best of author's knowledge, this distinction had not been clearly expressed in previous studies, most likely due to a lack of spatial resolution and temporal coverage in observations of the nuclei and the inner-comae acquired in cometary missions before Rosetta. Evidently, the fate of non-escaping portions of the dust ejecta from the nucleus had not been observed and deliberated. The OSIRIS observations presented in this study substantiated that not only ejection but also transport and

re-deposition of dust particles are fundamental mechanisms constantly re-shaping the nucleus on a global scale. This implies and, indeed, must result in a nucleus with a higher dust content than can be inferred from the coma. The results reaffirmed the necessity of characterizing cometary nuclei as “dustballs” instead of “snowballs” (Keller 1989). It should also be complemented that the dust-to-ice ratio of a comet nucleus may be non-uniform with depth in general, i.e., with ice-deficient dust deposits covering the icy interior. Hence, one particular focus of future studies should be on the detailed mechanisms of volatile outgassing and dust ejection thereby, governed by the thermal and mechanical properties of a dust-dominant nucleus, and the implications on the evolution of the nucleus.

List of Symbols

Below is an non-exhaustive list of mathematic symbols used in the dissertation, grouped according to topics. Inevitably, some symbols appear in different chapters and take various meanings. There should be little risk of confusion within the context of discussion in the respective chapters. This list is nonetheless provided for the purpose of clarification in case any misunderstanding arises.

Physical Constants

c	Speed of light
$C_\odot$	Solar constant
G	Gravitational constant
k_B	Boltzmann constant
$M_\odot$	Solar mass
σ	Stefan-Boltzmann constant

Orbit Parameters

a	Semi-major axis
e	Eccentricity
i	Inclination
Ω	Longitude of ascending node
ω	Argument of periapsis (perihelion)
M_0	Mean anomaly at certain epoch, t_0
n	Mean motion

Geometry and Photometry of Observation

α	Phase angle
β	Photometric latitude

γ	Photometric longitude
$\delta X, \delta Y$	Errors in pixel coordinates
$\boldsymbol{\delta}\mathbf{r}_\mathrm{C}$	Error vector of camera position
$\boldsymbol{\delta}\mathbf{R}_\mathrm{[C]}$	Error of camera orientation in terms of an additional rotation of the camera coordinate system
λ	Wavelength of radiation
φ	Photometric azimuth
$\boldsymbol{\psi}$	Error vector of camera orientation
A or A_λ	Normal albedo of nucleus surface
D or D_λ	Disk function at wavelength λ
e	Emission angle of light scattered off nucleus surface
i	Incidence angle of sunlight
$\mathbf{l}_\mathrm{P}$	Vector from camera focal point to observed point
p	Length of one pixel
$\mathcal{P}$ or $\mathcal{P}_\lambda$	Phase function at wavelength λ
$\mathbf{r}_\mathrm{P}^\mathrm{[C]}$	Position vector of an observed point in camera coordinate system
$\mathbf{r}_\mathrm{C}$ or $\mathbf{r}_\mathrm{C}^\mathrm{[BF]}$	Position vector of focal point of camera in 67P body-fixed coordinate system
$\tilde{\mathbf{r}}_\mathrm{C}$	Erroneous position vector of camera in 67P body-fixed coordinate system
r_f	Focal length of camera
$\mathbf{r}_\mathrm{P}$ or $\mathbf{r}_\mathrm{P}^\mathrm{[BF]}$	Position vector of an observed point in body-fixed coordinate system of 67P
$\mathbf{R}_\mathrm{[C]}^\mathrm{[BF]}$ or $\mathbf{R}_\mathrm{[C]}$	Rotation matrix transforming a vector from camera coordinate system to 67P body-fixed system
$\mathbf{R}_\mathrm{[BF]}^\mathrm{[C]}$	Rotation matrix transforming a vector from 67P body-fixed coordinate system to camera system
$\tilde{\mathbf{R}}_\mathrm{[BF]}^\mathrm{[C]}$	Erroneous rotation matrix transforming a vector from 67P body-fixed coordinate system to camera system
$\mathcal{R}$ or $\mathcal{R}_\lambda$	Radiance factor at wavelength λ

X, Y	Pixel coordinates
$\tilde{X}, \tilde{Y}$	Erroneous pixel coordinates

Thermal Modeling

α	Sublimation coefficient
ϵ	Emissivity of nucleus surface
κ	Heat conductivity
ϕ	Volume filling factor of dust mantle
Ψ	Reduction factor of water sublimation flux beneath dust mantle
ρ_d	Density of dust particle
ρ_i	Density of water ice
a	Heat diffusivity
$\mathcal{A}$	Bolometric Bond albedo
c	Specific heat capacity
C_D	Drag coefficient
$\mathscr{F}$	Icy area fraction of nucleus surface or subsurface
F_G	Gas drag force
H	Thickness of dust mantle in terms of diameters of dust particles
$\mathcal{I}$	Thermal inertia
ℓ	Latent heat of volatile ice
λ_G	Mean free path of gas molecules
$\hat{m}$	Mass of a single molecule
m_d	Mass of dust particle
P_G	Gas pressure
P_t	Tensile strength
P_V	Saturation vapor pressure
$Q_{(0)}$	Total energy input on nucleus surface
$Q_\odot$	Solar flux absorbed by nucleus surface
$Q_\otimes$	Flux of absorbed nucleus thermal radiation

$\bar{Q}_\odot$	Solar flux at current heliocentric distance
q_ϵ	Heat flux of thermal radiation from nucleus surface
q_κ	Heat flux of thermal conduction
q_Z	Heat flux consumed by ice sublimation
r_d	Radius of dust particle
$r_\odot$	Heliocentric distance
$T_{(0)}$	Temperature of nucleus surface
U	Internal energy of nucleus with arbitrary reference
$\dot{U}$	Change rate of internal energy of nucleus
v_T	Thermal speed of gas
X	Thickness of dust mantle
Z	Mass flux of sublimation
$Z^{\mathrm{H\text{-}K}}$	Sublimation flux given by Hertz-Knudsen equation

Geometry of Nucleus Landscape

α	Azimuthal angle
$\delta(\alpha, \varphi)$	Visibility of open sky in the direction (α, φ)
φ	Elevation angle
θ	Incidence angle
$A_{\mathrm{F}\,k}$	Area of facet k
$\mathbf{v}_i$	Position vector of a vertex i of a facet
$\mathbf{e}_{i,j}$	Edge vector from vertex j to vertex i
$\mathbf{n}_k$	Normal vector to local plane of facet k
$\mathbf{r}_{\mathrm{F}\,k}$	Position vector of centroid of facet k
$\mathbf{R}^{[\mathrm{H}]}_{[\mathrm{BF}]}$	Rotation matrix transforming a vector from 67P body-fixed coordinate system to local horizontal system
$w_{k,l}$	Mutual viewing factor between facets k and l
$v_{k,l}$	Visibility factor between facets k and l
$d_{k,l}$	Distance between centroids of facets k and l

$\mathbf{r}^{[H]}$	Position vector in the local horizontal coordinate system

Other Variables

β	Ratio of solar radiation and gravitational forces
F_{rad}	Solar radiation force
P_{rad}	Solar radiation pressure

Bibliography

Acton, C. H.: 1996, *Planet. Space Sci.* **44**, 65

Agarwal, J., A'Hearn, M. F., Vincent, J.-B., Güttler, C., Höfner, S., Sierks, H., Tubiana, C., Barbieri, C., Lamy, P. L., Rodrigo, R., Koschny, D., Rickman, H., Barucci, M. A., Bertaux, J.-L., Bertini, I., Boudreault, S., Cremonese, G., Da Deppo, V., Davidsson, B., Debei, S., De Cecco, M., Deller, J., Fornasier, S., Fulle, M., Gicquel, A., Groussin, O., Gutiérrez, P. J., Hofmann, M., Hviid, S. F., Ip, W.-H., Jorda, L., Keller, H. U., Knollenberg, J., Kramm, J.-R., Kührt, E., Küppers, M., Lara, L. M., Lazzarin, M., Lopez Moreno, J. J., Marzari, F., Naletto, G., Oklay, N., Shi, X., and Thomas, N.: 2016, *MNRAS* **462**, S78

A'Hearn, M. F.: 2004, *Overview of cometary science*, pp 17–22, The University of Arizona Press

A'Hearn, M. F., Belton, M. J. S., Delamere, W. A., Feaga, L. M., Hampton, D., Kissel, J., Klaasen, K. P., McFadden, L. A., Meech, K. J., Melosh, H. J., Schultz, P. H., Sunshine, J. M., Thomas, P. C., Veverka, J., Wellnitz, D. D., Yeomans, D. K., Besse, S., Bodewits, D., Bowling, T. J., Carcich, B. T., Collins, S. M., Farnham, T. L., Groussin, O., Hermalyn, B., Kelley, M. S., Kelley, M. S., Li, J.-Y., Lindler, D. J., Lisse, C. M., McLaughlin, S. A., Merlin, F., Protopapa, S., Richardson, J. E., and Williams, J. L.: 2011, *Science* **332**, 1396

A'Hearn, M. F., Belton, M. J. S., Delamere, W. A., Kissel, J., Klaasen, K. P., McFadden, L. A., Meech, K. J., Melosh, H. J., Schultz, P. H., Sunshine, J. M., Thomas, P. C., Veverka, J., Yeomans, D. K., Baca, M. W., Busko, I., Crockett, C. J., Collins, S. M., Desnoyer, M., Eberhardy, C. A., Ernst, C. M., Farnham, T. L., Feaga, L., Groussin, O., Hampton, D., Ipatov, S. I., Li, J.-Y., Lindler, D., Lisse, C. M., Mastrodemos, N., Owen, W. M., Richardson, J. E., Wellnitz, D. D., and White, R. L.: 2005, *Science* **310**, 258

Asphaug, E. and Benz, W.: 1996, *Icarus* **121**, 225

Barucci, M. A., Filacchione, G., Fornasier, S., Raponi, A., Deshapriya, J. D. P., Tosi, F., Feller, C., Ciarniello, M., Sierks, H., Capaccioni, F., Pommerol, A., Massironi, M., Oklay, N., Merlin, F., Vincent, J.-B., Fulchignoni, M., Guilbert-Lepoutre, A., Perna, D., Capria, M. T., Hasselmann, P. H., Rousseau, B., Barbieri, C., Bockelée-Morvan, D., Lamy, P. L., De Sanctis, C., Rodrigo, R., Erard, S., Koschny, D., Leyrat, C., Rickman, H., Drossart, P., Keller, H. U., A'Hearn, M. F., Arnold, G., Bertaux, J.-L., Bertini, I., Cerroni, P., Cremonese, G., Da Deppo, V., Davidsson, B. J. R., El-Maarry, M. R., Fonti, S., Fulle, M., Groussin, O., Güttler, C., Hviid, S. F., Ip, W., Jorda, L., Kappel,

D., Knollenberg, J., Kramm, J.-R., Kührt, E., Küppers, M., Lara, L., Lazzarin, M., Lopez Moreno, J. J., Mancarella, F., Marzari, F., Mottola, S., Naletto, G., Pajola, M., Palomba, E., Quirico, E., Schmitt, B., Thomas, N., and Tubiana, C.: 2016, *A&A* **595**, A102

Basilevsky, A. T., Krasil'nikov, S. S., Shiryaev, A. A., Mall, U., Keller, H. U., Skorov, Y. V., Mottola, S., and Hviid, S. F.: 2016, *Solar System Research* **50(4)**, 225

Belton, M. J. S., Feldman, P. D., A'Hearn, M. F., and Carcich, B.: 2008, *Icarus* **198**, 189

Biele, J., Ulamec, S., Maibaum, M., Roll, R., Witte, L., Jurado, E., Muñoz, P., Arnold, W., Auster, H.-U., Casas, C., Faber, C., Fantinati, C., Finke, F., Fischer, H.-H., Geurts, K., Güttler, C., Heinisch, P., Herique, A., Hviid, S., Kargl, G., Knapmeyer, M., Knollenberg, J., Kofman, W., Kömle, N., Kührt, E., Lommatsch, V., Mottola, S., Pardo de Santayana, R., Remetean, E., Scholten, F., Seidensticker, K. J., Sierks, H., and Spohn, T.: 2015, *Science* 349(1)

Blum, J., Gundlach, B., Mühle, S., and Trigo-Rodriguez, J. M.: 2014, *Icarus* **235**, 156

Bockelée-Morvan, D., Debout, V., Erard, S., Leyrat, C., Capaccioni, F., Filacchione, G., Fougere, N., Drossart, P., Arnold, G., Combi, M., Schmitt, B., Crovisier, J., de Sanctis, M.-C., Encrenaz, T., Kührt, E., Palomba, E., Taylor, F. W., Tosi, F., Piccioni, G., Fink, U., Tozzi, G., Barucci, A., Biver, N., Capria, M.-T., Combes, M., Ip, W., Blecka, M., Henry, F., Jacquinod, S., Reess, J.-M., Semery, A., and Tiphene, D.: 2015, *A&A* **583**, A6

Brin, G. D.: 1980, *ApJ* **237**, 265

Brin, G. D. and Mendis, D. A.: 1979, *ApJ* **229**, 402

Brouwer, D. and Clemence, G. M.: 1961, *Methods of celestial mechanics*, New York: Academic Press

Brownlee, D., Tsou, P., Aléon, J., Alexander, C. M. O. ., Araki, T., Bajt, S., Baratta, G. A., Bastien, R., Bland, P., Bleuet, P., Borg, J., Bradley, J. P., Brearley, A., Brenker, F., Brennan, S., Bridges, J. C., Browning, N. D., Brucato, J. R., Bullock, E., Burchell, M. J., Busemann, H., Butterworth, A., Chaussidon, M., Cheuvront, A., Chi, M., Cintala, M. J., Clark, B. C., Clemett, S. J., Cody, G., Colangeli, L., Cooper, G., Cordier, P., Daghlian, C., Dai, Z., D'Hendecourt, L., Djouadi, Z., Dominguez, G., Duxbury, T., Dworkin, J. P., Ebel, D. S., Economou, T. E., Fakra, S., Fairey, S. A. J., Fallon, S., Ferrini, G., Ferroir, T., Fleckenstein, H., Floss, C., Flynn, G., Franchi, I. A., Fries, M., Gainsforth, Z., Gallien, J.-P., Genge, M., Gilles, M. K., Gillet, P., Gilmour, J., Glavin, D. P., Gounelle, M., Grady, M. M., Graham, G. A., Grant, P. G., Green, S. F., Grossemy, F., Grossman, L., Grossman, J. N., Guan, Y., Hagiya, K., Harvey, R., Heck, P., Herzog, G. F., Hoppe, P., Hörz, F., Huth, J., Hutcheon, I. D., Ignatyev, K., Ishii, H., Ito, M., Jacob, D., Jacobsen, C., Jacobsen, S., Jones, S., Joswiak, D., Jurewicz, A., Kearsley, A. T., Keller, L. P., Khodja, H., Kilcoyne, A. L. D., Kissel, J., Krot, A., Langenhorst, F., Lanzirotti, A., Le, L., Leshin, L. A., Leitner, J., Lemelle, L., Leroux, H., Liu, M.-C., Luening, K., Lyon, I., MacPherson, G., Marcus, M. A.,

Marhas, K., Marty, B., Matrajt, G., McKeegan, K., Meibom, A., Mennella, V., Messenger, K., Messenger, S., Mikouchi, T., Mostefaoui, S., Nakamura, T., Nakano, T., Newville, M., Nittler, L. R., Ohnishi, I., Ohsumi, K., Okudaira, K., Papanastassiou, D. A., Palma, R., Palumbo, M. E., Pepin, R. O., Perkins, D., Perronnet, M., Pianetta, P., Rao, W., Rietmeijer, F. J. M., Robert, F., Rost, D., Rotundi, A., Ryan, R., Sandford, S. A., Schwandt, C. S., See, T. H., Schlutter, D., Sheffield-Parker, J., Simionovici, A., Simon, S., Sitnitsky, I., Snead, C. J., Spencer, M. K., Stadermann, F. J., Steele, A., Stephan, T., Stroud, R., Susini, J., Sutton, S. R., Suzuki, Y., Taheri, M., Taylor, S., Teslich, N., Tomeoka, K., Tomioka, N., Toppani, A., Trigo-Rodríguez, J. M., Troadec, D., Tsuchiyama, A., Tuzzolino, A. J., Tyliszczak, T., Uesugi, K., Velbel, M., Vellenga, J., Vicenzi, E., Vincze, L., Warren, J., Weber, I., Weisberg, M., Westphal, A. J., Wirick, S., Wooden, D., Wopenka, B., Wozniakiewicz, P., Wright, I., Yabuta, H., Yano, H., Young, E. D., Zare, R. N., Zega, T., Ziegler, K., Zimmerman, L., Zinner, E., and Zolensky, M.: 2006, *Science* **314**, 1711

Brownlee, D. E., Horz, F., Newburn, R. L., Zolensky, M., Duxbury, T. C., Sandford, S., Sekanina, Z., Tsou, P., Hanner, M. S., Clark, B. C., Green, S. F., and Kissel, J.: 2004, *Science* **304**, 1764

Bruck Syal, M., Schultz, P. H., Sunshine, J. M., A'Hearn, M. F., Farnham, T. L., and Dearborn, D. S. P.: 2013, *Icarus* **222**, 610

Capaccioni, F., Coradini, A., Filacchione, G., Erard, S., Arnold, G., Drossart, P., De Sanctis, M. C., Bockelee-Morvan, D., Capria, M. T., Tosi, F., Leyrat, C., Schmitt, B., Quirico, E., Cerroni, P., Mennella, V., Raponi, A., Ciarniello, M., McCord, T., Moroz, L., Palomba, E., Ammannito, E., Barucci, M. A., Bellucci, G., Benkhoff, J., Bibring, J. P., Blanco, A., Blecka, M., Carlson, R., Carsenty, U., Colangeli, L., Combes, M., Combi, M., Crovisier, J., Encrenaz, T., Federico, C., Fink, U., Fonti, S., Ip, W. H., Irwin, P., Jaumann, R., Kuehrt, E., Langevin, Y., Magni, G., Mottola, S., Orofino, V., Palumbo, P., Piccioni, G., Schade, U., Taylor, F., Tiphene, D., Tozzi, G. P., Beck, P., Biver, N., Bonal, L., Combe, J.-P., Despan, D., Flamini, E., Fornasier, S., Frigeri, A., Grassi, D., Gudipati, M., Longobardo, A., Markus, K., Merlin, F., Orosei, R., Rinaldi, G., Stephan, K., Cartacci, M., Cicchetti, A., Giuppi, S., Hello, Y., Henry, F., Jacquinod, S., Noschese, R., Peter, G., Politi, R., Reess, J. M., and Semery, A.: 2015, *Science* **347(1)**, aaa0628

Capanna, C., Gesquière, G., Jorda, L., Lamy, P., and Vibert, D.: 2013, *The Visual Computer* **29(6)**, 825

Capria, M. T., Coradini, A., De Sanctis, M. C., and Orosei, R.: 2000, *A&A* **357**, 359

Carroll, B. W. and Ostlie, D. A.: 2007, *An Introduction to Modern Astrophysics (Second Edition)*, Pearson, San Francisco

Choukroun, M., Keihm, S., Schloerb, F. P., Gulkis, S., Lellouch, E., Leyrat, C., von Allmen, P., Biver, N., Bockelée-Morvan, D., Crovisier, J., Encrenaz, P., Hartogh, P., Hofstadter, M., Ip, W.-H., Jarchow, C., Janssen, M., Lee, S., Rezac, L., Beaudin, G., Gaskell, B., Jorda, L., Keller, H. U., and Sierks, H.: 2015, *A&A* **583**, A28

Combes, M., Moroz, V. I., Crifo, J. F., Lamarre, J. M., Charra, J., Sanko, N. F., Soufflot, A., Bibring, J. P., Cazes, S., Coron, N., Crovisier, J., Emerich, C., Encrenaz, T., Gispert, R., Grigoryev, A. V., Guyot, G., Krasnopolsky, V. A., Nikolsky, Y. V., and Rocard, F.: 1986, *Nature* **321**, 266

Combi, M. R. and Delsemme, A. H.: 1980, *ApJ* **238**, 381

Crifo, J. F.: 1997, *Icarus* **130**, 549

Crifo, J.-F., Rodionov, A. V., Szegö, K., and Fulle, M.: 2002, *Earth Moon and Planets* **90**, 227

Davidsson, B., Lee, S., Hofstadter, M., Sierks, H., Barbieri, C., Gulkis, S., Keller, H. U., Koschny, D., Lamy, P., Rickman, H., Rodrigo, R., the MIRO Team, and the OSIRIS Team: 2016a, in *Comets: A new vision after Rosetta/Philae*

Davidsson, B. J. R. and Gutiérrez, P. J.: 2005, *Icarus* **176**, 453

Davidsson, B. J. R., Gutiérrez, P. J., and Rickman, H.: 2009, *Icarus* **201**, 335

Davidsson, B. J. R., Sierks, H., Güttler, C., Marzari, F., Pajola, M., Rickman, H., A'Hearn, M. F., Auger, A.-T., El-Maarry, M. R., Fornasier, S., Gutiérrez, P. J., Keller, H. U., Massironi, M., Snodgrass, C., Vincent, J.-B., Barbieri, C., Lamy, P. L., Rodrigo, R., Koschny, D., Barucci, M. A., Bertaux, J.-L., Bertini, I., Cremonese, G., Da Deppo, V., Debei, S., De Cecco, M., Feller, C., Fulle, M., Groussin, O., Hviid, S. F., Höfner, S., Ip, W.-H., Jorda, L., Knollenberg, J., Kovacs, G., Kramm, J.-R., Kührt, E., Küppers, M., La Forgia, F., Lara, L. M., Lazzarin, M., Lopez Moreno, J. J., Moissl-Fraund, R., Mottola, S., Naletto, G., Oklay, N., Thomas, N., and Tubiana, C.: 2016b, *A&A* **592**, A63

Davidsson, B. J. R. and Skorov, Y. V.: 2002, *Icarus* **159**, 239

de Sanctis, M. C., Capaccioni, F., Capria, M. T., Coradini, A., Federico, C., Orosei, R., and Salomone, M.: 1999, *Planet. Space Sci.* **47**, 855

De Sanctis, M. C., Capaccioni, F., Ciarniello, M., Filacchione, G., Formisano, M., Mottola, S., Raponi, A., Tosi, F., Bockelée-Morvan, D., Erard, S., Leyrat, C., Schmitt, B., Ammannito, E., Arnold, G., Barucci, M. A., Combi, M., Capria, M. T., Cerroni, P., Ip, W.-H., Kuehrt, E., McCord, T. B., Palomba, E., Beck, P., Quirico, E., VIRTIS Team, Piccioni, G., Bellucci, G., Fulchignoni, M., Jaumann, R., Stephan, K., Longobardo, A., Mennella, V., Migliorini, A., Benkhoff, J., Bibring, J. P., Blanco, A., Blecka, M., Carlson, R., Carsenty, U., Colangeli, L., Combes, M., Crovisier, J., Drossart, P., Encrenaz, T., Federico, C., Fink, U., Fonti, S., Irwin, P., Langevin, Y., Magni, G., Moroz, L., Orofino, V., Schade, U., Taylor, F., Tiphene, D., Tozzi, G. P., Biver, N., Bonal, L., Combe, J.-P., Despan, D., Flamini, E., Fornasier, S., Frigeri, A., Grassi, D., Gudipati, M. S., Mancarella, F., Markus, K., Merlin, F., Orosei, R., Rinaldi, G., Cartacci, M., Cicchetti, A., Giuppi, S., Hello, Y., Henry, F., Jacquinod, S., Rees, J. M., Noschese, R., Politi, R., and Peter, G.: 2015, *Nature* **525**, 500

Della Corte, V., Rotundi, A., Fulle, M., Gruen, E., Weissman, P., Sordini, R., Ferrari, M., Ivanovski, S., Lucarelli, F., Accolla, M., Zakharov, V., Mazzotta Epifani, E., Lopez-Moreno, J. J., Rodriguez, J., Colangeli, L., Palumbo, P., Bussoletti, E., Crifo, J. F., Esposito, F., Green, S. F., Lamy, P. L., McDonnell, J. A. M., Mennella, V., Molina, A., Morales, R., Moreno, F., Ortiz, J. L., Palomba, E., Perrin, J. M., Rietmeijer, F. J. M., Rodrigo, R., Zarnecki, J. C., Cosi, M., Giovane, F., Gustafson, B., Herranz, M. L., Jeronimo, J. M., Leese, M. R., Lopez-Jimenez, A. C., and Altobelli, N.: 2015, *A&A* **583**, A13

Dones, L., Weissman, P. R., Levison, H. F., and Duncan, M. J.: 2004, *Oort cloud formation and dynamics*, pp 153–174, The University of Arizona Press

El-Maarry, M. R., Groussin, O., Thomas, N., Pajola, M., Auger, A.-T., Davidsson, B., Hu, X., Hviid, S. F., Knollenberg, J., Güttler, C., Tubiana, C., Fornasier, S., Feller, C., Hasselmann, P., Vincent, J.-B., Sierks, H., Barbieri, C., Lamy, P., Rodrigo, R., Koschny, D., Keller, H. U., Rickman, H., A'Hearn, M. F., Barucci, M. A., Bertaux, J.-L., Bertini, I., Besse, S., Bodewits, D., Cremonese, G., Da Deppo, V., Debei, S., De Cecco, M., Deller, J., Deshapriya, J. D. P., Fulle, M., Gutierrez, P. J., Hofmann, M., Ip, W.-H., Jorda, L., Kovacs, G., Kramm, J.-R., Kührt, E., Küppers, M., Lara, L. M., Lazzarin, M., Lin, Z.-Y., Lopez Moreno, J. J., Marchi, S., Marzari, F., Mottola, S., Naletto, G., Oklay, N., Pommerol, A., Preusker, F., Scholten, F., and Shi, X.: 2017, *Science* **355**, 1392

El-Maarry, M. R., Thomas, N., Giacomini, L., Massironi, M., Pajola, M., Marschall, R., Gracia-Berná, A., Sierks, H., Barbieri, C., Lamy, P. L., Rodrigo, R., Rickman, H., Koschny, D., Keller, H. U., Agarwal, J., A'Hearn, M. F., Auger, A.-T., Barucci, M. A., Bertaux, J.-L., Bertini, I., Besse, S., Bodewits, D., Cremonese, G., Da Deppo, V., Davidsson, B., De Cecco, M., Debei, S., Güttler, C., Fornasier, S., Fulle, M., Groussin, O., Gutierrez, P. J., Hviid, S. F., Ip, W.-H., Jorda, L., Knollenberg, J., Kovacs, G., Kramm, J.-R., Kührt, E., Küppers, M., La Forgia, F., Lara, L. M., Lazzarin, M., Lopez Moreno, J. J., Marchi, S., Marzari, F., Michalik, H., Naletto, G., Oklay, N., Pommerol, A., Preusker, F., Scholten, F., Tubiana, C., and Vincent, J.-B.: 2015, *A&A* **583**, A26

El-Maarry, M. R., Thomas, N., Gracia-Berná, A., Pajola, M., Lee, J.-C., Massironi, M., Davidsson, B., Marchi, S., Keller, H. U., Hviid, S. F., Besse, S., Sierks, H., Barbieri, C., Lamy, P. L., Koschny, D., Rickman, H., Rodrigo, R., A'Hearn, M. F., Auger, A.-T., Barucci, M. A., Bertaux, J.-L., Bertini, I., Bodewits, D., Cremonese, G., Da Deppo, V., De Cecco, M., Debei, S., Güttler, C., Fornasier, S., Fulle, M., Giacomini, L., Groussin, O., Gutierrez, P. J., Ip, W.-H., Jorda, L., Knollenberg, J., Kovacs, G., Kramm, J.-R., Kührt, E., Küppers, M., Lara, L. M., Lazzarin, M., Lopez Moreno, J. J., Marschall, R., Marzari, F., Naletto, G., Oklay, N., Pommerol, A., Preusker, F., Scholten, F., Tubiana, C., and Vincent, J.-B.: 2016, *A&A* **593**, A110

Enzian, A., Cabot, H., and Klinger, J.: 1997, *A&A* **319**, 995

ESA: 2017a, *GAS CHANGES DURING 29 JULY OUTBURST FROM COMET 67P/C-G*, `http://sci.esa.int/rosetta/`

56329-gas-changes-during-29-july-outburst-from-comet-67p/, Retrieved: Feb. 17, 2017

ESA: 2017b, *ROSETTA'S TARGET: COMET 67P/CHURYUMOV-GERASIMENKO*, http://sci.esa.int/rosetta/14615-comet-67p/, Retrieved: Jan. 29, 2017

Fanale, F. P. and Salvail, J. R.: 1984, *Icarus* **60**, 476

Farnham, T. L., Bodewits, D., Li, J.-Y., Veverka, J., Thomas, P., and Belton, M. J. S.: 2013, *Icarus* **222**, 540

Festou, M. C., Keller, H. U., and Weaver, H. A.: 2004, *A brief conceptual history of cometary science*, pp 3–16, The University of Arizona Press

Filacchione, G., de Sanctis, M. C., Capaccioni, F., Raponi, A., Tosi, F., Ciarniello, M., Cerroni, P., Piccioni, G., Capria, M. T., Palomba, E., Bellucci, G., Erard, S., Bockelee-Morvan, D., Leyrat, C., Arnold, G., Barucci, M. A., Fulchignoni, M., Schmitt, B., Quirico, E., Jaumann, R., Stephan, K., Longobardo, A., Mennella, V., Migliorini, A., Ammannito, E., Benkhoff, J., Bibring, J. P., Blanco, A., Blecka, M. I., Carlson, R., Carsenty, U., Colangeli, L., Combes, M., Combi, M., Crovisier, J., Drossart, P., Encrenaz, T., Federico, C., Fink, U., Fonti, S., Ip, W. H., Irwin, P., Kuehrt, E., Langevin, Y., Magni, G., McCord, T., Moroz, L., Mottola, S., Orofino, V., Schade, U., Taylor, F., Tiphene, D., Tozzi, G. P., Beck, P., Biver, N., Bonal, L., Combe, J.-P., Despan, D., Flamini, E., Formisano, M., Fornasier, S., Frigeri, A., Grassi, D., Gudipati, M. S., Kappel, D., Mancarella, F., Markus, K., Merlin, F., Orosei, R., Rinaldi, G., Cartacci, M., Cicchetti, A., Giuppi, S., Hello, Y., Henry, F., Jacquinod, S., Reess, J. M., Noschese, R., Politi, R., and Peter, G.: 2016, *Nature* **529**, 368

Fink, U., Doose, L., Rinaldi, G., Bieler, A., Capaccioni, F., Bockelée-Morvan, D., Filacchione, G., Erard, S., Leyrat, C., Blecka, M., Capria, M. T., Combi, M., Crovisier, J., De Sanctis, M. C., Fougere, N., Taylor, F., Migliorini, A., and Piccioni, G.: 2016, *Icarus* **277**, 78

Finson, M. J. and Probstein, R. F.: 1968, *ApJ* **154**, 327

Fornasier, S., Hasselmann, P. H., Barucci, M. A., Feller, C., Besse, S., Leyrat, C., Lara, L., Gutierrez, P. J., Oklay, N., Tubiana, C., Scholten, F., Sierks, H., Barbieri, C., Lamy, P. L., Rodrigo, R., Koschny, D., Rickman, H., Keller, H. U., Agarwal, J., A'Hearn, M. F., Bertaux, J.-L., Bertini, I., Cremonese, G., Da Deppo, V., Davidsson, B., Debei, S., De Cecco, M., Fulle, M., Groussin, O., Güttler, C., Hviid, S. F., Ip, W., Jorda, L., Knollenberg, J., Kovacs, G., Kramm, R., Kührt, E., Küppers, M., La Forgia, F., Lazzarin, M., Lopez Moreno, J. J., Marzari, F., Matz, K.-D., Michalik, H., Moreno, F., Mottola, S., Naletto, G., Pajola, M., Pommerol, A., Preusker, F., Shi, X., Snodgrass, C., Thomas, N., and Vincent, J.-B.: 2015, *A&A* **583**, A30

Fornasier, S., Mottola, S., Keller, H. U., Barucci, M. A., Davidsson, B., Feller, C., Deshapriya, J. D. P., Sierks, H., Barbieri, C., Lamy, P. L., Rodrigo, R., Koschny, D., Rickman, H., A'Hearn, M., Agarwal, J., Bertaux, J.-L., Bertini, I., Besse, S., Cremonese, G., Da Deppo, V., Debei, S., De Cecco, M., Deller, J., El-Maarry, M. R., Fulle, M.,

Groussin, O., Gutierrez, P. J., Güttler, C., Hofmann, M., Hviid, S. F., Ip, W.-H., Jorda, L., Knollenberg, J., Kovacs, G., Kramm, R., Kührt, E., Küppers, M., Lara, M. L., Lazzarin, M., Moreno, J. J. L., Marzari, F., Massironi, M., Naletto, G., Oklay, N., Pajola, M., Pommerol, A., Preusker, F., Scholten, F., Shi, X., Thomas, N., Toth, I., Tubiana, C., and Vincent, J.-B.: 2016, *Science* **354**, 1566

Fougere, N., Altwegg, K., Berthelier, J.-J., Bieler, A., Bockelée-Morvan, D., Calmonte, U., Capaccioni, F., Combi, M. R., De Keyser, J., Debout, V., Erard, S., Fiethe, B., Filacchione, G., Fink, U., Fuselier, S. A., Gombosi, T. I., Hansen, K. C., Hässig, M., Huang, Z., Le Roy, L., Leyrat, C., Migliorini, A., Piccioni, G., Rinaldi, G., Rubin, M., Shou, Y., Tenishev, V., Toth, G., and Tzou, C.-Y.: 2016a, *A&A* **588**, A134

Fougere, N., Altwegg, K., Berthelier, J.-J., Bieler, A., Bockelée-Morvan, D., Calmonte, U., Capaccioni, F., Combi, M. R., De Keyser, J., Debout, V., Erard, S., Fiethe, B., Filacchione, G., Fink, U., Fuselier, S. A., Gombosi, T. I., Hansen, K. C., Hässig, M., Huang, Z., Le Roy, L., Leyrat, C., Migliorini, A., Piccioni, G., Rinaldi, G., Rubin, M., Shou, Y., Tenishev, V., Toth, G., and Tzou, C.-Y.: 2016b, *MNRAS* **462**, S156

Froeschle, C., Klinger, J., and Rickman, H.: 1983, in C.-I. Lagerkvist and H. Rickman (eds.), *Asteroids, Comets, and Meteors*, pp 215–224

Froeschlé, C. and Rickman, H.: 1986, *A&A* **170**, 145

Fulle, M.: 2004, *Motion of cometary dust*, pp 565–575, The University of Arizona Press

Fulle, M., Altobelli, N., Buratti, B., Choukroun, M., Fulchignoni, M., Grün, E., Taylor, M. G. G. T., and Weissman, P.: 2016a, *MNRAS* **462**, S2

Fulle, M., Barbieri, C., Cremonese, G., Rauer, H., Weiler, M., Milani, G., and Ligustri, R.: 2004, *A&A* **422**, 357

Fulle, M., Colangeli, L., Agarwal, J., Aronica, A., Della Corte, V., Esposito, F., Grün, E., Ishiguro, M., Ligustri, R., Lopez Moreno, J. J., Mazzotta Epifani, E., Milani, G., Moreno, F., Palumbo, P., Rodríguez Gómez, J., and Rotundi, A.: 2010, *A&A* **522**, A63

Fulle, M., Della Corte, V., Rotundi, A., Rietmeijer, F. J. M., Green, S. F., Weissman, P., Accolla, M., Colangeli, L., Ferrari, M., Ivanovski, S., Lopez-Moreno, J. J., Epifani, E. M., Morales, R., Ortiz, J. L., Palomba, E., Palumbo, P., Rodriguez, J., Sordini, R., and Zakharov, V.: 2016b, *MNRAS* **462**, S132

Fulle, M., Marzari, F., Della Corte, V., Fornasier, S., Sierks, H., Rotundi, A., Barbieri, C., Lamy, P. L., Rodrigo, R., Koschny, D., Rickman, H., Keller, H. U., López-Moreno, J. J., Accolla, M., Agarwal, J., A'Hearn, M. F., Altobelli, N., Barucci, M. A., Bertaux, J.-L., Bertini, I., Bodewits, D., Bussoletti, E., Colangeli, L., Cosi, M., Cremonese, G., Crifo, J.-F., Da Deppo, V., Davidsson, B., Debei, S., De Cecco, M., Esposito, F., Ferrari, M., Giovane, F., Gustafson, B., Green, S. F., Groussin, O., Grün, E., Gutierrez, P., Güttler, C., Herranz, M. L., Hviid, S. F., Ip, W., Ivanovski, S. L., Jerónimo, J. M., Jorda, L., Knollenberg, J., Kramm, R., Kührt, E., Küppers, M., Lara, L., Lazzarin, M., Leese, M. R., López-Jiménez, A. C., Lucarelli, F., Mazzotta Epifani, E., McDonnell,

J. A. M., Mennella, V., Molina, A., Morales, R., Moreno, F., Mottola, S., Naletto, G., Oklay, N., Ortiz, J. L., Palomba, E., Palumbo, P., Perrin, J.-M., Rietmeijer, F. J. M., Rodríguez, J., Sordini, R., Thomas, N., Tubiana, C., Vincent, J.-B., Weissman, P., Wenzel, K.-P., Zakharov, V., and Zarnecki, J. C.: 2016c, *ApJ* **821**, 19

Gaskell, R. W., Barnouin-Jha, O. S., Scheeres, D. J., Konopliv, A. S., Mukai, T., Abe, S., Saito, J., Ishiguro, M., Kubota, T., Hashimoto, T., Kawaguchi, J., Yoshikawa, M., Shirakawa, K., Kominato, T., Hirata, N., and Demura, H.: 2008, *Meteoritics and Planetary Science* **43**, 1049

Gortsas, N.: 2010, *Ph.D. thesis*, Technische Universtät Braunschweig

Gortsas, N., Kührt, E., Motschmann, U., and Keller, H. U.: 2011, *Icarus* **212**, 858

Grier, D. A.: 2007, *When Computers were Human*, Princeton University Press

Groussin, O., Jorda, L., Auger, A.-T., Kührt, E., Gaskell, R., Capanna, C., Scholten, F., Preusker, F., Lamy, P., Hviid, S., Knollenberg, J., Keller, U., Huettig, C., Sierks, H., Barbieri, C., Rodrigo, R., Koschny, D., Rickman, H., A'Hearn, M. F., Agarwal, J., Barucci, M. A., Bertaux, J.-L., Bertini, I., Boudreault, S., Cremonese, G., Da Deppo, V., Davidsson, B., Debei, S., De Cecco, M., El-Maarry, M. R., Fornasier, S., Fulle, M., Gutiérrez, P. J., Güttler, C., Ip, W.-H., Kramm, J.-R., Küppers, M., Lazzarin, M., Lara, L. M., Lopez Moreno, J. J., Marchi, S., Marzari, F., Massironi, M., Michalik, H., Naletto, G., Oklay, N., Pommerol, A., Pajola, M., Thomas, N., Toth, I., Tubiana, C., and Vincent, J.-B.: 2015a, *A&A* **583**, A32

Groussin, O. and Lamy, P.: 2003, *A&A* **412**, 879

Groussin, O., Sierks, H., Barbieri, C., Lamy, P., Rodrigo, R., Koschny, D., Rickman, H., Keller, H. U., A'Hearn, M. F., Auger, A.-T., Barucci, M. A., Bertaux, J.-L., Bertini, I., Besse, S., Cremonese, G., Da Deppo, V., Davidsson, B., Debei, S., De Cecco, M., El-Maarry, M. R., Fornasier, S., Fulle, M., Gutiérrez, P. J., Güttler, C., Hviid, S., Ip, W.-H., Jorda, L., Knollenberg, J., Kovacs, G., Kramm, J. R., Kührt, E., Küppers, M., Lara, L. M., Lazzarin, M., Lopez Moreno, J. J., Lowry, S., Marchi, S., Marzari, F., Massironi, M., Mottola, S., Naletto, G., Oklay, N., Pajola, M., Pommerol, A., Thomas, N., Toth, I., Tubiana, C., and Vincent, J.-B.: 2015b, *A&A* **583**, A36

Groussin, O., Sunshine, J. M., Feaga, L. M., Jorda, L., Thomas, P. C., Li, J.-Y., A'Hearn, M. F., Belton, M. J. S., Besse, S., Carcich, B., Farnham, T. L., Hampton, D., Klaasen, K., Lisse, C., Merlin, F., and Protopapa, S.: 2013, *Icarus* **222**, 580

Grün, E., Agarwal, J., Altobelli, N., Altwegg, K., Bentley, M. S., Biver, N., Della Corte, V., Edberg, N., Feldman, P. D., Galand, M., Geiger, B., Götz, C., Grieger, B., Güttler, C., Henri, P., Hofstadter, M., Horanyi, M., Jehin, E., Krüger, H., Lee, S., Mannel, T., Morales, E., Mousis, O., Müller, M., Opitom, C., Rotundi, A., Schmied, R., Schmidt, F., Sierks, H., Snodgrass, C., Soja, R. H., Sommer, M., Srama, R., Tzou, C.-Y., Vincent, J.-B., Yanamandra-Fisher, P., A'Hearn, M. F., Erikson, A. I., Barbieri, C., Barucci, M. A., Bertaux, J.-L., Bertini, I., Burch, J., Colangeli, L., Cremonese, G., Da Deppo, V., Davidsson, B., Debei, S., De Cecco, M., Deller, J., Feaga, L. M., Ferrari, M.,

Fornasier, S., Fulle, M., Gicquel, A., Gillon, M., Green, S. F., Groussin, O., Gutiérrez, P. J., Hofmann, M., Hviid, S. F., Ip, W.-H., Ivanovski, S., Jorda, L., Keller, H. U., Knight, M. M., Knollenberg, J., Koschny, D., Kramm, J.-R., Kührt, E., Küppers, M., Lamy, P. L., Lara, L. M., Lazzarin, M., Lòpez-Moreno, J. J., Manfroid, J., Epifani, E. M., Marzari, F., Naletto, G., Oklay, N., Palumbo, P., Parker, J. W., Rickman, H., Rodrigo, R., Rodrìguez, J., Schindhelm, E., Shi, X., Sordini, R., Steffl, A. J., Stern, S. A., Thomas, N., Tubiana, C., Weaver, H. A., Weissman, P., Zakharov, V. V., and Taylor, M. G. G. T.: 2016, *MNRAS* **462**, S220

Grün, E., Bar-Nun, A., Benkhoff, J., Bischoff, A., Dueren, H., Hellmann, H., Hesselbarth, P., Hsiung, P., Keller, H. U., and Klinger, J.: 1991, in R. L. Newburn, Jr., M. Neugebauer, and J. Rahe (eds.), *IAU Colloq. 116: Comets in the post-Halley era*, Vol. 167 of *Astrophysics and Space Science Library*, pp 277–297

Grün, E., Benkhoff, J., Fechtig, H., Hesselbarth, P., Klinger, J., Kochan, H., Kohl, H., Krankowsky, D., Lammerzahl, P., Seboldt, W., Spohn, T., and Thiel, K.: 1989, *Advances in Space Research* **9**, 133

Gulkis, S., Allen, M., von Allmen, P., Beaudin, G., Biver, N., Bockelée-Morvan, D., Choukroun, M., Crovisier, J., Davidsson, B. J. R., Encrenaz, P., Encrenaz, T., Frerking, M., Hartogh, P., Hofstadter, M., Ip, W.-H., Janssen, M., Jarchow, C., Keihm, S., Lee, S., Lellouch, E., Leyrat, C., Rezac, L., Schloerb, F. P., and Spilker, T.: 2015, *Science* **347(1)**, aaa0709

Gundlach, B. and Blum, J.: 2012, *Icarus* **219**, 618

Gundlach, B., Blum, J., Keller, H. U., and Skorov, Y. V.: 2015, *A&A* **583**, A12

Gundlach, B., Skorov, Y. V., and Blum, J.: 2011, *Icarus* **213**, 710

Gutiérrez, P. J., Ortiz, J. L., Rodrigo, R., and López-Moreno, J. J.: 2001, *A&A* **374**, 326

Hässig, M., Altwegg, K., Balsiger, H., Bar-Nun, A., Berthelier, J. J., Bieler, A., Bochsler, P., Briois, C., Calmonte, U., Combi, M., De Keyser, J., Eberhardt, P., Fiethe, B., Fuselier, S. A., Galand, M., Gasc, S., Gombosi, T. I., Hansen, K. C., Jäckel, A., Keller, H. U., Kopp, E., Korth, A., Kührt, E., Le Roy, L., Mall, U., Marty, B., Mousis, O., Neefs, E., Owen, T., Rème, H., Rubin, M., Sémon, T., Tornow, C., Tzou, C.-Y., Waite, J. H., and Wurz, P.: 2015, *Science* **347(1)**, aaa0276

Heiskanen, W. A. and Moritz, H.: 1967, *Physical geodesy*, San Francisco, W. H. Freeman [1967]

Hogg, F. S.: 1929, *JRASC* **23**, 55

Horn, B. K.: 1977, *Artificial intelligence* **8(2)**, 201

Hu, X., Shi, X., Sierks, H., Blum, J., Oberst, J., Fulle, M., Kührt, E., Güttler, C., Gundlach, B., Keller, H. U., Mottola, S., Pajola, M., Barbieri, C., Lamy, P. L., Rodrigo, R., Koschny, D., Rickman, H., Agarwal, J., A'Hearn, M. F., Barucci, M. A., Bertaux,

J.-L., Bertini, I., Boudreault, S., Büttner, I., Cremonese, G., Da Deppo, V., Davidsson, B., Debei, S., De Cecco, M., Deller, J., Fornasier, S., Groussin, O., Gutiérrez, P. J., Gutiérrez-Marqués, P., Hall, I., Hofmann, M., Hviid, S. F., Ip, W.-H., Jorda, L., Knollenberg, J., Kovacs, G., Kramm, J. R., Küppers, M., Lara, L. M., Lazzarin, M., López-Moreno, J. J., Marzari, F., Naletto, G., Oklay, N., Richards, M. L., Ripken, J., Thomas, N., Tubiana, C., and Vincent, J.-B.: 2017a, *MNRAS* **469**, S295

Hu, X., Shi, X., Sierks, H., Fulle, M., Blum, J., Keller, H. U., Kührt, E., Davidsson, B., Güttler, C., Gundlach, B., Pajola, M., Bodewits, D., Vincent, J.-B., Oklay, N., Massironi, M., Fornasier, S., Tubiana, C., Groussin, O., Boudreault, S., Höfner, S., Mottola, S., Barbieri, C., Lamy, P. L., Rodrigo, R., Koschny, D., Rickman, H., A'Hearn, M., Agarwal, J., Barucci, M. A., Bertaux, J.-L., Bertini, I., Cremonese, G., Da Deppo, V., Debei, S., De Cecco, M., Deller, J., El-Maarry, M. R., Gicquel, A., Gutierrez-Marques, P., Gutiérrez, P. J., Hofmann, M., Hviid, S. F., Ip, W.-H., Jorda, L., Knollenberg, J., Kovacs, G., Kramm, J.-R., Küppers, M., Lara, L. M., Lazzarin, M., Lopez-Moreno, J. J., Marzari, F., Naletto, G., and Thomas, N.: 2017b, *A&A* **604**, A114

Huebner, W. F., Benkhoff, J., Capria, M.-T., Coradini, A., De Sanctis, C., Orosei, R., and Prialnik, D. (eds.): 2006, *Heat and Gas Diffusion in Comet Nuclei*

Hughes, D. W.: 1987, *Philosophical Transactions of the Royal Society of London Series A* **323**, 349

Jorda, L., Gaskell, R., Capanna, C., Hviid, S., Lamy, P., Ďurech, J., Faury, G., Groussin, O., Gutiérrez, P., Jackman, C., Keihm, S. J., Keller, H. U., Knollenberg, J., Kührt, E., Marchi, S., Mottola, S., Palmer, E., Schloerb, F. P., Sierks, H., Vincent, J.-B., A'Hearn, M. F., Barbieri, C., Rodrigo, R., Koschny, D., Rickman, H., Barucci, M. A., Bertaux, J. L., Bertini, I., Cremonese, G., Da Deppo, V., Davidsson, B., Debei, S., De Cecco, M., Fornasier, S., Fulle, M., Güttler, C., Ip, W.-H., Kramm, J. R., Küppers, M., Lara, L. M., Lazzarin, M., Lopez Moreno, J. J., Marzari, F., Naletto, G., Oklay, N., Thomas, N., Tubiana, C., and Wenzel, K.-P.: 2016, *Icarus* **277**, 257

JPL: 2016, *67P/Churyumov-Gerasimenko*, JPL Small-Body Database Browser, `http://ssd.jpl.nasa.gov/sbdb.cgi?sstr=67P`, (Retrieved on Jan. 30, 2017)

Kaasalainen, M., Mottola, S., and Fulchignoni, M.: 2002, *Asteroid Models from Disk-integrated Data*, pp 139–150, The University of Arizona Press

Kaasalainen, M. and Torppa, J.: 2001, *Icarus* **153**, 24

Keller, H. U.: 1989, in J. J. Hunt and T. D. Guyenne (eds.), *Physics and Mechanics of Cometary Materials*, Vol. 302 of *ESA Special Publication*

Keller, H. U., Arpigny, C., Barbieri, C., Bonnet, R. M., Cazes, S., Coradini, M., Cosmovici, C. B., Delamere, W. A., Huebner, W. F., Hughes, D. W., Jamar, C., Malaise, D., Reitsema, H. J., Schmidt, H. U., Schmidt, W. K. H., Seige, P., Whipple, F. L., and Wilhelm, K.: 1986, *Nature* **321**, 320

Keller, H. U., Barbieri, C., Koschny, D., Lamy, P., Rickman, H., Rodrigo, R., Sierks, H., A'Hearn, M. F., Angrilli, F., Barucci, M. A., Bertaux, J.-L., Cremonese, G., Da Deppo, V., Davidsson, B., De Cecco, M., Debei, S., Fornasier, S., Fulle, M., Groussin, O., Gutierrez, P. J., Hviid, S. F., Ip, W.-H., Jorda, L., Knollenberg, J., Kramm, J. R., Kührt, E., Küppers, M., Lara, L.-M., Lazzarin, M., Moreno, J. L., Marzari, F., Michalik, H., Naletto, G., Sabau, L., Thomas, N., Wenzel, K.-P., Bertini, I., Besse, S., Ferri, F., Kaasalainen, M., Lowry, S., Marchi, S., Mottola, S., Sabolo, W., Schröder, S. E., Spjuth, S., and Vernazza, P.: 2010, *Science* **327**, 190

Keller, H. U., Barbieri, C., Lamy, P., Rickman, H., Rodrigo, R., Wenzel, K.-P., Sierks, H., A'Hearn, M. F., Angrilli, F., Angulo, M., Bailey, M. E., Barthol, P., Barucci, M. A., Bertaux, J.-L., Bianchini, G., Boit, J.-L., Brown, V., Burns, J. A., Büttner, I., Castro, J. M., Cremonese, G., Curdt, W., da Deppo, V., Debei, S., de Cecco, M., Dohlen, K., Fornasier, S., Fulle, M., Germerott, D., Gliem, F., Guizzo, G. P., Hviid, S. F., Ip, W.-H., Jorda, L., Koschny, D., Kramm, J. R., Kührt, E., Küppers, M., Lara, L. M., Llebaria, A., López, A., López-Jimenez, A., López-Moreno, J., Meller, R., Michalik, H., Michelena, M. D., Müller, R., Naletto, G., Origné, A., Parzianello, G., Pertile, M., Quintana, C., Ragazzoni, R., Ramous, P., Reiche, K.-U., Reina, M., Rodríguez, J., Rousset, G., Sabau, L., Sanz, A., Sivan, J.-P., Stöckner, K., Tabero, J., Telljohann, U., Thomas, N., Timon, V., Tomasch, G., Wittrock, T., and Zaccariotto, M.: 2007, *Space Sci. Rev.* **128**, 433

Keller, H. U., Mottola, S., Davidsson, B., Schröder, S. E., Skorov, Y., Kührt, E., Groussin, O., Pajola, M., Hviid, S. F., Preusker, F., Scholten, F., A'Hearn, M. F., Sierks, H., Barbieri, C., Lamy, P., Rodrigo, R., Koschny, D., Rickman, H., Barucci, M. A., Bertaux, J.-L., Bertini, I., Cremonese, G., Da Deppo, V., Debei, S., De Cecco, M., Fornasier, S., Fulle, M., Gutiérrez, P. J., Ip, W.-H., Jorda, L., Knollenberg, J., Kramm, J. R., Küppers, M., Lara, L. M., Lazzarin, M., Lopez Moreno, J. J., Marzari, F., Michalik, H., Naletto, G., Sabau, L., Thomas, N., Vincent, J.-B., Wenzel, K.-P., Agarwal, J., Güttler, C., Oklay, N., and Tubiana, C.: 2015a, *A&A* **583**, A34

Keller, H. U., Mottola, S., Skorov, Y., and Jorda, L.: 2015b, *A&A* **579**, L5

Kelley, M. S., Wooden, D. H., Tubiana, C., Boehnhardt, H., Woodward, C. E., and Harker, D. E.: 2009, *AJ* **137**, 4633

Knollenberg, J., Lin, Z. Y., Hviid, S. F., Oklay, N., Vincent, J.-B., Bodewits, D., Mottola, S., Pajola, M., Sierks, H., Barbieri, C., Lamy, P., Rodrigo, R., Koschny, D., Rickman, H., A'Hearn, M. F., Barucci, M. A., Bertaux, J. L., Bertini, I., Cremonese, G., Davidsson, B., Da Deppo, V., Debei, S., De Cecco, M., Fornasier, S., Fulle, M., Groussin, O., Gutiérrez, P. J., Ip, W.-H., Jorda, L., Keller, H. U., Kührt, E., Kramm, J. R., Küppers, M., Lara, L. M., Lazzarin, M., Lopez Moreno, J. J., Marzari, F., Naletto, G., Thomas, N., Güttler, C., Preusker, F., Scholten, F., and Tubiana, C.: 2016, *A&A* **596**, A89

Kochan, H., Feuerbacher, B., Joo, F., Klinger, J., Seboldt, W., Bischoff, A., Duren, H., Stoffler, D., Spohn, T., Fechtig, H., Grün, E., Kohl, H., Krankowsky, D., Roessler, K., Thiel, K., Schwehm, G., and Weishaupt, U.: 1989, *Advances in Space Research* **9**, 113

Kofman, W., Herique, A., Barbin, Y., Barriot, J.-P., Ciarletti, V., Clifford, S., Edenhofer, P., Elachi, C., Eyraud, C., Goutail, J.-P., Heggy, E., Jorda, L., Lasue, J., Levasseur-Regourd, A.-C., Nielsen, E., Pasquero, P., Preusker, F., Puget, P., Plettemeier, D., Rogez, Y., Sierks, H., Statz, C., Svedhem, H., Williams, I., Zine, S., and Van Zyl, J.: 2015, *Science* 349(2)

Kramer, E. A., Fernandez, Y. R., Lisse, C. M., Kelley, M. S. P., and Woodney, L. M.: 2014, *Icarus* **236**, 136

Kramer, T. and Noack, M.: 2015, *ApJ* **813**, L33

Krankowsky, D., Lammerzahl, P., Herrwerth, I., Woweries, J., Eberhardt, P., Dolder, U., Herrmann, U., Schulte, W., Berthelier, J. J., Illiano, J. M., Hodges, R. R., and Hoffman, J. H.: 1986, *Nature* **321**, 326

Królikowska, M.: 2003, *Acta Astron.* **53**, 195

Krüger, H., Seidensticker, K. J., Fischer, H.-H., Albin, T., Apathy, I., Arnold, W., Flandes, A., Hirn, A., Kobayashi, M., Loose, A., Péter, A., and Podolak, M.: 2015, *A&A* **583**, A15

Kührt, E.: 1984, *Icarus* **60**, 512

Kührt, E.: 1999, *Space Sci. Rev.* **90**, 75

Kührt, E. and Keller, H. U.: 1994, *Icarus* **109**, 121

Küppers, M., Bertini, I., Fornasier, S., Gutierrez, P. J., Hviid, S. F., Jorda, L., Keller, H. U., Knollenberg, J., Koschny, D., Kramm, R., Lara, L.-M., Sierks, H., Thomas, N., Barbieri, C., Lamy, P., Rickman, H., Rodrigo, R., A'Hearn, M. F., Angrilli, F., Bailey, M., Barthol, P., Barucci, M. A., Bertaux, J.-L., Burns, J. A., Cremonese, G., Curdt, W., De Cecco, M., Debei, S., Fulle, M., Gliem, F., Ip, W. H., Huhrt, E., Llebaria, A., Lopez Moreno, J. J., Marzari, F., Naletto, G., Sabau, L., Sanz Andres, A., Sivan, J. P., Tondello, G., and Wenzel, K.-P.: 2005, *Nature* **437**, 987

Lagerros, J. S. V.: 1997, *A&A* **325**, 1226

Lamy, P. L., Toth, I., Davidsson, B. J. R., Groussin, O., Gutiérrez, P., Jorda, L., Kaasalainen, M., and Lowry, S. C.: 2007, *Space Sci. Rev.* **128**, 23

Lamy, P. L., Toth, I., Fernández, Y. R., and Weaver, H. A.: 2004, *The sizes, shapes, albedos, and colors of cometary nuclei*, pp 223–264, The University of Arizona Press

Lamy, P. L., Toth, I., Groussin, O., Jorda, L., Kelley, M. S., and Stansberry, J. A.: 2008, *A&A* **489**, 777

Lamy, P. L., Toth, I., Weaver, H. A., Jorda, L., Kaasalainen, M., and Gutiérrez, P. J.: 2006, *A&A* **458**, 669

Lara, L. M., Lowry, S., Vincent, J.-B., Gutiérrez, P. J., Rożek, A., La Forgia, F., Oklay, N., Sierks, H., Barbieri, C., Lamy, P. L., Rodrigo, R., Koschny, D., Rickman, H., Keller, H. U., Agarwal, J., Auger, A.-T., A'Hearn, M. F., Barucci, M. A., Bertaux, J.-L., Bertini, I., Besse, S., Bodewits, D., Cremonese, G., Davidsson, B., Da Deppo, V., Debei, S., De Cecco, M., El-Maarry, M. R., Ferri, F., Fornasier, S., Fulle, M., Groussin, O., Gutiérrez-Marques, P., Güttler, C., Hviid, S. F., Ip, W.-H., Jorda, L., Knollenberg, J., Kovacs, G., Kramm, J.-R., Kührt, E., Küppers, M., Lazzarin, M., Lin, Z.-Y., López-Moreno, J. J., Magrin, S., Marzari, F., Michalik, H., Moissl-Fraund, R., Moreno, F., Mottola, S., Naletto, G., Pajola, M., Pommerol, A., Thomas, N., Sabau, M. D., and Tubiana, C.: 2015, *A&A* **583**, A9

Legland, D.: 2009, geom3d, MATLAB Central File Exchange, `https://de.mathworks.com/matlabcentral/fileexchange/24484-geom3d` (Retrieved: Mar. 1, 2015)

Levison, H. F., Dones, L., and Duncan, M. J.: 2001, *AJ* **121**, 2253

Lowry, S., Duddy, S. R., Rozitis, B., Green, S. F., Fitzsimmons, A., Snodgrass, C., Hsieh, H. H., and Hainaut, O.: 2012, *A&A* **548**, A12

Lowry, S. C., Fitzsimmons, A., Jorda, L., Kaasalainen, M., Lamy, P., and Toth, I.: 2006, in *AAS/Division for Planetary Sciences Meeting Abstracts #38*, Vol. 38 of *Bulletin of the American Astronomical Society*, p. 492

Marsden, B. G.: 1997, *Earth Moon and Planets* **79**, 3

Massironi, M., Simioni, E., Marzari, F., Cremonese, G., Giacomini, L., Pajola, M., Jorda, L., Naletto, G., Lowry, S., El-Maarry, M. R., Preusker, F., Scholten, F., Sierks, H., Barbieri, C., Lamy, P., Rodrigo, R., Koschny, D., Rickman, H., Keller, H. U., A'Hearn, M. F., Agarwal, J., Auger, A.-T., Barucci, M. A., Bertaux, J.-L., Bertini, I., Besse, S., Bodewits, D., Capanna, C., da Deppo, V., Davidsson, B., Debei, S., de Cecco, M., Ferri, F., Fornasier, S., Fulle, M., Gaskell, R., Groussin, O., Gutiérrez, P. J., Güttler, C., Hviid, S. F., Ip, W.-H., Knollenberg, J., Kovacs, G., Kramm, R., Kührt, E., Küppers, M., La Forgia, F., Lara, L. M., Lazzarin, M., Lin, Z.-Y., Lopez Moreno, J. J., Magrin, S., Michalik, H., Mottola, S., Oklay, N., Pommerol, A., Thomas, N., Tubiana, C., and Vincent, J.-B.: 2015, *Nature* **526**, 402

Mekler, Y., Prialnik, D., and Podolak, M.: 1990, *ApJ* **356**, 682

Mendis, D. A. and Brin, G. D.: 1977, *Moon* **17**, 359

Morbidelli, A.: 2005, *ArXiv Astrophysics e-prints*

Mottola, S., Arnold, G., Grothues, H.-G., Jaumann, R., Michaelis, H., Neukum, G., Bibring, J.-P., Schröder, S. E., Hamm, M., Otto, K. A., Pelivan, I., Proffe, G., Scholten, F., Tirsch, D., Kreslavsky, M., Remetean, E., Souvannavong, F., and Dolives, B.: 2015, *Science* 349(2)

Oberst, J., Giese, B., Howington-Kraus, E., Kirk, R., Soderblom, L., Buratti, B., Hicks, M., Nelson, R., and Britt, D.: 2004, *Icarus* **167**, 70

Özişik, M. N.: 1985, *Heat Transfer: A Basic Approach*, McGraw-Hill Book Company, New York

Pajola, M., Höfner, S., Vincent, J. B., Oklay, N., Scholten, F., Preusker, F., Mottola, S., Naletto, G., Fornasier, S., Lowry, S., Feller, C., Hasselmann, P. H., Güttler, C., Tubiana, C., Sierks, H., Barbieri, C., Lamy, P., Rodrigo, R., Koschny, D., Rickman, H., Keller, H. U., Agarwal, J., A'Hearn, M. F., Barucci, M. A., Bertaux, J.-L., Bertini, I., Besse, S., Boudreault, S., Cremonese, G., da Deppo, V., Davidsson, B., Debei, S., de Cecco, M., Deller, J., Deshapriya, J. D. P., El-Maarry, M. R., Ferrari, S., Ferri, F., Fulle, M., Groussin, O., Gutierrez, P., Hofmann, M., Hviid, S. F., Ip, W.-H., Jorda, L., Knollenberg, J., Kovacs, G., Kramm, J. R., Kührt, E., Küppers, M., Lara, L. M., Lin, Z.-Y., Lazzarin, M., Lucchetti, A., Lopez Moreno, J. J., Marzari, F., Massironi, M., Michalik, H., Penasa, L., Pommerol, A., Simioni, E., Thomas, N., Toth, I., and Baratti, E.: 2017, *Nature Astronomy* **1**, 0092

Pajola, M., Vincent, J.-B., Güttler, C., Lee, J.-C., Bertini, I., Massironi, M., Simioni, E., Marzari, F., Giacomini, L., Lucchetti, A., Barbieri, C., Cremonese, G., Naletto, G., Pommerol, A., El-Maarry, M. R., Besse, S., Küppers, M., La Forgia, F., Lazzarin, M., Thomas, N., Auger, A.-T., Sierks, H., Lamy, P., Rodrigo, R., Koschny, D., Rickman, H., Keller, H. U., Agarwal, J., A'Hearn, M. F., Barucci, M. A., Bertaux, J.-L., Da Deppo, V., Davidsson, B., De Cecco, M., Debei, S., Ferri, F., Fornasier, S., Fulle, M., Groussin, O., Gutierrez, P. J., Hviid, S. F., Ip, W.-H., Jorda, L., Knollenberg, J., Kramm, J.-R., Kürt, E., Lara, L. M., Lin, Z.-Y., Lopez Moreno, J. J., Magrin, S., Marchi, S., Michalik, H., Moissl, R., Mottola, S., Oklay, N., Preusker, F., Scholten, F., and Tubiana, C.: 2015, *A&A* **583**, A37

Pätzold, M., Andert, T., Hahn, M., Asmar, S. W., Barriot, J.-P., Bird, M. K., Häusler, B., Peter, K., Tellmann, S., Grün, E., Weissman, P. R., Sierks, H., Jorda, L., Gaskell, R., Preusker, F., and Scholten, F.: 2016, *Nature* **530**, 63

Preusker, F., Scholten, F., Matz, K.-D., Roatsch, T., Willner, K., Hviid, S. F., Knollenberg, J., Jorda, L., Gutiérrez, P. J., Kührt, E., Mottola, S., A'Hearn, M. F., Thomas, N., Sierks, H., Barbieri, C., Lamy, P., Rodrigo, R., Koschny, D., Rickman, H., Keller, H. U., Agarwal, J., Barucci, M. A., Bertaux, J.-L., Bertini, I., Cremonese, G., Da Deppo, V., Davidsson, B., Debei, S., De Cecco, M., Fornasier, S., Fulle, M., Groussin, O., Güttler, C., Ip, W.-H., Kramm, J. R., Küppers, M., Lara, L. M., Lazzarin, M., Lopez Moreno, J. J., Marzari, F., Michalik, H., Naletto, G., Oklay, N., Tubiana, C., and Vincent, J.-B.: 2015, *A&A* **583**, A33

Prialnik, D. and Mekler, Y.: 1991, *ApJ* **366**, 318

Reinhard, R.: 1986, *Nature* **321**, 313

Rickman, H. and Froeschlé, C.: 1986, *A&A* **170**, 161

Rindfleisch, T.: 1966, *Photogrammetric Engineering* **32**, 262

Rotundi, A., Sierks, H., Della Corte, V., Fulle, M., Gutierrez, P. J., Lara, L., Barbieri, C., Lamy, P. L., Rodrigo, R., Koschny, D., Rickman, H., Keller, H. U., López-Moreno,

J. J., Accolla, M., Agarwal, J., A'Hearn, M. F., Altobelli, N., Angrilli, F., Barucci, M. A., Bertaux, J.-L., Bertini, I., Bodewits, D., Bussoletti, E., Colangeli, L., Cosi, M., Cremonese, G., Crifo, J.-F., Da Deppo, V., Davidsson, B., Debei, S., De Cecco, M., Esposito, F., Ferrari, M., Fornasier, S., Giovane, F., Gustafson, B., Green, S. F., Groussin, O., Grün, E., Güttler, C., Herranz, M. L., Hviid, S. F., Ip, W., Ivanovski, S., Jerónimo, J. M., Jorda, L., Knollenberg, J., Kramm, R., Kührt, E., Küppers, M., Lazzarin, M., Leese, M. R., López-Jiménez, A. C., Lucarelli, F., Lowry, S. C., Marzari, F., Epifani, E. M., McDonnell, J. A. M., Mennella, V., Michalik, H., Molina, A., Morales, R., Moreno, F., Mottola, S., Naletto, G., Oklay, N., Ortiz, J. L., Palomba, E., Palumbo, P., Perrin, J.-M., Rodríguez, J., Sabau, L., Snodgrass, C., Sordini, R., Thomas, N., Tubiana, C., Vincent, J.-B., Weissman, P., Wenzel, K.-P., Zakharov, V., and Zarnecki, J. C.: 2015, *Science* **347(1)**, aaa3905

Sagdeev, R. Z., Szabo, F., Avanesov, G. A., Cruvellier, P., Szabo, L., Szego, K., Abergel, A., Balazs, A., Barinov, I. V., Bertaux, J.-L., Blamount, J., Detaille, M., Demarelis, E., Dul'Nev, G. N., Endroczy, G., Gardos, M., Kanyo, M., Kostenko, V. I., Krasikov, V. A., Nguyen-Trong, T., Nyitrai, Z., Reny, I., Rusznyak, P., Shamis, V. A., Smith, B., Sukhanov, K. G., Szabo, F., Szalai, S., Tarnopolsky, V. I., Toth, I., Tsukanova, G., Valnicek, B. I., Varhalmi, L., Zaiko, Y. K., Zatsepin, S. I., Ziman, Y. L., Zsenei, M., and Zhukov, B. S.: 1986, *Nature* **321**, 262

Schleicher, D. G.: 2006, *Icarus* **181**, 442

Schwehm, G. and Schulz, R.: 1999, *Space Sci. Rev.* **90**, 313

Sekanina, Z., Brownlee, D. E., Economou, T. E., Tuzzolino, A. J., and Green, S. F.: 2004, *Science* **304**, 1769

Shi, X., Hu, X., Sierks, H., Güttler, C., A'Hearn, M., Blum, J., El-Maarry, M. R., Kührt, E., Mottola, S., Pajola, M., Oklay, N., Fornasier, S., Tubiana, C., Keller, H. U., Vincent, J.-B., Bodewits, D., Höfner, S., Lin, Z.-Y., Gicquel, A., Hofmann, M., Barbieri, C., Lamy, P. L., Rodrigo, R., Koschny, D., Rickman, H., Barucci, M. A., Bertaux, J.-L., Bertini, I., Cremonese, G., Da Deppo, V., Davidsson, B., Debei, S., De Cecco, M., Fulle, M., Groussin, O., Gutiérrez, P. J., Hviid, S. F., Ip, W.-H., Jorda, L., Knollenberg, J., Kovacs, G., Kramm, J.-R., Küppers, M., Lara, L. M., Lazzarin, M., Lopez-Moreno, J. J., Marzari, F., Naletto, G., and Thomas, N.: 2016a, *A&A* **586**, A7

Shi, X., Hu, X., Sierks, H., Kührt, E., Güttler, C., Knollenberg, J., and Oklay, N.: 2016b, in *EGU General Assembly Conference Abstracts*, Vol. 18 of *EGU General Assembly Conference Abstracts*, p. 15876

Shkuratov, Y., Kaydash, V., Korokhin, V., Velikodsky, Y., Opanasenko, N., and Videen, G.: 2011, *Planet. Space Sci.* **59**, 1326

Sierks, H., Barbieri, C., Lamy, P. L., Rodrigo, R., Koschny, D., Rickman, H., Keller, H. U., Agarwal, J., A'Hearn, M. F., Angrilli, F., Auger, A.-T., Barucci, M. A., Bertaux, J.-L., Bertini, I., Besse, S., Bodewits, D., Capanna, C., Cremonese, G., Da Deppo, V., Davidsson, B., Debei, S., De Cecco, M., Ferri, F., Fornasier, S., Fulle, M., Gaskell, R., Giacomini, L., Groussin, O., Gutierrez-Marques, P., Gutiérrez, P. J., Güttler, C.,

Hoekzema, N., Hviid, S. F., Ip, W.-H., Jorda, L., Knollenberg, J., Kovacs, G., Kramm, J. R., Kührt, E., Küppers, M., La Forgia, F., Lara, L. M., Lazzarin, M., Leyrat, C., Lopez Moreno, J. J., Magrin, S., Marchi, S., Marzari, F., Massironi, M., Michalik, H., Moissl, R., Mottola, S., Naletto, G., Oklay, N., Pajola, M., Pertile, M., Preusker, F., Sabau, L., Scholten, F., Snodgrass, C., Thomas, N., Tubiana, C., Vincent, J.-B., Wenzel, K.-P., Zaccariotto, M., and Pätzold, M.: 2015, *Science* **347(1)**, aaa1044

Sierks, H., Lamy, P., Barbieri, C., Koschny, D., Rickman, H., Rodrigo, R., A'Hearn, M. F., Angrilli, F., Barucci, M. A., Bertaux, J.-L., Bertini, I., Besse, S., Carry, B., Cremonese, G., Da Deppo, V., Davidsson, B., Debei, S., De Cecco, M., De Leon, J., Ferri, F., Fornasier, S., Fulle, M., Hviid, S. F., Gaskell, R. W., Groussin, O., Gutierrez, P., Ip, W., Jorda, L., Kaasalainen, M., Keller, H. U., Knollenberg, J., Kramm, R., Kührt, E., Küppers, M., Lara, L., Lazzarin, M., Leyrat, C., Moreno, J. J. L., Magrin, S., Marchi, S., Marzari, F., Massironi, M., Michalik, H., Moissl, R., Naletto, G., Preusker, F., Sabau, L., Sabolo, W., Scholten, F., Snodgrass, C., Thomas, N., Tubiana, C., Vernazza, P., Vincent, J.-B., Wenzel, K.-P., Andert, T., Pätzold, M., and Weiss, B. P.: 2011, *Science* **334**, 487

Skorov, Y. and Blum, J.: 2012, *Icarus* **221**, 1

Skorov, Y. V., Lieshout, R. v., Blum, J., and Keller, H. U.: 2011, *Icarus* **212**, 867

Skorov, Y. V. and Rickman, H.: 1995, *Planet. Space Sci.* **43**, 1587

Smoluchowski, R.: 1981, *Icarus* **47**, 312

Soderblom, L. A., Becker, T. L., Bennett, G., Boice, D. C., Britt, D. T., Brown, R. H., Buratti, B. J., Isbell, C., Giese, B., Hare, T., Hicks, M. D., Howington-Kraus, E., Kirk, R. L., Lee, M., Nelson, R. M., Oberst, J., Owen, T. C., Rayman, M. D., Sandel, B. R., Stern, S. A., Thomas, N., and Yelle, R. V.: 2002, *Science* **296**, 1087

Spohn, T. and Benkhoff, J.: 1990, *Icarus* **87**, 358

Spohn, T., Knollenberg, J., Ball, A. J., Banaszkiewicz, M., Benkhoff, J., Grott, M., Grygorczuk, J., Hüttig, C., Hagermann, A., Kargl, G., Kaufmann, E., Kömle, N., Kührt, E., Kossacki, K. J., Marczewski, W., Pelivan, I., Schrödter, R., and Seiferlin, K.: 2015, *Science* 349(2)

Stern, S. A. and Colwell, J. E.: 1997, *ApJ* **490**, 879

Sunshine, J. M., Groussin, O., Schultz, P. H., A'Hearn, M. F., Feaga, L. M., Farnham, T. L., and Klaasen, K. P.: 2007, *Icarus* **190**, 284

Thomas, N., Davidsson, B., El-Maarry, M. R., Fornasier, S., Giacomini, L., Gracia-Berná, A. G., Hviid, S. F., Ip, W.-H., Jorda, L., Keller, H. U., Knollenberg, J., Kührt, E., La Forgia, F., Lai, I. L., Liao, Y., Marschall, R., Massironi, M., Mottola, S., Pajola, M., Poch, O., Pommerol, A., Preusker, F., Scholten, F., Su, C. C., Wu, J. S., Vincent, J.-B., Sierks, H., Barbieri, C., Lamy, P. L., Rodrigo, R., Koschny, D., Rickman, H., A'Hearn, M. F., Barucci, M. A., Bertaux, J.-L., Bertini, I., Cremonese, G., Da Deppo, V., Debei, S., de Cecco, M., Fulle, M., Groussin, O., Gutierrez, P. J., Kramm, J.-R., Küppers, M.,

Lara, L. M., Lazzarin, M., Lopez Moreno, J. J., Marzari, F., Michalik, H., Naletto, G., Agarwal, J., Güttler, C., Oklay, N., and Tubiana, C.: 2015a, *A&A* **583**, A17

Thomas, N., Sierks, H., Barbieri, C., Lamy, P. L., Rodrigo, R., Rickman, H., Koschny, D., Keller, H. U., Agarwal, J., A'Hearn, M. F., Angrilli, F., Auger, A.-T., Barucci, M. A., Bertaux, J.-L., Bertini, I., Besse, S., Bodewits, D., Cremonese, G., Da Deppo, V., Davidsson, B., De Cecco, M., Debei, S., El-Maarry, M. R., Ferri, F., Fornasier, S., Fulle, M., Giacomini, L., Groussin, O., Gutierrez, P. J., Güttler, C., Hviid, S. F., Ip, W.-H., Jorda, L., Knollenberg, J., Kramm, J.-R., Kührt, E., Küppers, M., La Forgia, F., Lara, L. M., Lazzarin, M., Moreno, J. J. L., Magrin, S., Marchi, S., Marzari, F., Massironi, M., Michalik, H., Moissl, R., Mottola, S., Naletto, G., Oklay, N., Pajola, M., Pommerol, A., Preusker, F., Sabau, L., Scholten, F., Snodgrass, C., Tubiana, C., Vincent, J.-B., and Wenzel, K.-P.: 2015b, *Science* **347(1)**, aaa0440

Thomas, P., A'Hearn, M., Belton, M. J. S., Brownlee, D., Carcich, B., Hermalyn, B., Klaasen, K., Sackett, S., Schultz, P. H., Veverka, J., Bhaskaran, S., Bodewits, D., Chesley, S., Clark, B., Farnham, T., Groussin, O., Harris, A., Kissel, J., Li, J.-Y., Meech, K., Melosh, J., Quick, A., Richardson, J., Sunshine, J., and Wellnitz, D.: 2013, *Icarus* **222**, 453

Tubiana, C.: 2008, Ph.D. dissertation, Technische Universität Braunschweig

Tubiana, C., Barrera, L., Drahus, M., and Boehnhardt, H.: 2008, *A&A* **490**, 377

Tubiana, C., Güttler, C., Kovacs, G., Bertini, I., Bodewits, D., Fornasier, S., Lara, L., La Forgia, F., Magrin, S., Pajola, M., Sierks, H., Barbieri, C., Lamy, P. L., Rodrigo, R., Koschny, D., Rickman, H., Keller, H. U., Agarwal, J., A'Hearn, M. F., Barucci, M. A., Bertaux, J.-L., Besse, S., Boudreault, S., Cremonese, G., Da Deppo, V., Davidsson, B., Debei, S., De Cecco, M., El-Maarry, M. R., Fulle, M., Groussin, O., Gutiérrez-Marques, P., Gutiérrez, P. J., Hoekzema, N., Hofmann, M., Hviid, S. F., Ip, W.-H., Jorda, L., Knollenberg, J., Kramm, J.-R., Kührt, E., Küppers, M., Lazzarin, M., Lopez Moreno, J. J., Marzari, F., Massironi, M., Michalik, H., Moissl, R., Naletto, G., Oklay, N., Scholten, F., Shi, X., Thomas, N., and Vincent, J.-B.: 2015, *A&A* **583**, A46

Veverka, J., Klaasen, K., A'Hearn, M., Belton, M., Brownlee, D., Chesley, S., Clark, B., Economou, T., Farquhar, R., Green, S. F., Groussin, O., Harris, A., Kissel, J., Li, J.-Y., Meech, K., Melosh, J., Richardson, J., Schultz, P., Silen, J., Sunshine, J., Thomas, P., Bhaskaran, S., Bodewits, D., Carcich, B., Cheuvront, A., Farnham, T., Sackett, S., Wellnitz, D., and Wolf, A.: 2013, *Icarus* **222**, 424

Vincent, J.-B., A'Hearn, M. F., Lin, Z.-Y., El-Maarry, M. R., Pajola, M., Sierks, H., Barbieri, C., Lamy, P. L., Rodrigo, R., Koschny, D., Rickman, H., Keller, H. U., Agarwal, J., Barucci, M. A., Bertaux, J.-L., Bertini, I., Besse, S., Bodewits, D., Cremonese, G., Da Deppo, V., Davidsson, B., Debei, S., De Cecco, M., Deller, J., Fornasier, S., Fulle, M., Gicquel, A., Groussin, O., Gutiérrez, P. J., Gutiérrez-Marquez, P., Güttler, C., Höfner, S., Hofmann, M., Hviid, S. F., Ip, W.-H., Jorda, L., Knollenberg, J., Kovacs, G., Kramm, J.-R., Kührt, E., Küppers, M., Lara, L. M., Lazzarin, M., Lopez Moreno, J. J., Marzari, F., Massironi, M., Mottola, S., Naletto, G., Oklay, N., Preusker,

F., Scholten, F., Shi, X., Thomas, N., Toth, I., and Tubiana, C.: 2016a, *MNRAS* **462**, S184

Vincent, J.-B., Bodewits, D., Besse, S., Sierks, H., Barbieri, C., Lamy, P., Rodrigo, R., Koschny, D., Rickman, H., Keller, H. U., Agarwal, J., A'Hearn, M. F., Auger, A.-T., Barucci, M. A., Bertaux, J.-L., Bertini, I., Capanna, C., Cremonese, G., da Deppo, V., Davidsson, B., Debei, S., de Cecco, M., El-Maarry, M. R., Ferri, F., Fornasier, S., Fulle, M., Gaskell, R., Giacomini, L., Groussin, O., Guilbert-Lepoutre, A., Gutierrez-Marques, P., Gutiérrez, P. J., Güttler, C., Hoekzema, N., Höfner, S., Hviid, S. F., Ip, W.-H., Jorda, L., Knollenberg, J., Kovacs, G., Kramm, R., Kührt, E., Küppers, M., La Forgia, F., Lara, L. M., Lazzarin, M., Lee, V., Leyrat, C., Lin, Z.-Y., Lopez Moreno, J. J., Lowry, S., Magrin, S., Maquet, L., Marchi, S., Marzari, F., Massironi, M., Michalik, H., Moissl, R., Mottola, S., Naletto, G., Oklay, N., Pajola, M., Preusker, F., Scholten, F., Thomas, N., Toth, I., and Tubiana, C.: 2015, *Nature* **523**, 63

Vincent, J.-B., Oklay, N., Pajola, M., Höfner, S., Sierks, H., Hu, X., Barbieri, C., Lamy, P. L., Rodrigo, R., Koschny, D., Rickman, H., Keller, H. U., A'Hearn, M. F., Barucci, M. A., Bertaux, J.-L., Bertini, I., Besse, S., Bodewits, D., Cremonese, G., Da Deppo, V., Davidsson, B., Debei, S., De Cecco, M., El-Maarry, M. R., Fornasier, S., Fulle, M., Groussin, O., Gutiérrez, P. J., Gutiérrez-Marquez, P., Güttler, C., Hofmann, M., Hviid, S. F., Ip, W.-H., Jorda, L., Knollenberg, J., Kovacs, G., Kramm, J.-R., Kührt, E., Küppers, M., Lara, L. M., Lazzarin, M., Lin, Z.-Y., Lopez Moreno, J. J., Lowry, S., Marzari, F., Massironi, M., Moreno, F., Mottola, S., Naletto, G., Preusker, F., Scholten, F., Shi, X., Thomas, N., Toth, I., and Tubiana, C.: 2016b, *A&A* **587**, A14

Weidenschilling, S. J.: 1977, *MNRAS* **180**, 57

Weidenschilling, S. J.: 2004, *From icy grains to comets*, pp 97–104, The University of Arizona Press

Weissman, P. R. and Kieffer, H. H.: 1981, *Icarus* **47**, 302

Werner, R. A. and Scheeres, D. J.: 1997, *Celestial Mechanics and Dynamical Astronomy* **65**, 313

Whipple, F. L.: 1950, *ApJ* **111**, 375

Whipple, F. L.: 1951, *ApJ* **113**, 464

Whipple, F. L.: 1955, *ApJ* **121**, 750

Xu, Z., Pankenier, D. W., and Jiang, Y.: 2000, *East Asian Archaeoastronomy: Historical Records of Astronomical Observations of China, Japan and Korea*, Amsterdam, The Netherlands: Gordon and Breach Science Publishers

Yeomans, D. K.: 2007, *Great Comets in History*, `http://ssd.jpl.nasa.gov/?great_comets`, Retrieved: Mar. 01, 2017

Yeomans, D. K. and Kiang, T.: 1981, *MNRAS* **197**, 633

Yeomans, D. K., Rahe, J., and Freitag, R. S.: 1986, *JRASC* **80**, 62

Publication

Refereed

- Hu, X., Shi, X., Sierks, H., Blum, J., Oberst, J., Fulle, M., Kührt, E., Güttler, C., Gundlach, B., Keller, H. U., Mottola, S., et al. (2017), Thermal modeling of water activity on comet 67P/Churyumov-Gerasimenko with global dust mantle and plural dust-to-Ice ratio, *Monthly Notices of the Royal Astronomical Society*, 469, S295-S311.

- Hu, X., Shi, X., Sierks, H., Fulle, M., Blum, J., Keller, H. U., Kührt, E., Davidsson, B., Güttler, C., Gundlach, B., et al. (2017), Seasonal erosion and restoration of the dust cover on comet 67P/Churyumov-Gerasimenko as observed by Rosetta/OSIRIS, *Astronomy & Astrophysics*, 604, A114.

- Shi, X., Hu, X., Sierks, H., Güttler, C., A'Hearn, M., Blum, J., El-Maarry, M. R., Kührt, E., Mottola, S., Pajola, M., et al. (2016), Sunset jets observed on comet 67P/Churyumov-Gerasimenko sustained by subsurface thermal lag, *Astronomy & Astrophysics*, 586, A7.

- Vincent, J.-B., Oklay, N., Pajola, M., Höfner, S., Sierks, H., Hu, X., Barbieri, C., Lamy, P. L., Rodrigo, R., Koschny, D., et al. (2016), Are fractured cliffs the source of cometary dust jets? Insights from OSIRIS/Rosetta at 67P/Churyumov-Gerasimenko, *Astronomy & Astrophysics*, 587, A14.

- El-Maarry, M. R., Groussin, O., Thomas, N., Pajola, M., Auger, A.-T., Davidsson, B., Hu, X., Hviid, S. F., Knollenberg, J., Güttler, C., et al. (2017), Surface changes on comet 67P/Churyumov-Gerasimenko suggest a more active past, *Science*, vol. 355, no. 6332, pp. 1392-1395.

- Blum, J., Gundlach, B., Krause, M., Fulle, M., Johansen, A., Agarwal, J., von Borstel, I., Shi, X., Hu, X., Bentley, M. S., et al. (2017), Evidence for the formation of comet 67P/Churyumov-Gerasimenko through gravitational collapse of a bound clump of pebbles, *Monthly Notices of the Royal Astronomical Society*, vol. 469, pp. S755-S773.

Acknowledgement

The work presented in this dissertation was carried out in the Department of Planets and Comets at Max Planck Institute for Solar System Research (MPS) in Göttingen, Germany. I gratefully acknowledge the financial support and the curriculum offered by the International Max Planck Research School for Solar System Science (IMPRS) at MPS. I thank our coordinator, Dr. Sonja Schuh, and her predecessor, Dr. Dieter Schmitt, for their assistance on numerous academic, administrational, and personal matters.

My advisors, Dr. Holger Sierks, Professor Dr. Jürgen Blum, and Professor Dr. Jürgen Oberst provided expert guidance and unfailing support throughout my research. I thank Professor Dr. Andreas Hördt for evaluating the dissertation and moderating the examination procedure.

This work benefitted from collaborations and discussions with the following colleagues, Dr. Xian Shi, Dr. Marco Fulle, Dr. Ekkehard Kührt, Dr. Carsten Güttler, Dr. Sebastian Höfner, Dr. Bastian Gundlach, Dr. Ingo von Borstel, Prof. Dr. Horst Uwe Keller, Dr. Stubbe Hviid, Dr. Björn Davidsson, Dr. Cecilia Tubiana, Dr. Jean-Baptiste Vincent, Dr. Nilda Oklay-Vincent, Dr. Stefano Mottola, among many others. I thank the OSIRIS Team and, in particular, the group at MPS, whose hard work made the imaging data of comet 67P available early for the analysis. Dr. Carsten Güttler provided the German translation of the abstract of this dissertation in English.

OSIRIS was built by a consortium led by MPS, in collaboration with CISAS, University of Padova, Italy, the Laboratoire d'Astrophysique de Marseille, France, the Instituto de Astrofísica de Andalucia, CSIC, Granada, Spain, the Scientific Support Office of the European Space Agency, Noordwijk, The Netherlands, the Instituto Nacional de Técnica Aeroespacial, Madrid, Spain, the Universidad Politéchnica de Madrid, Spain, the Department of Physics and Astronomy of Uppsala University, Sweden, and the Institut für Datentechnik und Kommunikationsnetze der Technischen Universität Braunschweig, Germany. The support of the national funding agencies of Germany (DLR), France (CNES), Italy (ASI), Spain (MEC), Sweden (SNSB), and the ESA Technical Directorate is gratefully acknowledged.